

# **Development of a Device for the Determination of Local Magnetic Properties of Thin Films on Whole Wafers**

Von der Fakultät für Maschinenbau  
der Gottfried Wilhelm Leibniz Universität Hannover  
zur Erlangung des akademischen Grades  
Doktor der Ingenieurwissenschaften  
Dr.-Ing.  
genehmigte Dissertation

von  
Dipl.-Ing.

Eike Christian Fischer

2023

1. Referent: Prof. Dr.-Ing. Hans Jürgen Maier
2. Referent: Prof. Dr.-Ing. Marc Christopher Wurz
3. Referent: Prof. Dr.-Ing. Gerhard Poll

Tag der Promotion: 8. März 2023

## Preface

Valued readers,

the present thesis has been created during my time as Research Assistant at the Institute of Micro Production Technology. It was financially supported by the state of Lower Saxony and by our industrial partner and client GlobalFoundries. As they came up with the request for a device for the examination of magnetic layers without the need of dicing the wafer in the first place, they made it possible for me to design and investigate a novel measurement device within the framework of a doctoral thesis. I hope it will help in the future to cut development times and costs short and maybe allow for new findings in magnetic layer deposition.

For my time at the IMPT with helpful and smart colleagues who made me really like working at the institute during the years, I want to thank all of them. Our head engineer Dr. Marc Wurz, who practically led the institute due to the absence of a professor did a very good job in keeping up the team spirit and spreading a good mood. I thank him aswell in supporting my graduation with his endurance in doing two jobs at once to keep the institute alive.

Finally, I want to say thanks to Prof. Hans Jürgen Maier who supervised my doctorate in his position as provisional director of our institute. In addition to the workload of his own institute and his own Ph.D. students, he kept an eye on us all.

Now, I can only wish you joy with reading my thesis.

Yours,  
Eike Christian Fischer



## Kurzfassung

Die Untersuchung lokaler magnetischen Eigenschaften von Dünnschichten erfordert ein empfindliches Messgerät und kleine chipförmige Proben, die in dessen Magnetfeld passen. Dafür muss der Wafer trenngeschliffen werden, was jedoch zur Folge hat, dass dieser im Anschluss nicht weiter prozessiert werden kann. Soll mehr als nur ein Punkt des Wafers untersucht werden, müssen viele dieser Chips einzeln analysiert werden. Im Gegensatz dazu ermöglicht das in dieser Arbeit entwickelte Gerät die Messung lokaler magnetischer Eigenschaften von durchgängigen Schichten auf ganzen Wafern. Dazu werden Techniken genutzt, die aus dem Bereich der Charakterisierung von Transformatorblechen bekannt sind. Das Prinzip, einen jochförmigen Magneten auf die Probe zu setzen, wurde so angepasst, dass Schichten mit einer Dicke von bis zu 100 nm untersucht werden können. Der Messkopf erzeugt dabei das notwendige Magnetfeld und enthält alle Sensoren, um die Hysteresekurve der Probe aufzuzeichnen. Mithilfe von Algorithmen wird dabei die magnetische Flussdichte in der Schicht berechnet, sodass keine Induktionsspule um die Probe gewickelt werden muss.

Durch die enge Abstimmung der entwickelten Hardware, Elektronik und Software können Messungen mit Feldern von bis zu 2,5 kA/m im Frequenzbereich von 50 Hz bis 50 kHz durchgeführt werden. Um dabei eine hohe Reproduzierbarkeit zu erlangen und orts aufgelöste Messungen zu ermöglichen, wurde ein motorisierter Teststand aufgebaut, der durch eine auf LabVIEW basierende Softwarelösung gesteuert wird. Die Charakterisierung des Systems hat Rauschpegel von 0,1 A/m für die Feldstärke und  $2 \cdot 10^{-11}$  Wb für den magnetischen Fluss ergeben, was einer Flussdichte von 25 mT in einer 100 nm dicken Schicht entspricht. Die erfassten Hysteresekurven von verschiedenen Proben wurde mit Referenzmessungen verglichen, die sowohl mit einem Vibrationsmagnetometer als auch mit einem Hystereseschleifenprüfer aufgezeichnet wurden. Die Ergebnisse belegen die Funktionsfähigkeit des Messgeräts, zeigen aber auch, dass es eine Abweichung bei der gemessenen Koerzitivfeldstärke gibt, während die Flussdichte gut mit der Referenzmessung übereinstimmt.

Zusammenfassend stellt diese neuartige Messmethode eine schnelle und bequeme Möglichkeit zur Untersuchung der magnetischen Eigenschaften von Dünnschichten dar. In einem entsprechenden Teststand könnte das Verfahren vollautomatische Testabläufe wie etwa das Kartografieren der Schicht auf einem Wafers innerhalb von Minuten ermöglichen. Da es zerstörungsfrei ist, könnte es zwischen verschiedenen Prozessschritten im Reinraum eingesetzt werden und damit Entwicklungszeiten reduzieren und die Qualitätssicherung erleichtern.

Schlagworte: Magnetische Dünnschichten, Magnetische Messtechnik, Zerstörungsfreie Messung



## Abstract

The examination of local magnetic properties of thin films requires a sensible measurement device and small chip-like specimens, which fit in the machine's magnetic field. Therefore, the carrier wafer has to be diced, which, however, renders it unusable for further processing. If more than a single spot on the wafer is of interest, multiple of these chips have to be examined one piece at a time. In contrast, the device developed within the scope of this thesis allows the measurement of local magnetic properties of continuous layers on whole wafers. For this purpose, it employs techniques known and used in the field of transformer sheet characterization. The principle of placing a magnetizing yoke on top of the specimen has been adapted in order to allow the investigation of layers with a thickness as low as 100 nm. The resulting measurement head generates the necessary field and contains all the sensors for the detection of the hysteresis loop of the specimen. Using algorithms, the flux density in the layer is calculated on the basis of the flux in the magnetizing yoke, which eliminates the need of placing a coil around the specimen.

Due to the close matching of the developed hardware, electronics, and software, magnetic measurements with excitation fields of up to 2.5 kA/m in the frequency range from 50 Hz to 50 kHz are feasible. In order to obtain a high reproducibility and enable spatially resolved measurements, a motorized test stand was constructed, which is controlled by a software solution implemented with LabVIEW. The characterization of the device revealed RMS noise levels of 0.1 A/m in terms of field strength and  $2 \cdot 10^{-11}$  Wb in terms of flux, which corresponds to a flux density of 25 mT in a 100 nm layer. The acquired hysteresis loops of different thin film samples are compared to reference measurements obtained both with a vibrating sample magnetometer and a hysteresis loop tracer. The results demonstrate the functionality of the device but also show that there is a deviation of the measured coercivity, while the flux density matches the references well.

In summary, this novel measurement method represents a fast and convenient way for the examination of the magnetic properties of thin films. Employed in a suitable test stand, it could enable fully automated test procedures like a mapping of the layer on a wafer within minutes. Since it is a non-destructive measurement method, it could be used in the clean room in between different process steps and therefore reduce development times and facilitate quality assurance.

Keywords: Magnetic thin films, Magnetic measurement technology, Non-destructive measurement





# Contents

<b>List of Figures</b>	<b>xvii</b>
<b>List of Tables</b>	<b>xix</b>
<b>List of Symbols</b>	<b>xxi</b>
<b>Abbreviations</b>	<b>xxv</b>
<b>1 Introduction</b>	<b>1</b>
<b>2 State of the Art</b>	<b>3</b>
2.1 Fundamentals of Electromagnetism . . . . .	3
2.1.1 Early Laws of Magnetism . . . . .	4
2.1.2 Maxwell's Equations . . . . .	7
2.1.3 Types of Magnetism . . . . .	7
2.1.4 Hysteresis Loop . . . . .	9
2.1.5 Demagnetization Effect . . . . .	10
2.2 Magnetic Thin Films . . . . .	13
2.2.1 Magnetic Domains . . . . .	13
2.2.2 Size Effects . . . . .	14
2.2.3 Domain Wall Mobility and Iron Loss . . . . .	15
2.2.4 Ferromagnetic Resonance and Magnetic Anisotropy . . . . .	17
2.3 Devices for the Measurement of the Magnetization . . . . .	17
2.3.1 Vibrating Sample Magnetometer . . . . .	18
2.3.2 Alternating Gradient Magnetometer . . . . .	20
2.3.3 Hysteresis Loop Tracer . . . . .	21
2.3.4 Transmission Line Method . . . . .	22
2.3.5 Permeameters . . . . .	23
2.3.6 Single Sheet Tester . . . . .	24
2.3.7 Conclusion . . . . .	27
2.4 Technologies for the Measurement of the Magnetic Field Strength . . . . .	28
2.4.1 Induction Coil . . . . .	29
2.4.2 Hall Probe . . . . .	32
2.4.3 Magnetoresistive Sensors (AMR, GMR, MTJ) . . . . .	34
2.4.4 Conclusion . . . . .	41

<b>3</b>	<b>Concept of the Measurement Device</b>	<b>43</b>
<b>4</b>	<b>Layout of the Measurement Head</b>	<b>49</b>
4.1	Review of Commercially Available Ferrite Cores . . . . .	49
4.2	Review of Suitable Magnetic Sensors . . . . .	55
4.3	Customized Core Shape and Sensor Array . . . . .	58
<b>5</b>	<b>Electronic Circuit</b>	<b>63</b>
5.1	Current Source . . . . .	64
5.1.1	Amplifier Selection . . . . .	65
5.1.2	Circuit and Board Design . . . . .	67
5.2	Programmable Waveform Generator . . . . .	69
5.2.1	IC Selection . . . . .	71
5.2.2	Component Calculation . . . . .	72
5.2.3	Circuit and Board Design . . . . .	74
5.3	Data Acquisition Device . . . . .	75
5.4	Amplification Circuit for the Magnetoresistive Sensor Array . . . . .	76
5.4.1	Amplifier Selection . . . . .	77
5.4.2	Circuit Design . . . . .	78
5.5	Amplification Circuit for the Induction Coil . . . . .	79
5.5.1	Analog Integration . . . . .	80
5.5.2	Digital Integration . . . . .	83
<b>6</b>	<b>Software</b>	<b>85</b>
6.1	Configuration of the Electronics . . . . .	86
6.2	Signal Processing Algorithms . . . . .	89
6.2.1	Signal Acquisition and Cycle Averaging . . . . .	89
6.2.2	Low Pass Compensation . . . . .	90
6.2.3	Flux Offset . . . . .	92
6.2.4	Center Loop . . . . .	93
6.2.5	Calculation of the Flux Density . . . . .	93
6.2.6	Demagnetization . . . . .	93
<b>7</b>	<b>System Assembly and Noise Characterization</b>	<b>95</b>
7.1	Measurement Stand . . . . .	95
7.1.1	Stepper Motor Controller . . . . .	97
7.1.2	Electronics Enclosure . . . . .	99
7.2	Noise Characterization . . . . .	100
7.2.1	DAQ Noise Measurements . . . . .	100
7.2.2	Calibration of the MR Sensors . . . . .	101
7.2.3	MR Sensor Noise Measurements . . . . .	102

7.2.4	Induction Coil Noise Measurements . . . . .	104
<b>8</b>	<b>Measurement of Magnetic Samples</b>	<b>109</b>
8.1	Reference Measurements . . . . .	109
8.1.1	Reference Hysteresis Loop Tracer . . . . .	110
8.1.2	Reference Samples . . . . .	111
8.1.3	Results . . . . .	112
8.2	First Measurement Series with the Developed System . . . . .	116
8.3	Improvements . . . . .	124
8.3.1	Consecutive Averaging . . . . .	124
8.3.2	Additional Induction Coil . . . . .	125
8.4	Second Measurement Series with the Developed System . . . . .	125
<b>9</b>	<b>Summary and Outlook</b>	<b>129</b>
	<b>Bibliography</b>	<b>133</b>



## List of Figures

2.1	Magnetic field caused by electric current . . . . .	3
2.2	External magnetic field lines of a bar magnet (a) and a solenoid (b) . . . . .	4
2.3	Field strength in a point A caused by a conductor loop . . . . .	5
2.4	Influence of ferromagnetic (a), para- or diamagnetic (b) and superconducting materials (c) on the propagation of magnetic fields . . . . .	8
2.5	Exemplary hysteresis loop of a soft magnetic sample . . . . .	9
2.6	Closed (a) and open (b) ring sample magnetized by a surrounding coil . . . . .	10
2.7	Demagnetization field $H_d$ and measured local flux density $B$ of a bar magnet [Cullity and Graham, 2009, pp. 49–50] . . . . .	11
2.8	Two special kinds of ellipsoids: the oblate and the prolate spheroid . . . . .	12
2.9	Visualization of the magnetic domains in a magnetic material at different states of magnetization (adapted from [Kallenbach et al., 2012, p. 33]) . . . . .	14
2.10	Coercivity vs. grain size for different soft magnetic alloys (adapted from [Herzer, 2013])	15
2.11	Conventional classification of losses in magnetic materials (adapted from [Hubert and Schäfer, 2008, p. 272]) . . . . .	16
2.12	Schematic draft of a vibrating sample magnetometer (VSM) . . . . .	19
2.13	Schematic draft of a hysteresis loop tracer employing a ring sample . . . . .	21
2.14	Ring sample placed against the shorted termination of a coaxial line . . . . .	23
2.15	Fahy Simplex permeameter . . . . .	24
2.16	Schematic of a single sheet tester (a) using a Chattock coil (b) for local $H$ measurements	25
2.17	Simulated and measured field strength between the poles of the yokes in a single sheet tester (based on data from Tumanski [2002]) . . . . .	26
2.18	Schematic of the needle probe method . . . . .	27
2.19	Properties of different magnetic measurement techniques based on data from Lenz and Edelstein [2006]; Tumanski [2011, 2013]; Colombo et al. [2016]; Deak et al. [2017] and Ripka [2021] . . . . .	28
2.20	Equivalent circuit (a) and normalized frequency response (b) of an actual induction coil	31
2.21	Normalized frequency response of an induction coil with a load resistor . . . . .	31
2.22	Schematic of a thin film hall sensor with the Lorentz force acting on the drifting electrons . . . . .	32
2.23	Comparison of the resistance change of different magnetoresistive sensors at room temperature (adapted from [Tumanski, 2011, p. 189]) . . . . .	35

2.24	Vectors of the acting fields, the magnetization and the current in a thin film strip subject to the AMR effect (a) and the resulting resistance of the strip in dependence of the field strength in $y$ -direction adapted from Tumanski [2011, p. 191] (b) . . . . .	36
2.25	Schematic of the barber pole structure (a) and an exemplary $R(H)$ plot of a barber pole based sensor from <i>Philips</i> [Tumanski, 2013] (b) . . . . .	37
2.26	MR ratio of $(\text{Fe/Cr})_n$ multilayer at a temperature of 4.2 K adapted from Baibich et al. [1988] . . . . .	38
2.27	Spin depending scattering of electrons passing a pair of ferromagnetic layers separated by a non-magnetic spacer layer (adapted from Ripka [2021, p. 119]) . . . . .	39
2.28	GMR spin valve layer configuration with synthetic magnetic antiferromagnet and resulting MR ratio (adapted from Reig et al. [2013, p. 4]) . . . . .	40
3.1	Schematic draft of the measurement head . . . . .	44
3.2	Simulated field propagation in an iron thin film magnetized by a central U-core (top view) . . . . .	45
3.3	Concept of the measurement electronics . . . . .	46
4.1	Dimensions of analyzed potential cores from <i>DMEGC</i> , <i>Epcos</i> and <i>Ferroxcube</i> . . . . .	49
4.2	Magnetic equivalent circuit for the core in air (a) and attached to a permalloy layer (b) . . . . .	51
4.3	Field strength in the center between the poles of the U-cores along the $z$ -axis in air and on top of a permalloy layer with $2 \mu\text{m}$ and $20 \mu\text{m}$ height . . . . .	52
4.4	Output voltage vs. field strength of the three sensors ‘KMY20 M’, ‘CT100’ and ‘TF952’ based on the data given in the individual data sheets . . . . .	56
4.5	DFN-6 package of the ‘CT100’ with the centrally located sensory area (red) . . . . .	57
4.6	Cross section of the designed core including the placement of the sensor and coils . . . . .	58
4.7	Results of the parametric simulations for the customized core in air, showing the field strength along the $y$ -axis (a) and the inductance for different widths $w$ (b) . . . . .	59
4.8	Fotograph of some of the customized cores (one with windings) (a) and of the sensor array printed circuit board (PCB) equipped with eight ‘CT100’ from <i>Crocus Technology</i> (b) . . . . .	60
4.9	Assembly of the measurement head consisting of an aluminum carrier with the mounted customized core and the ‘CT100’ sensor array . . . . .	61
4.10	Measurement of the inductance and the resistance of the windings vs. frequency . . . . .	61
4.11	Simulated course of the field strength along the $z$ -axis . . . . .	62
5.1	Schematic of the electronic circuit containing four PCBs and a DAQ . . . . .	63
5.2	Schematic of the enhanced Howland current source . . . . .	65
5.3	Schematic of the ‘Composite amplifier enhanced Howland current source’ (CAEHCS) . . . . .	66
5.4	Frequency depending mean power loss within the components in the output chain without (a) and with an additional series resistor of $5.6 \Omega$ (b) for a sinusoidal current $\hat{I} = 1 \text{ A}$ . . . . .	68

5.5	Decreased phase shift $\varphi$ with a series resistor is $R_{\text{ser}} = 5.6 \Omega$ . . . . .	68
5.6	Picture of the final version of the PCB featuring the ‘Composite amplifier enhanced Howland current source’ (CAEHCS) . . . . .	69
5.7	Simplified schematic of the signal generator consisting of a DAC (part of the DDS chip), a VGA and a trailing OP to convert the differential to a single-ended signal and to set the output amplitude . . . . .	70
5.8	Differential signals of the current outputs of the ‘AD9834’ . . . . .	71
5.9	Schematic of the signal generator with ‘AD9834’, ‘AD8330’ and ‘AD8310’ . . . . .	73
5.10	Picture of the final version of the programmable waveform generator . . . . .	74
5.11	Schematic of the internal structure of an instrumentation amplifier . . . . .	76
5.12	Schematic of the signal path from the magnetoresistive (MR) sensor to the amplifier (only one sensor shown) . . . . .	78
5.13	Calculated frequency response of the peak induction voltage $\hat{U}_{\text{ind}}$ per unit flux density in the B-coil of the customized core for different numbers of turns . . . . .	79
5.14	Calculated induced voltage in the B-coil with $n = 10$ turns loaded with different resistors $R_L$ . . . . .	80
5.15	Schematic of the loaded induction coil connected to successive integrators . . . . .	81
5.16	Resulting amplitudes and phase shift of the analog filter circuit connected to the loaded induction coil (calculated with LTspice) . . . . .	82
5.17	Measured phase shift (a) and resulting apparent coercivity $H_c$ at multiple measurement ranges (b) for different types of integration that were evaluated . . . . .	82
5.18	Calculated phase shift at different gains set for the ‘AD8253’ . . . . .	84
5.19	Amplification circuit with different gains realized with two stages and a multiplexer . . . . .	84
6.1	Simplified program flowchart of the microcontroller on the PCB of the programmable waveform generator . . . . .	87
6.2	Signal chain beginning with the data acquisition (blue box on the left), then passing multiple algorithms and leading to a graphical output of the course of $H$ and $B$ (icons on the right) . . . . .	89
6.3	Time-based qualitative measurement signals of $H$ and $\Phi$ with the low pass filter compensation disabled (top) and enabled (bottom) . . . . .	91
6.4	Measured offset flux in the core at 100 Hz in the open magnetic circuit (no material attached) . . . . .	92
7.1	Motorized stand with the measurement head from Fig. 4.9 mounted upside-down on a carriage . . . . .	95
7.2	Top view of the moveable carriage with the amplifier boards, stepper motor and toothed belt . . . . .	96
7.3	Bottom view of the moveable carriage with the mounted measurement head 10 mm above an exemplary sample (a) and in contact with it (b) . . . . .	97
7.4	Picture of the PCB comprising the stepper motor controller . . . . .	98

7.5	Picture of the PCB featuring the stepper motor controller . . . . .	100
7.6	Voltage noise spectral density of the NI 9775 DAQ inputs (10,000 points, 20 FFTs averaged) . . . . .	101
7.7	Calibration curves of the used ‘CT100’ MR sensors . . . . .	102
7.8	Voltage noise spectral density referred to the amplifier input of the ‘CT100’ sensors at different averaging presets (10,000 points, 20 FFTs averaged) . . . . .	103
7.9	Voltage noise referred to the amplifier input of the ‘CT100’ sensors in the time domain	103
7.10	‘CT100’ output signal at a 100 Hz sine wave excitation with an amplitude of 100 A/m	104
7.11	Voltage noise spectral density referred to the amplifier input of the induction coil at all gains without coil connected (10,000 points, 20 FFTs averaged) . . . . .	105
7.12	Voltage noise spectral density referred to the amplifier input of the induction coil at all gains with coil connected (10,000 points, 20 FFTs averaged) . . . . .	105
7.13	Voltage noise spectral density referred to the amplifier input of the induction coil at all gains with coil connected and 64 cycles averaged (10,000 points, 20 FFTs averaged)	105
7.14	Voltage noise referred to the amplifier input of the induction coil for all gains in the time domain with 64 cycles averaged . . . . .	106
7.15	Induction coil output signal at a 100 Hz sine wave excitation of different amplitudes captured at a gain of 70 dB and 64 cycles averaged . . . . .	107
7.16	Resulting flux in the induction coil at a 100 Hz sine wave excitation and different amplitudes captured at a gain of 70 dB and 64 cycles averaged . . . . .	107
7.17	FFT of the signal levels of the induction voltage and the resulting flux captured at a gain of 70 dB and 64 cycles averaged (10,000 points, 20 FFTs averaged) . . . . .	108
8.1	Reference measurement PCB placed in a homogenous magnetic field . . . . .	110
8.2	Reference samples used for characterization . . . . .	112
8.3	Reference measurements of the 80 $\mu\text{m}$ ‘FS1000’ ferrite sheet . . . . .	113
8.4	Reference measurements of the 50 $\mu\text{m}$ ‘MuMetall’ foil . . . . .	113
8.5	Reference measurements of the 23 $\mu\text{m}$ ‘Metglas’ foil . . . . .	113
8.6	Reference measurements of the 6 $\mu\text{m}$ CZT multilayer (easy axis) . . . . .	113
8.7	Reference measurements of the 6 $\mu\text{m}$ CZT multilayer (hard axis) . . . . .	114
8.8	Reference measurements of the 500 nm electroplated $\text{Ni}_{81}\text{Fe}_{19}$ layer . . . . .	114
8.9	Reference measurements of the 100 nm sputtered $\text{Ni}_{81}\text{Fe}_{19}$ layer . . . . .	114
8.10	Time based input voltages from the magnetic field sensor ‘CT100’ and the induction coil acquired for the determination of the hysteresis loop of the 100 nm $\text{Ni}_{81}\text{Fe}_{19}$ sample	115
8.11	Exemplary visualization of the steps for calculating the hysteresis loop in case of the 80 $\mu\text{m}$ ‘FS1000’ ferrite sheet from the measured flux in the yoke . . . . .	117
8.12	Measured hysteresis loop of the 80 $\mu\text{m}$ ‘FS1000’ ferrite sheet at 100 Hz and different currents . . . . .	118
8.13	Measured hysteresis loop of the 50 $\mu\text{m}$ ‘MuMetall’ foil at 100 Hz and different currents	118
8.14	Measured hysteresis loops of the 23 $\mu\text{m}$ ‘Metglas’ foil at 100 Hz and different currents	118



---

8.15	Measured hysteresis loops of the 6 $\mu\text{m}$ CZT multilayer (EA) at 100 Hz and different currents . . . . .	119
8.16	Measured hysteresis loops of the 6 $\mu\text{m}$ CZT multilayer (HA) at 100 Hz and different currents . . . . .	119
8.17	Measured hysteresis loops of the 500 nm $\text{Ni}_{81}\text{Fe}_{19}$ layer at 100 Hz and different currents	119
8.18	Hysteresis loops of the 500 nm $\text{Ni}_{81}\text{Fe}_{19}$ layer at 100 Hz and different excitation currents measured from a distance of 500 $\mu\text{m}$ between the ferrite core and the wafer .	121
8.19	Normalized course of the field strength recorded by the four MR sensors in the array during the hysteresis loop measurement of all samples . . . . .	122
8.20	Ferrite core with an additional induction coil, inserted in two laser-cut slots at the bottom . . . . .	125
8.21	Hysteresis loops of the 500 nm $\text{Ni}_{81}\text{Fe}_{19}$ layer measured at 100 Hz with different offset flux values used for the calculation . . . . .	126
8.22	Hysteresis loops of the 100 nm $\text{Ni}_{81}\text{Fe}_{19}$ layer measured at different excitation frequencies . . . . .	127
8.23	Measured and calculated offset flux for the 100 nm $\text{Ni}_{81}\text{Fe}_{19}$ sample . . . . .	127
8.24	Hysteresis loops of 6 $\mu\text{m}$ CZT layer (EA) measured at different excitation frequencies	128
8.25	Measured and calculated offset flux for easy axis of the 6 $\mu\text{m}$ CZT multilayer sample	128
9.1	Exemplary hysteresis loops of the 100 nm $\text{Ni}_{81}\text{Fe}_{19}$ sample measured at 100 Hz with different excitation angles . . . . .	131



## List of Tables

3.1	Realization of the necessary components of the measurement device . . . . .	47
4.1	Simulation results for different U-cores excited by a primary winding with $n = 10$ turns and a current of $I = 1$ A . . . . .	50
4.2	Product of the simulated magnetic flux density $B_{\max}$ and the width $w$ of the U-cores .	53
4.3	Physical and electrical properties of the sensors ‘KMY20 M’, ‘CT100’ and ‘TF952’ .	56
5.1	Attenuation and output amplitude of possible voltage dividers . . . . .	73
5.2	Specifications of different DAQ devices from <i>National Instruments</i> . . . . .	75
5.3	Electrical characteristics of the instrumental amplifiers ‘AD8421’ from <i>Analog Devices</i> and ‘INA849’ from <i>Texas Instruments</i> at a gain of 100 . . . . .	77
5.4	Arising noise for the ‘CT100’ sensor in combination with the amplifiers ‘AD8421’ and ‘INA849’ at a frequency of 1 kHz . . . . .	77
6.1	Structure of the command strings recognized by the microcontroller . . . . .	87
6.2	Resulting phase shift and attenuation at specific frequencies . . . . .	91
7.1	Transmission ratios and resolutions of the axes in the measurement stand . . . . .	98
7.2	Set speed and accelerations of the axes in the measurement stand . . . . .	99
7.3	Sensitivity, offset and non-linearity error of the ‘CT100’ MR sensors used . . . . .	102
7.4	Achieved RMS noise levels for the ‘CT100’ MR sensors in terms of voltage and field strength . . . . .	104
7.5	Achieved RMS noise levels for the induction coil at different gains and averaged for 64 cycles . . . . .	106
8.1	Magnetic samples used for the characterization of the measurement device . . . . .	111
9.1	Specifications of the Measurement System . . . . .	130



## List of Symbols

Sign	Unit	Description
$\alpha$	–	$\alpha = R/R_L$ represents the ratio between the resistance $R$ of a search coil and the load resistance $R_L$ applied on it.
$\beta$	–	$\beta = R \cdot \sqrt{C/L}$ represents the inverse of the Q-factor of a $RLC$ series circuit.
$\gamma$	–	Ratio between the applied frequency $f$ and the resonant frequency $f_0$ of a resonant circuit.
$\gamma_e$	$T^{-1}s^{-1}$	Gyromagnetic ratio of an electron ( $1.76 \cdot 10^{11} T^{-1}s^{-1}$ )
$\epsilon$	As/Vm	Permittivity
$\epsilon_0$	As/Vm	Permittivity of vacuum ( $8.854189 \cdot 10^{-12}$ As/Vm)
$\epsilon_r$	–	Relative permittivity
$\vartheta$	rad	Angle between the current and the magnetization vectors in MR sensors
$\Theta$	A	Magnetomotive force
$\lambda$	m	Wavelength
$\mu$	Vs/Am	Permeability
$\mu_0$	Vs/Am	Permeability of vacuum ( $1.256637 \cdot 10^{-6} \approx 4\pi \cdot 10^{-7}$ Vs/Am)
$\mu_H$	$T^{-1}$	Hall mobility
$\mu_r$	–	Relative permeability
$\pi$	–	Ratio of a circle's circumference to its diameter (3.141593)
$\rho$	$kg/m^3$	Mass density
$\rho$	$\Omega m$	Electrical resistivity
$\rho_0$	$\Omega m$	Electrical reference resistivity
$\varphi$	rad	Phase angle
$\Phi$	Wb	Magnetic flux
$\omega$	$s^{-1}$	Angular frequency
$A$	$m^2$	Area
$B$	T	Magnetic flux density
$B_r$	T	Remanence
$B_s$	T	Saturation flux density
$C$	F	Electrical capacity

## List of Symbols

---

<b>Sign</b>	<b>Unit</b>	<b>Description</b>
$C_w$	F	Electrical capacity of the wiring of a coil
$d$	m	Distance
$e_n$	$V/\sqrt{\text{Hz}}$	Voltage noise density
$e_t$	$V/\sqrt{\text{Hz}}$	Total voltage noise density
$f$	Hz	Frequency
$f_0$	Hz	Resonant frequency
$F$	N	Force
$G$	–	Gain
$G$	–	Geometry Factor of a Hall element
$h$	m	Height
$H$	A/m	Magnetic field strength
$H_{\text{app}}$	A/m	Apparent field strength
$H_c$	A/m	Coercivity field strength
$H_d$	A/m	Demagnetizing field
$H_k$	A/m	Anisotropy field strength
$H_{\text{tr}}$	A/m	True field strength
$I$	A	Current
$i_n$	$A/\sqrt{\text{Hz}}$	Current noise density
$k_B$	J/K	Boltzmann constant ( $1.380649 \cdot 10^{-23}$ J/K)
$l$	m	Length
$L$	H	Inductance of a coil
$m$	$\text{Am}^2$	Magnetic moment
$M$	A/m	Magnetization
$M_s$	A/m	Saturation magnetization
$n$	–	Number of turns
$N_d$	–	Demagnetizing factor
$q$	C	Charge of a carrier
$Q$	–	Quality factor

<b>Sign</b>	<b>Unit</b>	<b>Description</b>
$R$	$\Omega$	Electrical resistance
$R_0$	$\Omega$	Reference resistance
$r_i$	m	Inner radius of a ring
$R_L$	$\Omega$	Electrical resistance of the load on a search coil
$R_m$	$H^{-1}$	Magnetic resistance
$r_o$	m	Outer radius of a ring
$S_a$	$m^2$	Absolute sensitivity of a search coil
$S_p$	$m^2$	Operation sensitivity of a search coil at a given frequency and a given load connected to it
$S_V$	V/VT	Supply voltage related sensitivity of hall elements
$t$	s	Time
$T$	$s^{-1}$	Period
$T$	K	Kelvin-temperature
$U$	V	Voltage
$U_H$	V	Hall voltage
$U_{in}$	V	Input voltage
$U_{ind}$	V	Induction voltage
$U_{out}$	V	Output voltage
$v$	m/s	Speed
$V$	$m^3$	Volume of a body
$w$	m	Width
$X$	$\Omega$	Electrical reactance
$Z$	$\Omega$	Electrical impedance





## Abbreviations

AC	Alternating Current
ADC	Analog-Digital Converter
AGM	Alternating Gradient Magnetometer
AMR	Anisotropic Magnetoresistance
CIP	Current-in-Plane
CMOS	Complementary Metal-Oxide-Semiconductor
CMRR	Common-Mode Rejection Ratio
CPP	Current Perpendicular to the Plane
DAC	Digital-Analog Converter
DAQ	Data Acquisition
DC	Direct Current
DDS	Direct Digital Synthesis
FEM	Finite-Element Modeling
FFT	Fast Fourier Transformation
GBP	Gain Bandwidth Product
GMR	Giant Magnetoresistance
GPIO	General Purpose Input Output
GUI	Graphical User Interface
HTS	High Temperature Superconductor
I <sup>2</sup> C	Inter-Integrated Circuit
IC	Integrated Circuit
LDO	Low-Dropout
LTS	Low Temperature Superconductor
MR	Magnetoresistive
MTJ	Magnetic Tunnel Junction

## Abbreviations

---

OP	Operational Amplifier
PCB	Printed Circuit Board
PSRR	Power Supply Rejection Ratio
PWM	Pulse Width Modulation
RF	Radio Frequency
RMS	Root Mean Square
ROM	Read-Only Memory
SI	International System Of Units
SNR	Signal-To-Noise Ratio
SPI	Serial Peripheral Interface
SQUID	Superconducting Quantum Interference Device
SST	Single Sheet Tester
VGA	Variable Gain Amplifier
VI	Virtual Instrument
VSM	Vibrating Sample Magnetometer

# 1 Introduction

Magnetic materials are indispensable on any scale when it comes to the transformation of energy in modern electric machinery and electronic devices. Thus, they are still the subject of intensive research, even though the field of magnetism is one of the oldest in science. In large dimensions, magnetic materials are required in the power chain for the conversion of kinetic to electric energy. Vice versa, electric motors exploit the laws of magnetism to generate mechanical torque from electric current. The fact that electric motors consume about 40 % of all generated power in the world emphasizes the potential of improving the efficiency of mechanical-electrical energy conversion in either direction [Plötz and Eichhammer, 2011]. The choice of the specific magnetic alloy has a key role in this matter since the necessary periodic formation and decay of magnetic fields causes different kinds of energy losses in the material. Therefore, great efforts are put in improving the alloys used employing specialized measuring equipment. This is how the so called Epstein frame became popular, a by now standardized test setup to measure the core loss per kilogram transformer steel [IEC, 2008].

In smaller sizes, magnetic materials are employed in electric circuits in inductors for analog signal conditioning and more importantly in transformers for galvanic separation and voltage conversion. Especially the great demand for high voltage DC-DC converters resulting from the growing market of electric and hybrid electric vehicles has to be mentioned here. In addition to the requirement for high efficiency, a space-saving design is one of the main challenges, which led, for example, to the development of PCB integrated planar transformers. Due to their small size and their suitability for high voltages and high switching frequencies of up to 1 MHz, these types of transformers reach outstanding power densities of several kilowatts per liter in combination with wide bandgap semiconductors like silicon carbide or gallium nitride [Li et al., 2017; Fischer et al., 2021].

Even higher switching frequencies and power densities can be achieved in the microscopic scale using cleanroom facilities and working on wafer level. Already ten years ago, the general longing for integrated power supplies on chip level was reported because mobile electronics are in need of multiple different voltages and high currents, which are best provided by DC-DC converters located next to the chip at the ‘point of load’. Regarding the downsizing of transformers, the achievement of a fully complementary metal-oxide-semiconductor (CMOS) compatible process was mentioned as the ultimate goal of this development allowing for monolithic integration of the magnetic core together with the semiconductor circuits [Ó Mathúna et al., 2012]. In the meantime, miniature inductors operated in the two- or three-digit megahertz range have been presented by various researchers, proving the feasibility of highly integrated power converters [Le et al., 2021, pp. 13-14]. However, while many chip developers focus on nickel zinc ferrites, novel multilayer materials like FeSiCr seem superior due to lower high frequency losses [Hsiang, 2020] and also cobalt based alloys offer CMOS compatibility and are suitable for high frequencies [Selvaraj et al., 2020].

The multitude of articles that have appeared in the recent years regarding thin film inductors provide evidence that there is still much potential for finding novel alloys for the use in high frequency power converters and that there is a great demand for them. However, the development of magnetic thin films is not a trivial task as their properties vary with each alloy component, the processing parameters used and the subsequent thermal annealing. Yet, there is another issue, which complicates the process and concerns the determination of the magnetic properties of the thin films.

Standard silicon wafers used in today's market leading factories have a height of below one millimeter and a diameter of 300 mm while the step towards 450 mm is in full swing allowing for more cost-efficient processes [Zhang, 2014]. However, the transition is accompanied by high investments and challenges, as complete lines have to be replaced and handling systems have to be adapted [Marks et al., 2015]. Magnetic measurement technology faces even greater issues as there are generally two established methods, which have in common that they create a uniform magnetic field large enough to fit in the whole sample. A so called hysteresis loop tracer works with entire wafers, which requires huge coils and high currents to create a field of sufficient strength. It provides a single global measurement averaged over the wafer's size without information about local deviations. Hysteresis loop tracers are already extensive for 300 mm wafers with coils of half a meter in size and there is no known device for 450 mm so far. The determination of local properties of the magnetic films is possible using a vibrating sample magnetometer (VSM), which however has significant drawbacks. The sample size is limited to some millimeters and requires the dicing of the wafer into small chips. Unfortunately, the handling of these samples within the VSM is complicated, can hardly be automated and the measurement takes a couple of minutes. Most importantly, the diced chips are not applicable for further cleanroom processing and the wafer is not reusable in case of a process failure.

The motivation for this thesis arises from the lack of a non-destructive measuring device for local magnetic properties, which additionally enables the integration into the highly automated environment of modern cleanrooms. A device like that would facilitate the development of novel magnetic alloys and allow for easier quality assurance. Furthermore, with the help of local measurements, the uniformity of the layer deposition could be determined, which is particularly important for large wafers. The challenge of such a device is the generation of a spatially limited, yet homogeneous, magnetic field in a continuous layer and the measurement of the conducted magnetic flux without the possibility of winding a coil around it. Apart from the physical design of a corresponding measuring head, the development requires the layout of electronic circuits for the field generation and the processing of the sensor signals. Eventually, the necessary software must be developed to handle the data acquisition and control the measuring stand. The present thesis takes all these aspects into account.

## 2 State of the Art

The concept for this novel device arises from the boundary conditions given by the laws of electromagnetism and the peculiarities of magnetic thin films, which are therefore briefly summarized in section 2.1 and section 2.2 respectively. Afterwards, the state of the art is reviewed regarding the common methods for the measurement of the magnetization appearing in magnetic materials and the recent progress in this field, which is presented in section 2.3. Since the phenomenon of magnetization strongly depends on external magnetic fields, their strength must be necessarily recorded simultaneously. From the multitude of sensing techniques, the appropriate ones are discussed in section 2.4 with respect to their suitability for this application.

### 2.1 Fundamentals of Electromagnetism

Though magnetism was first observed from minerals (e.g. magnetite  $\text{Fe}_3\text{O}_4$ ) about 2500 years ago, it gained its great importance many years later with the discovery of magnetic fields caused by electric current. It was in 1820 when Hans Christian Oersted noticed his compass being influenced by a nearby cable. Though 18 years before, an Italian physicist made the same observation, Oersted was the first to recognize the potential of it and triggered the start of the development of electrical science and engineering. As found by Oersted, magnetic fields result not only from magnetic materials but also from electric current. Since the generation of magnetic fields was much easier to achieve through electricity, the use of electromagnets began shortly after [Cullity and Graham, 2009, p. 2].

The way the magnetic field is related to electric current is shown in Fig. 2.1. Electrons moving through a conductor cause a concentric circular field of the given direction around it. If the conductor is formed to a loop, the magnetic field in its center intensifies. By winding a coil with many of these loops next to each other, the field in its mid becomes uniform as was demonstrated in experiments with so called solenoids. These are specific coils, whose diameter is small in comparison to their length. As depicted in Fig. 2.2, solenoids feature a field very similar to the one of a bar magnet.

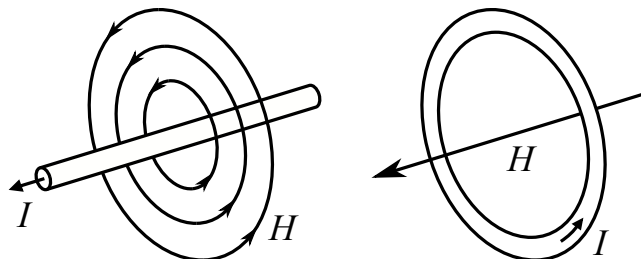


**Figure 2.1** Magnetic field caused by electric current

The depicted ‘lines of force’, as Michael Faraday (1791-1867) called them, show the course of the magnetic field with the arrows pointing in the direction of it. The outlet of the lines is called north-pole, the inlet is called south-pole. The increasing distance between the field lines demonstrates the decreasing field strength when moving away from the magnet or the coil. Though not shown for the bar magnet, the field lines continue in its inside in the same manner as they do for the solenoid. As they neither have a beginning nor an end and therefore no source or sink, the magnetic field is a source-free vortex field [Busch, 2015, p. 38].

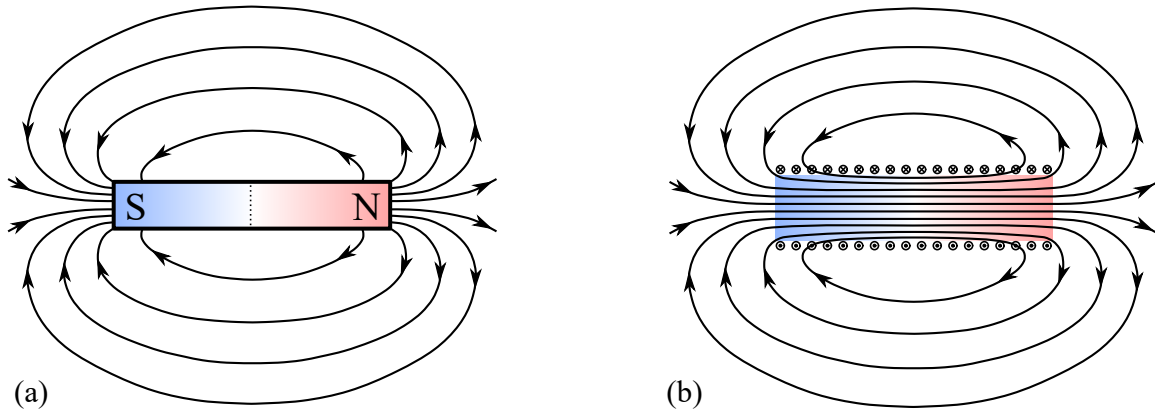


**Figure 2.2** External magnetic field lines of a bar magnet (a) and a solenoid (b)

### 2.1.1 Early Laws of Magnetism

The first persons to propose a rule for calculating the occurring field strength caused by electric current were the French mathematics and physicians Jean-Baptiste Biot and Felix Savart. In 1820, the same year that Oersted published his observations about the influence of currents on his compass, they formulated the following rule known as the Biot–Savart law:

$$d\vec{H} = \frac{I}{4\pi R^2} d\vec{l} \times \vec{u} \quad (2.1)$$

A current  $I$  flowing through a wire of infinitesimal length  $d\vec{l}$  causes a magnetic field of the strength  $d\vec{H}$  in a point A, that is located at a distance  $R$ . The vector  $\vec{u} = \frac{\vec{R}}{|\vec{R}|}$  describes the unit vector (a vector divided by its length) pointing from the origin of  $d\vec{l}$  to the point A. The vector product  $d\vec{l} \times \vec{u}$  implies that the resulting field  $d\vec{H}$  points in a direction orthogonal to both the current and the direction of  $\vec{u}$ . Eq. 2.1 is a simplification of the original equation assuming that the conductor has no width. It only delivers good results if  $R$  is large in relation to the wire’s diameter [Tumanski, 2011, pp. 42–43].

Using the law of Biot–Savart, it is possible to quantify the field strength caused by a conductor loop as depicted in detail in Fig. 2.3a.  $\vec{R}$  is obtained by vector addition:  $\vec{R} = \vec{x} - \vec{r}$ . As there is a right angle at the intersection of both vectors in this case, the corresponding unit vector  $\vec{u} = \frac{\vec{R}}{|\vec{R}|}$  has trigonometric edge lengths as shown in Fig. 2.3b. Accordingly  $d\vec{H}$  can be calculated using Eq. 2.2 and its axial

component  $dH_x$  in point A therefore accounts to Eq. 2.3. Eventually,  $\alpha$  can be replaced using the equations  $\sin \alpha = \frac{r}{R}$  and  $R = \sqrt{r^2 + x^2}$ , which leads to Eq. 2.4.

$$d\vec{H} = \frac{I}{4\pi R^2} \begin{pmatrix} 0 \\ -dl \\ 0 \end{pmatrix} \times \begin{pmatrix} \cos \alpha \\ 0 \\ -\sin \alpha \end{pmatrix} = \frac{I}{4\pi R^2} \begin{pmatrix} \sin(\alpha)dl \\ 0 \\ \cos(\alpha)dl \end{pmatrix} \quad (2.2)$$

$$dH_x = \frac{I}{4\pi R^2} \sin(\alpha)dl \quad (2.3)$$

$$dH_x = \frac{I}{4\pi} \frac{r}{(r^2 + x^2)^{\frac{3}{2}}} dl \quad (2.4)$$

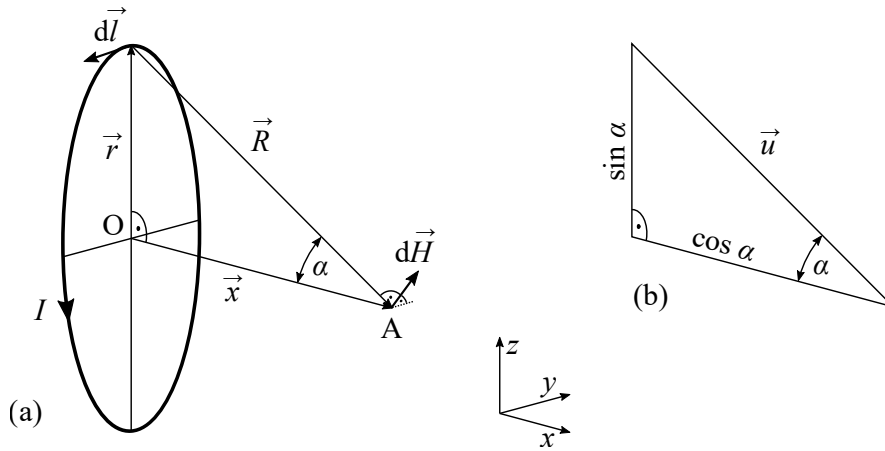


**Figure 2.3** Field strength in a point A caused by a conductor loop

The total field  $H_x$  is achieved by integrating Eq. 2.4 along the conductor loop. On the  $x$ -axis,  $H_y$  and  $H_z$  are zero as the parts  $dl$  with positive and negative  $y$  or  $z$  are equal and therefore cancel each other out. Eventually, with  $H = H_x$  and  $\oint dl = 2\pi r$ , the field strength  $H$  along the  $x$ -axis depends only on the value of  $x$  as noted in Eq. 2.5.

$$H(x) = \oint \frac{I}{4\pi} \frac{r}{(r^2 + x^2)^{\frac{3}{2}}} dl = \frac{I}{2} \frac{r^2}{(r^2 + x^2)^{\frac{3}{2}}} \quad (2.5)$$

At the point  $x = 0$  the field strength has its maximum of  $H = \frac{I}{2r}$  decaying in both directions of  $x$ . Assuming a current of 1 A and a radius of 0.5 m, the field strength accounts to 1 A/m.

Another typical field strength that can be calculated using the law of Biot–Savart is that of a straight conductor of infinite length. The course of the field lines is depicted in Fig. 2.1. The equation for the field strength in a point A at a distance  $R$  from a piece  $dl$  of conductor is similar to the one of the conductor loop but uses the cosine instead of the sine function [Tumanski, 2011, p. 42].

$$dH = \frac{I}{4\pi R^2} \cos(\alpha)dl \quad (2.6)$$

The field caused by the whole wire is derived by transforming Eq. 2.6 in order to replace  $dl$  by  $d\alpha$  and integrating it for  $\alpha$  in the range from  $-\frac{\pi}{2}$  to  $\frac{\pi}{2}$  with  $r$  being the radial distance to the conductor.

$$H = \int_{-\frac{\pi}{2}}^{\frac{\pi}{2}} \frac{I}{4\pi r} \cos(\alpha) d\alpha = \frac{I}{2\pi r} \quad (2.7)$$

In both exemplary cases, the results can also be achieved using the circuital law of André-Marie Ampère. It states that the magnetic field along any closed curve  $C$  is equal to the electric current that flows through the area enclosed by that curve independent of its shape. Regarding the field of a conductor with the length of the curve  $C = 2\pi r$ , Eq. 2.8 follows.

$$\oint_{2\pi r} H dl = I \quad \Rightarrow \quad H = \frac{I}{2\pi r} \quad (2.8)$$

Ampère's law is commonly used for calculating the magnetic field strength produced by a coil with the winding count  $n$ . With  $n$  times the current  $I$  passing the area of the curve  $C$ , the resulting field strength is  $n$  times bigger and Eq. 2.8 can be extended accordingly. Ampère's law allows the determination of the field strength in closed iron circle's and with some simplifications even if the iron circle features an air gap. However, as soon as it comes to alternating current (AC) circuits, stray fields and eddy currents have to be considered and the calculation becomes inaccurate. For these tasks, the method of finite-element modeling (FEM) is much more suitable [Ripka, 2021, pp. 1-4].

While the laws of Biot–Savart and Ampère express the link between the electric current and the magnetic field strength, there is also a relation of magnetism to the electric voltage as the English scientist Faraday discovered in 1831. Faraday's law states that a positively changing magnetic flux within the enclosed area of a conductor loop creates a negative voltage in that wire, which is called induction voltage  $U_{\text{ind}}$ . Since the flux  $\Phi$  is the product of the area of the loop  $A$  and the flux density  $B$ , a voltage can be induced by varying either of the values. However, in most applications  $A$  is constant and the measurement of the  $U_{\text{ind}}$  allows the determination of the flux density using Eq. 2.9.

$$U_{\text{ind}} = -\frac{d\Phi}{dt} = -A \frac{dB}{dt} \quad (2.9)$$

The flux density is the second physical dimension that is of importance for this thesis. As given in Eq. 2.10, it equals the sum of the field strength  $H$  and the magnetization  $M$  of the material within the conductive loop multiplied with the constant  $\mu_0$ . In non-magnetic materials,  $M$  is so small in comparison to  $H$  that it can be neglected while in magnetic materials, it is usually the other way round and  $H$  can often be neglected. Therefore, induction coils allow both the measurement of the field strength when wound around a non-magnetic body (or simply air) or of the magnetization, when wound around a magnetic body [Tumanski, 2013, pp. 44-45].

$$B = \mu_0 \cdot (H + M) \quad (2.10)$$



### 2.1.2 Maxwell's Equations

While the early laws of Biot–Savart and Ampère allow the calculation of the field strength in simple cases like the above mentioned one of the straight conductor, it is generally very complicated to determine the magnetic field, especially when time-varying effects are involved. Therefore, it is most often appropriate to compute the magnetic field in either magnetostatic or dynamic simulations using the method of FEM. The corresponding software, however, is not based on the laws mentioned in subsection 2.1.1 but on the four equations James Clerk Maxwell formulated in the mid of the 19<sup>th</sup> century. Together with Lorentz's law, which describes the electric and magnetic force acting on a charge, they represent the fundamentals of today's classical electrodynamics.

Maxwell's equations were not completely new but extended the findings of the already mentioned pioneers and combined them with the law from Gauss, which describes the electric field and the electric flux through a closed surface and is based on the Gauss-Ostrogradski theorem. The importance of Maxwell's equations lays in the combination of magnetic and electric effects, which so far have not been considered in combination but were usually calculated separately. By combining all these effects, he included practically all phenomena and principles of electromagnetics in coherent notations [Tumanski, 2011, pp. 45-48]. The equations are omitted at this point since it is more about illustrating the connection of magnetism to electric currents and fields. In a condensed wording, they state:

- I) Electric charges are source and sink of the electric field (Gauss' law for electric fields)
- II) The magnetic field is source-free, meaning there are no magnetic monopoles. The magnetic field lines form closed paths with neither a beginning nor an end (Gauss' law for magnetic fields)
- III) A time-varying magnetic flux leads to an electric vortex field (Faraday's law)
- IV) Electric currents and temporal changes of the electric flux density lead to a magnetic vortex field (extended Ampère's law)

### 2.1.3 Types of Magnetism

At the end of subsection 2.1.1, it was distinguished between magnetic and non-magnetic materials. However, technically also non-magnetic materials show a very small magnetization when exposed to a magnetic field and therefore are also magnetic. These weak forms of magnetism are called paramagnetism and diamagnetism while strongly magnetic materials are called ferromagnetic or ferrimagnetic, which again is a weaker form of ferromagnetism caused by the crystal structure. By introducing the term of relative permeability  $\mu_r$ , which can be derived from Eq. 2.10 by the transformations given in Eq. 2.11 and Eq. 2.12, it is possible to quantify the strengths of all types of magnetism.

$$B = \mu_0 \cdot (H + M) = \mu_0 \cdot \left(1 + \frac{M}{H}\right) \cdot H \quad (2.11)$$

$$\mu_r = 1 + \frac{M}{H} \quad \rightarrow \quad B = \mu_0 \cdot \mu_r \cdot H \quad (2.12)$$

In para- and diamagnetic materials,  $\mu_r$  is constant and differs from 1 only by a value in the range of  $10^{-4}$  to  $10^{-9}$ . Accordingly, the flux results mainly from the magnetic field and not from the magnetization ( $B \approx H$ ). In paramagnets, the magnetization direction equals the direction of the field with a resulting  $\mu_r$  of slightly greater than 1. In contrast, diamagnets show a magnetization of opposite direction to the magnetizing field causing a rejection from any strong magnetic pole ( $\mu_r < 1$ ). However, since diamagnets are so weakly magnetic, it is hard to notice the rejecting force. An exception are superconductors, special materials, that fully displace the magnetic field from their inside at temperatures close to zero Kelvin, which is called Meissner effect.

In ferro- and ferrimagnetic materials, the magnetization is multiple magnitudes higher than in para- or diamagnetic materials with a resulting  $\mu_r$  in the range of  $10^2$  to  $10^5$ . However,  $\mu_r$  is not constant but highly dependent on the field strength. These materials have a magnetic order, which means an alignment of the atoms' shells according to an external field with a distinct magnetization persisting if the field is removed. Their high permeability causes them to be more attractive, more *permeable* for magnetic fields. Fig. 2.4a shows how a homogeneous field is diverted by a ferromagnetic body and rather passes through the material than through air. From a very simplified point of view, this is similar to the electric current that rather flows through conductors than through insulators. Para- and diamagnetic materials with their low permeability cause no such disturbance on the magnetic field (Fig. 2.4b) with the exception of superconductors, which are perfectly diamagnetic and fully displace the magnetic field resulting in a relative permeability of zero (Fig. 2.4c).

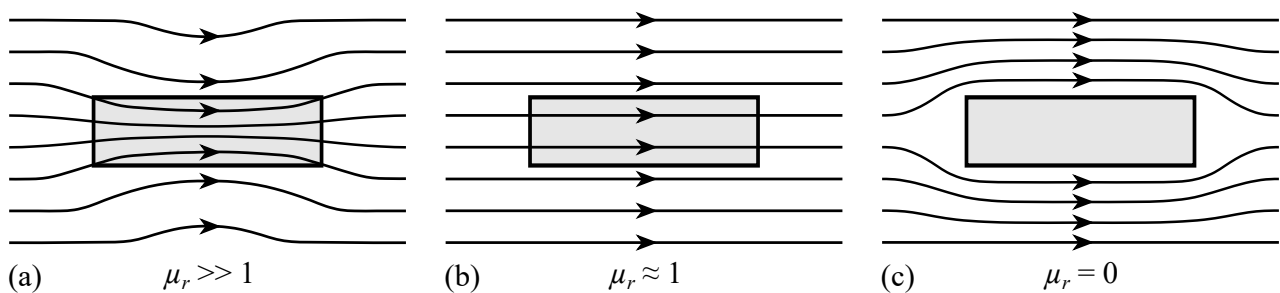


**Figure 2.4** Influence of ferromagnetic (a), para- or diamagnetic (b) and superconducting materials (c) on the propagation of magnetic fields

To complete the list, antiferromagnetism has to be mentioned as the last type of magnetism. Like ferrimagnets, antiferromagnets have a specific crystal structure. The smallest magnetic units in their inside (called ‘Weiss molecular fields’ by Pierre Weiss in 1906) show a magnetization and a magnetic order like ferromagnets, but are of antiparallel direction. Therefore, the magnetization of the neighboring fields cancel each other out resulting in a net magnetization of almost zero and their  $\mu_r$  resembles the one of paramagnetic materials [Ivers-Tiffée and von Münch, 2007, pp. 184-185].

Only ferro- and ferrimagnetic materials are of interest for electromagnetic applications as they allow the guidance of the magnetic field. Their magnetic properties depend on many parameters like the operating temperature and the condition of the material like the grain size or internal stress. To determine the suitability of materials for different applications, their internal flux density has to be recorded in dependence of the applied field strength, which leads to the so called hysteresis loop.

### 2.1.4 Hysteresis Loop

With the help of electromagnetic induction (Faraday's law), it is possible to acquire the flux density within a magnetic material as the sum of the field strength and its magnetization. By plotting the flux density as a function of the applied magnetic field, the non-linear magnetization process becomes apparent. The resulting graph reveals important characteristics like the maximum flux density, a material can exhibit, called the saturation flux density  $B_s$ . The remaining magnetization at zero field is called remanence  $B_r$  while the field strength, that has to be reached in order to fully cancel the persistent magnetization, is the coercivity  $H_c$ . All these values are indicated in an exemplary hysteresis loop depicted in Fig. 2.5. Apparently, there are two different flux densities for each value of the field strength leading to the name-giving loop. This phenomenon is called hysteresis and results from the fact that the flux density is not solely depending on the momentary value of the field strength but also on the prior magnetization state of the material. In a material, that was previously magnetized by a positive field, a value of zero flux density is only reached by applying a certain negative field and vice versa as indicated by the arrows [Cullity and Graham, 2009, pp. 18-20].

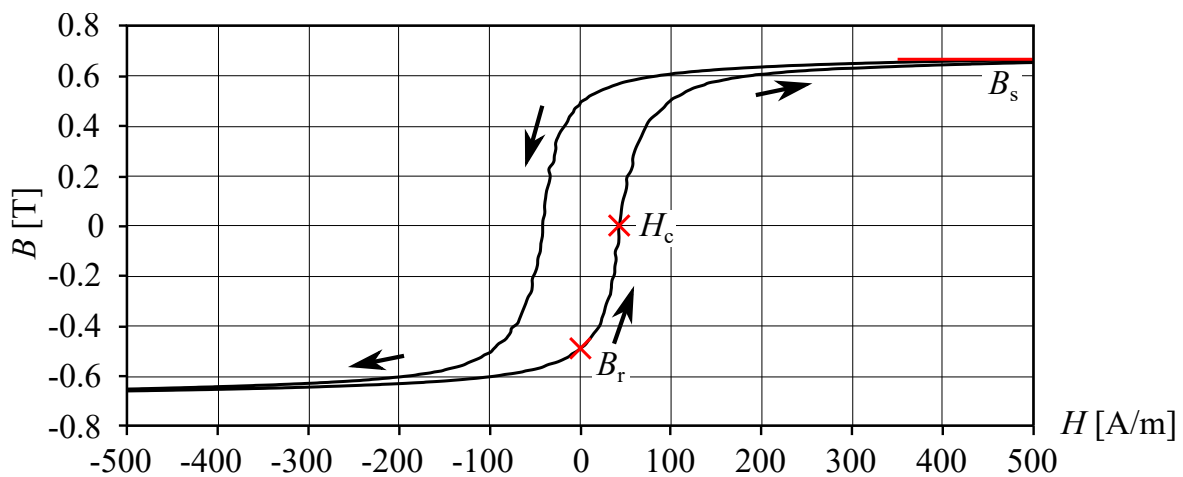


**Figure 2.5** Exemplary hysteresis loop of a soft magnetic sample

Ferromagnetic alloys are divided into two categories of soft and hard magnets, which can be classified by the corresponding hysteresis loop. Soft magnetic materials have a low coercivity below  $\approx 200$  A/m and hence their magnetization vector is easy to rotate. These are mainly iron (Fe), nickel (Ni) and cobalt (Co), their alloys and certain oxide ceramics. They are used in electromagnetic applications, where a quickly changing field is expected and a low remanent magnetization is wanted to reduce losses. This is because the area within the loop defines the energy that must be applied to rotate the field and therefore it is advantageous to use materials with a  $H_c$  as low as possible. Hard magnetic materials or permanent magnets on the other hand are used in application where a persistent magnetic field is desired as supporting field, e.g. in loudspeakers. Depending on the material, it is very hard to cancel their magnetization since a very high field strength is necessary. For neodymium magnets (NdFeB) for example,  $H_c$  is in the range of  $10^6$  A/m and subsequently the corresponding hysteresis loop is much wider, though the slopes may look similar.

As stated above, the saturation flux density  $B_s$  is another value of interest that can be derived from the hysteresis loop. It marks the point, at which the material is fully magnetized ( $M = \max$ ) and any further increase of the flux density is only due to the increasing field strength. While the coercivity is significantly different for hard and soft magnetic materials, the saturation flux density is not. Usual values for most hard and soft ferromagnetic materials are 0.7 – 2.5 T and the one of ferrimagnets about 0.1 – 0.5 T [Kallenbach et al., 2012, pp. 33-37].

In summary, the hysteresis loop can be understood as the profile of a magnetic material. However, there is not *the one* loop for a material. It will look different at higher or lower temperatures and its enclosed area increases at higher frequencies as it is related to power loss. Furthermore, it depends on the size and the prior mechanical treatment of the analyzed sample. Therefore, the most meaningful hysteresis loop is acquired at the final operating conditions and in the final place of operation. Especially this last requirement is sometimes challenging and therefore caused many developments in the field of magnetization measurements as is shown in section 2.3.

### 2.1.5 Demagnetization Effect

While it is quite straight-forward to acquire the flux density in a sample by winding a coil around it, the measurement of the field strength generating the flux is challenging. From the induction voltage, it is not possible to distinguish to which part the magnetization  $M$  and the field strength  $H$  cause it. Therefore, the measurement devices are usually designed to produce a uniform field that is measured at a point near the sample where it can be assumed to have the same value as inside of it. However, a feature of magnetic or magnetized bodies is the existence of poles as shown for the bar magnet in Fig. 2.2. Poles are only created when a magnetic circuit is open, which means that the flux lines are flowing partly through air or another non-magnetic material. If a ring-shaped ferromagnetic body is magnetized by a surrounding coil as depicted in Fig. 2.6a, almost all the flux stays in the body and subsequently there are no poles. If a part of that ring would be cut out, the flux had to leave the body at that point as electrically induced flux always forms a closed loop (Maxwell's 3<sup>rd</sup> equation). Subsequently, at both ends of the ring magnetic poles are formed as indicated in Fig. 2.6b.

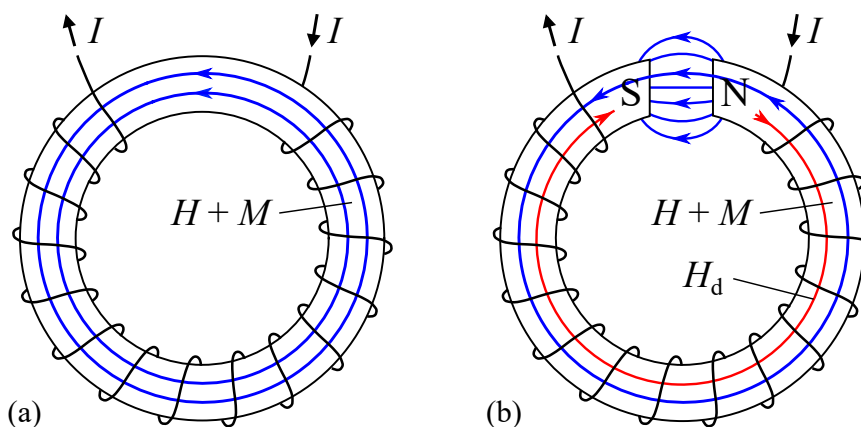


**Figure 2.6** Closed (a) and open (b) ring sample magnetized by a surrounding coil

The consequence of the existence of poles is the creation of a magnetic field between them, which has an important effect on the field strength in the inside of the magnetized body. In contrary to the induced flux, the magnetic field arising from magnetic poles does not form closed loops but leads from the northpole to the southpole (Maxwell's 2<sup>nd</sup> equation) even though the poles are created by current. Subsequently, inside the ring with the cutout a magnetic field is created in opposite direction to the flux lines, which maintain the original direction. This field is called demagnetization field  $H_d$  and decreases the final flux by the term  $\mu_0 H_d$  according to Eq. 2.13, where  $H_{\text{cur}}$  is the field caused by the current [Cullity and Graham, 2009, pp. 48–51].

$$B = \mu_0 \cdot (H_{\text{cur}} - H_d + M) \quad (2.13)$$

The issue of the demagnetizing field is its uncertain value, which can only be estimated and additionally varies from point to point inside the magnetized body. As an example, the varying demagnetization field strength of a bar magnet, that was determined qualitatively by the measurement of the flux density along the magnet, is shown in Fig. 2.7. Apparently, the flux density is lowest close to its poles, which correlates to the high demagnetization at these points.

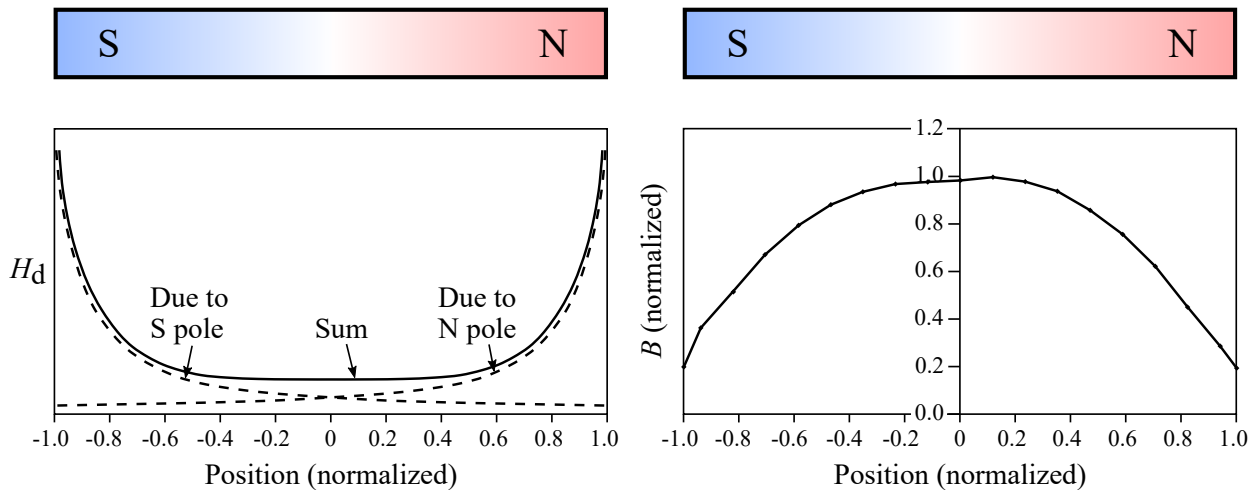


**Figure 2.7** Demagnetization field  $H_d$  and measured local flux density  $B$  of a bar magnet [Cullity and Graham, 2009, pp. 49–50]

This so called demagnetization effect is of great importance when a hysteresis loop is acquired in an open magnetic circuit, because the true field strength  $H_{\text{tr}}$  within the sample is lower than the apparent value  $H_{\text{app}}$  outside of it as it is decreased by the demagnetization field  $H_d$ . Since  $H_d$  is linearly dependent on the magnetization  $M$ , the demagnetization factor  $N_d$  was introduced as the relation between both values. Accordingly, the true field strength  $H_{\text{tr}}$  in a magnetized body can be expressed as

$$H_{\text{tr}} = H_{\text{app}} - N_d \cdot M. \quad (2.14)$$

The demagnetization field can never be larger than the magnetization that creates it. Accordingly, the maximum value of  $N_d$  is one. The observation that the demagnetization factor  $N_d$  is highest at

the points of a sample, where the most flux lines leak out of it, lead to the observation that it is related to the angle between the surface of the body and the course of the flux. The more the flux runs parallel to the surface, the lower the demagnetization factor. It therefore differs locally within most bodies as already shown in Fig. 2.7. It was shown mathematically that the ellipsoid is the only body with a constant demagnetization factor, which results in the possibility to exactly determine the true field strength in its inside. Depending on the size of the three axes  $a$ ,  $b$ ,  $c$  of the ellipsoid, it may be flat in the shape of an oblate spheroid (Fig. 2.8a) or rather long like a rounded cylinder (Fig. 2.8b). Therefore, the demagnetization factor is different for each spatial direction depending on the length of the axes. The longer an axis is in relation to the others, the lower the associated demagnetization factor. The oblate spheroid in Fig. 2.8 is therefore easy to magnetize in the direction of  $b$  or  $c$  but hard to magnetize in the direction of  $a$ . As the increase of the length of one axis makes the others smaller in relation, it is not possible to decrease all demagnetization factors at the same time. It could be shown that the sum of the three factors always equals one as noted in Eq. 2.15. For a sphere where  $a = b = c$ , all three factors have the same value of  $1/3$  [Osborn, 1945; Stoner, 1945].

$$N_a + N_b + N_c = 1 \quad (2.15)$$

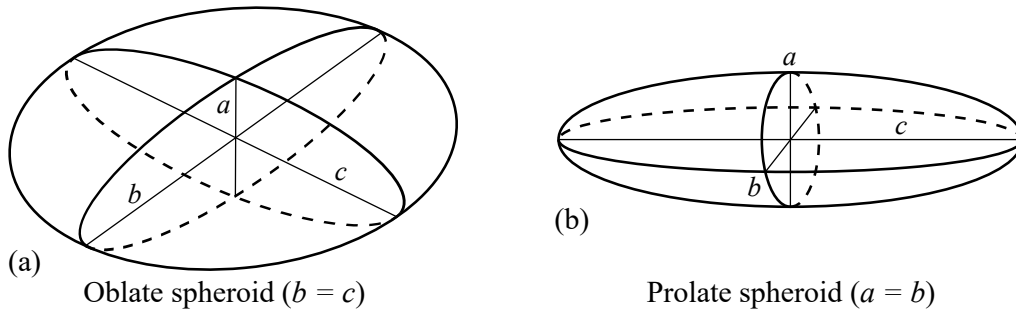


**Figure 2.8** Two special kinds of ellipsoids: the oblate and the prolate spheroid

In their publications, Osborn and Stoner provide compact equations as well as graphs and tables to obtain the direction-dependent demagnetization factors for different types of ellipsoids. However, since ellipsoids are complicated to manufacture, most bodies in technical application do not have a corresponding shape. Consequently, the demagnetization factors for ellipsoids are more of theoretical interest and not very helpful. The first values of practical relevance came from Bozorth [1951, pp. 846–848] for cylindrical samples. As for non-ellipsoidal bodies the demagnetization factors are not constant, the calculated values represent an average over the whole specimen. Decades later, Aharoni [1998] and Chen et al. [2005] published articles about the factors for rectangular prisms. While Aharoni offers a long equation to calculate them from the three dimensions of the prism, Chen et al. published data tables and graphs sorted by the ratio of the different edge lengths of the specimen. The tables of Chen et al. take into account the permeability of the material as well, which was shown to also influence the demagnetization factor. They refined their calculations for cylindrical rod and disk samples one year later [Chen et al., 2006].

In summary, the phenomenon of demagnetization makes it difficult to determine the true hysteresis loop of a magnetic sample. As the apparent field strength is larger than the one within the sample, the final graph is sheared along the x-axis. However, this has generally no effect on the coercivity because the magnetization  $M$  at this point is zero and so is  $H_d$ . Similarly, the saturation magnetization is not affected but apparently reached at a higher field strength. To account for the demagnetization, the above mentioned literature estimating the values for  $N_d$  are useful only if the specimen under evaluation closely fits the form specified by the authors. In the case of special geometries, the demagnetization factor has to be determined by own experiments. A possible way of largely decreasing the demagnetization effect is the use of customized measuring stands that form an almost closed magnetic circuit around the sample in order to avoid the creation of poles in the first place. As shown later in section 2.3, this is the typical method used for steel sheets used in electric machinery. In case of thin films no such methods exist, however, their extreme aspect ratio due to layer heights in the nanometer range results in a relatively low demagnetization effect.

## 2.2 Magnetic Thin Films

Due to the mentioned special geometry of thin films, their magnetic properties are significantly different from bulk materials. The reason for this lies in the magnetic domains, which is how the regions of the same magnetic orientation are called. Their impact on the magnetization process and the occurring losses are of great importance for high frequency applications and is considered in some detail.

### 2.2.1 Magnetic Domains

Domains are three-dimensional regions of identical magnetization vector clustered within a magnetic material with their size and shape depending on many different aspect like e.g. the crystal structure and the external magnetic field. Each domain is always fully magnetized considered separately its magnetization vector is pointing in a random direction. From a macroscopical viewpoint, however, the sum of the domains adapt the shape and magnetic orientation of minimal energy, which depends on the presence of an external magnetic field. Therefore, it is the average alignment of all the domains, that represents the magnetization state of a material. In a strong magnetic field, all domains align in the same direction – the material is said to be saturated ( $B_s$ ). While this is the state of minimal energy in a strong magnetic field, it will not persist when the field is removed. This is due the existance of very strong magnetic poles in a fully aligned magnetic body, which is energetically disadvantageous when no field is present. Instead, some domains will flip and the walls between them will appear again. Even though every wall holds a small amount of exchange energy caused by the neighbouring atoms with different magnetic orientation, the resulting multi-domain structure is energetically advantageous as it decreases the pole strength. These two conflicting types of energies eventually reach a state of equilibrium with the majority of the domains staying aligned in the direction of the previous field, what can be observed as remanence magnetization ( $B_r$ ) [Cullity and Graham, 2009, pp. 276-283].

### 2.2.2 Size Effects

The walls between the domains are typically in the range of 40 – 200 nm depending, however, on the material and the magnetization angle difference between the neighboring domains. A transition between two domains with a common  $90^\circ$  degree difference in the magnetization angle for example is spread over 150 atoms in iron, which is about 40 nm. The transition, therefore, is not sharp but rather smooth with a small angle between every neighboring atoms, as this results in a smaller exchange energy [Cullity and Graham, 2009, pp. 276-283].

Due to the shape of thin films, the magnetization direction usually lies in the plane as the demagnetization factor along the  $z$ -axis is very high. Accordingly, also the domains are orientated in the plane as shown in Fig. 2.9 illustrating an exemplary crystal with  $90^\circ$  and  $180^\circ$  walls appearing at the different magnetization states. The low height of thin films causes the domains to extend over the entire film thickness and also affects the shaping of the domain walls. While they normally rotate with their magnetic orientation pointing out of the plane, Néel showed that for films below a certain layer height, the rotation in the plane is energetically advantageous [Cullity and Graham, 2009, pp. 400-405].

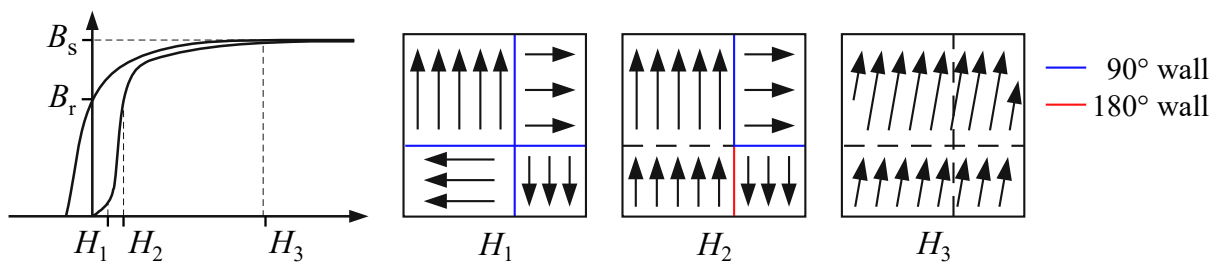


**Figure 2.9** Visualization of the magnetic domains in a magnetic material at different states of magnetization (adapted from [Kallenbach et al., 2012, p. 33])

There is another size effect that is of importance regarding magnetic thin films and results from the grain size. Generally, thin films feature much lower grain sizes in the range of 100 nm or less, which is related to how they are produced. Among chemical vapor deposition, thermal evaporation, electroplating and sputter deposition, the latter one is the most commonly used due to the high availability of deposition materials and alloys. During the process, ionized gas molecules are accelerated and strike a high-purity target material. The thus extracted atoms accumulate on the surface of the substrate, to which they will remain bonded. The interaction of the thin film with the substrate affects its behaviour and has to be taken into account when tailoring magnetic materials. The substrate's surface condition, the deposition parameters like chamber pressure, gas flow and temperature all have to be controlled [Cullity and Graham, 2009, pp. 397-398].

A resulting small grain size is of critical importance as it significantly affects the coercivity as is well understood, today. The chart from Herzer depicted in Fig. 2.10, which was first published in 1997 and extended in 2013, shows this correlation for various modern softmagnetic bulk materials and alloys. The black lines in the chart represent the trend lines based on the marked values measured and published by different authors. There is a proportional characteristic  $H_c \sim 1/D$  showing the tendency of an decreased coercivity at larger grain sizes, resulting in a lower hysteresis. Therefore, iron or



iron-silicon alloys like FeSi<sub>6.5</sub> with increased grain size play an important role in the energy sector. However, the quite modern (but expensive) nanocrystalline and amorphous materials have grain sizes of about 10 nm and reach an even lower hysteresis. It was observed that there is a reversal of the trend for grains smaller than  $D \approx 60$  nm with a drastically decreasing coercivity for lower values. The relation of  $H_c \sim D^6$  was determined experimentally and prove that slight grain size differences in this range have a huge impact on the coercivity [Herzer, 2013].

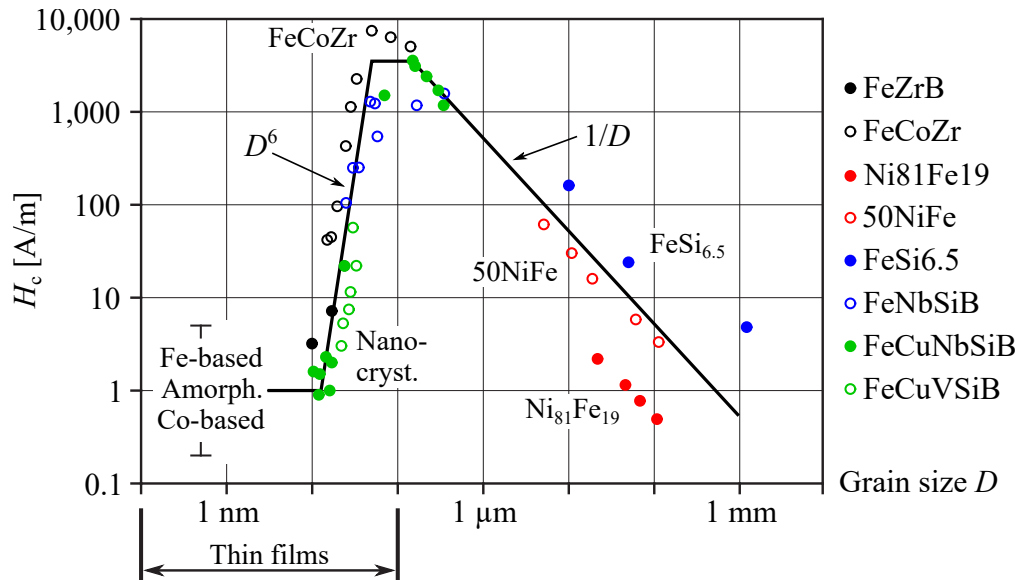


**Figure 2.10** Coercivity vs. grain size for different soft magnetic alloys (adapted from [Herzer, 2013])

### 2.2.3 Domain Wall Mobility and Iron Loss

While there is no size effect existent regarding the magnetization, the presented influences of thin films on the shaping of the domain walls and the hysteresis are very important. It is because the hindrance of the domain wall movement was shown as being the underlying physical cause for what is often referred to as ‘iron loss’ in magnetic materials. The easier the domain walls can move, the lower are the losses and the lower is the measured coercivity because it is directly related to the loss. From a conventional viewpoint, the losses in a magnetic material are divided in three terms, which are referred to as ‘hysteresis loss’, ‘eddy current loss’ and ‘anomalous loss’. Though modern literature partially rejects this classification of loss in magnetic materials, because they all result from the same cause, it is still common to use these terms [Cullity and Graham, 2009, pp. 448-449].

The classical loss breakdown is depicted in Fig. 2.11. As shown, the loss is given in dissipated power per magnetization cycle  $P/f$  (with the unit J/kg) and plotted over the frequency. The hysteresis loss per cycle is independent from frequency being a discontinuous process. It represents the energy necessary to relocate the domain walls (in low fields) and eventually to rotate the domains (in strong fields) as shown in Fig. 2.9. It can be measured in a quasi-static field when there are no frequency related losses arising from additional eddy currents [Hubert and Schäfer, 2008, pp. 271-272].

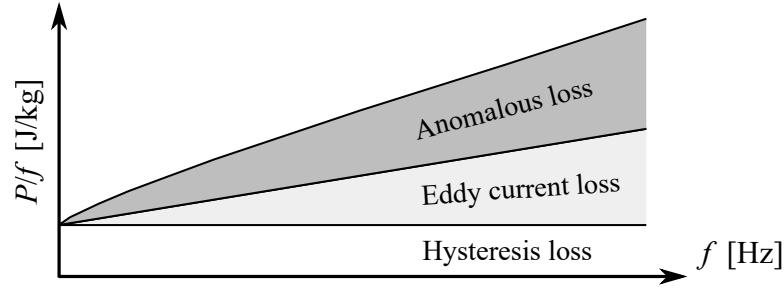


**Figure 2.11** Conventional classification of losses in magnetic materials (adapted from [Hubert and Schäfer, 2008, p. 272])

The second type of loss is the classical eddy current loss occurring in conductive media, which most magnetic alloys belong to (except for ferrites). Eddy currents are the main reason for the damping of the domain wall movement at high frequencies and therefore the main reason for loss in this case. Assuming a uniform sinusoidal induction process (based on a constant permeability) and a complete penetration of the magnetic sample, its value can be derived from Maxwell's equations. It is given in Eq. 2.16 where  $d$  is the sheet thickness,  $B$  is the maximum flux density,  $\rho$  is the resistivity and the 6 in the denominator is a geometrical factor used for laminations or sheets [Jiles, 1994].

$$P = \frac{\pi^2 d^2 B^2 f^2}{6\rho} \quad (2.16)$$

According to Eq. 2.16, the eddy current loss depends quadratically on the frequency. However, the linear increase shown in Fig. 2.11 results from the power per cycle  $P/f$  used as y-axis, which is obtained by dividing Eq. 2.16 by the frequency  $f$ . The loss can be effectively reduced by decreasing the sheet thickness  $d$ , which is why in power transformers for example, multiple insulated sheets are used instead of a continuous body. The same method is applicable in thin film technology by using multilayer stacks separated by non-conductive laminations. The use of amorphous materials with a higher resistivity  $\rho$  is also beneficial [Hsiang, 2020, pp. 16103-16106].

The distinction of the classical eddy current loss from the anomalous loss is entirely a theoretical one. It results from the imperfection of the given equation due to the made assumption of a constant permeability, which is not the case in magnetic materials. Therefore, the flux density does not linearly depend on the field strength and has no sinusoidal shape. Furthermore, the permeability varies locally and depends on the size of the domain walls. The resulting underestimation of the eddy current loss leads to a deviation between the predicted and measured values and the difference is misleadingly called anomalous loss [Cullity and Graham, 2009, pp. 440-445].

As early as 1958, a domain wall model was developed by Pry and Bean [1958], which dealt with the extra loss and received great attention. Though the domain wall damping is even better understood today [Hubert and Schäfer, 2008, pp. 271-272], its complexity makes the calculations of the true loss elaborate and yet inaccurate as e.g. Gao et al. [2020] showed recently. Therefore, measurements are mandatory and useful methods include the frequency related measurement of the hysteresis loop [Jiles, 1994] or of the (complex) permeability [Cullity and Graham, 2009, pp. 416-418].

### 2.2.4 Ferromagnetic Resonance and Magnetic Anisotropy

In order to meet the growing interest in inductors, which can be integration on the chip level, it is the aim of maximizing their operation frequency, enabling a significant size reduction. There are already transformers reported working in the range of several hundred megahertz [Le et al., 2021, pp. 13-14]. However, these either employ iron oxide based ferrites ( $\text{Fe}_2\text{O}_4$ ) or no core at all. While core-less inductors only reach low Q-factors meaning a low ratio of reactance to ohmic resistance, ferrites are not CMOS compatible because they require very high fabrication temperatures. Therefore, amorphous and nanocrystalline thin film alloys represent a novel approach for competing with ferrites showing a higher permeability and saturation flux density and lower losses at frequencies up to the gigahertz range [Fergen et al., 2002]. In this regime the ferromagnetic resonance frequency  $f_{\text{FMR}}$  is approached, which means a coupling of the oscillatory motion of the electron spins (precession) with the applied magnetic field. The consequence is that another type of loss appears causing the rotation of the spins to be converted to heat [Cullity and Graham, 2009, pp. 435-436].

Already in 1935 the Landau-Lifshitz equation was formulated, describing the damping caused by this effect. It was extended to the so called Landau-Lifshitz-Gilbert equation when Gilbert [2004] added another term to it. In this form it can be used to accurately describe the losses at high frequencies as Bottauscio et al. [2015] was able to verify by experiments. The equation can be transformed to obtain the ferromagnetic resonance frequency, which is given in Eq. 2.17. In it  $\gamma_e$  represents the gyromagnetic ratio of electrons and  $H_k$  is the anisotropy field strength [Neudert et al., 2004].

$$f_{\text{FMR}} = \frac{\gamma_e \mu_0}{2\pi} \sqrt{M_s H_k} \quad (2.17)$$

The interesting part of this equation is the dependence of the resonance frequency on the saturation magnetization and the anisotropy field strength. By imprinting a hard axis perpendicular to the magnetization direction, the losses in the material can be reduced and it is applicable for increased frequencies [Cullity and Graham, 2009, p. 419]. Therefore, materials with the possibility to induce an anisotropy field like CoFeHfO [Li and Lee, 2007], CoFeBSi [Bottauscio et al., 2015] and CoZrTa [Selvaraj et al., 2020] are most suitable for applications up to the gigahertz range.

To assist in developing these alloys, the frequency dependent acquisition of parameters like the coercivity but also of the anisotropy field strength and its direction is necessary. These requirements will be taken into account for the design of the measurement device.

## 2.3 Devices for the Measurement of the Magnetization

As stated in the introduction, there is a lack of non-destructive measurement technologies regarding the magnetization behavior of thin films. During production, entire wafers can be analyzed if there is a machine to apply a magnetic field of equivalent size. It is possible to dice out a little part of the wafer but one has to rely on the next ones to have the same properties. The repeatability of the processing technology, but also of the measurement techniques is therefore very important.

In general, the existing devices can be classified according to the frequency range they cover and whether the measurement is stepwise or continuous. The stepwise approach is working with the help of a changing direct current (DC) bias field and measuring the magnetization at this point by applying either a secondary high frequency AC field or causing the sample to oscillate periodically. The device that employs the latter method is the vibrating sample magnetometer, described in subsection 2.3.1. It is by far the most frequently used device in research and industry laboratories as it provides great flexibility and has a very high resolution, though the measurement of the hysteresis loop usually takes several minutes [Fiorillo, 2010, p. S133]. A less often used adaption is the alternating gradient magnetometer (AGM), which is presented in subsection 2.3.2.

Hysteresis loop tracers, on the other hand, achieve a continuous measurement in arbitrarily shaped alternating fields and often work in the range of the power frequency. However, there is no standard design for these devices and therefore multiple adaptations have been realized in the past with the aim to analyze magnetization parameters at elevated frequencies. As presented in subsection 2.3.3, partially these devices achieve the acquisition of hysteresis loops up to the megahertz range.

The most elaborate technology is the transmission line method described in subsection 2.3.4. Initially adapted for the use with thin films by Grimes et al. [1988], it is the only method that allows the evaluation of thin films up to the gigahertz range. Instead of acquiring hysteresis loops, it measures the frequency dependent complex permeability with the help of a network analyzer.

Eventually, this section covers some measurement methods applicable for the use with transformer sheets as they exploit some principles that are worth considering also for the use with thin films. They are explained in subsection 2.3.5 and 2.3.6 and lead to the conclusion of how the design of the developed device could look like.

### 2.3.1 Vibrating Sample Magnetometer

The vibrating sample magnetometer is based on the extraction method, a basic approach where a voltage is induced in a coil by extracting a magnetized sample out of its field. In the original design, a large solenoid generates a homogeneous static magnetic field in its inside by applying a direct current. According to Ampère's law, its field strength is proportional to the current and the corresponding coefficient can be determined with e.g. a hall probe. The analyzed specimen is now positioned centrally in the solenoid with a second coil wound around it, which serves as the sensor coil. When extracting the specimen from the induction coil, a change of the flux within its enclosed area induces a voltage  $U_{\text{ind}}$  in the coil. As the field strength of the solenoid remains constant throughout the whole experiment, it has no effect on the induction voltage. Subsequently, the integration of the induced voltage from  $t_1$  at the point before to  $t_2$  at the point after the extraction delivers the prior magnetization  $M$  of the sample as given in Eq. 2.18, where  $A$  is the cross sectional area of the specimen.

$$M = \frac{1}{\mu_0 A} \int_{t_1}^{t_2} U_{\text{ind}} dt \quad (2.18)$$

While the analyzed specimen can be of various shape and the method has a rather simple assembly, it lacks in terms of repeatability. Another downside is the measurement time, as one extraction cycle only delivers one data point and the procedure has to be repeated several times with different field strengths to gain a complete hysteresis loop. To overcome the repeatability issue, there were different approaches to construct a device with a continuously vibrating sample. Eventually, it was Foner [1959] who successfully introduced the vibrating sample magnetometer (VSM) with a design similar to the one depicted in Fig. 2.12. As shown, the analyzed sample is located between the poles of a large electromagnet allowing for much higher fields compared to solenoids. The poles may be moved to adjust the gap size for larger samples or to increase the field strength by decreasing the distance. The resulting field strength is therefore not calculated from the current in the magnetizing coils but is usually measured with a hall probe. The sample is attached to the end of a rod performing an oscillating movement perpendicular to the field. A set of four search coils sits within the air gap to detect the field gradient due to the vibrating sample. Foner initially proposed multiple layouts for how the search coils may be arranged, all of which provided sets of two antiseriably connected coils. This way, small variations of the field strength have no effect on the output signal as the individual induced voltages cancel out. In the most common search coil arrangement shown in the enlarged view in Fig. 2.12, the two coils on each side are connected to form one output. While the induction voltage from a change of the field strength has no effect, the moving sample causes a positive field gradient in one of the coils and a negative in the other as long as it is located between them. Due to the antiseriably connection, however, the induced voltages do not cancel out but sum up, showing the benefit of this method. The two coil pairs on the left and right compensate for symmetry errors as the sample will most probably not be centered perfectly [Cullity and Graham, 2009, pp. 67–70].

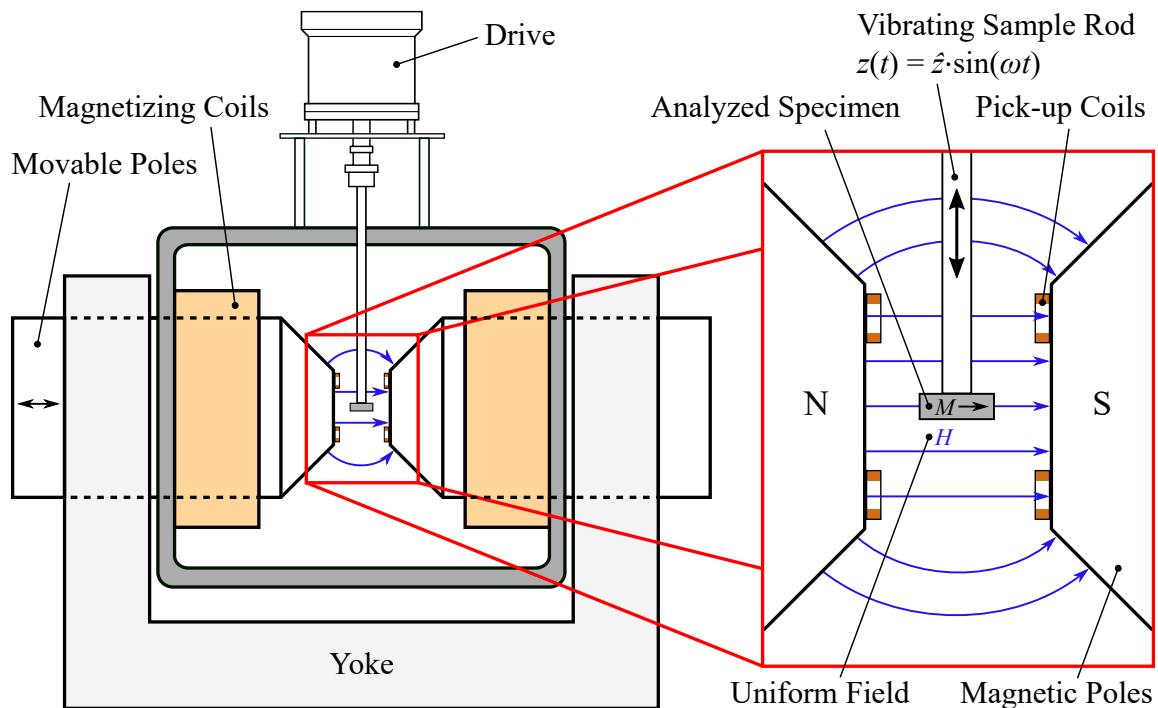


**Figure 2.12** Schematic draft of a vibrating sample magnetometer (VSM)

The VSM has to be calibrated using a specimen of similar dimensions as the sample under evaluation and with known magnetic moment, which is the product of the magnetization  $M$  and the calibration sample's volume  $V$ . During calibration the ratio of induction voltage per unit of magnetic moment is measured and used for the calculation of the magnetization of the unknown sample.

The vibration amplitude of the VSM is typically below one millimeter peak-to-peak and the signals within the search coils are small and require amplification. This is performed using lock-in amplifiers, sensitive only to signals of the vibration frequency. This way, VSMs are suitable for measuring small and weakly magnetic samples starting from  $M \cdot V = 10^{-8} \text{ Am}^2$ , corresponding to the saturation magnetization of about  $0.04 \mu\text{g}$  of iron. Careful sample preparation and high cleanliness therefore are mandatory. As for the basic extraction method, the open magnetic circuit requires demagnetization effects to be considered regarding the true field strength and the true magnetization. However, when examining thin films, the demagnetization factor  $N_d$  can be very small or even negligible [Cullity and Graham, 2009, p. 70].

### 2.3.2 Alternating Gradient Magnetometer

Another magnetometer relying on a moving magnetic sample is the alternating gradient magnetometer. Similar to the VSM, the sample is positioned at the end of a rod between the poles of an electromagnet and subjected to a uniform field. The difference to the VSM is that the sample is not moved up and down by a linear motor but vibrates due to a small alternating field, which overlays the static field in the same axis. This can be imagined as if the search coils of the VSM would be actively driven by a current. By tuning the frequency of this additional field gradient to the resonance frequency of the mechanical system, the vibration amplitude greatly increases. As it correlates with the magnetization of the sample, it serves as the measurement output, which was detected optically in first versions of the AGM. Today the measurement of the amplitude is based on piezoelectric bimorphs attached to the rod, which accurately detect its deflection [Flanders, 1988]. The AGM can be up to two magnitudes more sensitive than the vibrating sample magnetometer and offers an increased measurement speed, acquiring a complete hysteresis loop in about two minutes. On the downside, it is very limited in terms of sample size as an increasing mass can cause critical oscillations of the rod at resonance frequency leading to a potential damage of the device. This partly negates the advantage of the increased sensitivity compared to the VSM, which allows for larger samples resulting in larger magnetic moments [Pan, 2002, p. 497].

Both, the VSM and AGM are able to apply fields up to 2.5 tesla and are a good choice for the characterization of the quasi-static properties of samples with a strong anisotropy or even hard magnetic behavior. They offer great sensitivity due to the stepwise measuring method, which, however, leads to measurement times of several minutes and makes their use unattractive in industrial applications outside laboratories [Fiorillo, 2010, p. S123]. Furthermore, the sample has to be accurately fixed in the device by hand, which complicates a possible automation of the measurement procedure.

### 2.3.3 Hysteresis Loop Tracer

While VSMs usually have a similar design and are extensive machines with a huge watercooled electromagnet and an iron circuit of several hundred kilograms, hysteresis loop tracers are found with many different designs and their dimensions are usually much smaller. In contrast to the VSM, a voltage induction in the sampling coil is not achieved by a periodic movement of the sample but due to an alternating field. For bulk materials, it is desirable to use a ring specimen as shown in Fig. 2.13 as it represents a closed magnetic circuit and subsequently, there is no demagnetization effect due to the absence of poles (subsection 2.1.5). The working principle is as follows: A power amplifier connected to the primary winding applies a current  $I$ , which is proportional to the field strength (Ampère's law). The current is measured by detecting the voltage drop  $U_H$  across a shunt resistor and the field strength is calculated accordingly. The generated flux induces a voltage  $U_{\text{ind}}$  in the secondary winding, which is proportional to its change rate  $d\Phi/dt$  (Faraday's law). The induced voltage is therefore integrated over time to obtain the momentary values of the flux. The working principle of a hysteresis loop tracer is simple and in principle, there are no restrictions on the waveform regarding the achievement of reproducible measurements, though most commonly sinusoidal waveforms are used [Fiorillo, 2010, pp. S123-S125].

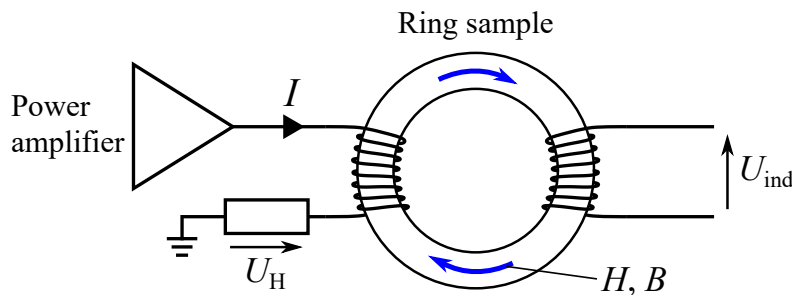


**Figure 2.13** Schematic draft of a hysteresis loop tracer employing a ring sample

As the flux is measured at a distinctive point on the ring rather than in the whole sample, hysteresis loop tracers employ a *fluxmetric* measurement. A VSM on the other hand measures the magnetization of the whole sample, which is called *magnetometric* [Cullity and Graham, 2009, p. 526]. However, despite the advantage of avoiding demagnetization effects, the use of ring samples has some drawbacks as for example, their manufacturing is mostly complicated and the windings must be made anew for each sample. In case of thin films, a ring specimen is generally not desirable as silicon can not be easily cut into this shape. Instead, open magnetic circuits are used allowing for variable specimen shapes. In order to measure the magnetization of a sample, it is placed in an induction coil of suitable size. However, due to the low cross-sectional area of the film and its probably moderate permeability, the air flux within the coil makes up for a significant part. Therefore, most commonly, two identical coils are used with one of them containing the specimen and the other being empty. By antiseriably connecting these coils, the induction voltage caused by the changing field strength is canceled and only the magnetization is measured, which requires a very accurate setup.

The excitation magnetic field is often generated by a Helmholtz coil pair, which means a pair of identical coaxial air coils whose distance equals their radius. According to simulations the field strength between the coils deviates by a maximum of 1.5 % within a sphere with a diameter of 1/3 of the diameter of the coils used [Huber and Urban, 1995]. Despite the high field uniformity Helmholtz coils allows for large specimens like a whole wafer to be investigated. On the downside, the necessarily large excitation coils limit the achievable field strength to about 10 kA/m and the high inductance restricts the applicable frequencies to below 100 Hz [Pan, 2002, pp. 495–496]. In order to allow the investigation of thin films in the kilohertz range, many adaptations of this standardized setup have been realized in the past using much smaller excitation coils to e.g. examine microwires or nanoparticles [Butta and Urdahl, 2009; Butta et al., 2009; Lenox et al., 2017]. By using smaller coils, the inductance of the primary winding is lower and the driving voltage can be significantly reduced. However, when increasing the measurement frequency up to the kilohertz range, the influence of the electrical circuitry has to be closely considered. High-speed amplifiers and analog-digital converters have to be employed in order to avoid phase shifts due to signal lag [Fiorillo, 2010, pp. S126-S127].

Generally, hysteresis loop tracers allow the measurement of the occurring loss in the magnetized sample by calculating the area enclosed by the hysteresis loop. As given in Eq. 2.19, the energy loss per cycle  $P/f$  (in J/kg) results by integration over one period  $T$  and division by the mass density  $\rho$  of the sample. There is a frequency limit of this method when approaching the megahertz regime as several problems arise due to the stray inductances and capacitances from the windings. Therefore, beyond this range, usually the transmission line method is applied [Fiorillo, 2010, pp. S126-S128].

$$\frac{P}{f} = \frac{1}{\rho} \int_0^T H(t) \frac{dB}{dt} dt \quad (2.19)$$

### 2.3.4 Transmission Line Method

This method is applicable in the frequency range above 100 kHz and the only one suitable for measurements above 10 MHz. It is based on detecting the disturbance on the propagation of electromagnetic waves the magnetic sample causes. Therefore, vector network analyzers are usually employed, which are capable of retrieving the impedance  $Z$  from the complex reflection and transmission coefficients of an attached network. Careful measurement setup and a compact fixture holding the sample during the measurement is crucial as the wavelength  $\lambda$  at 1 GHz for example is only 30 cm and unwanted reflections can appear [Fiorillo, 2010, pp. S128-129].

The shorted end of a coaxial line has proven as a useful setup allowing the embedding of a ring sample (inner radius  $r_i$ , outer radius  $r_o$  and height  $h$ ) with the central wire passing through its inner as depicted in Fig. 2.14. By locating the sample at the end of the line, it is ensured that dielectric effects can be ignored as long as the sample's height is much smaller than the quarter wavelength  $\lambda/4$ . The impedance of this setup is measured over the desired frequency range with ( $Z = R + jX$ ) and without ( $Z_0 = R_0 + jX_0$ ) sample in place. Afterwards, the difference  $Z - Z_0$  is calculated and transformed to the complex permeability  $\mu = \mu' + j\mu''$  according to Eq. 2.20 and 2.21, where  $\varphi$  is the phase angle.



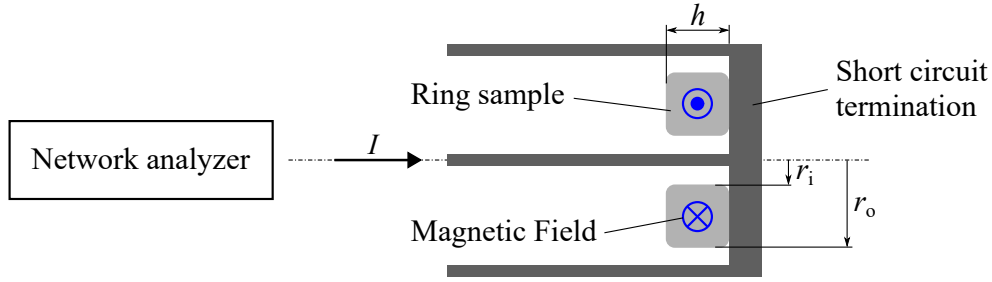


**Figure 2.14** Ring sample placed against the shorted termination of a coaxial line

$$\mu'(f) = 1 + \frac{X - X_0}{h \cdot f \cdot \mu_0 \cdot \ln(r_o/r_i)} = \frac{B}{H} \cos \varphi \quad (2.20)$$

$$\mu''(f) = \frac{R - R_0}{h \cdot f \cdot \mu_0 \cdot \ln(r_o/r_i)} = \frac{B}{H} \sin \varphi \quad (2.21)$$

When the imaginary part of the permeability  $\mu''$  differs from zero, it indicates that the field strength and the flux density are out of phase. This happens at frequencies close to the ferromagnetic resonance, when the magnetization of the sample is not able to keep up with the speed of the changing field due to the mass of the domain walls limiting their motion [Cullity and Graham, 2009, pp. 417-418]. The complex permeability can be used to calculate the loss per cycle using Eq. 2.22.

$$\frac{P}{f} = \frac{\pi B^2}{\rho} \frac{\mu''}{\mu'^2 + \mu''^2} \quad (2.22)$$

An adaption of the measurement setup for the use with thin films was presented by Grimes et al. [1988] and requires a precise sample holder and an external magnetic bias field. The high agreement between the corresponding results achieved with the transmission line method and the ones obtained with fluxmetric measurements could be demonstrated in the shared frequency band of 0.1 to 10 MHz by Beatrice et al. [2016]. By combining both devices, the authors were able of measuring the loss of different nanocrystalline thin film samples over eight orders of magnitude.

### 2.3.5 Permeameters

The presented measurement methods and their possible adaptations for the use with thin films reveal that only the principle of the hysteresis loop tracer allows for a localized (fluxmetric) measurement of a sample as large as a wafer. Unfortunately, the complex nature of electromagnetic waves prevents its application in the megahertz regime. Localized measurements on a whole wafer, which is the aim of this thesis, will therefore most likely be only possible in the kilohertz range. However, in literature there was no method found that only partially magnetizes a thin film in order to reduce the size of the excitation coils and increase the frequency range. It is therefore worthy to consider how the magnetic properties of transformer sheet samples are examined as their shape is very similar to the ones of thin films. In the field, different measurement techniques have evolved that apply fluxmetric measuring methods in combination with large samples.

Due to the large demagnetizing fields of transformers sheets, the use of closed magnetic circuits is the acknowledged way of recording their hysteresis loops. First principles date back to 1873, using a ring shaped specimen wound with a magnetizing coil and secondary sensing coil (Fig. 2.13). While this method generally is the most satisfactory one, it is also the most elaborate requiring the manufacturing of a ring shaped specimen of the investigated material, which has to be wound manually with two coils [Bozorth, 1951, pp. 843–845]. Therefore, different devices called permeameters were invented to facilitate the measurements. These devices feature a large sized yoke of low hysteresis, high permeability material that was closely attached to the bar-shaped specimen using screws or another clamping mechanism. For a long time, the Burrows permeameter was the most accepted one among them until the Fahy Simplex permeameter shown in Fig. 2.15 was found to achieve even better results [Sanford and Barry, 1927; Sanford, 1930].

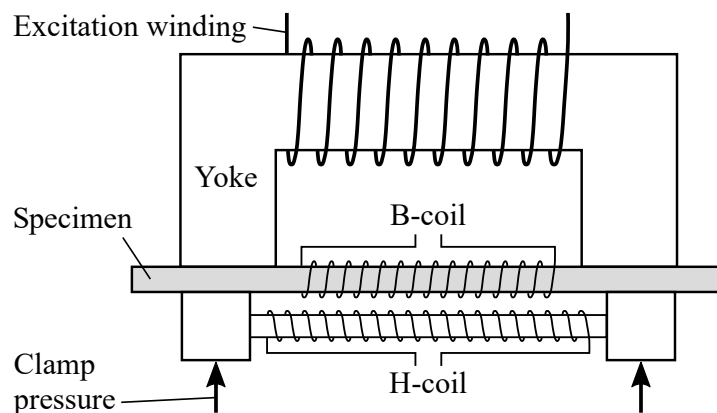


**Figure 2.15** Fahy Simplex permeameter

Permeameters allow for more comparable measurements between different materials and easier sample preparation as a bar or a strip is much easier to manufacture than a ring. A problem on the other hand is the measurement of the field strength, which may not simply be derived from the magnetizing current because of the small air gaps between the yoke and the specimen. Therefore, permeameters always contain a second coil wound on a non-magnetic body close to the specimen for the measurement of the field strength. This method is based on the assumption that the field strength close to the sample is the same as in its inside, which is not exactly true. Its uncertainty is one of the main problems of all kinds of permeameters, which partly results from the fact “that the field is not uniform over the length of the sample” [Cullity and Graham, 2009, p. 78]. However, the practical application and the good comparability inspired the development of the modern single sheet tester.

### 2.3.6 Single Sheet Tester

Since power conversion using transformers is one of the main applications in the steadily growing energy sector, a lot of research has been conducted in this field with the goal of decreasing the energy loss and increasing the overall efficiency [Shirkoohi and Kontopoulos, 1994]. In order to reduce eddy currents, transformer cores are not made from a massive body but consist of several thin isolated

sheets (subsection 2.2.3). They are not only subject to the primary alternating current that cause energy losses but also to rotational currents that have to be considered. Two devices have excelled in the recent decades for the accurate determination of the occurring losses: the single sheet tester (SST) and the Epstein frame. A SST resembles a permeameter with two yokes as shown in Fig. 2.16a. Due to the smaller and movable sample coil, it is able to measure fluxmetric magnetic properties along the sheet. The Epstein frame is shaped as a square consisting of multiple sheets forming the square's edges overlapping in the corners. All four edges are wrapped with magnetizing and measurement coils. While both principles are acknowledged and widely used, they have occupied scientists research worldwide for years looking for improvements in accuracy [Brix et al., 1982, 1984; Sievert, 1990; Zurek, 2005; Pfützner et al., 2011; Pfützner and Shilyashki, 2017; Müller et al., 2019].

Other research among SSTs is related to the problem of determining the field strength acting within the sample. Two different methods seem to have prevailed: The first makes use of a so called Chattock potentiometer proposed by Arthur Prince Chattock [1887]. It consists of a densely wound coil around a non-magnetic core used for measuring the differential field strength between two points in a sheet. It may have an arbitrary shape, though most often a halved toroid is used as shown in Fig. 2.16b. It resembles a halved Rogowski coil used for current measurements within conductors and is therefore also called Rogowski-Chattock coil. The application of this principle for magnetic field measurements in SSTs has been analyzed by Shirkoohi and Kontopoulos [1994] and more extensively by Abdalh and Dupré [2010], who point out that “inaccurate coil fabrication may cause a considerable error” in the measurement. Also Cullity and Graham [2009, pp. 42–43] conclude that small Chattock potentiometers are difficult to manufacture limiting their usage to larger devices.

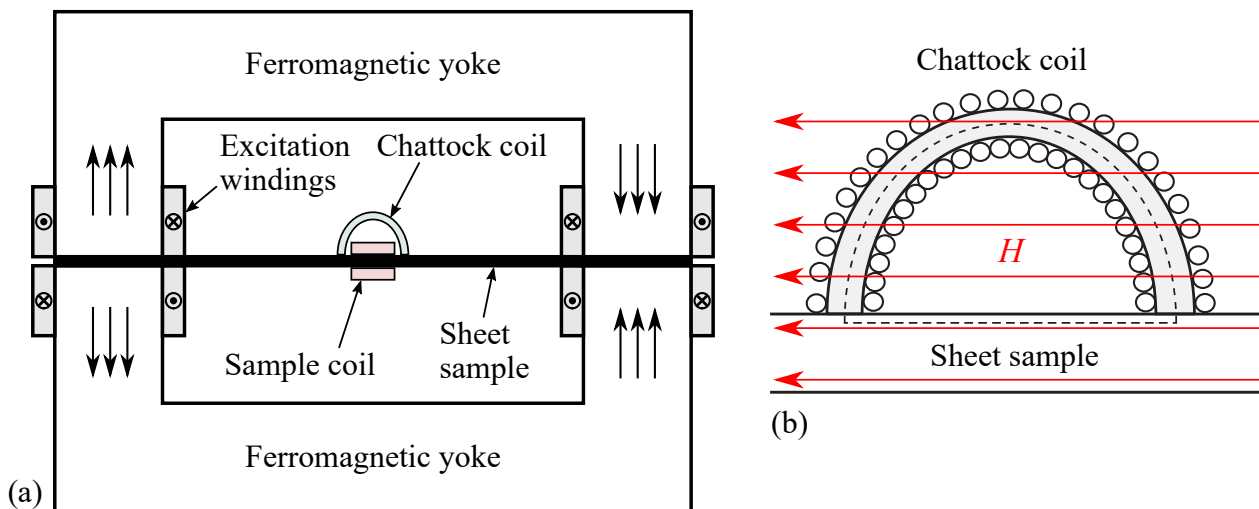


**Figure 2.16** Schematic of a single sheet tester (a) using a Chattock coil (b) for local  $H$  measurements

The second method for determining the field strength in the sheet was proposed by Nakata et al. [1987], who calculated the course of the field lines with the help of numerical simulations. Instead of a Chattock potentiometer, they used a straight air coil close to the specimen to detect the field strength similar to the arrangement in the Fahy Simplex permeameter. Their simulation showed that

decreasing the length of the H-coil to a maximum of about 85 % of the distance between the yokes' legs significantly reduces the measurement error. The actual innovation, however, concerns the use of a second H-coil close the first one. This way, the field strength at different distances from the sheet is measured allowing for the calculation of the gradient in order to extrapolate the field strength within the sheet. Nakata et al. state that the resulting error may be reduced to well below 0.1 % this way, regardless if only one yoke or two yokes are used. When only one coil is used, the error is in the order of a few percent and linearly increases with the distance to the sheet.

Tumanski [2002] repeated the simulations from Nakata et al. and compared the results to measurements he performed with very thin coils positioned at different distances from the sheet. The results from the simulations and the measurements for one (1U) and two (2U) yokes are shown in Fig. 2.17. Though the simulations and measurements differ from each other in terms of amplitude, they show similar trends. When two magnetizing yokes are used the distance of the H-coil from the sheet is not critical as long as it is not too close to it as the stray field of the specimen causes some disturbances. Interestingly, the so far usually strongly recommended use of two yokes seems not to be necessary when using two H-coils to measure the field. Tumanski states that “surprisingly for multicoil measurements this [one yoke] system is advantageous” as the field shows a linear gradient and can be extrapolated with very good results, better even compared two a two-yoke configuration, which may not be feasible for certain applications. The principle of using multiple H-coils was also exploited by Miyagi et al. [2010] in their ‘miniature’ SST and adapted by Stupakov [2012], who replaced it by an array of hall probes placed at different distances to the sheet.

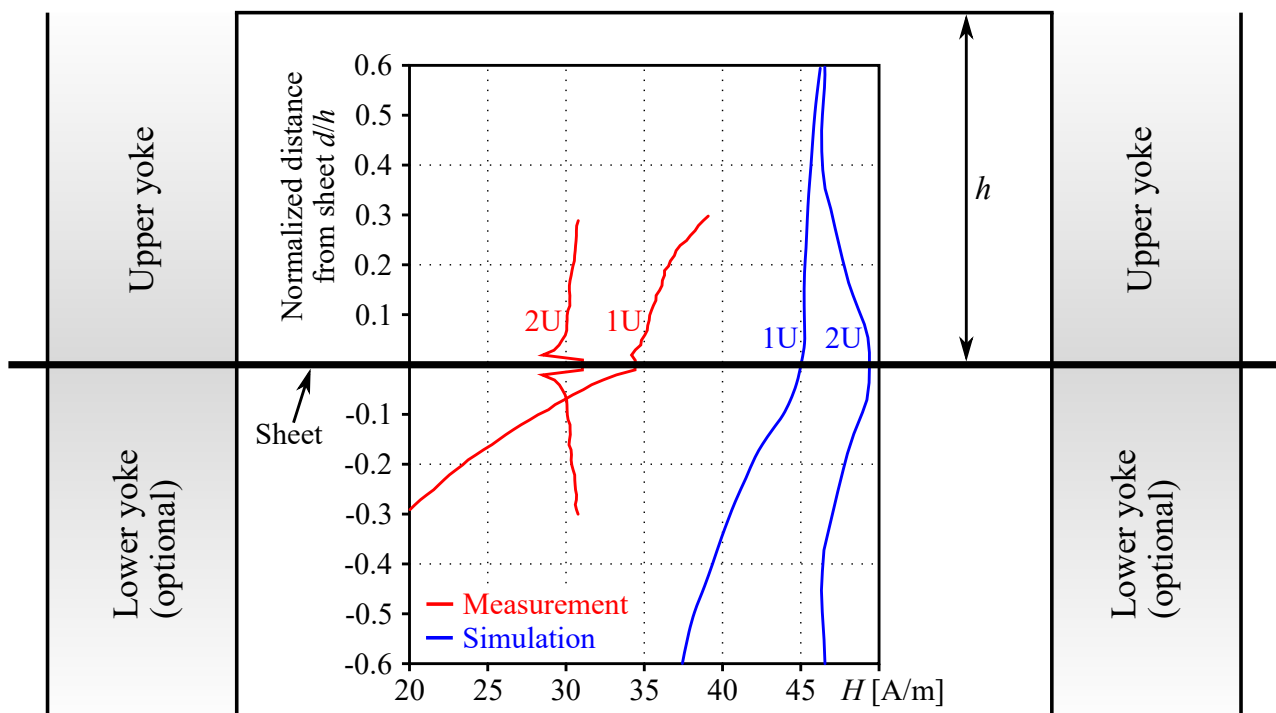


**Figure 2.17** Simulated and measured field strength between the poles of the yokes in a single sheet tester (based on data from Tumanski [2002])

With the possibilities offered by more sensitive measurement devices that became available, researchers began to look closer on the uniformity of the sheets. Subsequently, the use of large induction coils wound around the sheet was problematic as only average values were measured. A (partly) destructive alternative was the puncturing of the sheet and passing the wire of the search coil through it. It required a subsequent annealing to release the stress induced by the drilling [Brix et al., 1982]. To overcome this issue, Brix et al. [1984] proposed the so called ‘needle probe method’, which was further investigated in the years after [Senda et al., 1999, 2000; Pfützner and Krismanić, 2004; Abdallah et al., 2009]. As shown in Fig. 2.18, two electrically connected needles are placed on the top of the steel sheet, measuring the voltage difference occurring at the surface due to the eddy currents inside the sheet. In a thin material, the voltage between the two needles corresponds approximately to one half of the induced voltage of an induction coil with one winding. As this method does not require drilling, it is regarded as non-destructive.

The use of the needle probe method lead to the possibility of performing localized measurements very easily, for example for analyzing the grains of sheet steel or for defect characterization [Stephane et al., 2010]. Although, it is considered to be not quite as accurate as the use of coils, it is widely used for two-dimensional testing of electrical steel sheets [Tumanski, 2007]. As a modification, Zurek [2005] proposed the use of electrodes instead of needles since electrodes would not harm the specimen. Though this technique yields many uncertainties, a recent adaption making use of printed needle electrodes on top of a specimen showed good results [Nguedjang Kouakeuo et al., 2020].

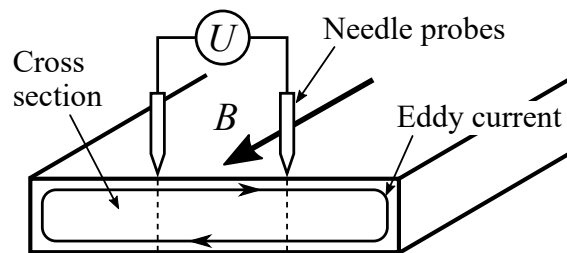


**Figure 2.18** Schematic of the needle probe method

### 2.3.7 Conclusion

Surprisingly, it was the review of the measurement techniques for transformer sheets, which revealed useful techniques for the examination of thin films. Placing a small yoke on the wafer to generate a spatially limited magnetic field appears to be a suitable method to enable local measurements. The detection of the magnetization of the sample is challenging, however, as it is doubtful that the output signal of needle-like electrodes is accurate enough. Instead, the measurement of the change of the flux in the yoke when it is attached to the layer is considered. Regarding the measurement of the field strength, the researchers have shown that the extrapolating of the values of multiple sensors located at different distances from the layer provides good results. Induction coils and hall probes were mostly used for this purpose, though with magnetoresistive sensors probably superior principles are available. Accordingly, these measurement techniques will be reviewed in the next section.

## 2.4 Technologies for the Measurement of the Magnetic Field Strength

In the almost 200 years since the discovery of Faraday’s law and the subsequent possibility of using induction coils for flux sensing, many other ways have been found to quantify the magnetic field strength. However, the corresponding devices are not equally sensitive and suitable only for a distinct range of the magnetic field strength. Furthermore, they differ regarding the frequency bandwidth they cover and their size. For the use in the measurement application described in the previous section, only those sensors come into question, which can be made small enough to fit in the inside of the magnetizing yoke. Apart from the induction coil (subsection 2.4.1), these are namely the hall probe (subsection 2.4.2) and the three most popular types of magnetoresistive (MR) sensors (subsection 2.4.3). The typical range and the bandwidth of these devices are listed in Fig. 2.19.

As can be seen, the field strength in the table is given in Tesla, the unit of the flux density. This is due to the fact that technically, it is always the flux density that is being measured. However, as the magnetization in non-magnetic materials is negligibly small, the flux equals the field strength with an insignificant error (subsection 2.1.1). The detectable field ranges from  $10^{-15}$  to  $10^1$  T, resulting in a total of 16 magnitudes. The mentioned metrologies clearly differ here with most of them covering five to seven magnitudes while the bandwidth mostly ranges from static fields to at least 1 kHz. An exception is the induction coil, which is not able to detect static fields.

The list also includes three other popular sensing technologies for comparison. The fluxgate is a quite old method [Aschenbrenner and Goubau, 1936], which, however, is still used in space or for geophysical prospecting. By exploiting the behavior of periodically saturated magnetic cores, it extends the use of induction coils to static fields. The method of optical pumping and the superconducting quantum interference device (SQUID) are the most elaborate methods applicable when extremely sensitive measurements are required for example in the field of non-invasive functional brain imaging. While the SQUID is known for decades and requires a superconducting ring for operation, the optically pumped magnetometer is a more recent technology exploiting magneto-optical effects and is believed to be a less costly alternative to SQUIDs in future applications [Coussens et al., 2021].

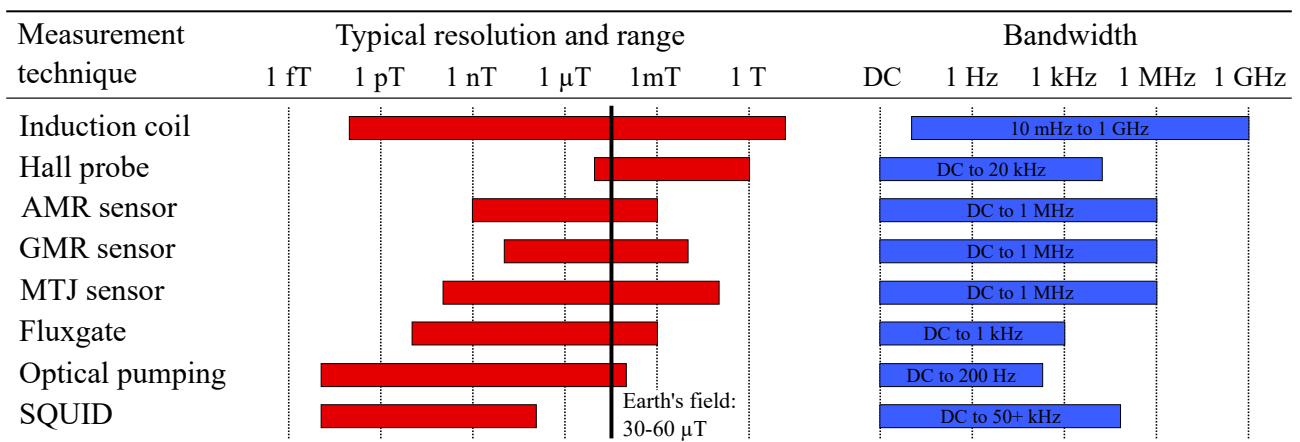


**Figure 2.19** Properties of different magnetic measurement techniques based on data from Lenz and Edelstein [2006]; Tumanski [2011, 2013]; Colombo et al. [2016]; Deak et al. [2017] and Ripka [2021]

### 2.4.1 Induction Coil

Despite their suitability for measuring the magnetization, induction coils can be used to measure the field strength as well if they are wound around a non-magnetic material where  $H \approx B/\mu_0$ . Following Faraday's law, the induced voltage depends linearly on the derivation of the flux density and signal integration is necessary to obtain the momentary field strength. This process will be reviewed in this subsection in more detail.

As shown in Fig. 2.19, induction coils offer a high versatility as they can be designed to detect a wide range of field strengths. Their sensitivity can be adapted by varying the number of turns or the cross-sectional area, thereby setting the effective measurement range. However, when it comes to high frequencies, the inductance and winding capacity have to be considered.

In the simplest case, the induction coil can be used for the measurement of a sinusoidal field strength of the form

$$H(t) = \hat{H}\sin(\omega t). \quad (2.23)$$

The derivative of this waveform equals a cosine function and therefore, the induced waveform is known and analog integration is not necessary. It is also possible to measure the induction voltage and perform a manual phase shift of  $\pi/2$ . The peak value of the induction voltage is the same as for its integrated form and is given in Eq. 2.25.

$$U_{\text{ind}}(t) = -nA\mu_0\hat{H}\frac{d(\sin(\omega t))}{dt} = -nA\mu_0\hat{H}\omega\cos(\omega t) \quad (2.24)$$

$$\hat{U}_{\text{ind}} = 2\pi f n A \mu_0 \hat{H} \quad (2.25)$$

However, it is more complicated if the induction coil is used for measuring a waveform of indeterminate appearance. In this case, when not only the maximum value of the field but also its waveform is desired, the induction voltage has to be integrated over time using either analog or digital signal integration methods [Tumanski, 2007, p. R37]. The debate about which integrator design is the better one continues until today and is not easy to resolve. Active analog integrators do not dampen the signal, while introducing offset and phase errors [Marconato et al., 2020]. Xia et al. [2015], however, overcame most of these issues by introducing extensive compensating electronics in their circuitry. Also Ming et al. [2019] proposed additional passive elements in their active filter used for the detection of fast switch currents to improve the filter's output signal. Passive integrators do not have these issues but can only be used for higher frequencies in order not to decrease the signal-to-noise ratio (SNR) by signal attenuation. Digital integration is said to achieve the best results due to the lack of capacitor discharge and drift errors. However, when looking at Eq. 2.25, it is noticeable that the induction voltage depends linearly on the frequency at which the flux density is changing. An induction coil used for a wide bandwidth of frequencies therefore has a wide bandwidth of output amplitude. Since an analog-digital converter (ADC) is generally limited to a certain input voltage, it is usually chosen to be slightly higher than the maximum output signal from the coil (occurring at the maximum

expected frequency). Consequently, signals of lower frequency and therefore lower amplitude are digitized with a decreased resolution. With each magnitude, it decreases by  $\log_2 10 = 3.32$  bits, which has to be considered when using digital integration methods. Eventually, the individual measuring task decides on the most useful signal handling [Marconato et al., 2020].

Apart from the integrator design issue, induction coils have the advantage of achieving a great linearity and can be used up to frequencies in the megahertz range or even above. Limitations arise only from the winding capacity, which forms a low pass in combination with the inductance of the coil. Ueda and Watanabe [1975] took a close look on the resulting frequency response of induction coils and analyzed potential problems. They formulated the value of absolute sensitivity  $S_a$  defined as the induction voltage per unit frequency of a sinusoidal flux density in an induction coil with the cross section  $A$  and the amount of turns  $n$

$$S_a = 2\pi nA. \quad (2.26)$$

Analogue to Eq. 2.25, the induction voltage is derived by multiplying  $S_a$  with the frequency and the flux density. However, the real output voltage measurable at the terminals of the coil depends on the inductance of the coil  $L$  and its wiring capacity  $C$ . Together these elements form a resonant circuit with the resonant frequency  $f_0$ .

$$f_0 = \frac{1}{2\pi\sqrt{LC}} \quad (2.27)$$

Ueda and Watanabe [1975] considered the effect of these frequency-dependent elements and formulated the operation sensitivity  $S_p$  of a real induction coil comprising an inductance and a wiring capacity. The equation for calculation  $S_p$  is given in Eq. 2.28.

$$S_p = \frac{S_a}{\sqrt{(1 + \alpha)^2 + (\beta^2 + \frac{\alpha^2}{\beta^2} - 2) \cdot \gamma^2 + \gamma^4}} \quad (2.28)$$

$$\alpha = \frac{R}{R_L} \quad \beta = R \cdot \sqrt{\frac{C}{L}} \quad \gamma = \frac{f}{f_0} \quad (2.29)$$

The value  $R_L$  contained in  $\alpha$  describes a load connected to the coil. If only a measurement device is connected, this value will typically be in the megaohm range, while the resistance of the coil  $R$  is generally much lower. In this case,  $\alpha$  may be treated as zero. Both the equivalent circuit of the real induction coil without load and its frequency response are shown in Fig. 2.20. The orange graph depicts the normalized sensitivity  $S_p/S_a$  in relation to the normalized frequency  $f/f_0$ . It shows the low pass effect of the inductance and the capacity and the occurring resonance peak at  $f = f_0$ . The black graph shows the normalized output voltage  $U_{out}/B$  as the combination of the induction voltage linearly increasing with frequency and the filter's frequency response. The exact value of  $f_0$  depends on  $L$  and  $C$  (Eq. 2.27), which both increase with the size of the coil and the winding count. It typically varies between 10 Hz for very large coils and about 10 kHz for smaller ones.



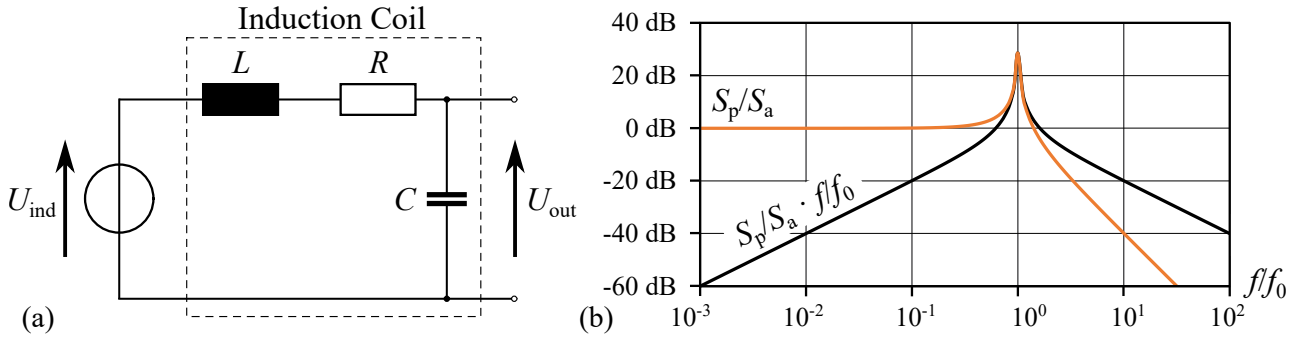


**Figure 2.20** Equivalent circuit (a) and normalized frequency response (b) of an actual induction coil

The frequency response illustrates the rather complicated behavior of induction coils. The maximum frequency up to which a coil may be used is primarily given by the winding capacity. In his book about inductors, Albach analyzes different winding techniques that help to reduce the capacity [Albach, 2017, pp. 45-69], which, however, result in complex coils not easy to manufacture. Another still very common method to deal with parasitic capacitance is to apply a load resistor to the coil's windings as suggested by Ueda and Watanabe [1975]. This way the coil becomes self-integrating above the lower corner frequency  $f_l$ , which arises due to the inductance and the combined resistance forming a first order low pass filter (Eq. 2.30). A second low pass filter is formed by the load resistor  $R_L$  and  $C$  causing a pole at the higher corner frequency  $f_h$  (Eq. 2.31) [Tumanski, 2007, pp. R35–R36].

$$f_l = \frac{R + R_L}{2\pi L} \quad (2.30)$$

$$f_h = \frac{1}{2\pi C \cdot R_L} \quad (2.31)$$

Together, Eq. 2.30 and 2.31 demonstrate that a decreasing value for the load resistor increases the bandwidth with a flat frequency response. The resulting graphs for different values of  $\alpha$  are depicted in Fig. 2.21. While even a small load  $R_L = 10R$  ( $\alpha = 0.1$ ) already effectively eliminates the resonance peak, a heavier load  $\alpha > 10$  is necessary to achieve a flat frequency response in the range between  $f_l$  and  $f_h$  and the necessary load resistor has to be chosen individually.

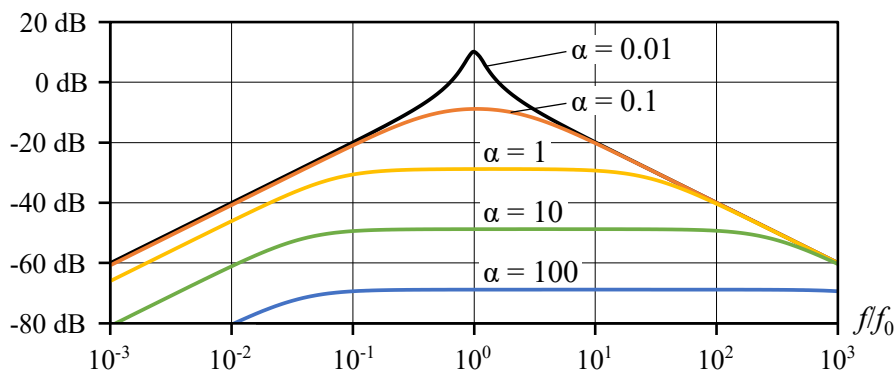


**Figure 2.21** Normalized frequency response of an induction coil with a load resistor

Aside from its positive effect of increasing the usable frequency range, the load resistor has the negative side effect to decrease the signal amplitude. Especially the slope at frequencies below  $f_1$  has to be mentioned here as the signal is not integrated in this range but is attenuated anyway. Therefore, passive or active integration circuits or the combination of both as proposed by Pettinga and Siersema [1983] might be worth considering. These additional filters can be designed to only work in a small frequency range in order not to further decrease the weak signal at low frequencies.

In summary, induction coils serve as very flexible magnetic sensors, that may be used to measure the flux density across a wide frequency range with variable sensitivity. Regarding the acquisition of the field strength, there are some special designs like the Chattock coil (subsection 2.3.6). However, induction coils are unsuitable if the magnetic field is static and there are usually better alternatives for very slowly changing magnetic fields. Furthermore, the necessary integration of the output signal is not a trivial task and requires a careful electric filter design.

### 2.4.2 Hall Probe

Another suitable sensor is the hall probe, a sensor that is widely employed because of its useful range starting at the earth's field strength and reaching the typical saturation flux density of most magnetic materials of about 2 T. Furthermore, its low cost, ease of operation and the linear output signal are beneficial. The hall sensor is based on the Lorentz force acting on the passing electrons in a metall or semiconductor thin film as shown in Fig. 2.22, if an orthogonal magnetic field is applied. The resulting force  $\vec{F}_L$  linearly depends on the vector product of  $\vec{B}$  and the electrons' drift speed  $\vec{v}$ :

$$\vec{F}_L = q\vec{v} \times \vec{B}. \quad (2.32)$$

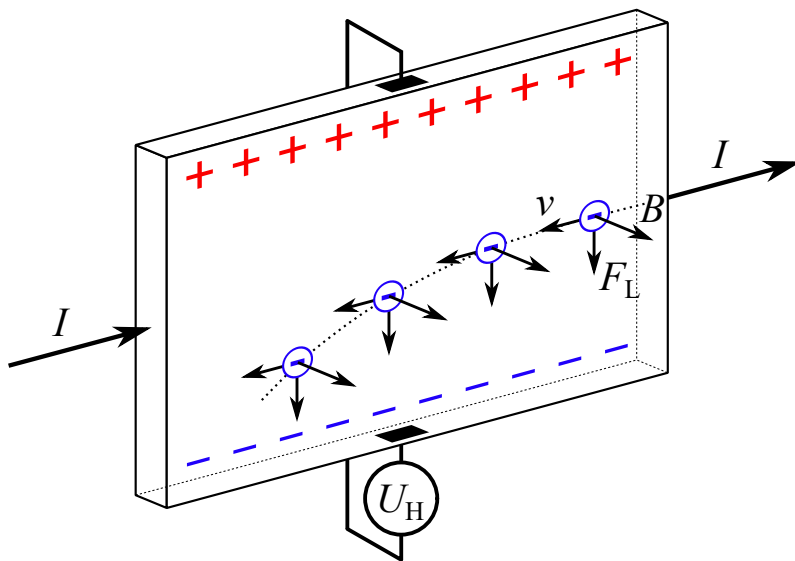


**Figure 2.22** Schematic of a thin film hall sensor with the Lorentz force acting on the drifting electrons

Subsequently, the negatively charged electrons are forced to one side of the conductor leaving positive holes on the other. Due to this charge shift, an electric field  $E$  between the sides is occurring causing a Coulomb force to act on the electron in opposite direction. Eventually, the charge carriers are in a state of equilibrium as the sum of the two forces becomes zero. According to Eq. 2.34, the resulting hall voltage  $U_H$  measurable between the sides of the thin film is proportional to the electric field, which depends on the magnetic field strength and represents the sensor concept [Ripka, 2021, pp. 136-139].

$$\vec{F}_{\text{tot}} = q\vec{E} + q\vec{v} \times \vec{B} = 0 \quad (2.33)$$

$$\vec{E} = \frac{\vec{U}_H}{d} = -\vec{v} \times \vec{B} \quad (2.34)$$

Equation 2.34 also shows that the hall voltage depends on the velocity of the electrons, which increases with the voltage difference in the direction of the current. When the hall effect was initially observed by Edwin Hall in the late 19<sup>th</sup> century, he used a thin rectangle of gold and therefore a good conductor. Hence, already a small voltage applied across the specimen led to a high current. To be able to detect the hall voltage, he had to apply a very strong field. Nowadays, semiconductors are used instead of metallic conductors as there are fewer conducting electrons featuring a much higher drift velocity or mobility. In other words these materials have a higher resistance and the same current is reached by a higher voltage. Subsequently, a notable hall voltage may be measured even if only small field strengths in the millitesla or even microtesla range are acting [Lenz and Edelstein, 2006]. The resulting sensitivity as the hall voltage per field strength can therefore effectively be increased by a higher hall mobility  $\mu_H$ . Also a geometry correction factor  $G$  and the ratio of width to length  $w/l$  have to be taken into account. Eventually, the supply voltage related sensitivity  $S_V$  amounts to

$$S_V = \mu_H \cdot \frac{w}{l} \cdot G. \quad (2.35)$$

The value of the term  $w/l \cdot G$  has its maximum for  $w/l \approx 0.7$  and  $G = 0.667$  and therefore the sensitivity solely depends on the hall mobility [Ripka, 2021, pp. 141–142].

$$S_{V,\text{max}} = 0.471\mu_H \quad (2.36)$$

While the resulting sensitivity in silicon amounts to approximately 0.066 V/VT, it is about a magnitude higher in doped Indium-Antimon (InSb). Therefore, this material was subject to extensive research and soon proved as a well suited material for hall devices. The problem of its large temperature coefficient of 2 %/K due to the narrow bandgap energy of 0.17 eV was effectively overcome by the use of thin film devices. The resulting small height caused a resistance high enough to allow a constant voltage driving instead of constant current driving. Since the temperature dependency of electron mobility and the hall voltage  $U_H$  are the same, this driving techniques reduced the error to  $\pm 0.2$  %/K. Nevertheless, the small temperature range of only  $\pm 40$  degrees around room temperature was still a problem of these devices. The key solution was the molecular beam epitaxy technology allowing the epitaxial growth of single crystal thin films. This way Indium-Arsenic (InAs) and Indium-Gallium

(InGa) structures could be applied as hall elements onto existing silicon layers. Both semiconductors improve the temperature range, the temperature gradient, the linearity of the output signal and offset. The offset describes the output signal of the hall device existing even if no field is present. It is a parasitic component and limits the use of hall sensors in the lower field range. For non-periodic signals, it cannot be distinguished from the real part of the output signal as the offset varies with time and temperature. It is typically caused by small geometric symmetry errors or unequal doping of the semiconductor but also mechanical stress and other effects play a role. Usually, the total error accounts to less than 0.1 % of the applied voltage.

Despite the advantages of InAs, InGa and other semiconductors, most commercially available hall sensors are based on silicon regardless of its poor temperature characteristics, its non-linearity and the modest sensitivity. This is because of its compatibility with CMOS processes allowing for a monolithic integration of a hall element together with additional amplifiers and analog or digital circuitry, which is able to improve and linearize the output signal. Furthermore, it is possible to build two-axis or even three-axis sensors on a single die using silicon. Therefore, the focus for most hall sensors is laid on low-cost production rather than maximum precision. This trend is also supported by the success of magnetoresistive sensors, which are more suitable at lower magnetic fields as they do not have the offset and drift problems of semiconductors [Ripka, 2021, pp. 163–166].

### 2.4.3 Magnetoresistive Sensors (AMR, GMR, MTJ)

Magnetoresistive (MR) sensors are based on the effect that a material changes its resistance when it is exposed to a magnetic field and exists in different forms. The anisotropic magnetoresistance (AMR) effect was the first one to be discovered by William Thomson (Lord Kelvin) in 1857. It was observed in many different metals at rather strong fields and only far below zero degrees Celsius, which made sensors based on this effect unattractive in comparison to hall sensors. It was not until the era of micro technology that the effect was found to be present at rather low fields and at room temperature in ferromagnetic materials making it much more useful as a new kind of measurement technology. Extensive research in the field of thin films led to the finding of the giant magnetoresistance (GMR) effect in 1988, which is based on a more complex physical phenomenon than the AMR effect. Some years later magnetic tunnel junction (MTJ) devices were developed as a new class of GMR sensors. Apart from these three sensor types that all are commercially available today, there are other rather unimportant magnetoresistive sensors, which never found their way into the market and therefore will not be discussed [Tumanski, 2011, pp. 189–191].

The physical cause for the AMR effect lies in quantum mechanics and the interaction of conducting electrons with the electrons in the atomic shell. The shell is clustered into several orbitals with definite electron residence probabilities. All electrons have a spin causing a magnetic moment which can only have two states: spin-up or spin-down. The total spin is given by the sum of all individual electron spins in the atomic shell. In completely filled orbitals this spin is compensated, meaning that the number of spin-up electrons equals the number of spin-down electrons and subsequently there is no magnetic moment. The ferromagnetic materials iron, cobalt and nickel have an uncompensated

(non-zero) spin in their 3d-orbital. Moreover, the energy levels of the spin-up and spin-down electrons in their 3d-orbital are different from another, so that even across multiple atoms the spins do not compensate but the spin-up electrons dominate. As the 3d-orbital is relatively far away from the core, the contained electrons interact with the electrons of neighboring atoms causing the spins to align. The resulting magnetic order is what is called ferromagnetism and the above condition that there are interacting electrons in the atomic shell are the prerequisite for it [Bozorth, 1951, pp. 434-442].

The decisive factor for the AMR effect is that there is also an interaction with conducting electrons. If the magnetization and the direction of the current are in parallel, the electrons are scattered and distracted from their original path. The subsequent increase of the resistance is observed as the magnetoresistive effect. The amount of the MR ratio, however, depends on the orientation of the orbitals and how its three-dimensional shape affects the conducting electrons. As scientist are not yet able to predict it with sufficient accuracy, it has to be determined experimentally and is known for certain elements and alloys only [Ripka, 2021, p. 100].

Generally, all MR sensors are classified by their MR ratio, meaning the amount of resistance change  $\Delta R/R$  at a specific magnetic field. Figure 2.23 shows this correlation not only for AMR, GMR and MTJ sensors presented in this chapter but also for the element bismuth (Bi) and the semiconductor InSb. The historically used bismuth shows an acceptable MR ratio but unfortunately only at high fields. Known from its success in hall elements, InSb replaced it later showing a higher MR ratio and working at lower fields. However, the magnetic field still has to be large in comparison to the other sensors and hall elements have a much better performance in this range.

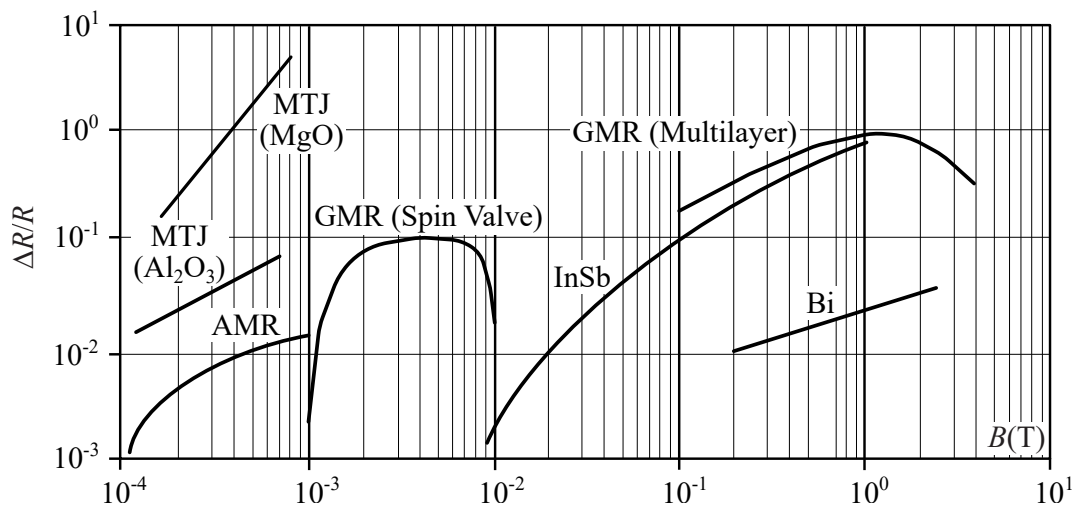


**Figure 2.23** Comparison of the resistance change of different magnetoresistive sensors at room temperature (adapted from [Tumanski, 2011, p. 189])

While the magnetoresistive ratio of AMR sensors is relatively small amounting to  $\Delta R/R_0 \approx 2 - 3 \%$ , it is the magnetic range and the ease of construction what makes this type of sensor attractive. A ferromagnetic thin film (Fe, Co, Ni or an alloy of them) of some 10 to 100 nm height is needed to be able to measure an external field with better sensitivity than hall sensors. Often permalloy is used, an alloy consisting of 81 wt.-% nickel and 19 wt.-% iron. It is known for its very high permeability, near-zero

magnetostriction and significant magnetoresistive effect [Tumanski, 2001; Ripka and Janosek, 2010]. The Voigt-Thomson law in Eq. 2.37 describes the resistivity of such a thin film subject to the AMR effect. Here  $\rho_0$  is the initial resistivity at zero field and  $\vartheta$  is the angle between the current direction and the direction of the magnetization  $M$  within the layer of the thin film [Tumanski, 2011, p. 191].

$$\rho(\vartheta) = \rho_0 + \Delta\rho \cos^2\vartheta \quad (2.37)$$

The direction of the magnetization and subsequently the angle  $\vartheta$  depend on the three fields acting in the thin film as shown in Fig. 2.24a. Apart from the external magnetic field, there is a demagnetization field  $H_d$  in opposite direction of  $M$  (subsection 2.1.5) and an anisotropy field  $H_k$ , which is given by the form. Accordingly, the easy magnetic axis lies in the direction of the current path and it is harder to magnetize it perpendicular to that direction. Subsequently, the initial angle  $\varphi$  will be close to zero and the sensitive axis of the thin film is perpendicular to it in order to change it from its original state. The current passing through the strip will most likely point in the direction of  $H_k$  and it follows that  $\vartheta = \varphi$ . When applying an external field  $H$ , the angle  $\varphi$  changes. The resulting direction of  $M$  can be retrieved by finding the minimum of the stored energy in the thin film. Assuming that there is only a single domain and that  $H_y$  is small in comparison to  $H_k$ , it follows [Tumanski, 2001, pp. 18-21]

$$\sin \varphi = \frac{H_y}{H_x + H_k}. \quad (2.38)$$

It is possible to rewrite Eq. 2.37 with  $\vartheta = \varphi$  and insert Eq. 2.38, which leads to

$$R = R_0 + \Delta R \cos^2\varphi \quad (2.39)$$

$$= R_0 + \Delta R (1 - \sin^2\varphi) \quad (2.40)$$

$$= R_0 + \Delta R \left( 1 - \frac{H_y^2}{(H_x + H_k)^2} \right). \quad (2.41)$$

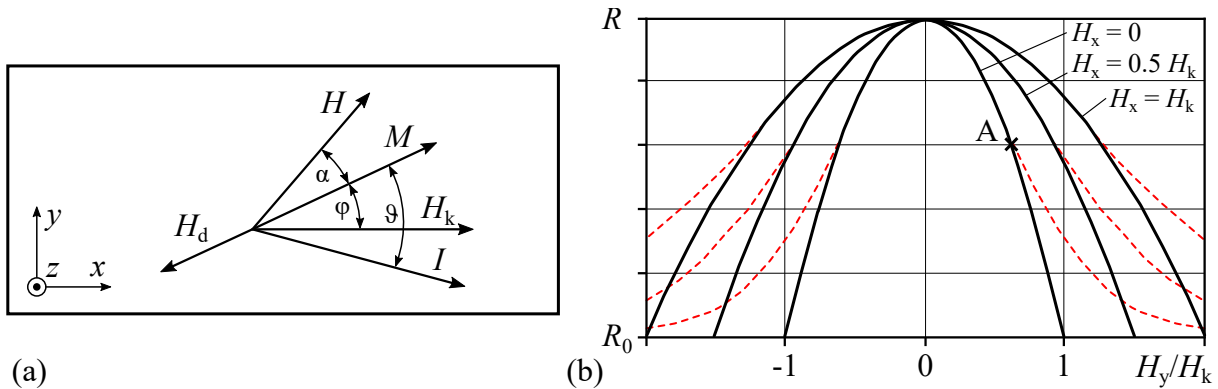


**Figure 2.24** Vectors of the acting fields, the magnetization and the current in a thin film strip subject to the AMR effect (a) and the resulting resistance of the strip in dependence of the field strength in  $y$ -direction adapted from Tumanski [2011, p. 191] (b)

Equation 2.41 defines the resistance for  $|H_y| < |H_x + H_k|$ , while  $R = R_0$  for  $|H_y| > |H_x + H_k|$ . Resulting graphs of  $R(H)$  for different values of  $H_x$  are depicted in Fig. 2.24b (solid black line). However, Tumanski did not consider the demagnetization effect reducing the acting field strength, which is why the measured  $R(H)$  plot (dashed red line) differs from the analytical solution when  $H_y$  approaches the value  $H_k$ . Ripka replaced  $H_k$  with  $H_0 = H_k + H_d$  in his work, which is certainly true for  $H \ll H_0$  and gives better results as  $H_d$  is usually larger than  $H_k$  [Ripka, 2021, pp. 100-103]. While the real AMR response therefore should be found in experiments, the analytical solution shows good correlation for small values of  $H_y$ , which is the desired range of the sensor.

Unfortunately, the parabolic response curve has the least sensitivity and highest non-linearity at the point of low external fields. As high values of  $H_x$  further decrease the sensitivity, the sensor should be operated at  $H_x = 0$  and close to a point A marked in the graph in Fig. 2.24b where it shows a high linearity and a high gradient. This is achieved by the so called ‘barber pole’ structure, which is commonly used in commercially available AMR sensors today. By depositing strips of a highly conducting material like aluminum or gold across the ferromagnetic layer at an angle of about  $45^\circ$  the angle of the current  $\vartheta$  is inclined as shown in Fig. 2.25a. Subsequently, the point of operation is shifted and the sensor output looks as depicted in the plot in Fig. 2.25b [Ripka and Janosek, 2010].

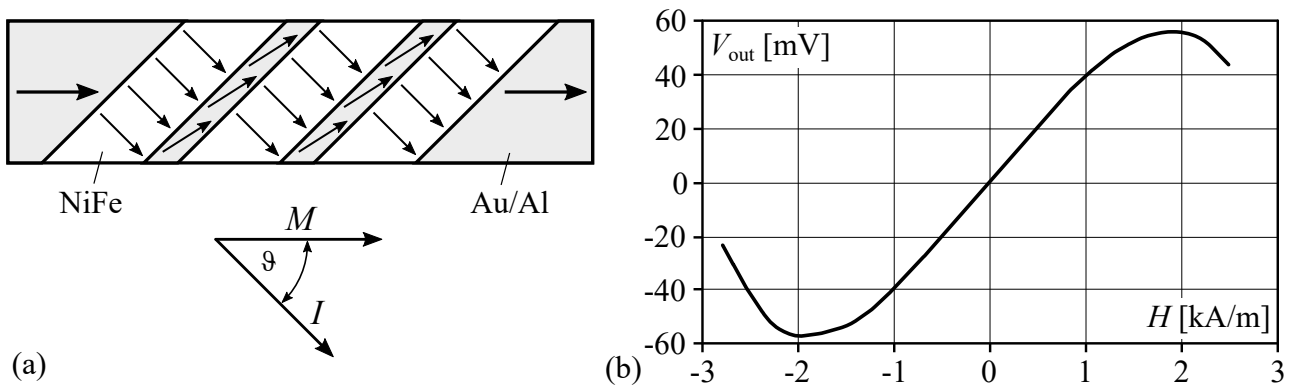


**Figure 2.25** Schematic of the barber pole structure (a) and an exemplary  $R(H)$  plot of a barber pole based sensor from Philips [Tumanski, 2013] (b)

In earlier versions, Au/Al strips were deposited in etched cavities within the ferromagnetic layer causing the magnetization vector to be changed. Therefore, this principle works as desired only if the strips are placed on top of it [Tumanski, 2011, pp. 193–194]. As shown in Fig. 2.24b, AMR sensors are subject to a cross field error, that arises due to the change of the output function by a field in x-direction. Also, temperature drift and offset are sources of error. However, most of these effects can be compensated by applying a current pulse to a flipping coil integrated within the sensor chip, inverting the output slope. While standard AMR sensor bridges can be operated at frequencies up to 1 MHz, the technology of periodically flipping the domain in the sensor limits the bandwidth according to the flipping frequency. Sometimes, also a compensation coil is integrated to enable offset trimming. The popular industrial AMR sensor from Honeywell ‘HMC1001’ for example features both a compensation and a flipping coil and achieves a resolution of 1 nT. The upper limit of the magnetic range of AMR sensors is given by  $H_0$ , typically in the range of a few millitesla [Ripka, 2021, p. 110].

In the late 1980s, another magnetoresistive effect was almost simultaneously found and reported by the research groups of Albert Fert in France [Baibich et al., 1988] and the group surrounding Peter Grünberg in Germany [Binasch et al., 1989]. They observed a much bigger change in resistance when they analyzed a thin film stack consisting of two iron layers with a chromium layer of approximately one nanometer in between them. In the unmagnetized state, the resistance was high and decreased when the stack was exposed to a strong magnetic field of some hundred millitesla. In Fig. 2.26 the resulting MR ratio is depicted for a multilayer of several Fe/Cr layers. While the graph shows the results at 4.2 K, the authors point out that the effect is observed at room temperature as well but with a lower resistance change and a lower transition field strength. The field strength, at which the low resistant state is reached, depends primarily on the thickness of the chromium layer. Its height also affects the MR ratio, which may also be increased by an increased number of stacks. As this new kind of magnetoresistive effect was shown to be much stronger than the AMR effect even at room temperature, it was called *giant* magnetoresistive (GMR) effect.

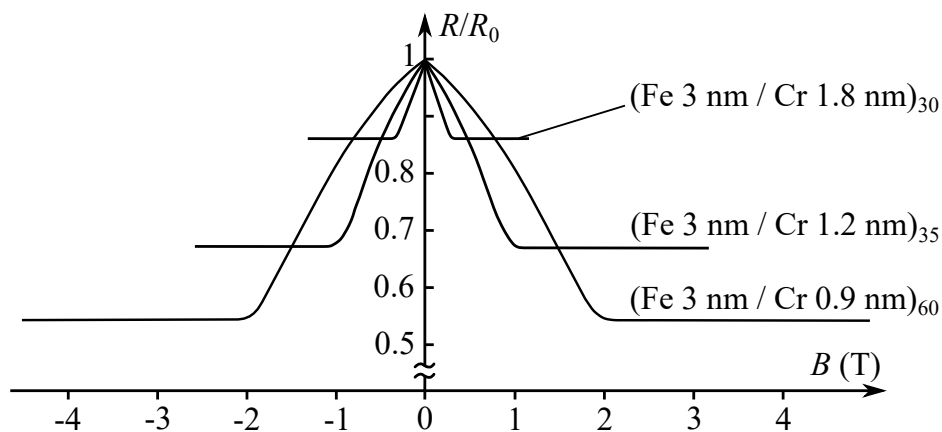


**Figure 2.26** MR ratio of  $(\text{Fe/Cr})_n$  multilayer at a temperature of 4.2 K adapted from Baibich et al. [1988]

Both research groups explain the high resistance state with an antiferromagnetic coupling of the iron layers, which becomes stronger if the chromium layer is decreased in height. The conduction electrons traveling through the multilayer stack are scattered when they pass the Fe/Cr interface and their spin does not match the spin (the magnetization) of the involved ferromagnetic layer. Subsequently, all conduction electrons that cross the layers are scattered at either of the interfaces as always one of the Fe films does not match the electron's spin. In a strong magnetic field however, the antiferromagnetic coupling is overcome and all layers align in one direction. Consequently, half of the crossing electrons (those with the 'right' spin) travel easily across the layers, while the others are scattered at every interface, in sum resulting in a decreased resistance. Both cases are shown in Fig. 2.27. With this discovery, Fert and Grünberg provided the so far greatest evidence that current transport is spin dependent for which they were awarded with the Nobel Prize in 2007 [Reig et al., 2013, pp. 1–3].

It is important to note that in the shown configuration, when the current is run in the plane (CIP), the electrons must be able to cross from one ferromagnetic layer to the other. This is only the case if the thickness of the non-magnetic layer is in the range of the mean free path length of the electrons. On



the other hand, it must not be too small as then the antiferromagnetic coupling becomes too strong. Usually a thickness of 1.8–2.2 nm is used today. In CIP configuration, only a part of the electrons is scattered due to spin effects. There are also other effects in thin films causing electron scattering at layer interfaces regardless of their spin. According to the Fuchs-Sondheimer theory, also specular reflection may appear causing the electrons to stay in the individual layers. Taking into account all these effects, the resistance of the layers is higher in comparison to bulk materials. Subsequently, the relation of the resistance change due to the GMR effect to the base resistance is decreased, being a second order effect only [Reig et al., 2013, pp. 6–8].

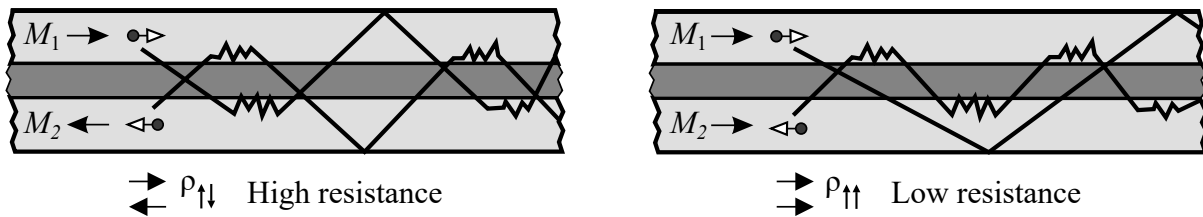


**Figure 2.27** Spin depending scattering of electrons passing a pair of ferromagnetic layers separated by a non-magnetic spacer layer (adapted from Ripka [2021, p. 119])

While multilayer structures feature a linear output signal, a disadvantage is their low sensitivity resulting from the rather strong field that is necessary to overcome the antiferromagnetic coupling (see Fig. 2.26). The GMR effect was also observed in sandwich structures of two different ferromagnetic materials separated by a thin copper layer. Though they exhibit no antiferromagnetic coupling, their individual coercivities cause the layers to align with the external field at different strengths. A similar MR ratio can be achieved but the output signal is error-prone due to the hysteresis loops of both magnetic layers. It is the ‘spin valve’ GMR configuration that finally prevailed exploiting the effect of a ferromagnetic-antiferromagnetic coupling. Accordingly, one of the ferromagnetic layers is fixed in its magnetic direction by applying an antiferromagnetic layer (usually a Mn based alloy) adjacent to it. This ‘pinning’ layer’s magnetization is imposed during sputter deposition and hard to overcome. The other ferromagnetic layer is free to rotate and as there is no coupling with the ‘pinned’ layer it is sensitive at much lower field strengths compared to the classical multilayer. The pinning effect of the antiferromagnetic alloy is often enhanced by a so called synthetic antiferromagnet, a sandwich of two ferromagnetic thin films separated by a 0.5 – 1 nm ruthenium layer as depicted in Fig. 2.28a. This additional structure reduces the net magnetic moment and therefore withstands higher external fields. It also reduces the stray field of the pinning layer affecting the sensory free layer. The subsequent relationship of the magnetoresistive rate versus field strength therefore is slightly more complex as shown in Fig. 2.28b. At low field strengths the free layer switches its direction according to the external field with the high resistance reached for the antiferromagnetic configuration of the ferromagnetic layers. At a much larger field of about 50 mT the direction of the antiferromagnetic coupling of the pinned layer is overcome and the resistance of the structure decreases again. The MR ratio of spin valve sensors can be enhanced up to 20 % by different methods, for example by inserting an additional CoFe layer between the NiFe and the Cu layer [Reig et al., 2013, pp. 4–5].

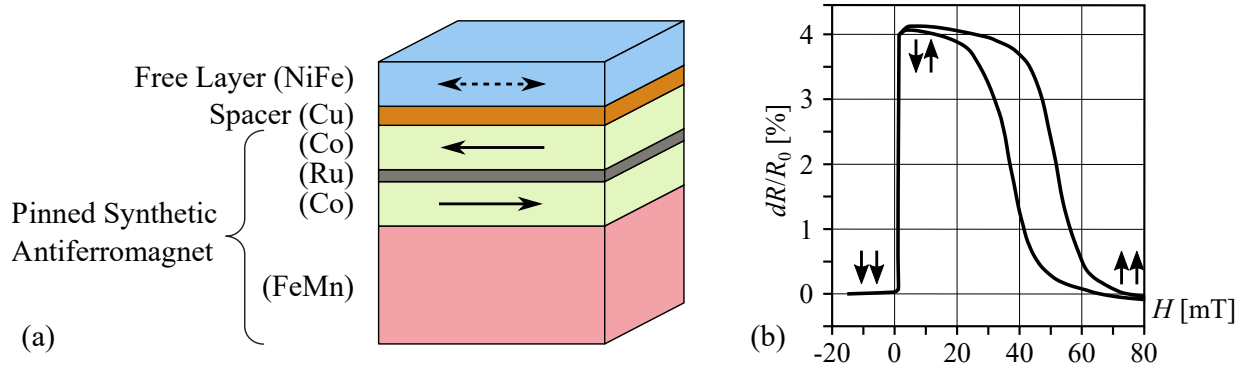


**Figure 2.28** GMR spin valve layer configuration with synthetic magnetic antiferromagnet and resulting MR ratio (adapted from Reig et al. [2013, p. 4])

The utilization of magnetoresistive reading heads in hard disk drives starting in 1991 led to a boost of the annual growth rate (CGR) of the areal density of the saved data. By replacing the primarily used AMR sensors with GMR sensors starting in 1997, the CGR increased further to a 100 % [Munce and Thiele, 2006]. Despite this success of GMR sensors, it was evident that an even higher magnetoresistive rate could be reached by making the current flowing perpendicular to the plane (CPP) rather than alongside of it. Subsequently, all electrons would experience the spintronic effects of the ferromagnetic layers, rather than only a part of them. However, due to the very thin layers of GMR sensors accounting to a total height of approximately 20 nm, the resulting areal resistance is in the range of  $10^{-2}$ – $10^{-3} \Omega\mu\text{m}^2$ . This low resistance makes it difficult to detect the resistance change even if the MR ratio is increased in comparison to the current-in-plane structure [Kubota et al., 2018].

At this point, the pioneering experiments of Tedrow and Meservey [1971] on spin dependent tunneling of electrons through isolators caught the interest of researchers decades after their observation. The first sensor-like structure featuring a magnetic tunnel junction (MTJ) between two ferromagnetic layers was proved working at a temperature of below 4.2 K by Julliere [1975] showing an MR ratio of 14 %. However, it was not until the success of MR sensors in magnetic recording that magnetic tunnel junctions were developed further. Miyazaki and Tezuka [1995] were the first ones to show a significant MR ratio of 18 % at room temperature using an  $\text{Al}_2\text{O}_3$  barrier between two Fe layers. The advantage of MTJs is the much higher areal resistance and the possible perpendicular current transport causing the higher magnetoresistive rate. With these sensors applied in reading heads of hard disk drives, the data density was increased up to 1 Tb/inch<sup>2</sup> today [Yang and Zhang, 2021].

The construction of a MTJ is very similar to the spin valve shown in Fig. 2.28 with the main difference that the spacer layer is replaced by a thin insulator. As for the GMR, different quantum effects play a role and the simple model from Julliere considering only the properties of the ferromagnetic layers was soon found to not be sufficient. Indeed, the properties of the insulator have to be taken into account also [Reig et al., 2013, pp. 14-16]. Subsequently, a significant breakthrough was the replacement of the previously used  $\text{Al}_2\text{O}_3$  barrier with MgO, which increased the MR ratio by a factor of ten, reaching up to 500 % [Ikeda et al., 2007].

The interest in magnetoresistive sensors today continues unabated, as the publications in this field reach a higher number than ever before. Apart from read heads, the focus is laid on magnetic random-access memory, graphene based materials, current sensing and biomedical applications [Yang and Zhang, 2021]. Among the latter application, requiring a linear output rather than the mere distinction between two states, the magnetic vortex state is of special interest, providing a hysteresis-free and very linear output signal [Wurft, 2018; Wurz and Prediger, 2021].

In their comparison of magnetoresistive sensors, Stutzke et al. [2005] reach the conclusion that AMR sensors achieve the lowest noise among them. They assume that the higher noise of GMR and MTJ sensors is caused by the multiple layers used in these types. Depending on the individual sensor, AMR sensors reach about 1 nT resolution, while it is about 10 nT for GMR devices. Though, MTJs have about the same noise as GMR sensors, they achieve about the same resolution as AMR sensors due to their high sensitivity. Deak et al. [2017] carried out a similar comparison, pointing out that there is a linear behaviour of sensor noise to die size. Their comparison of predicted and achieved noise showed a good correlation supporting this assumption. They also conclude that MTJ achieve lower noise levels today and allow the detection of fields in the upper picotesla range outperforming AMR sensors. Technically, magnetoresistive mechanisms have no intrinsic frequency limitations and work up to the gigahertz range. In real systems however, parasitic effects like the skin effect and the integrated electronics limit the bandwidth to the megahertz regime [Reig et al., 2013, pp. 114–115].

### 2.4.4 Conclusion

Regarding the targeted application of measuring the field strength created by a yoke placed on a wafer to allow for localized hysteresis measurements, all three reviewed sensing technologies come into question. The induction coil provides the greatest flexibility and a linear output signal, which, however, depends on the frequency. Especially in the lower frequency range, the hall probe is advantageous, while its limited speed prevents the usage above approximately 20 kHz. Among the magnetoresistive sensors, the technologies of the AMR and MTJ are suitable as – in contrast to the spin valve – they achieve an almost linear output signal. Both types work in the range from quasi-static fields up to the megahertz regime. However, the measurable field of the AMR sensor is limited to about 2 kA/m due to the anisotropy field strength (Fig. 2.25).

Eventually, the sensor will be selected from the commercially available ones or custom-made in case of the induction coil. Therefore, the availability of sensors has to be taken into account and also the limitation of the measurement system are important. Before the final size of the components, the achievable excitation frequency range, and the necessary field strength are not yet known, it is not wise to commit to a distinct technology. Therefore, the next step is to discuss the general concept of the measurement device and decide on a sensor afterwards.



### 3 Concept of the Measurement Device

The four sections covered by the state of the art outline the framework conditions for the task of measuring localized magnetic properties of a ferromagnetic layer on a whole silicon wafer. As reviewed in section 2.2, the trend in soft magnetic thin films is towards novel materials that allow for increased frequencies up to the gigahertz range. Unfortunately, the evaluation of magnetic properties in this frequency range is elaborate and small specimens are mandatory. However, the measurement of the anisotropy field regarding its strength and direction and also the maximum magnetization are crucial to decrease the losses in this regime. Here, a novel measurement system can support in improving the fabricated thin films: The abilities to apply a wide range of excitation field strengths and frequencies and to vary the magnetization angle are considered as necessary features.

According to section 2.3, the single sheet tester used in the field of transformer sheet characterization serves as a suitable model for the design of a corresponding measurement system for wafers capable of these features. By placing a magnetizing yoke on a variable spot on the wafer, the local magnetic properties between its two poles can be detected. Small dimension will most certainly be advantageous allowing for higher frequencies and higher field strengths to be applied. However, a small core also limits the size of the sensor, which has to fit between the poles to measure the field. From section 2.4, it becomes evident that there are different useful principles available and especially the recent progress of MR sensors is noteworthy. As Brix et al. and Tumanski have shown, the field strength between the poles of the yoke changes linearly in relation to the distance from the sheet. Therefore, either one single sensor as close to the magnetic layer as possible may be used with little error or two sensors are employed and the field strength in the layer is extrapolated. Simulations will have to be carried out to prove the suitability of this method for the desired application.

While the measurement of the field strength seems straight-forward, it is the measurement of the flux density that will be challenging. The winding of a coil around the whole wafer is not practical as it would result in a very large coil with large air flux to be considered. The use of the needle-probe method in combination with electrodes is interesting but the reported results show quite large inaccuracies. Therefore, the method pursued in this thesis is the measurement of the flux density in the yoke and calculating the flux in the layer on the basis of this value. It requires that the open circuit has been previously characterized by simulations and measurements in order to correct the measured flux density by the influence of the core. Its permeability should be as linear as possible and it should exhibit low hysteresis. The fact that usual coatings in microtechnology are so thin that even the smallest yokes have a much larger cross section than the layers is beneficial in this case. Consequently, it will be operated far away from the saturation region and hysteresis and non-linearity errors will most probably be negligible. To allow for measurements in a wide frequency range, a largely frequency independent ferrite material will be chosen for the core.

Eventually, the measurement head representing the key element of the whole system will look similar to the schematic draft in Fig. 3.1: The ferrite U-core used as the yoke will be placed on top of the silicon wafer with the ferromagnetic coating under evaluation. The magnetizing primary coil is wound around the top of the core and another pickup coil for measuring the flux is wound at one side of it. The two sensors (induction coil in this case) are located at different distances from the sheet to allow for the extrapolation of the field strength in the thin film. The blue arrows show the magnetic field vectors radiating out and into the poles of the yoke passing the air and the wafer on the way.

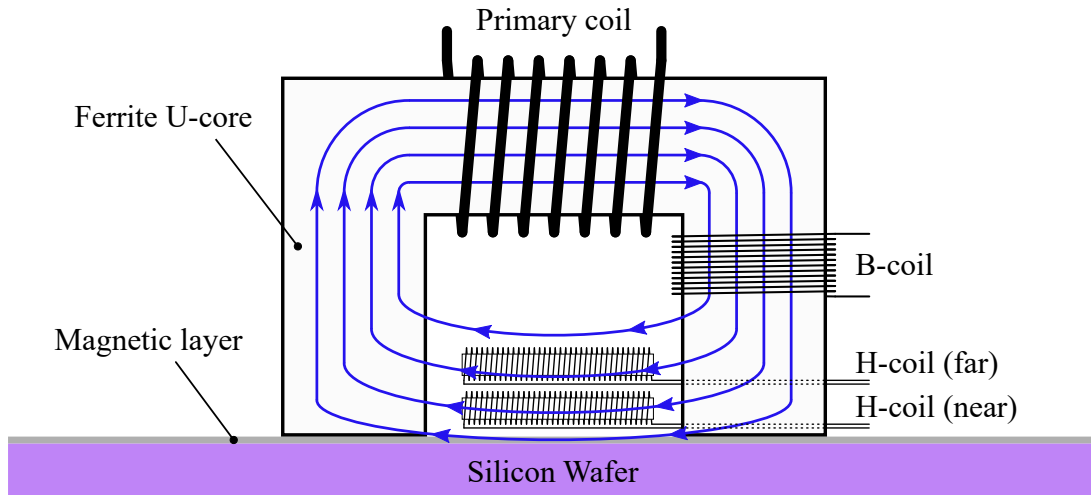


**Figure 3.1** Schematic draft of the measurement head

Due to the almost linear magnetization behavior of the core in this setup, the device is expected to provide quite accurate hysteresis measurement results as long as the field strength applied to the layer is largely uniform and the cross section of the specimen is known. However, both is not given if the core is smaller than the specimen width, which is the case for a two-dimensional extended wafer. This inevitably causes a non-uniform magnetization at the sides of the core and an unknown cross section, which is regarded as a major challenge of this thesis. (Therefore, in classic SSTs the analyzed sheets usually have the same width as the yoke.) The propagation of the magnetic field is shown in an exemplary simulation in Fig. 3.2 in a top view of a small U-core placed on an iron thin film with a radius of 30 mm. While the field strength right between the poles of the core is rather uniform, it decreases exponentially outside of it as indicated in the graph in the lower part of the figure. The calculation of the flux density in the layer based on the measurement of the flux in the core is therefore difficult, simply because there is no clear value for the flux density but rather a gradient. Therefore, a head with a large area of uniform field and a fast decaying field to its outside will be advantageous.

In addition to the design and construction of the measurement head, certain electronic devices have to be developed to allow for the control of the device and the data acquisition. Alternating fields with frequencies ranging from quasi-static 50 Hz up to several or even a hundred kilohertz are targeted, which put high demands on the circuits and electronic devices used (subsection 2.3.3). Limiting factors hereby are the speed and output power of the amplifier driving the current of the primary winding and the inductance of the core, which forms a low pass filter in combination with the resistance of

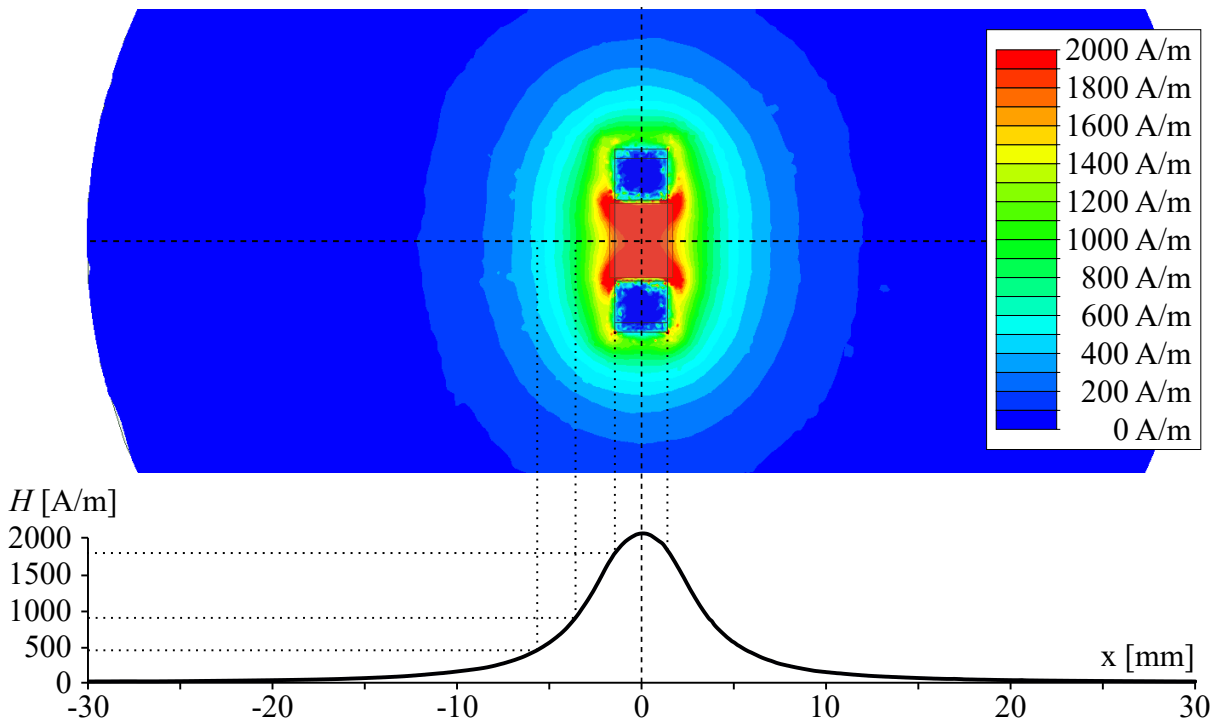


**Figure 3.2** Simulated field propagation in an iron thin film magnetized by a central U-core (top view)

the winding. Also, suitable sensors or sensor arrays capable of determining the field strength with the same speed are necessary. According to Fig. 2.19, summarizing the important properties of magnetic field sensors based on the conducted literature research, only magnetoresistive sensors and induction coils achieve the desired speed. Hall probes are maybe another possibility if the final measurement speed will not exceed 20 kHz, which seems to be the limit of state-of-the-art sensors. Their low resolution, however, is a further downside that has to be kept in mind. Thin film sensors, whether hall probe or magnetoresistive, have the advantage of small size and simple evaluation. Induction coils on the other hand have no hysteresis and are perfectly linear but require signal integration, which is a possible source of error as described in subsection 2.4.1. They can be made in virtually any size, though a smaller cross section reduces their sensitivity. To achieve a sufficient output amplitude, they have to feature a high winding count and should be made to order by a specialized company. On the other hand, the pickup coil for detecting the flux density can be wound manually, probably requiring only some ten turns. Similar to potential H-coils, the signal has to be integrated over time by an analog circuit or in the digital domain by software.

A software is generally needed to handle the control of the measurement head and to record, process and visualize the incoming data. LabVIEW was chosen as it provides handy features like a customizable graphical user interface (GUI) and contains several interface drivers as well as sophisticated algorithms for functional analysis. A so called virtual instrument (VI) was developed, which is composed of a vast variety functions selected to one's needs. Furthermore, there are multiple data acquisition (DAQ) devices from the developer *National Instruments* available that can be integrated in LabVIEW, fully handling analog-to-digital data conversion, buffering and transmission to the com-

puter. This provides a reliable and comfortable way to acquire the measurement data and a suitable device was chosen according to the required resolution and frequency bandwidth. However, these two parameters are in conflict with each other and a compromise had to be made between resolution and speed. Still, even when using ready-made ADCs, another PCB had to be developed and fabricated for analog signal conditioning. As shown in Fig. 3.3, it has to comprise analog amplification circuits not only for the measurement data but also for the driving of the primary coil.

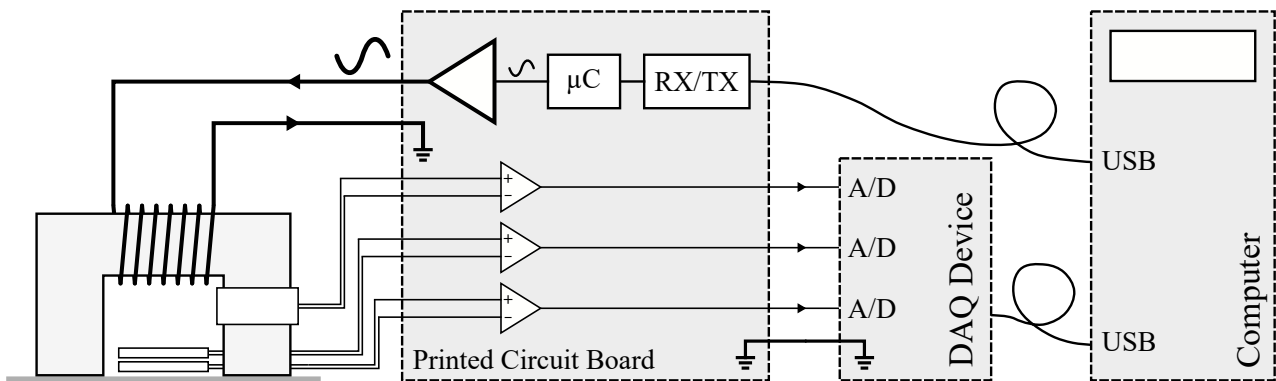


**Figure 3.3** Concept of the measurement electronics

To drive the primary coil, a crucial device is a fast and resilient power amplifier. Its output current should be as high as possible to be able to reduce the number of turns, thus reducing the inductance of the winding. The amplifier has to be provided with a waveform of the desired frequency. To avoid the occurrence of non-linearities due to discontinuous waveforms such as triangle or sawtooth, it is preferable to use a sine wave, which must be generated by a microcontroller ( $\mu\text{C}$ ) or a specific integrated circuit (IC). Another circuit is required to amplify and, if necessary, integrate the signals of the magnetic field sensors and the induction coil. Especially in the case of the B-coil, high voltage gradients are to be expected in case of materials with a steep hysteresis loop. Therefore, amplifiers with a high gain bandwidth product (GBP) and a high slew rate have to be used, which are capable of accurately following the input signal even at high frequencies. The output signals of the signal amplification circuit has to match the input range of the ADCs, which often accounts to  $\pm 10\text{ V}$  for the DAQ devices from *National Instruments*.

All the described necessary components of the measurement system are summarized in Table 3.1 assigned to the three categories measurement head, electronics and software. As outlined in this chapter, the components require a certain matching to each other, though it is useful to proceed in the order of the table. Hence, the first item to be chosen is the ferrite core and afterwards, the primary and the B-coils can be designed and fabricated. The final sensors for the magnetic field have to be selecting according to the size of the core as they have to fit between its poles. Simulations will help to calculate the resulting magnetic properties of the circuit regarding its inductance and the final field propagation. Eventually all these components have to be assembled in a robust measurement head that can be moved on a specimen to determine local properties. The design and analyzation of the measurement head is subject of chapter 4.



Once this step is complete, the development of the PCBs follows, serving as the link between the measurement head and the data acquisition. The electronics have to be designed in order to support a frequency range starting at 50 Hz and reaching as high as possible. As outlined in this chapter, the maximum frequency is highly depending on the inductance of the core used and is estimated to be in the upper two-digit kilohertz range. Depending on the possible output current, the amount of turns on the primary coil have to be adapted in order to minimize the inductance while making sure to reach the maximum desired field strength. Since it is the aim to capture the hysteresis loop of the analyzed material, the magnetic field strength has to rise high enough to completely saturate it. Usual weak magnetic materials saturate well below 100 A/m. However, to have some headroom and to be able to also saturate the hard axis, a value of 2000 A/m achieved at maximum current seemed as a useful range and therefore was targeted. The consideration of the electronic components follows in chapter 5, providing a detailed solution for the PCB shown as a sketch in Fig. 3.3.

Afterwards, the source code of the microcontroller employed in the electronics has to be written and adapted according to the selected amplifiers and the other integrated circuits necessary for the operation of the measurement head. Therefore, the microcontroller enables the communication between the hardware and the developed virtual instrument running on the attached computer. The VI contains different algorithms to calculate the hysteresis loop from the measurement data acquired by the chosen DAQ device. All these software elements are subject of chapter 6.

**Table 3.1** Realization of the necessary components of the measurement device

Category	Component	Realization
Measurement head (Chapter 4)	Yoke	Ferrite U-core of appropriate size
	Magnetic field sensor	Commercial thin film sensor or induction coil
	Flux sensor (B-coil)	Manual winding
	Primary coil	Manual winding
Electronic circuit (Chapter 5)	Amplification circuits	Developed according to the chosen sensors
	Analog-digital converter	Commercial DAQ device from <i>National Instruments</i>
Software (Chapter 6)	Microcontroller source code	Written in C/C++
	Virtual instrument	Developed using LabVIEW

All realized components were then assembled in a motorized stand, which allows for reproducible measurements to be obtained. The design of the stand and its characterization in terms of noise is covered in chapter 7, allowing the classification of the device regarding the achievable resolution. Eventually, the carried out hysteresis loop measurements of different thin film samples and magnetic foils made with the developed device are reported in chapter 8 and compared with reference measurements. The conclusion in chapter 9 summarizes what has been achieved and the gained knowledge during the work on the thesis. Furthermore, the newfound possibilities in the fabrication of magnetic thin films resulting from the integration of the measurement device will be discussed.

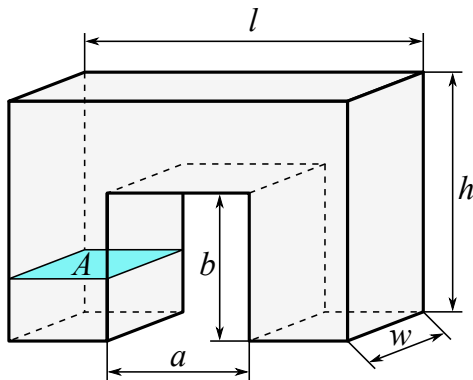


## 4 Layout of the Measurement Head

According to presented concept in the previous chapter, the design of the measurement head is the first element that has to be developed and is a prerequisite for the subsequent design of the electronics. As a first step, the ferrite yoke that will be used to create a local magnetization in the thin film layer has to be chosen. Unfortunately, the manufacturing of a customized shape or the adaption of an existing U-core by milling or grinding is a difficult task, since ferrite is brittle and fragile. The requesting of an individual mold from a manufacturer on the other hand is usually possible for very large quantities only. Hence, commercially available cores will be considered to evaluate the necessity for a customized one (section 4.1). Afterwards, suitable sensors for the detection of the field strength will be assessed. As the sensor has to fit between the poles of the core, its size is a crucial property (section 4.2). Eventually, the final components and the designed measurement head is presented in section 4.3.

### 4.1 Review of Commercially Available Ferrite Cores

A market analysis revealed that useful ferrite U-cores are available from *DMEGC*, *Epcos* and *Ferroxcube*. The dimensions of the four smallest available types from these companies are given in the table in Fig. 4.1, sorted by their size.



		<i>Epcos</i> B67350	<i>DMEGC</i> UF10B	<i>Ferroxcube</i> U10/8/3	<i>DMEGC</i> UF6.9
$l$	mm	15.2	10.5	9.9	6.9
$h$	mm	11.2	7.9	8.2	3.1
$w$	mm	6.7	5.0	2.9	2.0
$a$	mm	5.2	5.2	4.4	3.8
$b$	mm	5.9	5.6	5.0	1.8
$A^*$	mm <sup>2</sup>	32.0	12.4	8.1	2.8

\* $A$  includes deduction due to chamfers at the edges

**Figure 4.1** Dimensions of analyzed potential cores from *DMEGC*, *Epcos* and *Ferroxcube*

All these cores were analyzed in three-dimensional Maxwell simulations to estimate the most important properties: the achieved field strength between the poles, the maximum flux density in the core's cross section  $A$  and the inductance. Since ferrite features isotropic magnetic behavior that does not differ much from producer to producer, this first comparison considered only the shape of the cores. In

each simulation, a current of 1 A was applied to the primary winding with 10 turns placed around the core as shown in the schematic in Fig. 3.1. The results for the core in air and attached to a cylindrical permalloy layer with a diameter of 60 mm and a thickness of 2  $\mu\text{m}$  and 20  $\mu\text{m}$ , respectively, are given in Table 4.1. Regarding the field strength, higher values are better, indicating that less turns are necessary to achieve the targeted value of 2000 A/m. The magnetic field linearly increases with the number of turns but at the same time, the inductance grows quadratically. It limits the maximum frequency that can be applied to the core and therefore lower values are better. Also, for the maximum flux density in the core, lower values are preferable. The more the core approaches the saturation region at around 300 to 500 mT, the more its coercivity alters the measurement of the analyzed material.

**Table 4.1** Simulation results for different U-cores excited by a primary winding with  $n = 10$  turns and a current of  $I = 1$  A

		<i>Epcos</i> B67350	<i>DMEGC</i> UF10B	<i>Ferroxcube</i> U10/8/3	<i>DMEGC</i> UF6.9
Max. field strength in wafer plane [A/m]	Air	1566	1368	1687	1860
	Permalloy 2 $\mu\text{m}$	1835	1341	1633	1700
	Permalloy 20 $\mu\text{m}$	1998	256	363	125
Max. flux density in area $A$ [mT]	Air	8.1	12.5	20.7	28.3
	Permalloy 2 $\mu\text{m}$	10.1	16.7	25.3	35.6
	Permalloy 20 $\mu\text{m}$	23.2	38.5	53.6	86.2
Inductance [ $\mu\text{H}$ ]	Air	6.52	3.68	3.37	1.49
	Permalloy 2 $\mu\text{m}$	7.30	4.15	3.81	1.74
	Permalloy 20 $\mu\text{m}$	12.36	7.01	6.23	3.25
Coercivity (from datasheet) [A/m]		23	15	16	15

Regarding the maximum field strength, there are two peculiarities. On the one hand, there is a tendency of increasing values towards the smaller cores. On the other hand, the field strength usually decreases when the core is attached to the thin film layer and the layer height increases. However, this is not the case for the first core ‘B67350’.

The first of these observations primarily is due to the varying air gap length (dimension  $a$ ), which ranges from 5.2 mm in case of the ‘B67350’ to 3.8 mm for the ‘UF6.9’. This can be explained with Ampère’s law, stating that the magnetomotive force  $\Theta = nI$  equals the product of the field strength along a closed flux line and its length (subsection 2.1.1). In the case of the given U-core, however, the magnetic circuit is open and the field strength is not constant over its length. As a strong simplification, it can be assumed that there are two different field strengths: the one in the ferrite U-core  $H_{\text{FeO}}$  and the one in the air gap  $H_a$ , which leads to Eq. 4.1. In reality though, there is a non-linear progression in the transition from one material to the other [Albach, 2017, pp. 167-172].

$$\Theta = nI = \oint \vec{H} d\vec{s} = H_{\text{FeO}} l_{\text{FeO}} + H_a l_a \quad (4.1)$$

Assuming that the flux density is more or less equal within the circuit, the field strength in air will be much higher than inside the core  $H_a \gg H_{\text{FeO}}$  due to air's low permeability. And since both lengths  $l_a$  and  $l_{\text{FeO}}$  are of similar magnitude, the term  $H_{\text{FeO}}l_{\text{FeO}}$  is negligible and Eq. 4.1 may be rewritten as

$$H_a \approx \frac{nI}{l_a} = \frac{nI}{a} \quad (4.2)$$

The antiproportionality  $H_a \sim \frac{1}{a}$  explains why the smaller cores with a shorter air gap length  $a$  achieve a higher field strength between the core's poles. The largest one 'B67350', however is an exception due to its greater width and larger cross section revealing the errors introduced by the simplifications. Its cross section, which is almost three times the size of the next smaller one 'UF10B' is also the reason why it is the only core, for which the field strength raises when it is attached to the permalloy layer. For the other ones, the field strength decreases in this case, especially when the thickness of the permalloy layer is increased. The high permeability of the permalloy layer acts as a magnetic short circuit causing the magnetic resistance  $R_m$  between the two poles to decrease.  $R_m$  is defined as the length of a volume segment divided by its cross section and its permeability.

$$R_m = \frac{l}{\mu_0 \mu_r A} \quad (4.3)$$

Therefore, the magnetic resistance resembles the electric resistance, which also depends on the length of a conductor and its cross section. The conductivity, however, is replaced by the permeability of the material, which is not constant for ferromagnetic materials. It is large at low magnetic fields, which results in a low magnetic resistance according to Eq. 4.3. The more the material is saturated, the more the permeability drops and  $R_m$  increases. The corresponding magnetic circuit of a U-core is visualized in Fig. 4.2, showing the individual segments of the magnetic circuit that results for the core placed in free air (a) and on top of a softmagnetic layer (b).

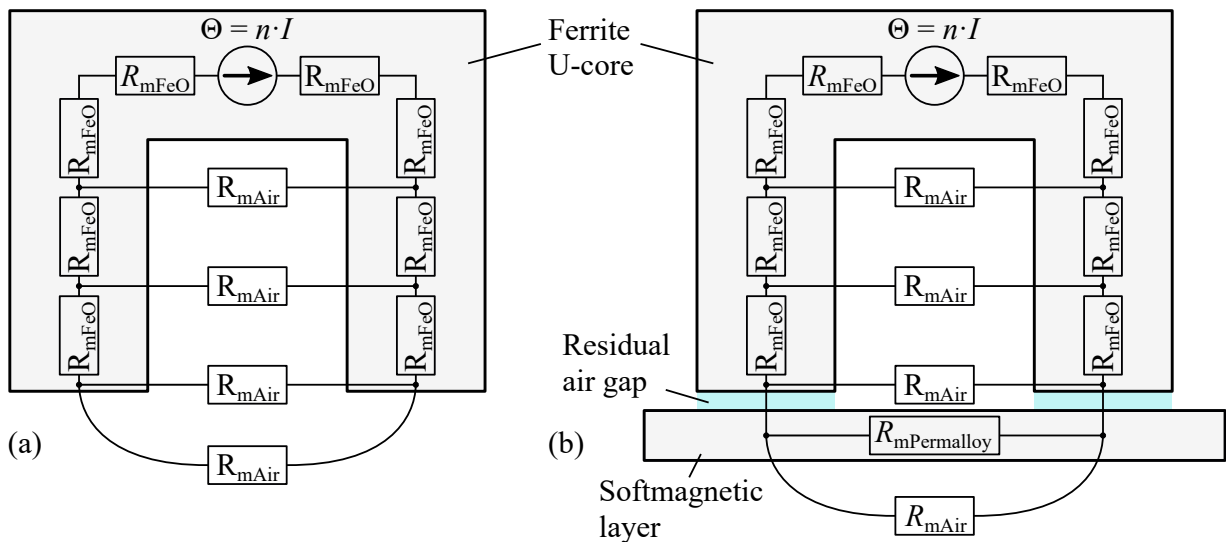


**Figure 4.2** Magnetic equivalent circuit for the core in air (a) and attached to a permalloy layer (b)

The depicted cores in Fig. 4.2 resemble electric circuits where the primary winding, which generates the magnetomotive force  $\Theta = nI$ , is the voltage source and the ferromagnetic material behaves like a conductor (high permeability) while air behaves like an insulator (low permeability). In case (a), when the circuit is open, the magnetic flux has to leave the ferrite core to close the loop and there is only little flux due to the high magnetic resistance of air while in case (b), the circuit is closed by the magnetic layer. In contrast to the in reality always remaining minor air gap drawn between the core and the layer, the gap was assumed as being zero in the simulations.

As stated in Eq. 4.3, the resistance of each segment increases with its length  $l$  and decreases with its cross section  $A$  and the field strength dependent relative permeability  $\mu_r$ . This way, the magnetic resistances of the cores can be calculated accordingly. However, for the segments of the magnetic circuit made up of air, it becomes difficult since the air flux is not conveyed in a definite cross section but rather in an uncertain area between the poles. The primary coil and the resistance of the core  $R_{m\text{FeO}}$  form the source of the magnetic field. According to Eq. 4.3, the resistance of the core is smaller, when its cross section is larger. This explains the different behavior of the field strength achieved by the core type ‘B67350’ being the only one, for which the magnetic field does not drop when it is attached to the permalloy layer. Due to its lower magnetic resistance in comparison to the smaller cores, the resulting field strength at the poles is still large. Staying in the analogy to electric circuits, this effect is similar to a voltage source with a high internal resistance. If a small resistance is connected, the voltage at its output terminals breaks down.

The resulting courses of the field strength along the z-axis of all cores are depicted in Fig. 4.3, which visualizes this break-down effect. The graphs show the decrease of the field strength for the three smaller cores when attached to a ferromagnetic layer while the ‘B67350’ benefits from it with the result of a very constant field strength in the region of  $z \geq 0$ . The striking slope of the ‘UF6.9’ sample between 1.5 and 2 mm results from its small dimension  $b = 1.8$  mm and is not of importance. However, due to the low height of this core, there is a noticeable gradient of the field strength, which could lead to errors when extrapolating the field strength in the layer.

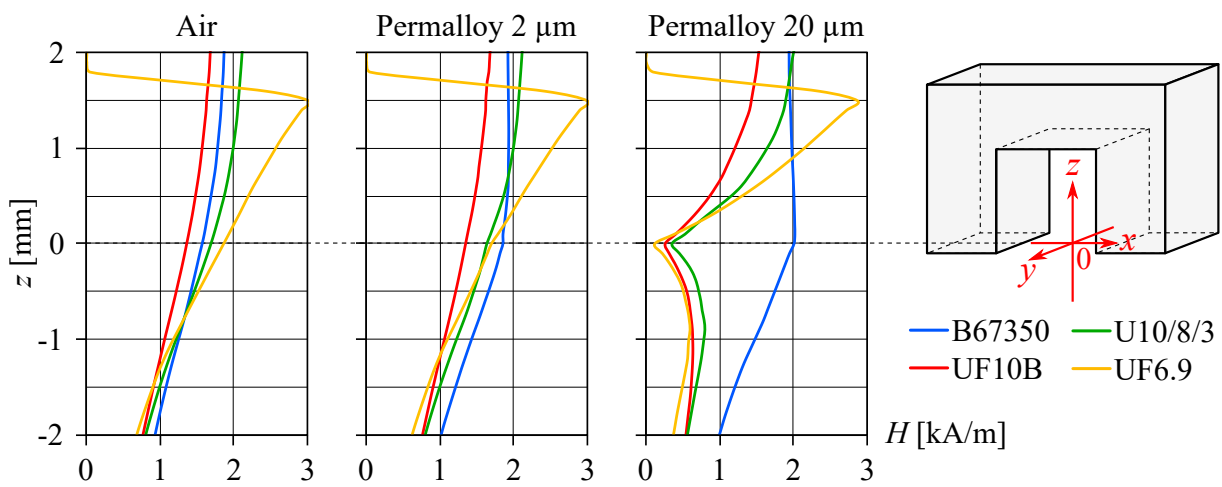


**Figure 4.3** Field strength in the center between the poles of the U-cores along the z-axis in air and on top of a permalloy layer with  $2 \mu\text{m}$  and  $20 \mu\text{m}$  height

It has to be noted that permalloy was used in these simulations and the final field strength will depend on the magnetic properties of the individual materials and their thickness. The first important finding from the results is that a large cross section  $A$  is advantageous regarding the investigation of relatively thick layers. Furthermore, an increased dimension  $b$  will most probably result in a lower gradient of the field strength along the  $z$ -axis in the region between the poles where the sensor(s) for the field strength will be placed and a small air gap will significantly increase the field strength between the poles.

Apart from the greater immunity to a field break down, a larger core cross section also has the advantage of decreasing the flux density in the core. The maximum values from the simulations given in Table 4.1 show that the flux density is generally higher for smaller cores. This is in part logical, since the magnetomotive force generated by the winding is equal in all simulations. Since the resulting flux has to pass a smaller cross section in the smaller cores, a higher density results. However, the same magnetomotive force does not necessarily create the same flux as it depends on the individual magnetic resistance  $R_m$  of the circuits. It is primarily given by the air between the poles as its magnetic resistance is much higher than the one of the core. The largest part of the flux passes the inner faces of the core and only a small fraction passes through the outer faces due to the higher resistance resulting from the greater distance to the other pole. Therefore, it is the size of the inner face of the core that has a significant influence on the magnetic resistance, and thus also on the flux density. If the core is wider for example, the cross section of the air involved in the flux guidance grows too. Indeed, when comparing the individual widths of the cores  $w$  with the maximum flux densities  $B_{\max}$ , there is an antiproportional relationship between both values with  $B_{\max} \cdot w \approx \text{const.}$  for all cores. Interestingly, the length of the poles  $b$  and also the distance  $a$  between them do not seem to play a role. The resulting values  $B_{\max} \cdot w$  are given in Table 4.2, showing the similarity between the four cores. This similarity is not only present if the core is placed in air but also when it is attached to the permalloy layers. Hence, a simple way for decreasing the flux density in the core is to increase its width  $w$ .

**Table 4.2** Product of the simulated magnetic flux density  $B_{\max}$  and the width  $w$  of the U-cores

		<i>Epcos</i> B67350	<i>DMEGC</i> UF10B	<i>Ferroxcube</i> U10/8/3	<i>DMEGC</i> UF6.9
	Air	54.27	62.5	60.03	56.60
$B_{\max} \cdot w$ [ $10^{-9}$ Tm]	Permalloy 2 $\mu\text{m}$	67.67	83.5	73.37	71.20
	Permalloy 20 $\mu\text{m}$	155.44	192.50	155.44	172.40

A large width has another advantage as the following consideration shows. From the simulation results, it is observed that the permalloy layer is not only magnetized right below the core but also at the sides of it, since the magnetic field extends in a circular region around it. When dividing the magnetized area in a width-dependent part of the area below the core and a fixed part at the two sides of the core, the increase of the width of the core will reduce the relation of the fixed flux to the width-dependent flux. The larger the core becomes, the smaller is the influence of the outside faces.

On the downside, a large cross section  $A$  and a large width  $w$  that have proven advantageous regarding a high field strength and a low flux density, result in a higher inductance. According to Eq. 4.4, the inductance scales with the inverse of the overall magnetic resistance  $R_m$  of the magnetic circuit [Albach, 2017]. However, as already stated, the overall magnetic resistance is primarily given by the size of the air gap while the influence of the core resistance is small. Therefore, the inductance is decreased much more effectively by decreasing the amount of turns as it scales with  $n$  squared.

$$L = \frac{n\Phi}{I} = \frac{n\Theta}{I \sum_i R_{m,i}} = \frac{n^2}{\sum_i R_{m,i}} \quad (4.4)$$

A low inductance is important to allow for high frequency measurements because it forms a low pass filter in combination with the winding's resistance. Calculating with the value of the core type 'B67350' on the 20  $\mu\text{m}$  permalloy layer, the resulting impedance at an exemplary frequency of  $f = 100$  kHz leads to the following impedance:

$$\underline{Z} = R + j\omega L = R + j2\pi f \cdot 12,36\mu\text{H} = R + j7.77 \Omega. \quad (4.5)$$

The value  $R$  is the ohmic resistance of the winding, which will probably be in the range of  $0.01 \Omega$  to  $0.1 \Omega$  and therefore is negligible in comparison to the reactance  $X = j\omega L$ . The amount of the impedance  $Z$  with  $X \gg R$  therefore is as:

$$Z = \sqrt{R^2 + X^2} \approx \sqrt{X^2} = X. \quad (4.6)$$

Hence, the exemplary current of  $I = 1$  A used in the simulations is forced into the winding by a voltage of  $U = I \cdot Z = 7.77$  V. For the type 'UF6.9' from *DMEGC* on the other hand, a voltage of 2.04 V is sufficient due to the core's lower inductance. In the application, the maximum voltage that can be supplied to the winding will be limited to a certain value given by the selected power amplifier in the electronic circuit. Once this voltage is known, it is possible to calculate the maximum achievable frequency. However, as can be seen from the calculated values in Table 4.1, the inductance increases significantly when the core is attached to a thick ferromagnetic layer. Furthermore, it also has to be noted that the inductance is much higher if the layer is not in saturation as its permeability is much higher in that case. All these considerations show that a sufficient overhead should be taken into account and a low core inductance is crucial regarding the maximum frequency range. As stated in Eq. 4.4, the easiest way to decrease it, is to lower the number of turns. However, a minimum quantity is necessary to reach the required field strength of 2000 A/m. According to Eq. 4.2, the decrease of the amount of turns while maintaining a sufficient field strength can be achieved by lowering the pole distance (air gap length)  $a$ .

It becomes evident that it is not trivial to select the most fitting U-core for the desired measuring task. The aim of finding a small core that achieves a high field strength with few turns and a preferably small resulting flux density in the core is quite clear. However, since almost all physical dimensions of the



core play a certain role and affect each other, the ‘perfect’ shape is not easy to estimate. Nonetheless, on the basis of the theoretical consideration and simulations some advantageous physical dimensions were figured out. To summarize, the ideal core should have a high cross section  $A$ , preferably achieved by increasing its width  $w$  and not the length  $l$ . As crucial dimension, the pole distance  $a$  should be as short as possible to be able to decrease the amount of turns and therefore the resulting inductance that inevitably increases when extending the cross section of the core. The influence of the dimension  $b$  is not as clear as for the other dimensions. From the course of the field strength in Fig. 4.3, it seems to be advantageous if  $b \geq a$  as this causes the graph to be rather flat.

Unfortunately, the desired core shape is not available in the portfolios of possible suppliers. The ‘UF6.9’ from *DMEGC* seems to be the one with the smallest air gap length  $a$ , while its other dimensions are disadvantageous. On the other hand, the larger cores ‘UF10B’ and ‘B67350’ seem to be a good compromise due to their higher width, which could be further increased by placing multiple cores side by side. On the downside, their pole distance is relatively large with 5.2 mm, which requires many windings to achieve the desired 2000 A/m, thereby increasing the inductance. Due to these restrictions of the available cores, the request of a customized core shape seems advisable. However, before deciding on its dimensions, the possible sensors that may be placed between the poles have to be reviewed as they define the minimum size of the air gap.

## 4.2 Review of Suitable Magnetic Sensors

The (preferably small) pole distance of the U-core has been revealed as the crucial dimension due to its beneficial impact on the field strength and the inductance. Therefore, potential sensors will not only be rated by their sensitivity, their bandwidth and linearity but also by their size, since the sensors have to fit in the air gap. As pointed out in chapter 3, only magnetoresistive sensors and induction coils will be taken into account, being the only ones offering sufficient bandwidth. Based on the previous research on magnetoresistive effects (see subsection 2.4.3), sensors featuring a MTJ seem the most suitable for the desired application due to their good linearity and high field range. AMR sensors with barber pole configuration also show a good linearity while being limited to a range of about one millitesla. Giant magnetoresistance (GMR) sensors on the other hand usually have the least linearity and are most often used as threshold sensors. A market research revealed that the vast majority of available sensors has its sensible axis in perpendicular direction to the plane, which would be disadvantageous regarding the assembly in the air gap of the U-core. The AMR type ‘KMY20 M’ from *TE Connectivity* and the MTJ types ‘CT100’ from *Crocus Technology* and ‘TF952’ from *Sensitec* on the other hand are sensing the field in direction of the plane and were therefore considered. Table 4.3 lists the important properties of these sensors derived from the datasheets [TE, 2017; Cro, 2020; Sen, 2020]. Both the ‘KMY 20 M’ and the ‘CT100’ have been introduced to the market already while for the ‘TF952’ only samples can be requested from the manufacturer.

Regarding the footprint, the AMR sensor is much larger than the two MTJ types as the package also contains hard magnets for the auxiliary field. This is necessary to prevent an accidental demagne-

tization of the sensor. Furthermore, its linear range only covers  $\pm 1.6$  kA/m. Above that range the sensitivity decreases as can be seen in the graph in Fig. 4.4, which shows the course of the output voltage of the three sensors in relation to the measured field strength. The linearity of the two other graphs in the chart displays the benefits of the quite recent technology of the MTJ.

**Table 4.3** Physical and electrical properties of the sensors ‘KMY20 M’, ‘CT100’ and ‘TF952’

Property	Unit	<i>TE Connectivity</i>	<i>Crocus Technology</i>	<i>Sensitec</i>
		KMY20 M	CT100	TF952
Market introduction		November 2008	June 2019	<i>Not yet released</i>
Technology		AMR	MTJ	MTJ
Configuration		Full bridge	Full bridge	Full bridge
Package		SOT223	DFN-6	Die (flip-chip)
Footprint	[mm] x [mm]	6.5 x 6.7	1.5 x 1.5	1.1 x 1.16
Sensitivity	[mV/V/kA/m]	$5.5 \pm 1.5$	$5.7 \pm 0.9$	$11.3 \pm 3.8$
Max. supply voltage	[V]	10	5.5	5.5
Bridge resistance	[k $\Omega$ ]	$1.7 \pm 0.5$	$30 \pm 10$	$100 \pm 60$
Linear range	[kA/m]	$\pm 1.6$	$\pm 40$	$\pm 16$
Offset error	[mV/V]	$\pm 1.5$	$\pm 5$	$\pm 3$
Linearity error	[%]	<i>n.a.</i>	0.5 (at $\pm 16$ kA/m)	2 (at $\pm 4$ kA/m)

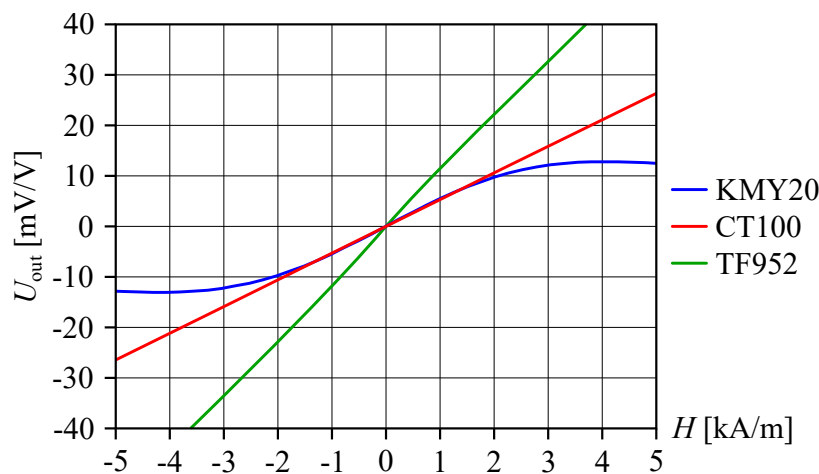


**Figure 4.4** Output voltage vs. field strength of the three sensors ‘KMY20 M’, ‘CT100’ and ‘TF952’ based on the data given in the individual data sheets

As given in Table 4.3 and Fig. 4.4, the ‘TF952’ has a sensitivity twice as high as the ‘CT100’, however, its linearity is worse accounting to 2 % in a range of  $\pm 4$  kA/m and 5 % within  $\pm 16$  kA/m compared to 0.5 % within  $\pm 16$  kA/m for the ‘CT100’. Also the high bridge resistance may be problematic as will be discussed later in this section. In conclusion, the laid out properties made the ‘CT100’ the favored sensor, mainly because the ‘TF952’ was not yet commercially available. The volume of the ‘CT100’ is given by the footprint of 1.5 mm x 1.5 mm and height of 0.45 mm while the sensory elements are centrally located within the package as depicted in Fig. 4.5.

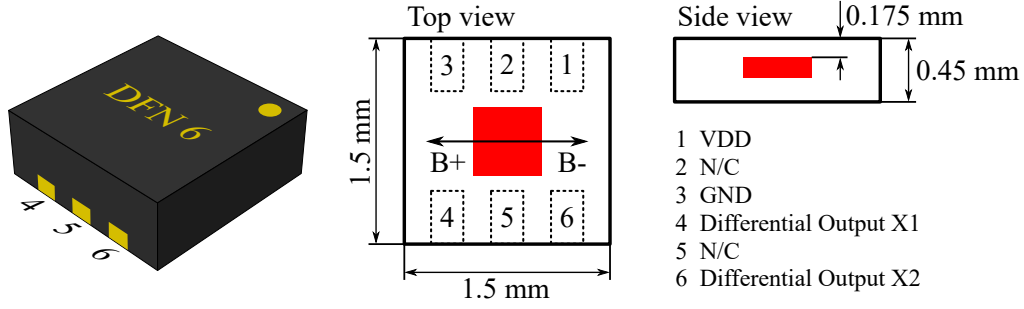


**Figure 4.5** DFN-6 package of the ‘CT100’ with the centrally located sensory area (red)

From the small size it is hard to imagine that an induction coil of the same size as the MR sensor can outperform its sensitivity, it was calculated for comparison. According to the data sheet, the ‘CT100’ features a frequency independent value of  $5.7 \text{ mV/V/kA/m}$  accounting to  $S_{\text{CT100}} = 2.85 \cdot 10^{-5} \text{ V/A/m}$  at a supply voltage of  $5 \text{ V}$ . On the other hand, the sensitivity of induction coils is linearly increasing with frequency as described in subsection 2.4.1. Due to the small size, the use of the simplified Eq. 2.25, which does not take into account the effects of the coil’s inductance and winding capacity, may be used since both values will be negligible for frequencies below the megahertz range. Based on a sine wave excitation, the frequency at which the coil offers the same sensitivity as the ‘CT100’ can be calculated by inserting the sensitivity value into the equation.

$$S_{\text{CT100}} \cdot \hat{H} = \hat{U}_{\text{ind}} = 2\pi f n A \mu_0 \cdot \hat{H} \quad (4.7)$$

$$S_{\text{CT100}} = 2\pi f n A \mu_0 \quad (4.8)$$

The coil cross section  $A$  equals the cross section of the sensor of  $1.5 \text{ mm} \cdot 0.45 \text{ mm} = 6.75 \cdot 10^{-7} \text{ m}^2$ . With an estimated wire diameter of  $30 \mu\text{m}$ , it appears reasonable to use 50 turns in a row and assume three winding layers, resulting in 150 turns. Inserting this value into Eq. 4.8 and solving for  $f$  yields

$$f = \frac{S_{\text{CT100}}}{2\pi n A \mu_0} = 35.7 \text{ kHz}. \quad (4.9)$$

Accordingly, an induction coil of equivalent size as the ‘CT100’ would show a higher sensitivity for excitation frequencies greater than  $35.7 \text{ kHz}$ . Since this represents the higher end of the desired frequency spectrum, it is not appealing to choose a coil over the MTJ based sensor. In addition, the complicated and probably expensive process of manufacturing a miniature coil of that size and the error-prone signal integration have to be taken into account. However, a disadvantage of the ‘CT100’ is its high bridge resistance as even a small parasitic capacitance between the two sensor outputs will distort the output signal. An exemplary  $10 \text{ cm}$  long cable between the sensor output and the subsequent operational amplifier will introduce a parasitic capacitance of approximately  $10 \text{ pF}$ , which together with the bridge resistance forms a low pass filter with a corner frequency of

$$f_{-3\text{dB}} = \frac{1}{2\pi RC} = \frac{1}{2\pi \cdot 30 \text{ k}\Omega \cdot 10 \text{ pF}} = 530 \text{ kHz} \quad (4.10)$$

While this frequency seems very high and sufficiently far away from the desired operating range, attention has to be paid to the phase shift the capacity introduces. At an exemplary excitation frequency of 10 kHz, the phase error still amounts to

$$\varphi = -\arctan(2\pi fRC) = -1.08^\circ \quad (4.11)$$

At this point, it is difficult to tell if a phase shift of  $\varphi \approx \pm 1^\circ$  is already critical. However, it has to be kept in mind that the recorded voltages for the field strength and the flux density will finally be put in relation to each other and that any phase shift will introduce an error in the measurement. Nonetheless, the use of the ‘CT100’ sensors was pursued. Its small size emphasizes the need for a customized core shape with a pole distance just big enough to fit the sensor, since even for the type ‘UF6.9’ with its 3.8 mm, there would be plenty of space left in the air gap.

### 4.3 Customized Core Shape and Sensor Array

After further research, the Chinese supplier for magnetic cores *DMEGC* was found to provide customized shapes in low quantities. Subsequently, a core was designed following the guidelines formulated at the end of section 4.1. The pole distance was chosen to be 2 mm, being just wide enough to allow for the ‘CT100’ MTJ based magnetoresistive sensors to be placed in the air gap. The width of the two legs of the core were chosen to be of the same size. This way, the total length (dimension  $l$  in Fig. 4.1) accounts to 6 mm. With a chosen overall height  $h$  of 6 mm and the height of the air gap  $a = 4$  mm, a constant cross section is achieved throughout the core and the condition  $b \geq a$  is met. In Fig. 4.6, the final cross section is depicted in a schematic drawing, also showing the placement of the coils and the sensors on a printed circuit board.

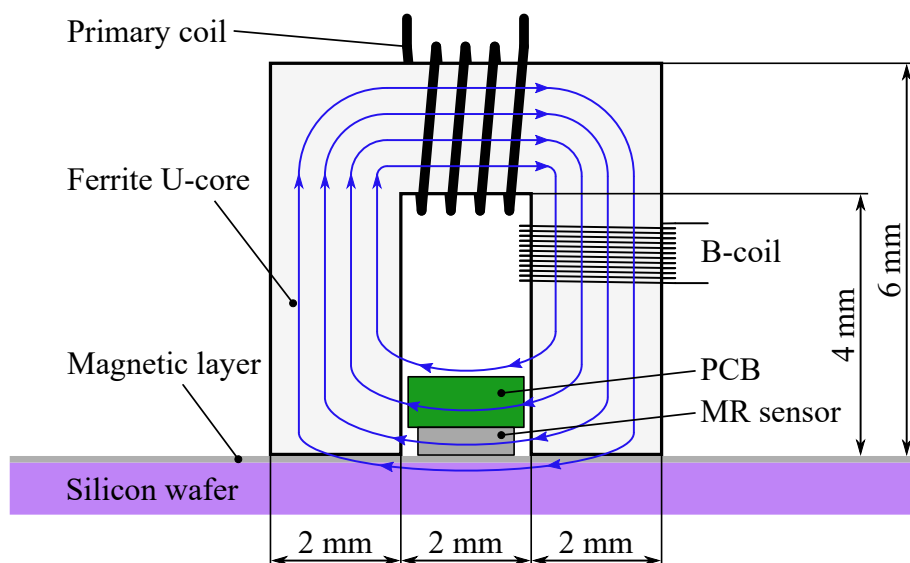


**Figure 4.6** Cross section of the designed core including the placement of the sensor and coils

While the shaping of the cross section shown in Fig. 4.6 is pretty straight forward with the indicated dimensions being primarily set in dependence of the size of the magnetic field sensor, the width  $w$  of the core requires some more attention. As observed from the simulation results of the commercially available cores, it is advantageous to choose a high value for  $w$  to decrease the flux density in the core and to decrease the influence of the core's outside faces with the non-linear field propagation in this area. On the downside, a high core width increases the core's inductance and the size of the magnetized area with the effect of having a lower spatial resolution to detect local properties in the magnetic layer. Therefore, a parametric simulation was carried out with a total of six analyzed values for  $w$  ranging from 2 mm to 12 mm to evaluate the effect of an increasing width. At this point, the power amplifier driving the primary winding was selected already and according to the data sheet, it provides a maximum current of  $I_{\max} = 1$  A. Therefore, a value of  $n = 6$  turns was chosen to reach a magnetomotive force of  $nI = 6$  A required for a field strength of at least 2000 A/m including a sufficient margin. The simulation results of the core placed in air are shown in Fig. 4.7 with the field along the  $y$ -axis (direction of  $w$ ) given in (a) and the inductance given in (b).

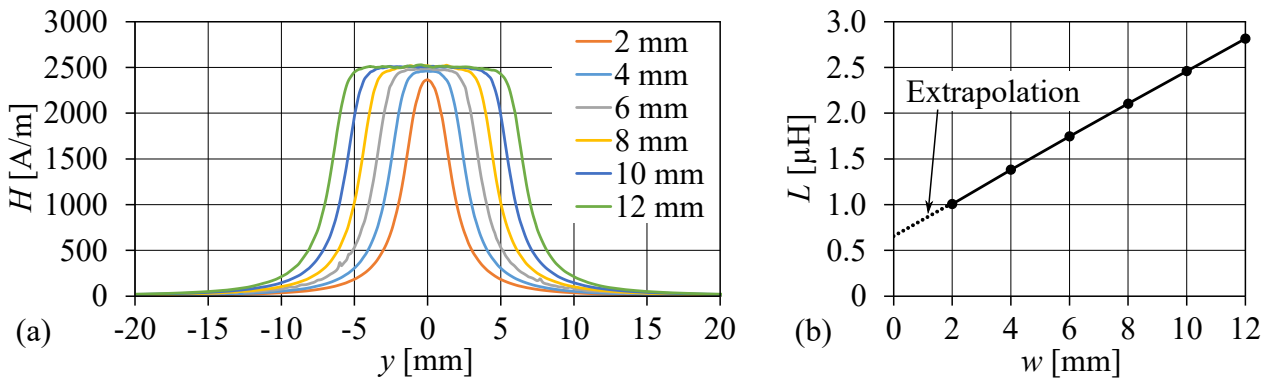


**Figure 4.7** Results of the parametric simulations for the customized core in air, showing the field strength along the  $y$ -axis (a) and the inductance for different widths  $w$  (b)

From the course of the field strength along the  $y$ -axis, there are some important observations: The orange line for the 2 mm core illustrates that the maximum value is reached only in a small range and that there is no part without influence from the sides of the core. In comparison to the other curves, it is the only one that does not reach a value of 2500 A/m. All other cores show a constant field strength in a certain  $y$ -range, which is estimated to reach from  $-\frac{1}{2}(w - a)$  to  $+\frac{1}{2}(w - a)$  (with  $a$  being the size of the air gap). This observation is particularly interesting when comparing with the previous results (section 4.1), as the 'B67350' from *Epcos* is the only one with  $w > a$ , explaining its stronger field strength despite its larger air gap.

The parallel course of the decaying field at the sides of the cores validates the assumption that the propagated field can be divided into two parts as formulated in the end of section 4.1. There seems to be a similar field decay at the sides of the core for  $|y| > \frac{1}{2}(w - a)$  with a similar shape regardless of the core's width while the field is constant at the inside for  $|y| < \frac{1}{2}(w - a)$ . The course of the inductance depicted in Fig. 4.7b supports this observation as the graph has a linear form, described by  $f(x) = mx + c$ . The slope  $m$  represents the linear increase resulting from the width dependent induc-

tance and the offset  $c$  results from the fixed inductance originating from the sides. This finding reveals that a high ratio  $w/a$  is advantageous since the influence of the sides becomes smaller in relation. In order to completely neglect this offset, a ratio of at least ten, better yet 20, would be necessary, resulting, however, in an extensively large core. Therefore, a width of  $w = 12$  mm was chosen as a compromise of size and an inductance of approximately  $2.8 \mu\text{H}$ , which is lower than most of the values of the cores listed in Table 4.1. Regarding the final measurement, a resulting ratio of  $w/a = 6$  means that a non-negligible flux component is passing at the sides of the core, where the field strength is still high. The graph in Fig. 4.7a illustrates the non-linear field strength at these points. Hence, the cross section of the examined magnetic layer involved in the flux guiding varies as a function of the field strength. To address this issue, not only a single centrally located MTJ sensor was used but an array was designed with a total number of eight ‘CT100’ sensors in a row. This way, the true course of the field strength can be interpolated from the eight measurement values and the flux carrying area can be estimated.

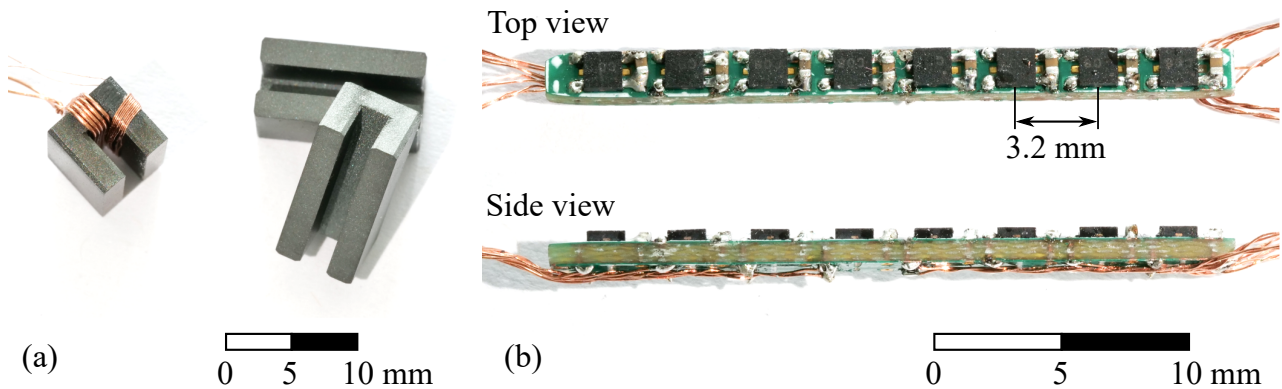


**Figure 4.8** Photograph of some of the customized cores (one with windings) (a) and of the sensor array PCB equipped with eight ‘CT100’ from *Crocus Technology* (b)

Some of the customized cores with the final outer dimensions of 12 mm x 6 mm x 6 mm are depicted in Fig. 4.8a. There is a primary winding wound around one core with  $n = 6$  turns of  $300 \mu\text{m}$  diameter wire. According to the simulations, a field strength of  $2500 \text{ A/m}$  is achieved at a maximum current of 1 A, meeting the targeted value of  $2000 \text{ A/m}$  with an additional 25 % margin. Regarding the B-coil, ten turns of  $100 \mu\text{m}$  diameter wire were used as a first approach while the final turn count can be adapted according to the layout of the electronic circuit. However, from the space around the core, a maximum number of 20 turns is estimated resulting in a two times higher sensitivity. The sensor array consisting of eight MTJ sensors soldered to a carrier PCB is depicted in Fig. 4.8b. As the board has to fit in the air gap between the core’s poles, it has a width of 1.9 mm. The DFN packages housing the sensors have a center-to-center distance of 3.2 mm, a value that can hardly be decreased further as its contact pads and also a  $100 \text{ nF}$  supply decoupling capacitor for each sensor require some space. The assembly of the core and sensor array fixed to an aluminum carrier is shown in Fig. 4.9. This measurement head was placed (upside down) on the magnetic layer under evaluation. In the final assembly, the head will be mounted to a robot in order to move it across the wafer. The sensor array is

attached to a spring loaded carrier to be able to vary the final distance to the wafer and compensate for the unknown height of the PCB resulting from the wires connected to its backside. The whole carrier will also be spring loaded to ensure a close contact between the ferrite core and the wafer. The red arrows in the picture illustrate the field propagation with their decreasing thickness representing the decreasing field strength at the sides of the core.

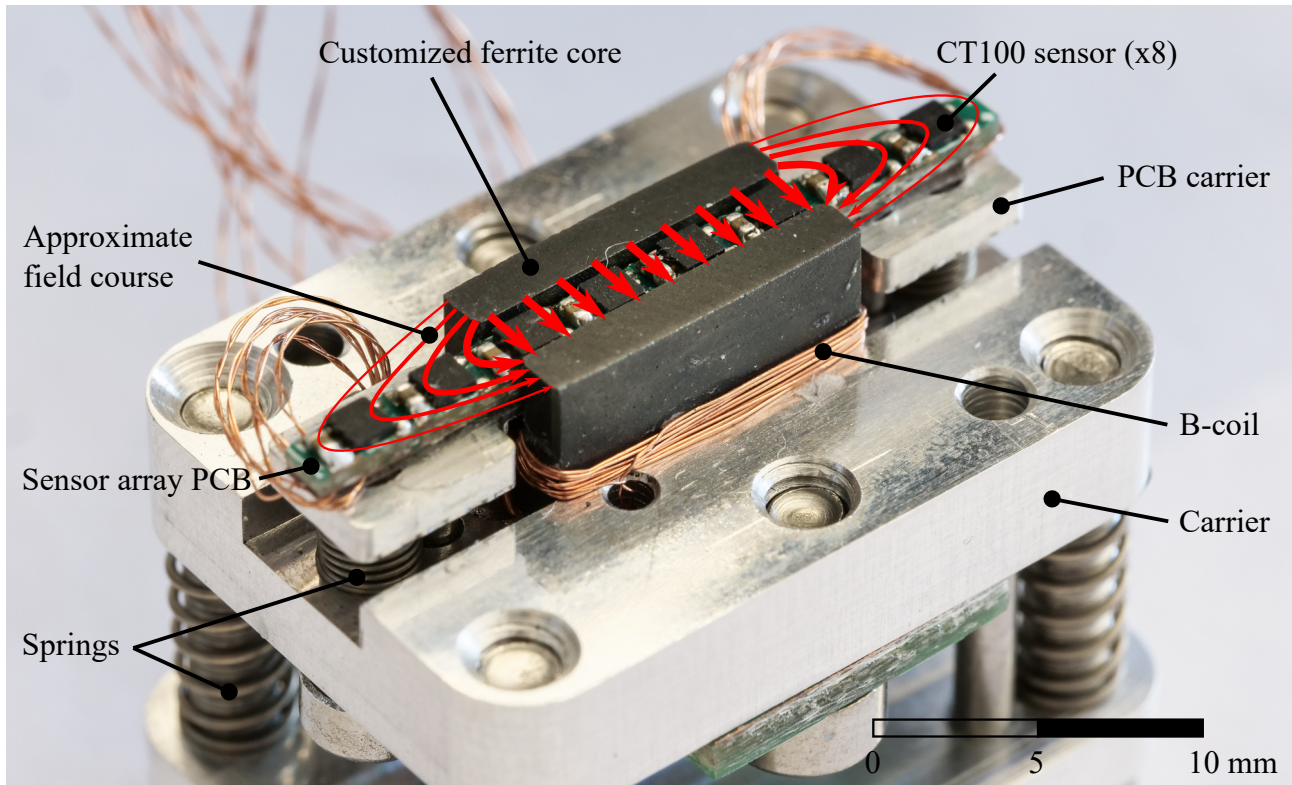


**Figure 4.9** Assembly of the measurement head consisting of an aluminum carrier with the mounted customized core and the ‘CT100’ sensor array

Measurements of the windings revealed that the primary coil showed an inductance of  $2.9 \mu\text{H}$  at  $f = 1 \text{ kHz}$ , corresponding closely to the value from the simulation while the inductance of the B-coil amounted to  $7.2 \mu\text{H}$ . The resistances at this frequency were  $188 \text{ m}\Omega$  and  $901 \text{ m}\Omega$  respectively. The course in Fig. 4.10 shows that the inductance decreases slowly with frequency while the resistance increases due to the skin effect. However, there are no restrictions to use the core up to  $f = 1 \text{ MHz}$ .

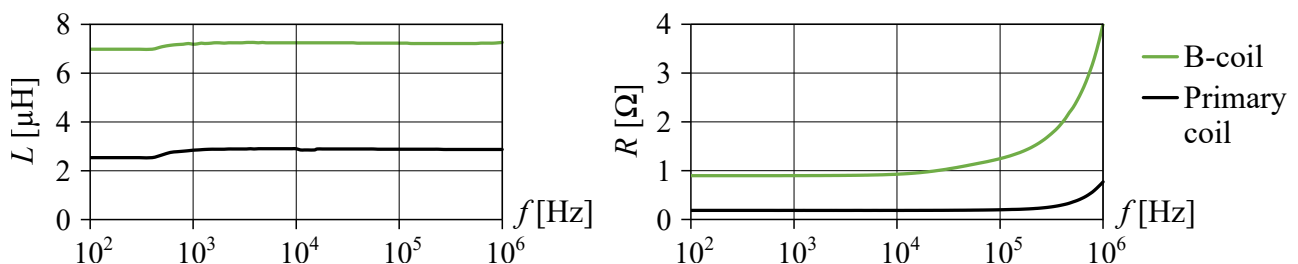


**Figure 4.10** Measurement of the inductance and the resistance of the windings vs. frequency

From the head assembly, it becomes clear that the field strength will not be measured at two different distances from the magnetic layer. Subsequently, it can not be extrapolated as it was proposed by Nakata et al. [1987] and formulated as an aim in chapter 3. This decision is based on the simulation results regarding the course of the field strength along the z-direction. They are shown in Fig. 4.11 both for the core placed in air and on top of a permalloy layer and resemble the results from Tumanski, he acquired during the measurement of a single sheet tester (Fig. 2.17). The shaded rectangle marks the area blocked by the wafer, the sensor packages and the PCB underneath. Therefore, a possible second sensor array would have to be placed at least 1.3 mm away from the layer. The resulting extrapolation is visualized by the red lines in the chart and makes clear that the error would only be slightly reduced for the core placed in air but more importantly, it is increased even for the permalloy layer. The only advantageous possibility would be to measure the field strength below the wafer, which would, however, result in a much more complicated measurement setup as the correct alignment of both sensor arrays is required. Therefore, only one array was used.

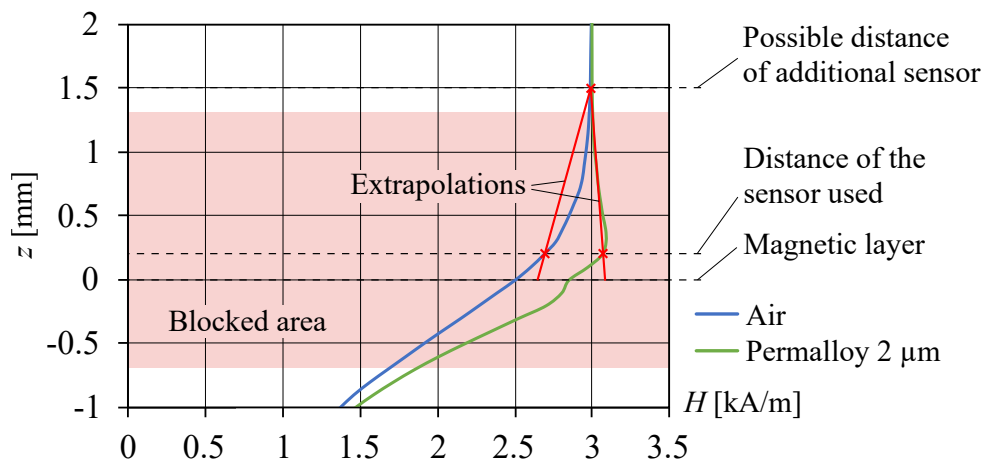


**Figure 4.11** Simulated course of the field strength along the z-axis



## 5 Electronic Circuit

With the measurement head being designed and assembled, the next element in the list towards a functional device is the electronic circuit used to supply the necessary currents to the head and to amplify the signals from the attached sensors. As shown schematically in Fig. 5.1, the circuit is split into different sub-circuits with a section in this chapter dedicated to each of them. Similarly, they will be manufactured on separate PCBs to simplify bug-fixing.

The first section 5.1 covers the amplification circuit for the primary coil necessary to create a reliable magnetic field at variable frequencies. In order to achieve a fixed field strength regardless of the impedance of the primary winding, the corresponding circuit is based on current feedback as the field strength is linearly depending on it. This current source is fed with a sine wave signal, which is generated by a special digital-analog converter (DAC) in combination with a variable gain amplifier (VGA) placed on the second PCB (section 5.2). As the desired output signal is set by the LabVIEW application on the host computer, a microcontroller is necessary to handle the signal transfer between the different circuits. A suitable DAQ device to be integrated in LabVIEW is chosen and discussed in section 5.3. It is the core part for capturing the voltages representing the field strength and the flux density. However, these signals have to be pre-processed in terms of amplification and integration. Therefore, the last two sections of this chapter cover the circuits designed for the conditioning of the signals from the magnetic field array (section 5.4) and the induction coil (section 5.5).

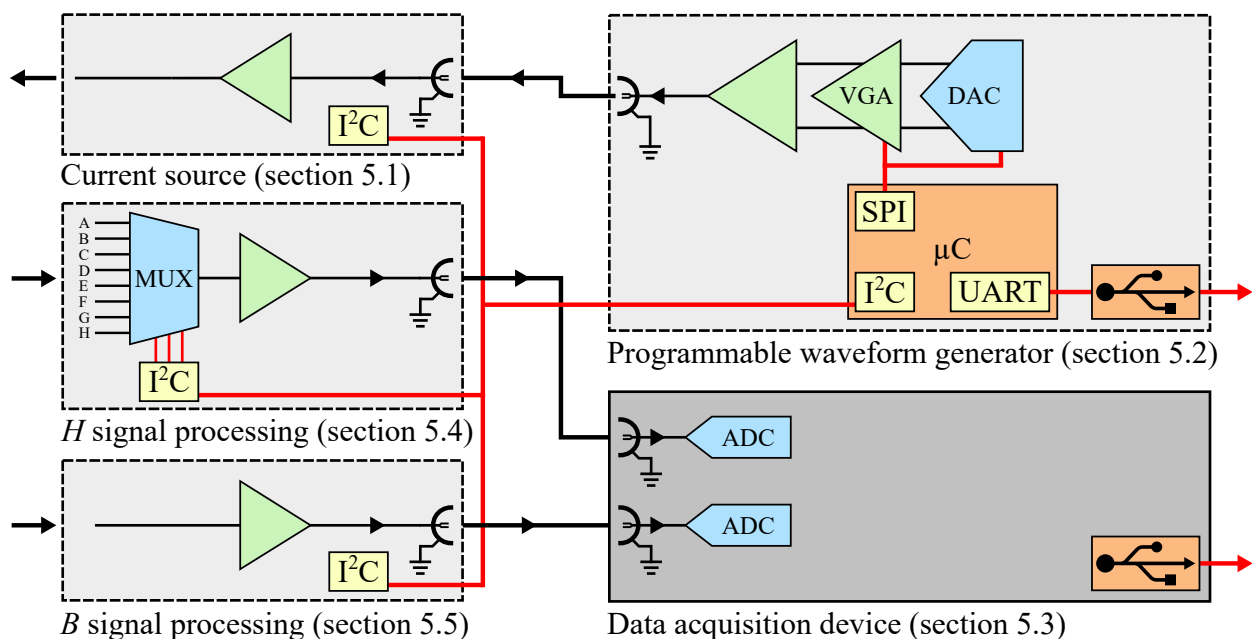


**Figure 5.1** Schematic of the electronic circuit containing four PCBs and a DAQ

The schematic in Fig. 5.1 also visualizes the resulting signal distribution between the boards with the analog signals in black color and the digital ones in red. One USB connections is needed for the control of the generated voltage and therefore is attached to the microcontroller, translating the incoming commands for the DAC and VGA attached via the serial peripheral interface (SPI) bus. The USB link may also be used for exchanging status information with the boards, which are connected by the inter-integrated circuit (I<sup>2</sup>C) bus designated for this purpose. This is necessary for example to select one of the eight channels from the field sensor array connected to a multiplexer. A second USB connection is used for data transmission from the ADCs integrated in the DAQ. As there are many suitable devices available on the market, it was not custom designed but was obtained from *National Instruments* instead for a seamless integration in the virtual instrument.

### 5.1 Current Source

In contrast to the data acquisition device, the purchase of a ready-built current source is not that simple as these devices are usually optimized according to the requirements of the application. There are some quite universal devices on the market, however, these can hardly be customized if necessary. Therefore, the self-development based on an operational amplifier (OP) is the method of choice.

The circuit symbol of an OPs corresponds to a triangle as shown in Fig. 5.1. It is an integrated circuit with usually one output and two inputs, which are called inverting (marked with ‘-’) and non-inverting (marked with ‘+’). The most popular voltage feedback OP controls its output voltage in dependence on the voltage difference between its inputs. If the voltage at the non-inverting input is larger than the one at the inverting input the output voltage increases and if it is the inverting input with the higher voltage, it is decreased. Therefore, a feedback network between the output and the inputs is mandatory for the OP to work as desired. This network is established by placing resistors with appropriate values between the inputs and the output. Eventually, a small voltage difference at the inputs leads to a larger accurately controlled signal at the output in order to cancel out any occurring input voltage difference. While this ensures a basic voltage amplification, many more functions can be achieved by adapting the feedback chain with additional passive components. This way OPs can sum or subtract voltages with different weighing or achieve signal integration or derivation. The minimum and maximum voltages the OP can handle are given by the supply, as e.g. the output may never exceed it but is limited to a certain range from slightly above the negative to slightly below the positive supply voltage.

Another feature of an OP is the ability to convert a voltage to a current to obtain a voltage controlled current source. A popular circuit with that function was invented about 1962 by Bradford Howland, who gave it its name ‘Howland current source’ or ‘Howland current pump’ [Tex, 2013]. Though initially designed for lower currents, it provides good service as well for high currents in the improved or enhanced design that is shown in Fig. 5.2, which features an increased efficiency and is covered in different application notes like Ape [2013]; Tex [2013]; Jiang [2018]. Despite its general usage for applications where an adjustable current is needed, Ghodke et al. [2005] reported its good suitability also for inductive loads in their hysteresis loop tracer with currents as high as 2 A.

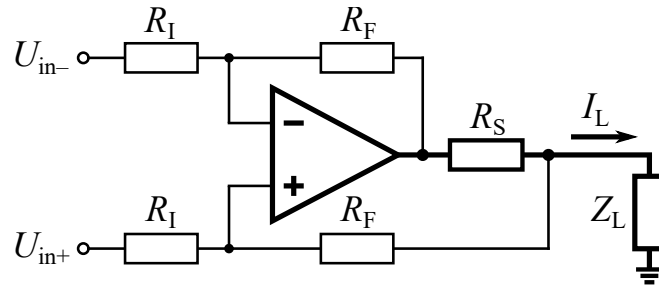


**Figure 5.2** Schematic of the enhanced Howland current source

Input voltages can be applied to both the inverting input  $U_{in-}$  and the non-inverting input  $U_{in+}$  across the input resistors  $R_I$ , though usually only one input is used while the other is tied to ground. The voltage drop across the sense resistor  $R_S$  located behind the output is determined differentially by both inputs connected before and after  $R_S$  via the feedback resistors  $R_F$ . Usually, they have the same value and so have the resistors  $R_I$  to make sure that the relation  $R_I R_F$  accounts to the same value for both inputs. An unavoidable error is introduced, however, since the feedback impedance at the inverting input is  $R_I \parallel R_F$  while it is  $R_I \parallel (R_F + R_S)$  at the non-inverting input. Therefore,  $R_S$  has to be chosen much smaller than  $R_F$  for the error to be negligible or a trim resistor has to be included in one of the feedback chains. Eventually, the output current  $I_L$  across the load  $Z_L$  is given by

$$I_L = \frac{R_F}{R_I} \cdot \frac{U_{in+} - U_{in-}}{R_S}. \quad (5.1)$$

Another option to overcome the error introduced by the sense resistor (not present in the original Howland current source) is to insert another amplifier as impedance converter between  $R_S$  and  $R_F$ . This way, the additional resistance of  $R_S$  is hidden from the non-inverting input and does not matter anymore. It is replaced by the output impedance of the OP, which typically is close to zero.

### 5.1.1 Amplifier Selection

While a low output impedance is a common feature among operational amplifiers, there are many more properties that distinguish the individual parts from each other. At present, *Analog Devices* alone has more than 700 different OPs available in its portfolio with the custom parts not even included. Hence, there are many thousand different types available on the market due to the fact that most amplifiers' electrical properties can only be improved with a negative effect on the others. Therefore, they are developed with respect to specific use cases. There are amplifiers with high precision offering low input offset voltages and a high temperature stability with the drawback of being rather slow. High speed types on the other hand tend to be less precise but offer a higher slew rate resulting in a faster settling time of the output signal and the support for higher frequencies and higher gains. However, attention must be paid to the circuit design as these parts are sensitive to parasitic capacities resulting in output peaking and instabilities.

In this case, the desired high output current (chapter 3) restricts the number of potential devices. In their hysteresis loop tracer, Ghodke et al. [2005] successfully employed the high current and high voltage amplifier ‘OPA544’ from *Texas Instruments*. It is part of a family of closely related low-cost OPs designed to drive a variety of loads for instrumentation applications [Tex, 2019]. The type ‘OPA548’ is also part of the family but capable of even higher currents up to 3 A and therefore shortlisted for suitable devices. Following the publication from Jiang [2018], another recent OP suitable for a powerful current source is the type ‘ADA4870’ from *Analog Devices*. It is based on their “extra fast complementary bipolar” technology allowing the combination of high voltages in high speed signal processing applications for waveform generation or for piezo or ultrasound drivers [Ana, 2014b]. From the drive capabilities, the ‘OPA548’ is clearly ahead of the ‘ADA4870’ as it can be supplied with a 50 % higher voltage and its output current is three times as high. On the other hand, the ‘OPA548’ can not compete with the speed of the ‘ADA4870’, which is about a hundred times faster. It achieves an output step of 10 V to within 0.1 % of the final value in about 80 ns resulting in a maximum slew rate of 2500 V/ $\mu$ s [Jiang, 2018]. In combination with a GBP of at least 52 MHz, it is well equipped for signals up to the lower megahertz range. Regarding the noise, both devices will probably achieve similar values in the final circuit.

In summary, the different optimization of both OPs is clearly visible from the data sheets. The ‘OPA548’ offers good DC characteristics and achieves high output currents at a moderate noise level while being unsuitable for frequencies in the higher kilohertz range. The ‘ADA4870’ on the other hand is designed for high frequencies and high currents with resulting disadvantages for the input stages, causing comparably large bias currents and current noise. However, by introducing another OP as primary amplifier in front of the ‘ADA4870’, these drawbacks can be overcome as proposed in the amplifier’s data sheet [Ana, 2014b]. Jiang has studied this composite amplifier design with the aim of building a high speed and high precision current source by implementing different suitable amplifiers from *Analog Devices* in combination with the ‘ADA4870’. The resulting circuit, named ‘Composite amplifier enhanced Howland current source’ (CAEHCS), is shown in Fig. 5.3. Apart from the ‘ADA4870’, two additional ‘ADA4898’ are included, each as primary amplifier and as impedance converter to compensate the error introduced by  $R_S$ .

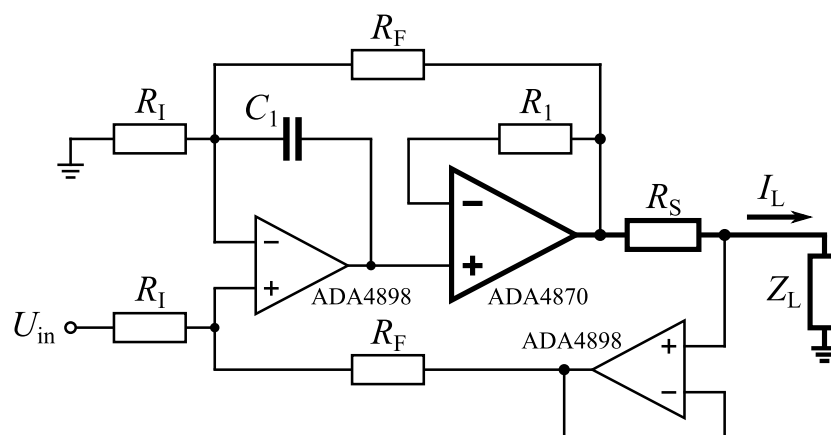


**Figure 5.3** Schematic of the ‘Composite amplifier enhanced Howland current source’ (CAEHCS)

The ‘ADA4898’ is a high precision, high voltage and low noise amplifier that decouples the inputs of the ‘ADA4870’ from the signal source and the feedback signal. It features much lower input bias currents and lower current noise but has enough speed to not significantly slow down the whole circuit. Jiang points out the exceptional DC characteristics of the composite design while the high speed is maintained. He determined a final settling time of 100 ns, a bandwidth of 10 MHz and a slew rate of 12.6 A/ $\mu$ s, while the current offset has decreased from over 10 to 0.2 mA. Though, another evaluated amplifier ‘LT6275’ even shows slightly better characteristics, the ‘ADA4898’ was chosen due to availability. With a maximum current of 1 A and the high speed capabilities, the circuit shown in Fig. 5.3 is well suited for high frequency hysteresis loop measurements.

### 5.1.2 Circuit and Board Design

The board layout is designed with respect to the guidelines from the data sheets. Sufficiently large ceramic capacitors are placed close to the power supplies of all amplifiers and high frequency traces are as short as possible and cleared from copper. Additionally, 330  $\mu$ F electrolytic capacitors are employed for the  $\pm 15$  V rails, which will be supplied externally. Apart from the power plug, there are SMA connectors for the in- and outputs and a I<sup>2</sup>C bus connector. The bus is used for exchanging data with the main PCB as shown in Fig. 5.1 and allows the power-up and shutdown of the ‘ADA4870’ and the monitoring of its internal die temperature, which is mapped to an analog output voltage. Additionally, a short circuit event triggered at currents above 1.2 A can be detected via the bus.

The heat dissipated by the amplifier requires closer attention. According to the measurement of the primary winding (Fig. 4.10), its resistance is approximately 200 m $\Omega$  in the range up to 10 kHz. In this range, the imaginary part  $X_L$  is still small and does not have to be taken into account. To force a current of 1 A into the coil, a voltage of only  $U = I \cdot R = 200$  mV is necessary. As the supply voltage accounts to 15 V, the excess voltage of 14.8 V is dissipated within the sense resistor and the amplifier. With a resistance of  $R = 2.2 \Omega$ , the voltage drop across the resistor is 2.2 V and most dissipation occurs within the amplifier with a remaining voltage drop of  $15 \text{ V} - 2.2 \text{ V} - 0.2 \text{ V} = 12.6 \text{ V}$ . The resulting mean power loss  $P_{\text{mean}}$  across the OP for a sinusoidal excitation is

$$P_{\text{mean}} = \frac{\hat{U}}{\sqrt{2}} \cdot \frac{\hat{I}}{\sqrt{2}} = \frac{\hat{U} \cdot \hat{I}}{2} = 6.3 \text{ W}. \quad (5.2)$$

According to the data sheet, the package of the ‘ADA4870’ using only the copper area around it as the heat sink has a thermal resistance from junction to ambient of  $\theta_{JA} \approx 16 \text{ }^\circ\text{C}/\text{W}$  in still air. Subsequently, the 6.3 W of power loss would cause a junction temperature of 102  $^\circ\text{C}$  above ambient resulting in a total of  $\approx 125 \text{ }^\circ\text{C}$ , which is close to the maximum allowed temperature of 150  $^\circ\text{C}$  [Ana, 2014b]. Therefore, a heat sink was connected to the backside of the PCB, which effectively decreased the junction temperature to values below 75  $^\circ\text{C}$ . Additionally, another series resistance  $R_{\text{ser}}$  behind the two sense resistors  $R_{S1}$  and  $R_{S2}$  was introduced. By choosing a value of 5.6  $\Omega$ , the heat is rather dissipated in this resistor than in the amplifier as shown in Fig. 5.4. This way, the mean power loss in the OP is reduced to 3.5 W (red shaded area).

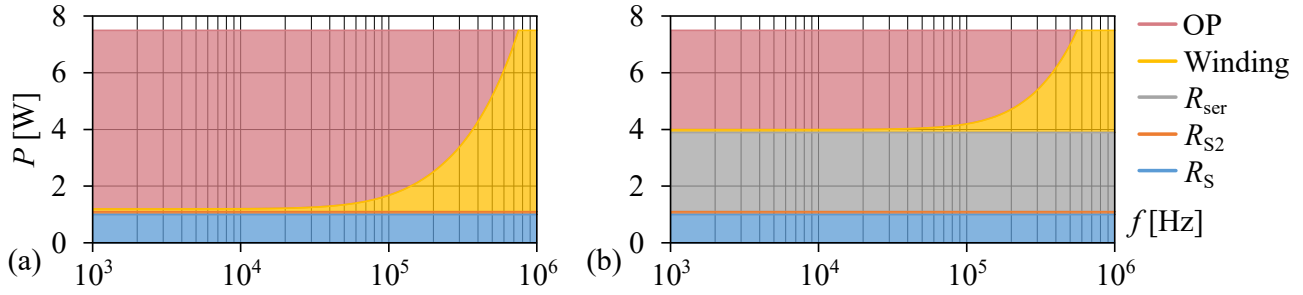


**Figure 5.4** Frequency depending mean power loss within the components in the output chain without (a) and with an additional series resistor of  $5.6 \Omega$  (b) for a sinusoidal current  $\hat{I} = 1 \text{ A}$

While the same result could be reached by decreasing the supply voltage, there is a good reason to introduce the resistor  $R_{\text{ser}}$  instead. It is because the inductance of the primary winding forms a low pass filter in combination with all the resistors in the output chain. Without the additional series resistor, the corner frequency of this filter equals

$$f_{-3\text{dB}} = \frac{R}{2\pi L} = 130 \text{ kHz} \tag{5.3}$$

With the additional resistor, it is almost four times as high, accounting to 440 kHz, which increases the possible application range of the measurement system. However, these values are based on the inductance measurement performed in air (Fig. 4.10). As the inductance increases if the core is attached to a ferromagnetic material, the corner frequency will decrease, which emphasizes the benefit of the additional resistor. Furthermore, it also stabilizes the output of the amplifier as the phase shift between the voltage and the current is decreased as illustrated in the graph in Fig. 5.5. A higher phase shift means that the load becomes increasingly inductive with the result that the amplifier loses control of the output signal and may become unstable.

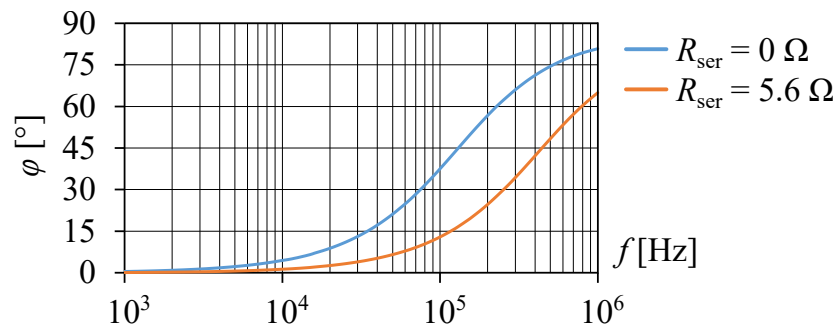


**Figure 5.5** Decreased phase shift  $\varphi$  with a series resistor is  $R_{\text{ser}} = 5.6 \Omega$

The chosen value for  $R_{\text{ser}}$  is a trade-off between stability and output power. While a higher value would further increase the corner frequency, it would also increase the voltage drop across the resistor with the consequence that less voltage would be available for the winding. The resistor was chosen as high load type to withstand a mean dissipated power of up to 5 W and inserted afterwards in the latest version of the current source as a final improvement.

Regarding the analog signal handling, the final circuit matches in great parts the schematic of the CAEHCS shown in Fig. 5.3. The input voltage signal is fed into the non-inverting input of the primary amplifier ‘AD4898’, while its inverting input is tied to ground. Both  $R_I$  and  $R_F$  are chosen to have a value of  $1\text{ k}\Omega$  and  $R_S$  has a value of  $2\ \Omega$ . According to Eq. 5.1, the resulting output current therefore is half the input voltage  $I_L = U_{in+}/2$  and the maximum output of  $1\text{ A}$  is reached at an input voltage of  $2\text{ V}$ . To be able to measure this current (for debugging and characterization purposes), another  $0.2\ \Omega$  resistor is placed behind  $R_S$ . The voltage drop across this resistor is rather small and therefore is amplified by an instrumentation amplifier, type ‘AD8421’ from *Analog Devices* offering both high precision and high speed. It is chosen primarily due to its use for amplifying the signals of the magnetic field sensor array (section 5.4). The final board is shown in Fig. 5.6.

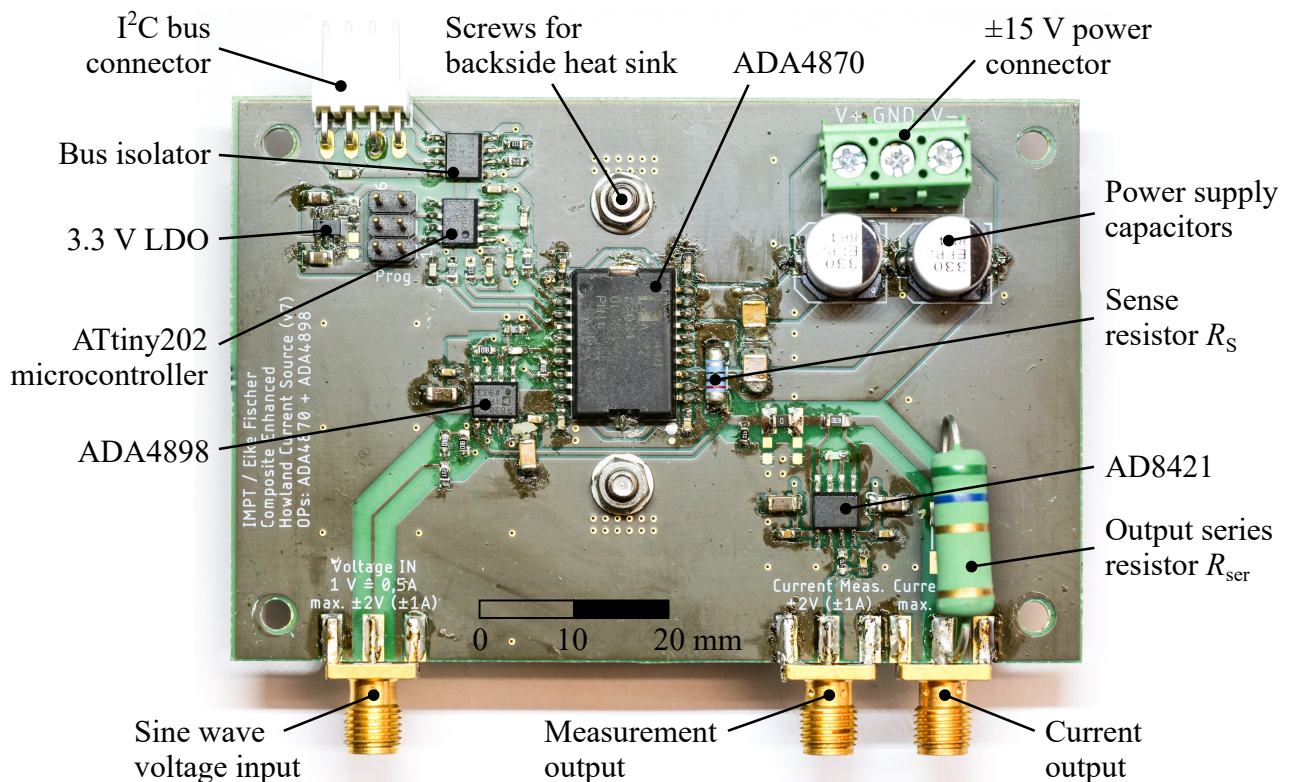


**Figure 5.6** Picture of the final version of the PCB featuring the ‘Composite amplifier enhanced Howland current source’ (CAEHCS)

## 5.2 Programmable Waveform Generator

With the voltage controlled current source being laid out and thoroughly tested, the second mandatory electronic sub-circuit is the ‘programmable waveform generator’, which generates the necessary sine wave signal. While earlier, sine waves were mostly generated by analog circuits with trimmable resistors and capacitors, the method of direct digital synthesis (DDS) is very common today. This

principle is based on a fast DAC and a non-volatile read-only memory (ROM) that holds  $2^n$  amplitude values of a sine wave corresponding to  $2^n$  different phase values from 0 to  $2\pi$ . The last required part is a phase accumulation register of relatively large size, 32 bit or more, combined with a high frequency oscillator. At each pulse of the oscillator, a user programmable phase shift is added up on the phase register and the corresponding amplitude of the resulting phase is read from the ROM and converted to an analog voltage by the DAC. While the phase is calculated with very high resolution (e.g. 32 bit), the ROM does not need to hold that many values. Usually, the resolution of a DDS system is limited by the DAC and subsequently the size of the ROM is chosen slightly higher. For example, if the DAC has a resolution of 12 bit, meaning it can output 4096 different voltages, a sufficient size of the ROM would be 14 bit = 16,384 values corresponding to a phase resolution of  $2\pi/16,384$ . Therefore, the phase accumulation register is truncated to the size of the ROM.

Eventually, the programmable frequency range and resolution of a DDS are defined by the size of the phase accumulator register and the speed of the oscillator. For example with a 100 MHz clock and a 32 bit phase register, the output frequency can be tuned to values, which are multiples of  $f_{\text{res}}$  (Eq. 5.4). While a lower clock speeds increases the resolution, it also results in a decreased DAC sampling speed with the consequence that high frequency signals are composed of a lower number of samples. As a general rule, frequencies of more than 1/10 of the clock speed should be avoided.

$$f_{\text{res}} = \frac{100 \text{ MHz}}{2^{32}} = 0.023 \text{ Hz.} \quad (5.4)$$

With the DDS technology, a simple way of generating sine waves over a wide frequency spectrum is available. The amplitude of the output signal, however, is usually fixed in order not to decrease the resolution of the DAC. To be able to vary the output amplitude, the signal can be amplified or attenuated in the analog domain by using operational amplifiers. A convenient way is the use of a variable gain amplifier, which usually provides a linear-to-logarithmic gain interface and is available with a gain range of up to 80 dB today [Hunter, 2014]. Hunter states that by using VGAs, “traditional designs [that] used high-performance discrete devices, a large number of integrated devices in parallel, or an expensive ASIC” can be avoided and the complexity of a signal generator’s output stage can be greatly reduced. Eventually, only three devices are necessary to build a complete signal generator as shown in Fig. 5.7: a DDS chip, a VGA and an OP to convert the so far differential signal to a ground referred signal of the desired amplitude.

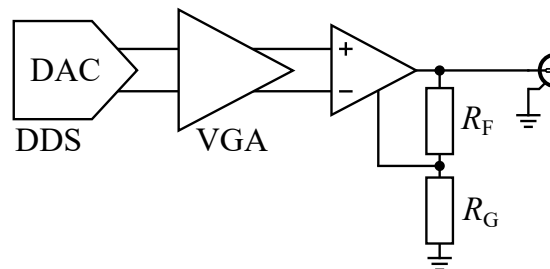


**Figure 5.7** Simplified schematic of the signal generator consisting of a DAC (part of the DDS chip), a VGA and a trailing OP to convert the differential to a single-ended signal and to set the output amplitude



### 5.2.1 IC Selection

According to Fig. 5.7, the necessary devices were selected following the recommendations of Hunter. Therefore, the ‘AD9834’ was chosen as the DDS chip, which may be provided with a clock of up to 50 MHz. In combination with the internal 28 bit phase accumulation register, the frequency resolution accounts to  $f_{\text{res}} = 0.186$  Hz. This is sufficient, having in mind that the desired minimum frequency of the measurement is 50 Hz. The DAC has a resolution of 10 bit and the ROM stores the amplitude information of 4096 different phase angles, corresponding to a resolution of 12 bit. It features two current sources generating two sine waves with a phase shift of  $180^\circ$ . This way, the signal becomes differential and a differential voltage of close to  $\pm 0.6$  V is achieved between the outputs as illustrated by the black line in Fig. 5.8 [Ana, 2014a].

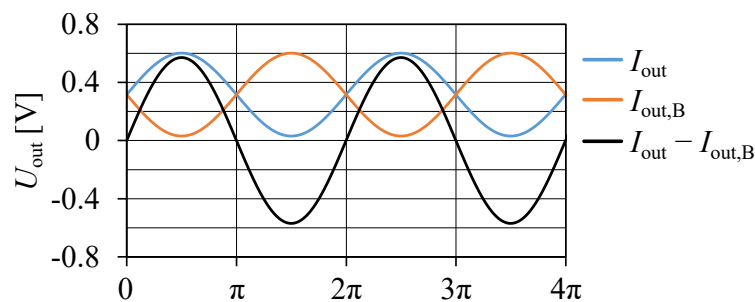


**Figure 5.8** Differential signals of the current outputs of the ‘AD9834’

The next device in the signal chain is the variable gain amplifier, which should offer the possibility to vary the output of the current source in a range of at least 40 dB equivalent to a current range from 10 mA to 1 A. From the 77 devices in the portfolio of *Analog Devices*, only 26 are capable of handling low frequency signals of 50 Hz or less, which is mandatory for this application. Among these, most have a digital gain programming interface, which allows only for a coarse gain setting, while an analog gain setting provides greater flexibility. Eventually, there were seven VGAs that came into consideration. From these, only the novel ‘AD8338’ presented by Hunter [2014] and the older ‘AD8330’ feature a differential signal path and a sufficient gain range. These two devices were therefore evaluated based on their electrical properties given in their data sheets.

From the characteristics, the ‘AD8330’ clearly is the faster device. It offers a 30 times higher slew rate and an eight times higher bandwidth at a similar noise level as the ‘AD8338’ while the resulting higher current consumption is not of great importance in a non-battery-powered application like this. The wide logarithmic gain range of 80 dB of the latter device allows for greatest flexibility and is a unique feature among VGAs. However, the ‘AD8330’ has a second gain setting input that allows a further adjustment of its 50 dB gain range, which effectively increases the range to 100 dB from  $-30$  to  $70$  dB with the only downside that an additional input pin has to be driven. Since both devices seem to achieve good performance, it was decided to evaluate each of them in corresponding circuits. However, eventually only the circuit with the ‘AD8330’ was fully functional with everything working as desired and the device running stable at different frequencies and gains. It was therefore chosen, though its increased speed is not necessary in this application.

As illustrated in Fig. 5.7, a final amplifier is necessary to convert the differential output of the VGA to a ground referred signal. For this purpose, Hunter proposes the high speed type ‘AD8130’, which features an ‘active feedback’ design, meaning that it contains individual amplifiers for the signal inputs on one hand and the feedback circuit on the other. Hence, there is no influence of the gain setting resistors on the input signal as it is the case for standard OPs and an excellent rejection of common-mode noise is the benefit [Ana, 2005]. Therefore, the ‘AD8130’ is suitable for receiving differential signals from a twisted-pair cable, while being capable of rejecting high frequency noise. Its special design achieves a similar result as an instrumentation amplifier that is aimed for separating low-amplitude signals from common-mode signals but focuses more on high gains, which is not required here. A general option of converting a differential to a single-ended signal is to build a summing circuit with two amplifiers. According to Tran and Rombola [2017], the ‘ADA4807’ is suitable for this task featuring low distortion, low noise and high speed.

The characteristics of the amplifiers reveal the similarities between them. Both are designed for high frequency signals featuring a high slew rate, large bandwidth and an excellent common-mode rejection that even at 10 MHz accounts to more than 60 dB in case of the ‘ADA4807’ and 70 dB in case of the ‘AD8130’. Any of these devices is suitable as trailing amplifier providing sufficient speed and low noise at the same time. Though, the noise of the ‘ADA4807’ is slightly lower, it is reasonable to select the ‘AD8130’ as proposed by Hunter since it requires no external components at unity gain configuration. Another advantage, albeit a small one, is its supply voltage range of  $\pm 12$  V, which provides a great flexibility if a higher output amplitude should become necessary.

### 5.2.2 Component Calculation

Since the three devices are selected, the voltage levels between them have to be considered in order to fully take advantage of the 50 dB gain range of the VGA. With the  $\pm 0.6$  V input signal from the ‘AD9834’ and an output swing of  $\pm 2$  V required for driving the current source, the constraints are set. Another condition is the supply voltage of the VGA, which allows a maximum differential output voltage of  $\pm 2.6$  V. This eliminates the need for further amplification as it corresponds to a (theoretical) current of  $\pm 1.3$  A. Hence, the trailing amplifier ‘AD8310’ can be operated at unity gain as initially intended and no additional resistors are needed.

As the logarithmic gain interface of the ‘AD8330’ is only capable of amplifying the signal, the input voltage requires attenuation. Without it, the output may only be varied in the range of  $\pm 0.6$  V to  $\pm 2.6$  V, equivalent to a gain of 0 to 12.7 dB. As stated in the previous subsection, the gain may be adjusted by up to  $-30$  dB by applying a voltage to the secondary input of the ‘AD8330’, called  $V_{\text{mag}}$ . However, care must be taken as this method also affects the maximum output swing of the device, which is limited to  $\pm 4V_{\text{mag}}$ . As  $V_{\text{mag}}$  is internally biased to 0.5 V, its limitation on the output swing accounts to  $\pm 2$  V, which is just enough for a current of  $\pm 1$  A. In order to have some margin,  $V_{\text{mag}}$  should be raised slightly by supplying a voltage of 0.6 V to this input, which increases the gain by  $0.6/0.5 = 1.58$  dB. This method results in a comfortable output span of  $\pm 2.4$  V but reduces the usable logarithmic gain range further to 11.1 dB, which is far away from the possible 50 dB.

The remaining 38.9 dB can only be made available by attenuating the input voltage accordingly. The required  $200\ \Omega$  output resistance for the DDS chip was subsequently split up in two resistors and the voltage for the VGA was picked up in between. Since resistors are available with distinct values, Table 5.1 contains suitable pairs and the resulting attenuation and output amplitude of the voltage divider. It reveals that the combination of a  $200\ \Omega$  and  $2.2\ \Omega$  accurately achieves the necessary signal attenuation while the total resistance is only slightly increased to  $202.2\ \Omega$ , resulting in a negligible error of 1.1 % compared to the desired  $200\ \Omega$ . The differential voltage at the inputs of the ‘AD8330’ now accounts to  $\pm 6.5\ \text{mV}$ . Eventually, the whole gain range can be used and the output voltage of the programmable waveform generator can be varied between  $\pm 8\ \text{mV}$  and  $\pm 2.4\ \text{V}$ , which corresponds to an output current of  $\pm 4\ \text{mA}$  and  $\pm 1.2\ \text{A}$  respectively. The final circuit is illustrated in Fig. 5.9.

**Table 5.1** Attenuation and output amplitude of possible voltage dividers

$R_1$ [ $\Omega$ ]	$R_2$ [ $\Omega$ ]	$R_1 + R_2$ [ $\Omega$ ]	Attenuation [dB]	Output amplitude [mV]
191	6,8	197,8	-29,3	$\pm 20,6$
200	4,7	204,7	-32,8	$\pm 13,8$
200	3,3	203,3	-35,8	$\pm 9,7$
200	2,2	202,2	-39,3	$\pm 6,5$

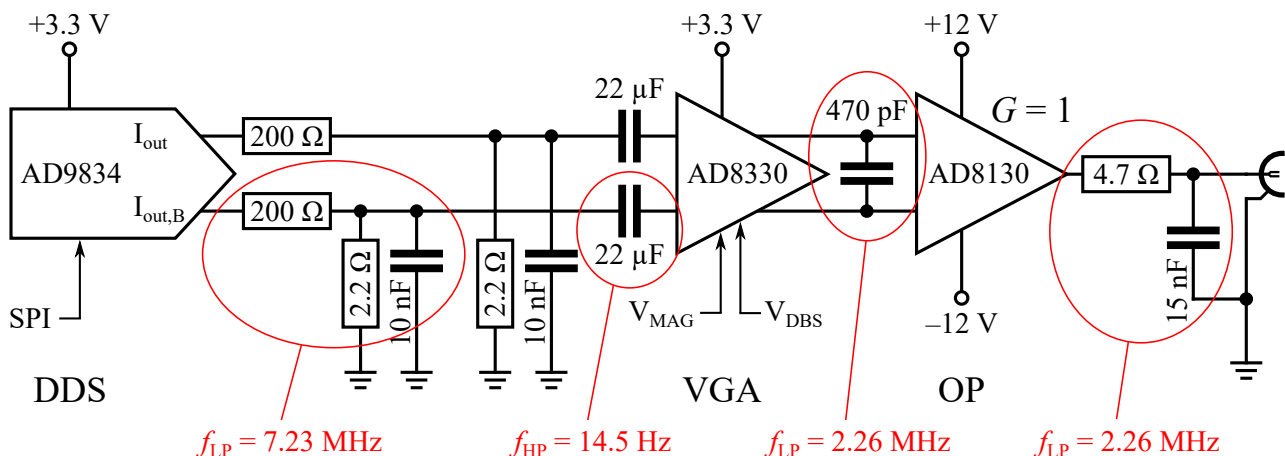


**Figure 5.9** Schematic of the signal generator with ‘AD9834’, ‘AD8330’ and ‘AD8310’

The circuit also contains the supply voltages and some necessary capacitors for filtering purposes. In total, there are three first order low pass filters (LP) and one first order highpass filter (HP). The frequencies given in the figure correspond to the  $-3\ \text{dB}$  points of each filter. The first low pass right behind the ‘AD9834’ prevents a feedthrough of the  $50\ \text{MHz}$  clock that is used for generating the DDS frequency. The following  $22\ \mu\text{F}$  capacitors are required by the ‘AD8330’ in order to couple the different voltage levels. Its impact on the lowest desired frequency of  $50\ \text{Hz}$  is small, accounting to a 4 % decrease in amplitude. The two remaining low passes limit the bandwidth of the device to around  $2.3\ \text{MHz}$ , therefore effectively eliminating high frequency noise. Their combined attenuation of a signal with the maximum desired frequency of  $500\ \text{kHz}$  accounts to  $0.42\ \text{dB}$  or 4.7 %.

### 5.2.3 Circuit and Board Design

Since the analog output section is fully specified, the remaining auxiliary devices and necessary signals for a functional waveform generator are chosen and the board layout is designed. While the ‘AD9834’ is controlled in the digital domain via SPI bus, the ‘AD8330’ requires two analog voltages provided to its input pins  $V_{mag}$  and  $V_{dbs}$ . Therefore, an additional low-noise DAC, type ‘LTC2632’, which is also controlled via SPI, is located close to the amplifier. It achieves a voltage step size of 0.61 mV, which corresponds to an output current resolution of 0.02 dB.

In order to operate the SPI bus, a microcontroller is necessary serving as information hub. It has to handle the commands from the host computer, evaluate them and put them on the bus. Due to thorough experience with the ‘ATmega’ series from *Microchip Technology Inc.*, the device ‘ATmega168’ was chosen. It is an 8-bit microcontroller with sufficient speed and connectivity for this application. However, as it does not natively support the USB bus, the widely known ‘FT232’ IC from *FTDI* was used as interface between the microcontroller’s serial port and the bus.

The final version of the PCB is depicted in Fig. 5.10. The intermediate improvements primarily concerned the selection of the VGA as stated in subsection 5.2.1. In the recent versions, the power source was changed from USB to the external  $\pm 15$  V supply and more low-dropout (LDO) regulators were added. The analog and the digital parts are now supplied individually in order to prevent noise degradation of the analog signals. At the bottom edge of the board, there are two SMA connectors to be able to simultaneously output the signal to the current source and to an oscilloscope for evaluation.

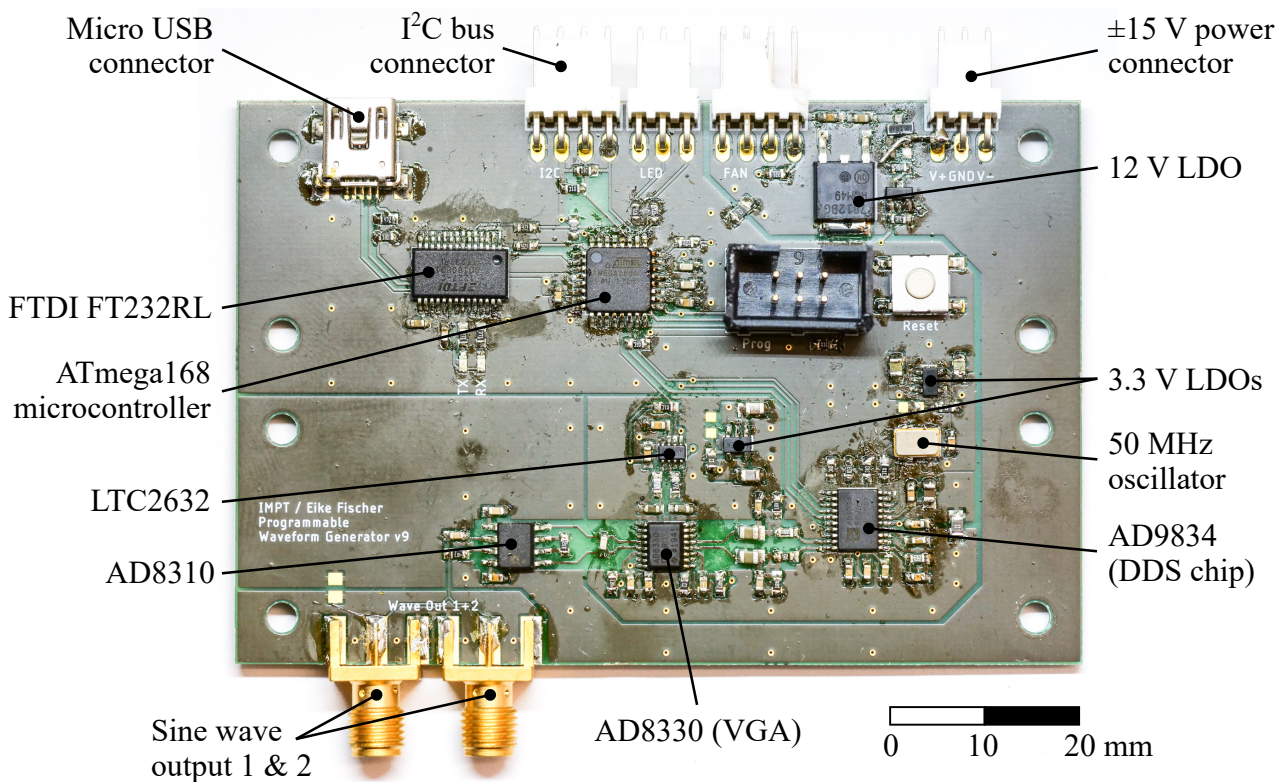


**Figure 5.10** Picture of the final version of the programmable waveform generator

### 5.3 Data Acquisition Device

With the two mandatory PCBs for generating a sinusoidal current for the primary coil of the measuring head being built and evaluated, it is necessary to deal with the acquisition of the input signals next. The voltages from the magnetoresistive sensors and the induction coil have to be amplified and integrated in the latter case. However, in order to set the necessary gain and select the right amplifiers, the DAQ device should be chosen first. This is because at the desired application frequency of up to the three-digit kilohertz range, its internal ADCs will most probably restrict the measurement accuracy due to their limited speed and resolution. As for the DACs in the DDS device, these properties are again in conflict with each other and the right combination should be chosen carefully. Common resolutions among ADCs are e.g. 24 bit at 5 kS/s, 16 bit at 5 MS/s or 8 bit at 5 GS/s. The higher extreme of 24 bit is considered unsuitable, since the corresponding speed would result in only 100 measured values during a period even at the lowest frequency of 50 Hz. From the other point of view, a useful minimum amount of readings should be 1000, which requires a sampling speed of 50 kS/s. The same applies to the voltage: the distinction of 1024 levels, corresponding to a resolution of 10 bit, seems a useful minimum. Subsequently, the specifications of some devices from *National Instruments* that fit these requirements are gathered in Table 5.2. All of them have four channels with an input impedance of 1 M $\Omega$  and feature simultaneous sampling.

**Table 5.2** Specifications of different DAQ devices from *National Instruments*

Device	NI 9223	NI 9775	PXIe-5172	PXIe-5160
Price (excl. VAT)	2,500 EUR	3,200 EUR	14,000 EUR	20,700 EUR
Input voltage range	$\pm 10$ V	$\pm 10$ V	multiple	multiple
Measurement speed	1 MS/s	20 MS/s	250 MS/s	1250 MS/s
ADC resolution	16 bit	14 bit	14 bit	10 bit
Signal-to-noise ratio	84 dB	68 dB	75 dB	57 dB

The first two devices ‘NI 9223’ and ‘NI 9775’ are part of the ‘C Series’, that is characterized by its portable and compact design. The latter two on the other hand belong to the professional ‘PXI’ series. All of them require a chassis to be fit in, which, however, is much more expensive for the ‘PXI’ series. Due to these costs, only the compact series came into question. From these two, the ‘NI 9223’ offers a 2 bit higher resolution but is 20 times slower in speed. Eventually, the ‘NI 9775’ represents the best compromise, achieving 1000 readings per measurement up to frequencies of 20 kHz and still 100 at 200 kHz. On the downside, it has a quite low signal-to-noise ratio, which decreases the resolution to effectively 12 bit. Another general drawback of the devices of the ‘C Series’ is the high input voltage range of  $\pm 10$  V, which requires a high slew rate of the connected amplifiers in order to fully utilize the range. If only a range of  $\pm 5$  V is used for example, one bit of resolution is lost.

## 5.4 Amplification Circuit for the Magnetoresistive Sensor Array

The input range of the DAQ device limits the choice of suitable amplifiers as they have to be supplied with at least  $\pm 12$  V to be able to drive the output within a range of  $\pm 10$  V leaving a headroom of 2 V. Most modern instrumental amplifiers, however, are low voltage types with a single-supply of 5 V or less and would have to be combined with an additional OP [Kitchin and Counts, 2006, p. 5-1].

An instrumentation amplifier is different from a normal OP as it includes three amplifiers as shown in Fig. 5.11. Two of them are working as buffer amplifiers for the inputs resulting in a very high input impedance. Therefore, these devices are perfectly suitable for measuring voltages from sensors with high source resistances like MTJ sensors, which is about  $30 \text{ k}\Omega$  in case of the ‘CT100’ used (Table 4.3). As illustrated, the third amplifier is wired as a classical subtractor, therefore amplifying the voltage difference between its inputs while common-mode signals are rejected. The gain can be set accordingly by varying the ratio  $R_F/R_2$ . However, this would require two resistors provided by the user and the inevitable variations between them would counteract the achievable precision. Hence, the key feature of the design in Fig. 5.11 is the possibility to set the gain with a single external resistor  $R_G$ . Eventually, the output voltage  $U_{\text{out}}$  accounts to

$$U_{\text{out}} = (U_{\text{in}+} - U_{\text{in}-}) \cdot \left(1 + \frac{2R_1}{R_G}\right) \cdot \frac{R_F}{R_2} + U_{\text{ref}}. \quad (5.5)$$

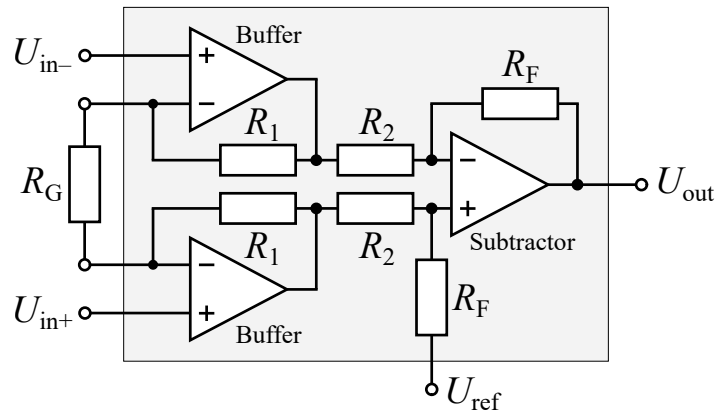


**Figure 5.11** Schematic of the internal structure of an instrumentation amplifier

Since the amplifiers and all resistors except  $R_G$  are integrated on the same chip, there is a high conformity between the OPs and all elements are thermally coupled. Therefore, instrumentation amplifiers are suitable for high gains with the accompanied advantage of very high common-mode rejection. They are optimized for acquiring signals in the millivolt or even microvolt range superimposed by a DC or AC voltage several magnitudes higher and offer high precision and low noise. On the downside, they are usually quite slow and in frequency compensated devices, an increased gain antiproportionally reduces the bandwidth. A current feedback mechanism on the other hand, increases the GBP at higher gains at the cost of a higher input current [Kitchin and Counts, 2006, p. 3-2].

### 5.4.1 Amplifier Selection

Subsequently, in order to select the appropriate amplifier for the magnetic field sensor array, the necessary gain for the used ‘CT100’ was calculated. According to the data sheet, it has a sensitivity of  $S_{CT100} = 2.85 \cdot 10^{-5}$  V/A/m at a supply voltage of 5 V [Cro, 2020]. Within the desired range of  $\pm 2.5$  kA/m, its amplitude therefore accounts to  $\pm 71.25$  mV. To fully utilize the  $\pm 10$  V input range of the selected DAQ, a gain of 100 fits well, leaving some margin for higher fields that may occur. Amplifiers offering a sufficient bandwidth at this gain necessarily incorporate the current feedback technique. The top picks that met these requirements are the type ‘AD8421’ from *Analog Devices* and ‘INA849’ from *Texas Instruments*, whose properties are listed in Table 5.3

**Table 5.3** Electrical characteristics of the instrumental amplifiers ‘AD8421’ from *Analog Devices* and ‘INA849’ from *Texas Instruments* at a gain of 100

Property	Unit	AD8421	INA849
Market introduction		May 2012	November 2020
Supply voltage range	[V]	$\pm 4$ to $\pm 18$	$\pm 2.5$ to $\pm 18$
Input offset voltage (max.)	[ $\mu$ V]	60	35
Input bias current (max.)	[nA]	2	20
Slew rate	[V/ $\mu$ s]	35	35
Bandwidth ( $-3$ dB)	[MHz]	2	8
Settling time to 0.01 %	[ $\mu$ s]	0.6	0.6
Input voltage noise @ 1 kHz	[nV/ $\sqrt{\text{Hz}}$ ]	3.5	2
Input current noise @ 1 kHz	[pA/ $\sqrt{\text{Hz}}$ ]	0.2	0.8
Common-mode rejection ratio @ 100 kHz	[dB]	100	107

The amplifiers hardly differ from each other as both achieve similar speed and common-mode rejection ratio (CMRR). However, the noise will be considered in more detail as the high bridge resistance of the ‘CT100’ causes the current noise to be more important than the voltage noise and it is four times higher in the ‘INA849’. It consists of three types: voltage noise, current noise and Johnson noise arising in every resistor due to thermal effects. All noise components are calculated for both amplifiers in connection with the ‘CT100’ and summarized in Table 5.4.

**Table 5.4** Arising noise for the ‘CT100’ sensor in combination with the amplifiers ‘AD8421’ and ‘INA849’ at a frequency of 1 kHz

Noise Component	Equation	Unit	AD8421	INA849
Voltage noise density	$e_n$	[nV/ $\sqrt{\text{Hz}}$ ]	3.5	2.0
Current noise density	$i_n \cdot R$	[nV/ $\sqrt{\text{Hz}}$ ]	6.0	24.0
Johnson noise density	$\sqrt{4k_B T R}$	[nV/ $\sqrt{\text{Hz}}$ ]	22.3	22.3
Combined noise density	$e_t = \sqrt{e_n^2 + (i_n R)^2 + 4k_B T R}$	[nV/ $\sqrt{\text{Hz}}$ ]	23.3	32.8
Output noise	$e_t \cdot \sqrt{f} \cdot G$	[mV <sub>RMS</sub> ]	3.3	4.6
Field strength equivalent	$e_t \cdot \sqrt{f} \cdot S_{CT100}^{-1}$	[A/m <sub>RMS</sub> ]	1.16	1.63

Apparently, the noise is dominated by the Johnson component ( $T = 300 \text{ K}$ ) that exceeds the voltage noise by one magnitude in both amplifiers. However, the combined noise for the 'INA849' is 50 % higher compared to the 'AD8421', which benefits from its lower current noise density. In terms of output amplitude, it accounts to 4.6 and 3.3  $\text{mV}_{\text{RMS}}$  respectively, calculated for a bandwidth of 2 MHz. As the voltage noise of the ADC of the 'NI 9775' accounts to 2.8  $\text{mV}_{\text{RMS}}$ , it suits the sensor noise and emphasizes the choice of the DAQ since a higher resolution would not further improve the measurement accuracy. Eventually, the resulting field strength noise will be about  $\pm 1.2 \text{ A/m}_{\text{RMS}}$  regardless of the chosen amplifier. The decision for the 'AD8421' is ultimately justified only by availability.

### 5.4.2 Circuit Design

Regarding the design of the whole circuit, it must be considered that there are a total of eight sensors in the array in order to provide information about the course of the field strength over the y-axis, which is illustrated in Fig. 4.7a. Depending on the applied field strength, the region that passes the flux varies. The array therefore provides the possibility to calculate this region by interpolating the field strength of the eight sensors. However, it is not necessary to acquire the signals of the all the sensors at the same time, since the signal is periodical and the measurement takes only a fraction of a second allowing to read out the sensors one after another. This consideration led to using an analog input multiplexer (mux), that allows the switching between the sensors. This way, only one instrumental amplifier is necessary and only one of the inputs of the DAQ device is used. Multiplexers are based on CMOS switches, that hardly alter the signal and have a flat frequency response up to the higher megahertz range. Therefore, the selection of a suitable device is not crucial and a possible one is the 'MAX4559' from *Maxim Integrated*. It offers eight input channels switched in pairs, necessary for the differential measurement of the full bridge, integrated in the 'CT100' sensors. At a supply voltage of 3.3 V, the on-resistance of the multiplexer accounts to 180  $\Omega$ , which makes 360  $\Omega$  for two channels. That increases the resistance seen by the amplifier only by about 1 % compared to the sole bridge resistance and the influence on the noise is negligible. The resulting signal path from the sensor to the amplifier is depicted in Fig. 5.12.

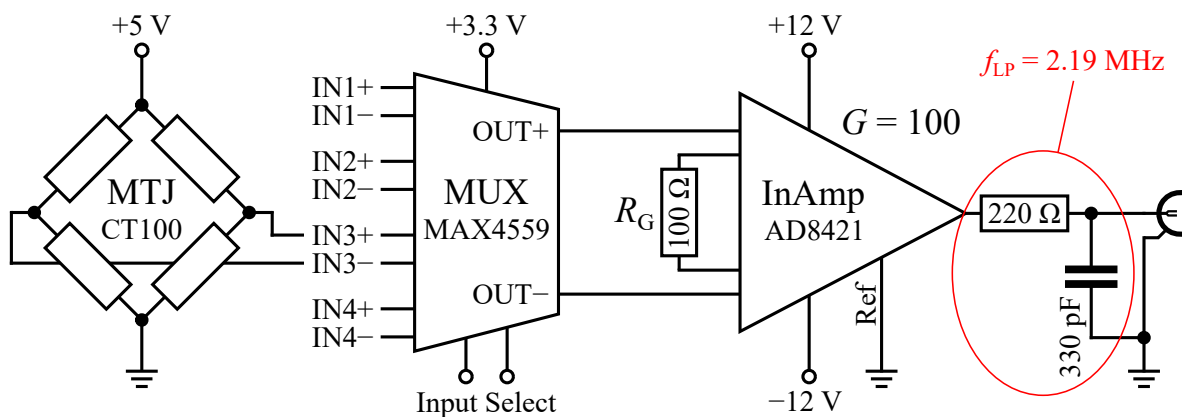


**Figure 5.12** Schematic of the signal path from the MR sensor to the amplifier (only one sensor shown)



As shown, the instrumental amplifier ‘AD8421’ is supplied with  $\pm 12$  V, though it could also be run at  $\pm 15$  V, a voltage already available from the shared power supply. However, measurements have shown that the output signal of the amplifier was heavily distorted at high field strengths. This issue could be attributed to the high current drawn by the current source, which apparently causes voltage drops high enough to influence the operation of the amplifier. By connecting the measurement circuit to a different power supply, the signal degradation disappeared. The same result could be achieved by generating a reduced  $\pm 12$  V with the help of low noise LDOs with a high power supply rejection ratio (PSRR) of more than 75 dB up to frequencies of 1 MHz. The input selection pins of the multiplexer are addressed via I<sup>2</sup>C bus using a so called general purpose input output (GPIO) extender providing eight remote input/output pins. Eventually, there will be two identical circuits like the one shown in Fig. 5.12 in order to read out all the eight sensors using two inputs of the ‘NI 9775’.

## 5.5 Amplification Circuit for the Induction Coil

A third input of the DAQ device is used for acquiring the signal of the induction coil, which will be considered in terms of amplitude and noise. Its signal is significantly different from the MR sensors as it does not correspond to the momentary flux but to its gradient. This causes two difficulties, since the signal requires integration and linearly increases with frequency as shown in the frequency response chart in Fig. 2.20. In order to calculate the frequency response of the induction coil, that is wound around the customized core as depicted in Fig. 4.8a, the equations from subsection 2.4.1 are utilized. Based on the core cross section of  $A = 24 \text{ mm}^2$  and a winding with  $n = 10$  turns, the absolute sensitivity is given in Eq. 5.6. The peak induction voltage per unit flux density is acquired by multiplying the sensitivity and the frequency, which eventually leads to the graph in Fig. 5.13.

$$S_a = 2\pi \cdot n \cdot A = 1.51 \cdot 10^{-3} \text{ m}^2. \quad (5.6)$$

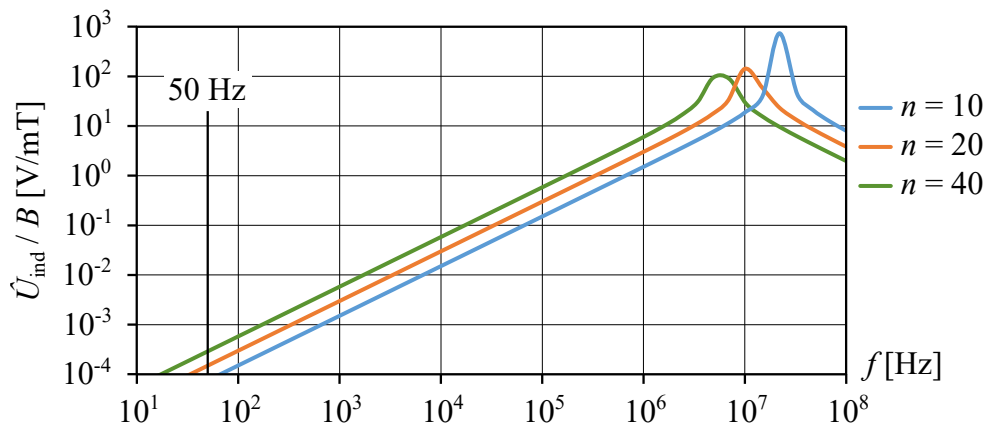


**Figure 5.13** Calculated frequency response of the peak induction voltage  $\hat{U}_{ind}$  per unit flux density in the B-coil of the customized core for different numbers of turns

Due to the linear correlation, the curve is perfectly straight up to the resonance peak at about 20 MHz, which results from the winding's inductance and capacity and causes the signal to decrease at higher frequencies. While the inductance value was taken from the measurement shown in Fig. 4.10, the capacity was estimated to be 10 pF, originating mainly from the 10 cm long feed line. For comparison, the graph also contains curves for windings with  $n = 20$  and  $n = 40$  turns, that consequently have a two or four times higher sensitivity respectively. Since the inductance and the capacity increase as well, the resonance peak occurs at lower frequencies. However, it is still far away from the desired measurement range.

The graph illustrates the arising difficulties when using an induction coil over a wide frequency spectrum as the amplitude of the induced voltage covers the same range. As discussed in subsection 2.4.1, there is an ongoing debate on how to deal best with the signal of an induction coil. Analog filters obtain the necessary integration in order to convert the measured gradient of the flux density to its absolute value with the side effect of achieving a flat frequency response that can be easily fed into an ADC. However, this method is known to produce certain errors, which are generally avoided by using digital integration. On the downside, the ADC would have to deal with an input signal that varies by a factor of up to 10,000 in strength (calculating with a maximum frequency of 500 kHz), which would require a ADC resolution of at least 16 bit. Another option would be to set up an amplifier circuit with different gains and choose it according to the frequency. Due to the associated lower effort, an analog integrator will be considered first to be able to evaluate its performance.

### 5.5.1 Analog Integration

Tumanski reviewed the findings in analog integrator design for induction coils. Though originally formulated for the use with air coils to measure the field strength, these also apply to coils wound around ferromagnetic materials. Accordingly, the easiest way to achieve the integration of the signal is the method of 'self-integration', which only requires a resistor placed across the output terminals of the coil. The inductance of the coil and the combined resistance of the wire and the additional resistor  $R_L$  subsequently form a low pass filter [Tumanski, 2007]. However, due to the low inductance of the B-coil used in this work, the effect is limited to high frequencies as Fig. 5.14 demonstrates.

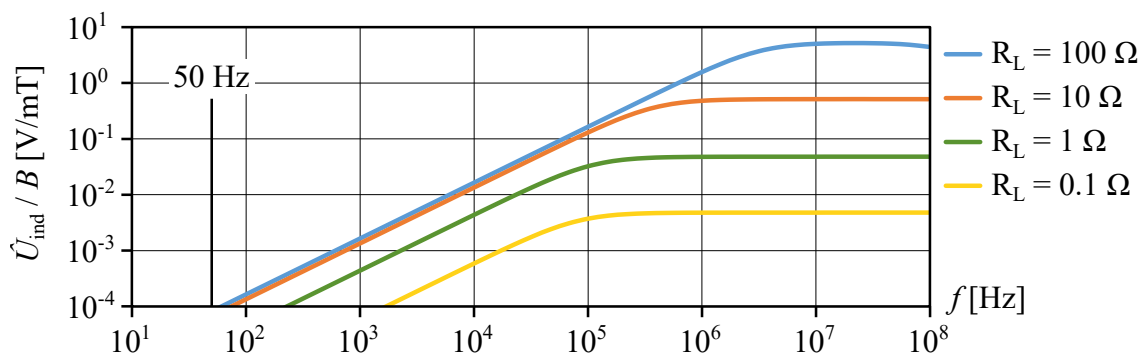


**Figure 5.14** Calculated induced voltage in the B-coil with  $n = 10$  turns loaded with different resistors  $R_L$

Apparently, resistor values of below  $10\ \Omega$  do not significantly increase the filter range but strongly reduce the amplitude in the whole bandwidth, which is not desirable. By choosing a value of  $10\ \Omega$ , the frequency  $f_{SI}$ , above which a ‘self-integration’ is achieved, accounts to

$$f_{SI} = \frac{R_{Cu} + R_L}{2\pi L} = 382\ \text{kHz} \quad (5.7)$$

This represents rather the higher end of the intended measurement range. To enable signal integration below this frequency, the load resistor is combined with a passive integrator, consisting of a resistor  $R_S$  in series and a capacitor  $C_P$  in parallel. It resembles a low pass filter, with the only difference that the operation is intended above its cutoff frequency and therefore must be chosen smaller than  $f_{SI}$ . A necessary adaption of the filter is the insertion of a resistor  $R_P$  in series with the capacitor, in order to cancel the filter’s effect above  $f_{SI}$ . The ‘self-integrator’ and the passive integrator ideally merge by fulfilling the equation  $R_P \cdot C_P = L/R_L$  [Pettinga and Siersema, 1983].

Due to the nature of passive filters, they are only capable of decreasing the strength of the incoming signal and the lower the cutoff frequency  $f_{PI}$  of the passive integrator is chosen, the higher is its attenuation and the lower is the output amplitude. At  $f_{PI} = 100\ \text{Hz}$  for example, the peak output is decreased to about  $0.1\ \text{mV/mT}$ , which would drastically degrade the SNR. Therefore, the passive integrator works in an intermediate range and merges into another, active integrator that takes care of the lowest part of the intended measurement range. It is based on an OP that features a capacitor  $C_F$  in the feedback chain. Eventually, the final filter circuit was composed as shown in Fig. 5.15.

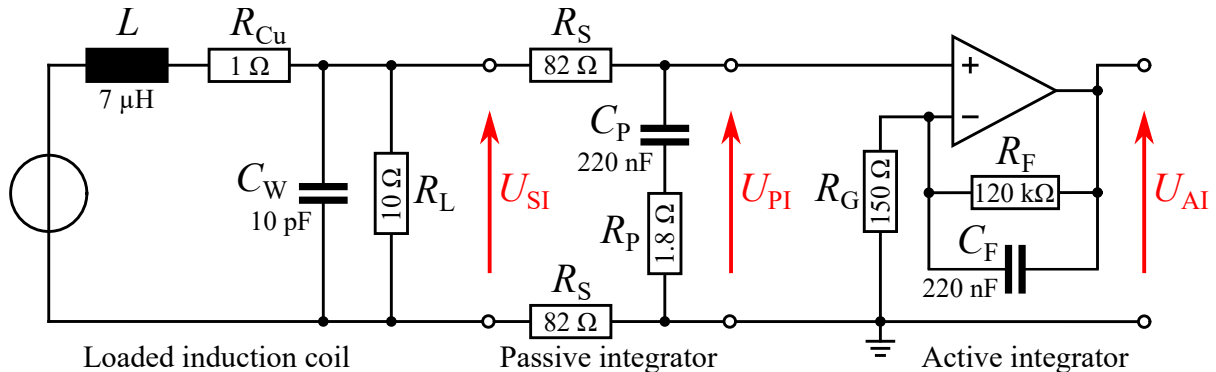


**Figure 5.15** Schematic of the loaded induction coil connected to successive integrators

The design is also set up in LTspice, a software used to simulate electric circuits. The indicated voltages behind the coil  $U_{SI}$ , behind the passive integrator  $U_{PI}$  and behind the active integrator  $U_{AI}$  have been calculated and are shown in the graph in Fig. 5.16. The individual application spectrum of the different filters can be well recognized and the resulting output voltage  $U_{AI}$  is absolutely level in the range from about  $30\ \text{Hz}$  to  $3\ \text{MHz}$ . However, the course of the phase shift reveals that the output reaches the necessary  $90^\circ$  firstly at  $1\ \text{kHz}$ . In order to move this point to lower frequencies, the active integrator would have to be adapted. Apart from that, there is a deviation of the phase shift above  $1\ \text{kHz}$ , which is a weakness of the composite filter design as they do not perfectly merge. Eventually, the phase shift drops rapidly above  $50\ \text{kHz}$ , which stems from the limited speed of the amplifier.

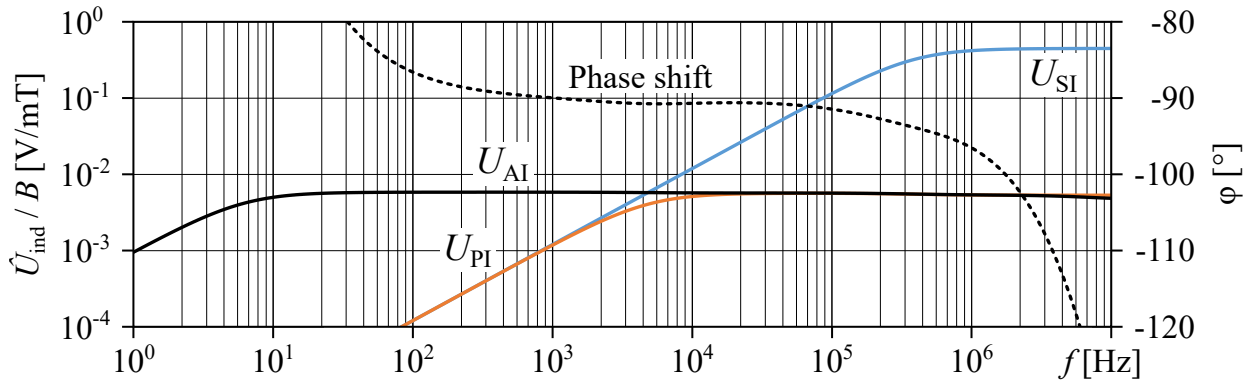


**Figure 5.16** Resulting amplitudes and phase shift of the analog filter circuit connected to the loaded induction coil (calculated with LTspice)

In section 4.2, it was pointed out that a phase error between the signals for  $H$  and  $B$  of one degree is expected to be critical. Therefore, the computed deviation in Fig. 5.16 has to be regarded as a serious issue even if it accounts only to a few degrees at certain frequencies. This is especially true, when keeping in mind that the simulation software assumes perfect components but capacitors have an uncertainty of  $\pm 5\%$ . The only solution would be to solely employ a passive integrator since this not only avoids the merging error between multiple filters but also the falling phase shift occurring at increasing frequencies. Even though, this will inevitable result in a very low signal amplitude and the phase shift at lowest frequencies cannot be overcome, a corresponding circuit was set up and tested. The results are shown in Fig. 5.17a, which contains the measured phase shift of the different integrators. Apart from the two analog designs, the results from a digital integration performed within LabVIEW are shown for comparison. To demonstrate the effect of an undesired phase shift, Fig. 5.17b shows the resulting apparent coercivity. The error of  $H_c$  depends also on the maximum applied field and becomes larger, the higher the amplitude is chosen.

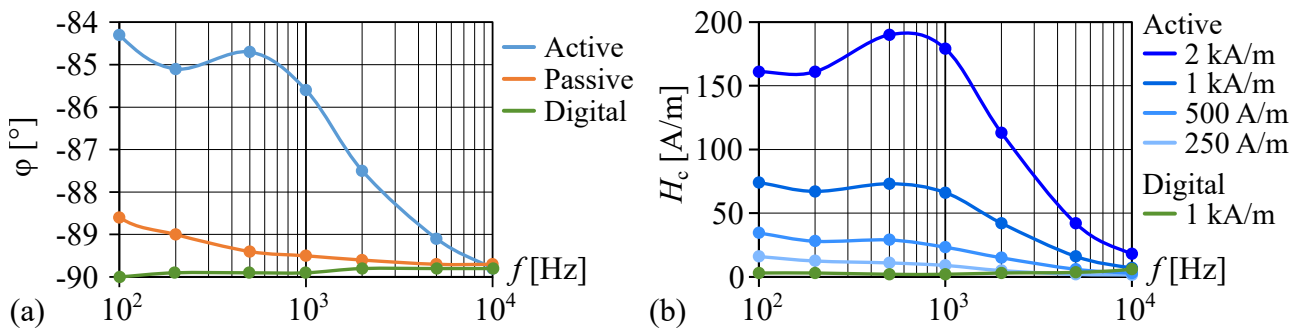


**Figure 5.17** Measured phase shift (a) and resulting apparent coercivity  $H_c$  at multiple measurement ranges (b) for different types of integration that were evaluated

The measurements demonstrate the importance of a correct phase shift of  $-90^\circ$  achieved by the integrator since a deviation of only one degree corresponds already to an error of almost 50 A/m in a measurement range of 2 kA/m or to 20 A/m in a measurement range of 1 kA/m. They also reveal that the active integrator circuit features an even higher phase shift than computed and in consequence that

it is not applicable at frequencies below 10 kHz. The analog circuit, which only contains a passive integrator shows better results. However, due to the strong attenuation of the signal, a successive amplification in two stages with a combined gain of 40,000 (92 dB) is necessary and the occurring noise is not tolerable. In conclusion, the superiority of digital integration is clearly recognizable by the measured phase shift of below  $0.2^\circ$ , which lies within the range of measurement uncertainty. Therefore, a digital integration was considered as the better concept for this application. Furthermore, the effect of the phase shift on the apparent coercivity underlines the importance of using amplifiers that alter the phase as little as possible. Consequently, a value of about  $0.2^\circ$  is regarded as maximum tolerable deviation, which at higher frequencies can only be achieved by high speed OPs.

### 5.5.2 Digital Integration

The integration process in the digital domain is performed by software by sampling the input signal at a desired frequency, multiplying it with the time difference between two measurements and eventually summing up the values. As the output amplitude of the coil depends on the excitation frequency, this principle works well in a small range only as otherwise the signal's amplitude becomes too weak or too strong exceeding the capabilities of the analog-digital converter. To allow the usage over a wide frequency range, the induction coil signal has to be amplified or attenuated by a suitable circuit. A solution approach is to use an amplifier with variable gain as it is also employed in the programmable waveform generator. Using again the 'AD8330', a maximum amplification range of 60 dB can be achieved with the help of its linear gain interface. The device features a high bandwidth of 180 MHz at all gains with the result that the phase shift will be minimal in the desired measurement range. However, there are certain disadvantages of the 'AD8330', that have to be considered. Since its gain is set by an analog signal, a small error is caused by possible inaccuracies of this voltage. Furthermore, the impact of the current input interface of the amplifier incorporates a load resistance of 1 k $\Omega$  causing a phase shift of  $0.2^\circ$  at 78 kHz resulting from self-integration of the coil. Due to the internal structure of the device, it is not trivial to adapt the input interface in order to increase the maximum frequency and other amplifiers are possibly more suitable [Ana, 2016, p. 21].

Eventually, the choice fell on the 'AD8253' from *Analog Devices*, which features a digital interface that allows the selection of a gain between 0 and 60 dB in 20 dB steps. This results in the same attenuation range the 'AD8330' offers but with more precise although much coarser gain settings. Another advantage of the 'AD8253' is its wider input and output voltage, which accounts to  $\pm 10$  V at a  $\pm 12$  V supply while the VGA is limited to input voltages of  $\pm 1.5$  V. On the downside, it is much slower than the 'AD8330' with further decreasing speed at higher gains. To evaluate this limitation, the occurring phase shift at all gains of the device were simulated with LTSpice and are shown in Fig. 5.18. As expected the phase shift is larger for high gains where the speed is lower and becomes smaller at lower gains. This represents the typical behavior of a voltage feedback system with a constant GBP. For comparison, the direct measurement of the voltage at the coil with a load resistor of 5 k $\Omega$  is shown as well. As for a gain setting of 0 dB of the amplifier, it yields no amplification. However, since it avoids the speed limitation of the amplifier, it offers an at least 20 times lower phase shift.

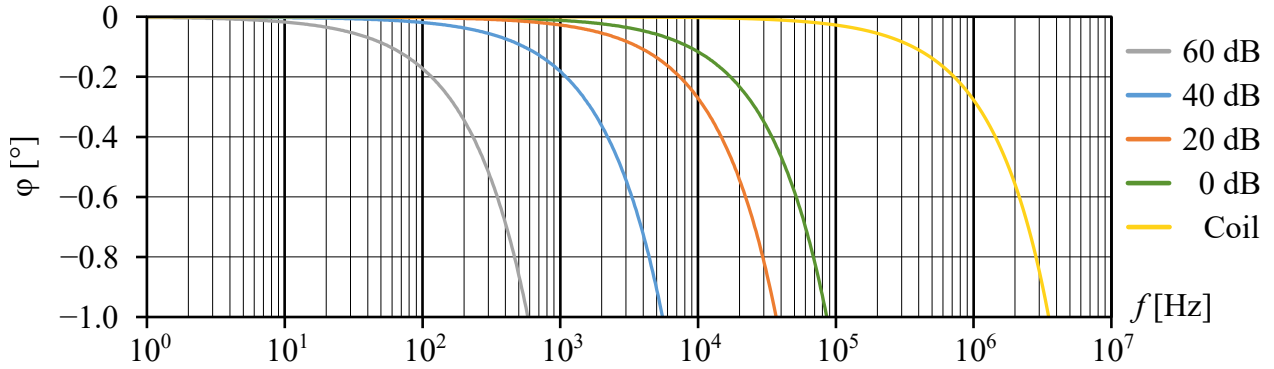


**Figure 5.18** Calculated phase shift at different gains set for the ‘AD8253’

To face the low speed of the ‘AD8253’ at high gains, a two-stage amplification circuit was designed, which is depicted in Fig. 5.19. The high speed amplifier ‘AD8129’, which is the sister device of the ‘AD8130’, suitable for higher gains, is placed in front of the ‘AD8253’. This way, lower gains can be selected but in total the same amplification is achieved. As depicted, the circuit also comprises a multiplexer, which allows the bypassing of the ‘AD8253’. Therefore, the additionally inserted ‘AD8130’ set to a gain of 10 dB or the ‘AD8129’ set to a gain of 30 dB can be connected directly to the input of the DAQ. If eventually the chosen gains are too high, they can easily be adapted. If a higher gain is necessary, however, the ‘AD8253’ allows a further increase by up to 60 dB. The benefit of the circuit is the exceptional high CMRR of the ‘AD8130’ and ‘AD8129’.

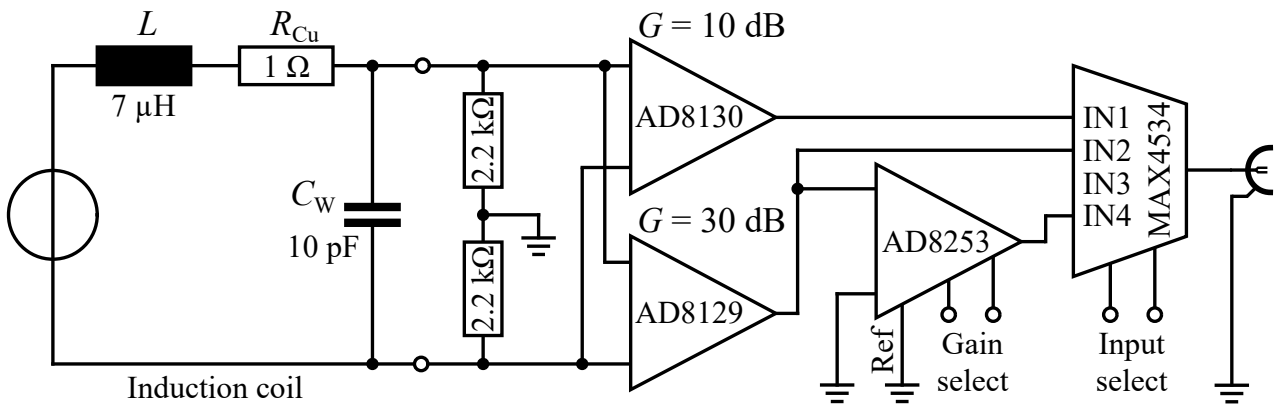


**Figure 5.19** Amplification circuit with different gains realized with two stages and a multiplexer

## 6 Software

With hardware and electronics being designed and tested, the only remaining step towards a complete system is the development of the software, which is necessary to bring all the functional parts and the user together. In order to operate the measurement head and record the desired data, LabVIEW was used. It is a software designed for data acquisition and control of many kinds of electronic devices. It is capable of handling I/O ports and protocols of a computer and working with data files on the harddrive. In contrast to most programming environments, LabVIEW features a graphical interface rather than a text input for source code. This way, a so called virtual instrument (VI) is created by choosing different building blocks from a toolbox, all representing a specific function. Similar to other programming languages, these functions have inputs and outputs, which can be anything from a single boolean value to a complex data stream of double-precision floats, an error code or an I/O configuration structure. To establish a data transfer between the different functions, they are simply connected by lines, whose color indicates the type of data. The setup of this 'block diagram' defines how the VI will work eventually and is usually hidden from the user. Therefore, there is a second window, the 'front panel', which serves as a graphical user interface (GUI). It can be freely designed with controls, selectors, data tables, graphs and so on that have their representative in the 'block diagram', to which they are linked.

The realized VI has two functions: It is necessary to establish a data connection with the programmable waveform generator, whose microcontroller is the information hub of the whole measurement electronics (see Fig. 5.1). Therefore, all relevant configurations like the frequency and amplitude setting or the selection of one of the eight magnetoresistive sensors have to be passed from LabVIEW to the controller. This communication is setup rather easily in LabVIEW by using the included serial interface functions and sending the desired commands in form of a short text to the output port. However, it requires the controller to deal with these texts by translating them to the appropriate electric signals. Both the realization in the VI and the setup of the microcontroller are described in section 6.1.

The second feature that the VI has to provide is the acquisition of the measurement data. This includes the control of the DAQ device, the sampling of the input voltages, the transfer of the data to the host computer and most importantly the subsequent processing and interpretation of this data in order to obtain a hysteresis loop. Therefore, algorithms were implemented that extract the hysteresis loop of the evaluated material from the flux measured within the ferrite core. These algorithms are presented and described in detail in section 6.2.

## 6.1 Configuration of the Electronics

The programmable waveform generator is accessed by the VI over a serial ‘RS-232’ interface, which is dating back to the 1960s. However, due to its simplicity and its native support by many microcontrollers, it is still very commonly used today for this kind of application. To work with a recent computer, all it requires is an interfacing chip like the ‘FT232’ from *FTDI*, which translates from a current USB bus to RS-232. This chip is employed on the PCB as shown in Fig. 5.10 and emulates a serial interface over USB that can be addressed by the VI like a real one located on the computer’s motherboard. The serial interface allows the exchange of short text messages (called strings) between the computer and the microcontroller at rather low speeds, which is why these strings are typically of short size.

The utilized 8-bit microcontroller ‘ATmega168’ from *Microchip Technology Inc.* is programmed in order to react on the string commands sent by the LabVIEW application. The corresponding source code was written in ‘C/C++’ language in their proprietary programming environment ‘Microchip Studio’. Like most 8-bit microcontrollers, the ‘ATmega168’ is simple in its use and the run program is structured in two parts. At startup, a configuration section is executed, which contains the commands to setup the integrated peripherals. As desired, specific pins are set as input or outputs and different hardware units like timers, counters, ADC’s, bus interfaces and so on are enabled. While this configuration is loaded just once, the actual task is processed in a continuous loop with the contained commands executed sequentially from beginning to end. Breaks from this loop are only possible by interrupts that generally have a higher priority and allow the instantaneous execution of a short section of code whereupon the controller continues at the point where it left the loop. Interrupts are hardware triggered events that have to be activated separately and vary from device to device. This way, microcontrollers can react in real time on e.g. incoming signals, a received data byte or a timer event.

For the present case, three interrupts were configured. The first one is executed whenever a byte is received via the serial interface, which is setup at a transfer rate of 38.4 kbit/s during startup. By setting a variable, the interrupt signals the main loop that data was received and that it has to handle the next bytes until the input string is complete. The second interrupt is triggered by a timer event occurring every two seconds and signals the controller to send diagnostic information to the computer. The third interrupt is triggered by the attached fan, whose tachometer generates a pulse on one of the microcontroller’s inputs. It increments a counter value used to calculate the rounds per minute.

Eventually, the main loop of the program is kept simple as it consists of only two conditions that are checked. The first one is met if the corresponding variable signals that there was a first data byte received via the serial interface. Subsequently, the whole serial input string is received and evaluated. Depending on its content, the controller sets the desired frequency, the desired output current at the primary coil or executes another command. The other condition is met every two seconds and makes the controller report the diagnostic information, which contains the speed of the fan and the temperature of the current output amplifier’s die. Therefore, the controller has to retrieve this data from the PCB of the current source that is connected via I<sup>2</sup>C bus. The corresponding (simplified) program flowchart is depicted in Fig. 6.1.



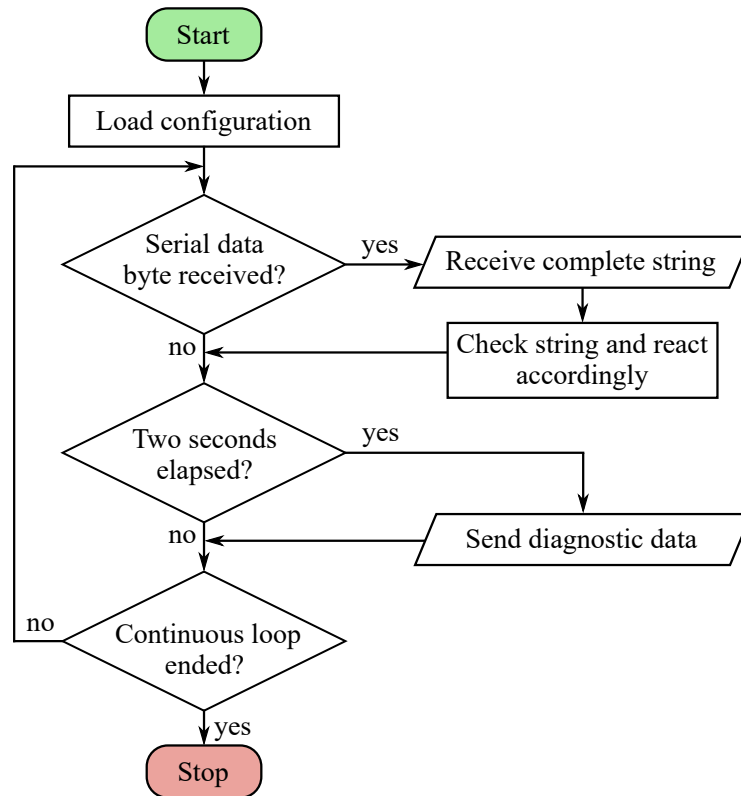


**Figure 6.1** Simplified program flowchart of the microcontroller on the PCB of the programmable waveform generator

The possible strings recognized by the microcontroller are listed in Table 6.1. They are distinguished by the first transmitted character, which in some cases is followed by a second register selection and end with a hexadecimal (hex) value of different length. Hex characters hold decimal values from 0 to 15 wherein the values from 10 to 15 are represented by the letters A to F. This data format is chosen as it can be handled by the microcontroller much faster than a decimal value. Two hex characters store the information of 8 bit, four are necessary for a 16 bit value and eight for 32 bit.

**Table 6.1** Structure of the command strings recognized by the microcontroller

Command	First char	Second char	Remaining number of hex chars
Set output amplitude	A		4 (12 bit DAC output)
Set output frequency	F	0/1 (frequency register)	8 (28 bit frequency value)
Set output phase	P	0/1 (phase register)	4 (12 bit phase offset)
Set fan speed	C		2 (8 bit PWM value)
Select amplifier state	S		2
Select MTJ sensor	H		2
Select B-coil gain	B		2

Like most 8-bit microcontrollers, the ‘ATmega168’ only employs a basic arithmetic logic unit and subsequently, e.g. the calculation with floating point values and even a division would require a signif-

ificant amount of clock cycles as these operations are not natively supported. Therefore, the necessary calculations and the following hex conversion are done on the host computer within the LabVIEW application and the final value is then sent to the microcontroller, which can directly forward it to the corresponding IC with lowest latency. For example, to set an output frequency of 1 kHz, an 28 bit binary value has to be written to the frequency register FREQREG of the DDS chip AD9834 via the SPI bus. The value is obtained by the equation given in the data sheet [Ana, 2014a, p. 20].

$$\text{FREQREG} = 1 \text{ kHz} \cdot \frac{2^{28}}{50 \text{ MHz}} \quad (6.1)$$

$$\text{FREQREG} = 5,368.71 \quad (6.2)$$

This value is truncated to 5,368, converted to the necessary 8 characters long hex value 0x000014F8 and then sent to the controller together with a preceding ‘F’ and ‘0’ to chose the frequency register 0 since the AD9834 has two frequency registers for further purposes. The controller converts each two hex characters to a byte and sends four consecutive bytes to the chip, which eventually outputs a sine wave with a frequency of 999.87 Hz. The small error results from the fact that only integer multiples of the lowest frequency can be set. It accounts to  $2^{28}/50 \text{ MHz} = 186.26 \text{ mHz}$ .

Similarly to the frequency, the calculation of the output amplitude is also done in LabVIEW and requires some more steps. To set a current of 0.5 A for example, the variable gain amplifier has to amplify the input voltage of 6.5 mV to  $\pm 1 \text{ V}$ , which corresponds to a gain of 43.74 dB. Since there is a fixed additional gain of 1.58 dB resulting from the linear gain interface (see subsection 5.2.2), the logarithmic gain interface has to provide an amplification of 42.16 dB. At a slope of 30 mV/dB, a voltage of 1.265 V has to be supplied to the  $V_{\text{dbs}}$  pin. The employed DAC has a resolution of 12 bit and a reference voltage of 2,500 mV. Hence, the output value transmitted to the DACB register is 2,072 as decimal or 0x818 as hex value. To summarize, the whole equation is as follows.

$$\text{DACB} = \left( \log \left( 0.5 \text{ A} \cdot \frac{2 \text{ V/A}}{6.5 \cdot 10^{-3} \text{ V}} \right) \cdot 20 \text{ dB} - 1.58 \text{ dB} \right) \cdot 30 \text{ mV/dB} \cdot \frac{2^{12}}{2,500 \text{ mV}} \quad (6.3)$$

$$\text{DACB} = 2,072.58 \approx 0x818 \quad (6.4)$$

Within LabVIEW, the above calculations and the subsequent serial transmission are triggered by an event case structure that is executed after a value change in a linked numeric control, which can e.g. be a text input box, a rotary knob or a slider. For each of the commands listed in Table 6.1, a control is created and handled by an associated case within that structure. Adjustable limitation on the input range of the controls ensure that only permitted values can be set and transmitted. Nonetheless, the microcontroller checks the incoming values for completeness and if they are within the boundaries to prevent unforeseen behavior.

## 6.2 Signal Processing Algorithms

After system startup and the setting of an output frequency and amplitude as just described, the only step left is the activation of the primary amplifier, which is in standby mode by default. After sending a switch-on command, it enters the operational state and creates a sinusoidal magnetic field in the ferrite core around which the primary coil is wound. The field is detected by the magnetoresistive sensors located between its poles and also in the B-coil, a low voltage is induced due to the small resulting flux in the open magnetic circuit. However, before the first measurements are made, there are different considerations on how to improve and correct the measured signals. Therefore, different algorithms were programmed in LabVIEW as shown in the signal chain in Fig. 6.2.

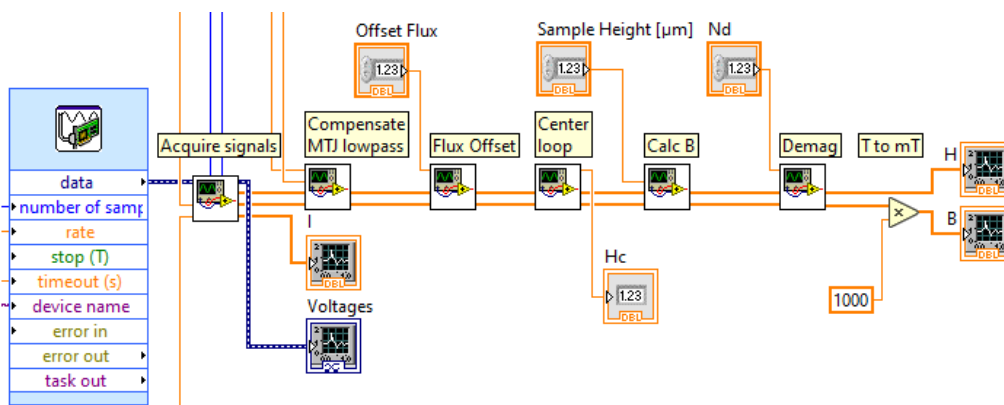


**Figure 6.2** Signal chain beginning with the data acquisition (blue box on the left), then passing multiple algorithms and leading to a graphical output of the course of  $H$  and  $B$  (icons on the right)

### 6.2.1 Signal Acquisition and Cycle Averaging

The signals flow from left to right: the blue box represents the configuration of the DAQ device regarding the measurement speed and the amount of samples taken. These values are calculated according to the chosen excitation frequency and the desired amount of samples per measurement. At by default selected 1,000 data points and an excitation of e.g. 100 Hz, the sampling speed accounts to 100 kHz. Due to the periodicity of the signal however, the amount of samples can be selected as a multiple of 1,000. This is what the first algorithm in the indicated 'acquire signals' subVI does. By default, 16 consecutive sine wave cycles are averaged, which effectively increases the SNR. Therefore, a total of 16,000 samples are recorded instead of only 1,000. After averaging, a possible voltage offset is corrected by summing up all values and subtracting their average from each individual value. This leads to a signal course that is symmetric to the x-axis, which is usually the case for hysteresis loops. Afterwards, the zero-crossing point of the field strength is found and all signals are rearranged in the form that the graphs always start at this point. This eliminates the 'jumping' of the graphs between consecutive hysteresis loop measurements that results from the asynchronous signal generation and

acquisition. Consequently, the reading would start randomly at any point along the sine wave. However, from the knowledge of the signal, it is possible to separate the readings at any point and append the samples before that point after the last one. Eventually, this procedure makes the reading of the time-based graphs much more comfortable to the eye but has essentially no effect on the shape of the hysteresis loop, since there is no information about the time stamp stored within the data pairs.

The final step of this first subVI is the conversion of the signals from voltages to the desired values of  $H$  and  $\Phi$ . Therefore, they are divided by the applied gain and inserted in the equations presented in the chapters before. Regarding the MTJ sensors, this means that the voltage has to be divided by the bridge supply voltage and the sensitivity given in Table 4.3.

$$H(t) = \frac{U_{\text{MTJ}}(t)}{5 \text{ V} \cdot 5.7 \cdot 10^{-6} \text{ m/A}} \quad (6.5)$$

For the calculation of the flux, Faraday's law given in Eq. 2.9 is the basis and accordingly, the induction voltage is integrated over time and subsequently divided by the amount of turns  $n$  (Eq. 6.6). The integration is achieved by an algorithm provided by LabVIEW, which only requires the acquisition time  $dt$  between two samples as additional input parameter. The output is not a single value but the time-dependent course of the integrated signal.

$$\Phi(t) = \frac{1}{n} \int U_{\text{ind}}(t) dt \quad (6.6)$$

Eventually, the 'acquire signals' subVI has four outputs at its right side. The dotted blue line is a complex signal including all the input voltages after averaging and voltage offset correction. It is used to display the input voltages and allows the user to check that no voltage clipping occurs. The three bold orange lines indicate the three output arrays  $H(t)$ ,  $\Phi(t)$  and  $I(t)$  (from top to bottom), each containing the user-selected amount of data points. Similarly as for the voltages, the current in the primary coil  $I$  is used for information purposes only and not of further interest for the calculation of the hysteresis loop. It is acquired by the current sense resistor located on the current source PCB.

### 6.2.2 Low Pass Compensation

Before any subsequent algorithm is applied, which manipulates the field strength or flux values in dependence of the other one (like a demagnetization field compensation, which depends on the flux density), the second subVI deals with the low pass filtering effect of the MTJ-based magnetic field sensor. As described in section 4.2, the effect is caused by the relatively high resistance of the sensor and the capacity of the cable between the sensor and the instrumentation amplifier. In the final measurement stand that will be presented in the next chapter, the resulting filter cutoff frequency was determined empirically as approximately 140 kHz. Accordingly, at higher excitation frequencies, the measured field strength includes both a significant amplitude and phase error. However, other than the flux density, which has an arbitrary shape, the signal of the field strength is sinusoidal and hence, it is possible to calculate and compensate these errors. The real amplitude of the signal is restored by

multiplying the field strength with the inverse of the calculated attenuation. This gain accounts to

$$G = \sqrt{\left(\frac{f}{140 \text{ kHz}}\right)^2 + 1}. \quad (6.7)$$

The correction of the phase error is realized by shifting the measurement value of the field strength in relation to the flux values. At 1,000 data points per sine wave for example, the phase difference between two samples accounts to  $360^\circ/1000 = 0.36^\circ$ . Hence, integer multiples  $N$  of this error can easily be compensated by reassigning the measured value of the flux density at  $t = x$  to the value of the field strength  $N$  samples later ( $t = x + N$ ). However, an algorithm was programmed that also allows for fractional phase shifts to be corrected by applying the method of linear interpolation. The final shift of  $R$  positions within the measured H-array is calculated as follows

$$R = \arctan\left(\frac{f}{140 \text{ kHz}}\right) \cdot \frac{1000}{2\pi}. \quad (6.8)$$

The resulting phase shift and attenuation at specific frequencies are listed in Table 6.2. It reveals that up to frequencies of 10 kHz, the attenuation is negligible as the error is well below 1 %. The phase shift on the other hand should already be considered at above 1 kHz. Fig. 6.3 visualizes the effect of the low pass compensation on the measurement results at different frequencies.

**Table 6.2** Resulting phase shift and attenuation at specific frequencies

Frequency	Attenuation	Phase shift	Array offset @ 1000 data point
1 kHz	25.6 ppm	$0.41^\circ$	$R = 1.14$
10 kHz	0.26 %	$4.09^\circ$	$R = 11.35$
100 kHz	18.7 %	$35.5^\circ$	$R = 98.72$

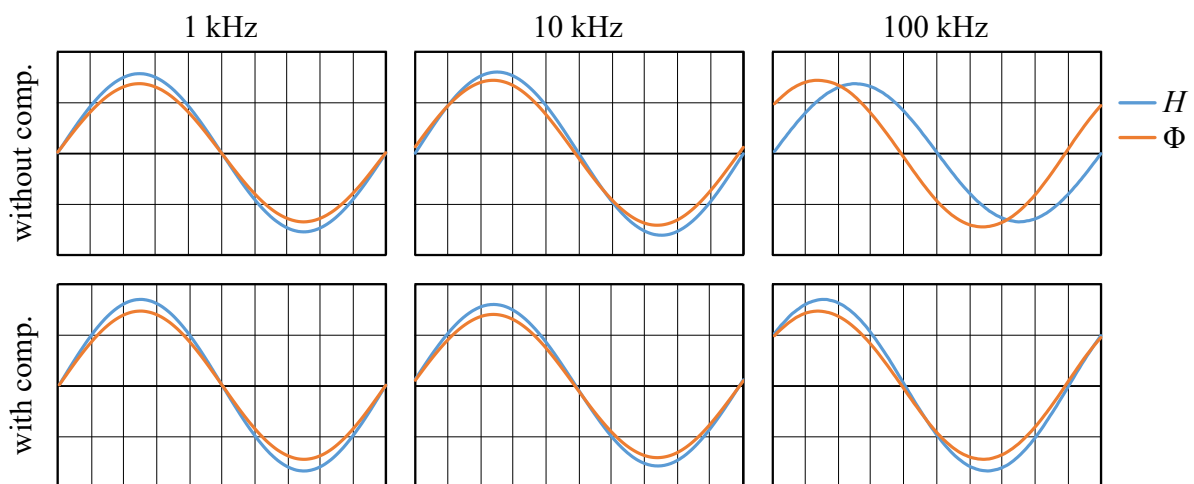


**Figure 6.3** Time-based qualitative measurement signals of  $H$  and  $\Phi$  with the low pass filter compensation disabled (top) and enabled (bottom)

### 6.2.3 Flux Offset

After low pass compensation the data arrays can be regarded as containing almost error-free measurement data, which is important to apply the subsequent algorithms that put both arrays in relation. This first one subtracts the offset flux from the measurement results. To understand the need for this step, it is important to once more point out the difference of this measuring method in comparison to the common ones. Both in the VSM and in the classical hysteresis loop tracer, the involved pickup coils measure only the flux that is flowing within the analyzed specimen. In this method however, the flux is measured at a different point in the closed magnetic circuit in order to avoid the need for a custom-made winding around the specimen with all the related drawbacks. Consequently, this method is based on the assumption that the flux in the analyzed material can be calculated from the flux at a different point in the same circuit. However, this requires some closer considerations: As illustrated by the flux lines in Fig. 4.6, the B-coil not only detects the flux passing the material at the lower end of the core but also the one traveling through the air. This becomes even more clear when looking at the magnetic equivalent circuit depicted in Fig. 4.2. Regardless if there is a material attached to the core (b) or not (a), there is always some offset flux. A B-coil position closer to the bottom tips of the core, however, decreases the measured offset flux. On the other hand, there is probably a large demagnetizing field at the tips of the core similar to the bar magnet whose flux density decreases at the ends as shown in Fig. 2.7. Conversely, this means that the offset flux can not be measured properly as the demagnetization is large when the circuit is open but small when it is closed by an attached ferromagnetic material. Moreover, the circuit changes from closed to open during the measurement as the material approaches the saturation region and therefore passes over to act like a non-magnetic material. In summary, the B-coil should be placed far away from the poles of the core. Although the offset flux is larger this way, the demagnetization should be small and negligible in all cases.

The graph in Fig. 6.4 shows the offset flux in relation to the field strength in the air gap measured by a B-coil with  $n = 10$  located right below the primary coil. The graph reveals a linear and more importantly, a hysteresis-free relationship between  $H$  and  $\Phi$ , that results from the small flux density occurring in the core, which is well below 10 mT and therefore sufficiently far away from the non-linear saturation region, which begins at around 350 mT for ferrite. Subsequently, this offset flux can simply be calculated by multiplying the measured field strength with the determined gradient of  $186 \cdot 10^{-12}$  Wb/A/m and afterwards be subtracted from the measured flux.

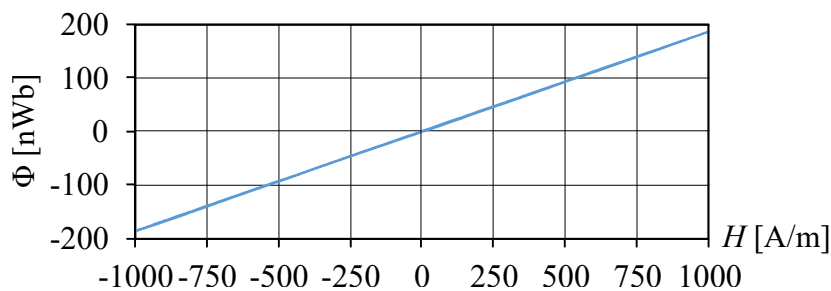


**Figure 6.4** Measured offset flux in the core at 100 Hz in the open magnetic circuit (no material attached)

### 6.2.4 Center Loop

As next step, the hysteresis loop is being centered along the vertical axis by finding both points at which the flux is zero in the measured  $\Phi$ -array and looking up the corresponding values of the field strength within the H-array. This algorithm also uses the method of linear interpolation and subsequently, the look-up value does not need to be an integer but can be any fractional value between 0 and 999 in case of the default 1000 data points. By calculating the average of both values, the H-offset is found and subtracted from all the values in the H-array. As a byproduct, the positive/negative coercivity is found by simply subtracting the offset value from either of the two H-values used for calculating the average. As shown in Fig. 6.2, this ‘center loop’ algorithm has an array input and output for each  $H(t)$  and  $\Phi(t)$ . However, there is no change to any value of the  $\Phi$ -array and it is only passed through to point out the successive signal processing algorithms within the VI.

### 6.2.5 Calculation of the Flux Density

Consequently, the remaining flux is close to zero and indicates that the measurement head is operated in air. However, if it is attached to a ferromagnetic material, the flux increases and can be converted to a flux density by dividing it by the involved cross section. Therefore, the ‘Calc B’ subVI requires the sample height as input parameter while the sample width is determined by the width of the B-coil. As described in section 4.3 and depicted in Fig. 4.7a, the field strength between the two poles of the core unfortunately is not constant over its length. Based on the simulations, the field strength is constant within the central 11 mm only and decreases at the sides of it. As a first approximation, the flux-carrying width is computed as the sum of a fixed part and a field strength dependent part increasing at  $2 \mu\text{m}/\text{A}/\text{m}$ . The exact calculation of the cross section has to be found during the characterization and is part of the next chapter.

### 6.2.6 Demagnetization

The last algorithm to be applied is the compensation of the demagnetization effect. As described in subsection 2.1.5, demagnetization means the occurrence of an internal field in a magnetized body that counteracts the induced magnetization and therefore reduces its effective strength. As already described, it plays a role in the U-core regarding the measurement of the flux density altering the true value, which appears to be smaller than it really is due to the superimposed demagnetization field. While this issue is overcome by choosing a position for the B-coil with a negligible demagnetization effect, it also plays a role within the analyzed specimen. In the case that  $B$  is measured, the determination of the true field strength  $H_{\text{tr}}$  is more complex compared to the simple calculation based on the magnetization  $M$ . The equation using  $B$  is as follows [Cullity and Graham, 2009, p. 63]

$$H_{\text{d}} = N_{\text{d}} \left( \frac{B/\mu_0 - H_{\text{a}}}{1 - N_{\text{d}}} \right). \quad (6.9)$$

However, two simplifications are possible. The first one concerns the denominator where the value  $N_d$  can be neglected, since the value is expected to be well below 0.01, which is due to one of the benefits of this novel measuring method that the analyzed specimens are not only thin but have a widely extended plane. The second simplification concerns the term  $H_a$ , which is typically much smaller than  $B/\mu_0$  in case of soft magnetic samples with high permeabilities. Due to the maximum field strength of about 2000 A/m, the error will be small, e.g. 0.25 %, if a flux density of 1 T is reached within the material. Therefore, the measured field strength can be neglected as well and it is only the flux density  $B$  that has a significant effect on the demagnetizing field.

$$H_d = N_d \cdot \frac{B}{\mu_0} \quad (6.10)$$

Generally, it should be kept in mind that the demagnetization correction is not totally correct, since the values for  $N_d$  “are not exact or well-defined except for ellipsoids” [Cullity and Graham, 2009, p. 63]. Therefore, the described simplifications do not matter much and the real values for  $N_d$  have to be determined empirically.



## 7 System Assembly and Noise Characterization

In order to achieve reliable results, a motorized multi-axis measurement stand was constructed around the previously shown measurement head (Fig. 4.9). It enables the placement of the measurement head on various positions on the sample with high repeatability. According to the design of the head, it is mounted upside-down with the ferrite U-core and the MR sensor array pointing downwards. This way, the wafer or sheet sample under evaluation can be fixed on a horizontal surface with the head moving above it. Subsequently, the noise characterization is performed using this assembly with the measurement head placed in air resulting in an open magnetic circuit.

### 7.1 Measurement Stand

The realized stand features three mechanical axes, which allow the linear motion of the head along the vertical z-axis and the horizontal x-axis and its rotation around the z-axis (Fig. 7.1).

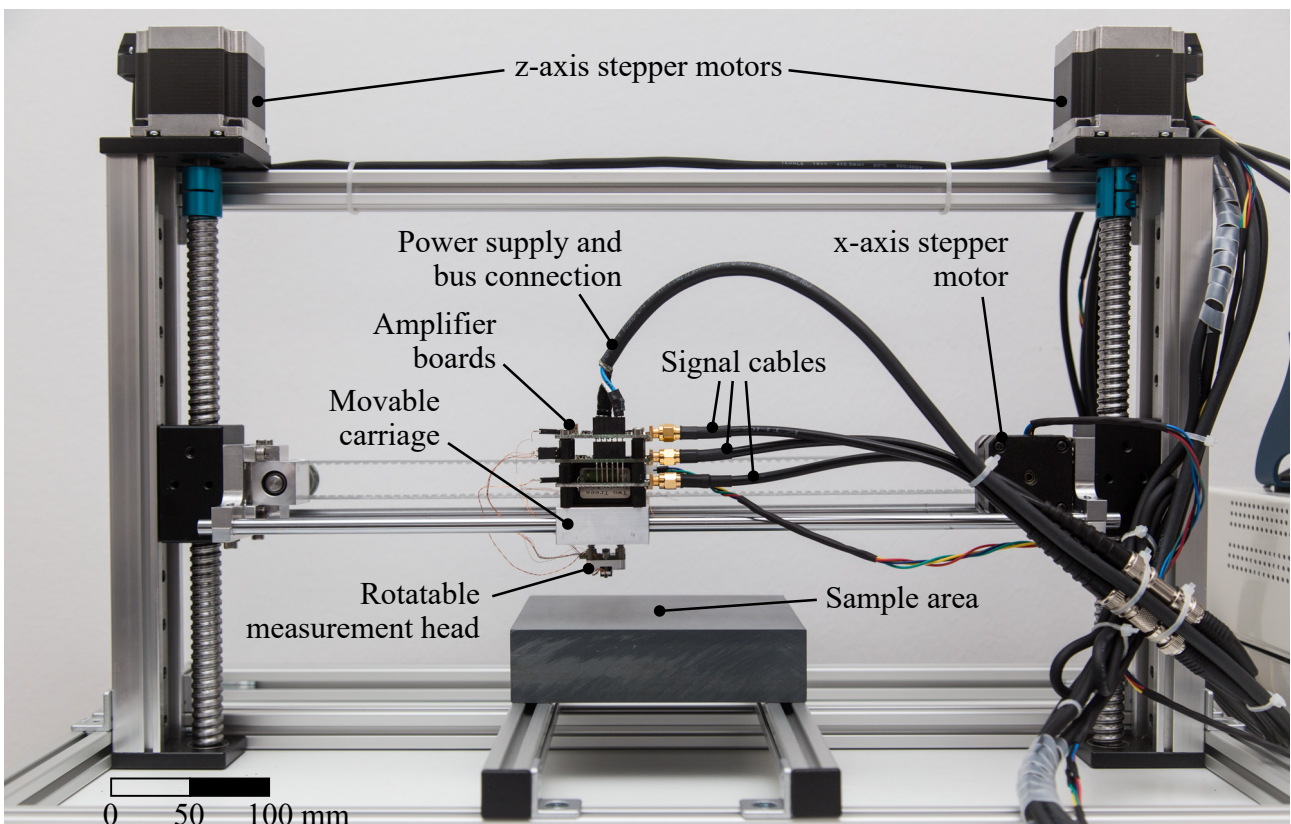


**Figure 7.1** Motorized stand with the measurement head from Fig. 4.9 mounted upside-down on a carriage

The vertical movement is realized by two rugged ball screws providing a high mechanical stability and a high positioning accuracy, which is estimated to be around  $10 \mu\text{m}$ . The ball screws are powered by two large NEMA 23 stepper motors, which are electrically connected in series to provide them with the same current and ensure a simultaneous stepping.

Regarding the x-axis, a movable carriage with two 45 mm linear ball bearings is mounted on two precision shafts with a diameter of 8 mm and a length of 45 cm. The carriage is driven by a toothed belt, which not only holds the measurement head but also serves as a mount for the amplifier boards, whose circuits were presented in section 5.4 and section 5.5. By locating the amplifiers close to the measuring point, the line capacity and the picked up noise on the low voltage links are kept as small as possible. The corresponding PCBs were designed with respect to the available space on the carriage, that accounts to 45 mm x 25 mm. Each circuit has its own board as shown in detail in Fig. 7.2, which allows them to be stacked on top of each other. This saves spaces and has the advantage that changes to either circuit can be done easily without having to replace all of the components. Apart from the amplifier boards, there is a separate PCB that provides two  $\pm 12 \text{ V}$  LDO regulators and an I<sup>2</sup>C bus repeater shared by all circuits using feed-through connectors. Furthermore, the bottom-most board (which is hidden from view in Fig. 7.2) connects the output from the current source with the primary coil and comprises the high load output series resistor  $R_{\text{ser}}$ , which was mentioned at the end of section 5.1 and initially located on the current source PCB.

Apart from the two linear axes, there is a third one that allows a  $\pm 90^\circ$  rotation of the head using a low profile NEMA 17 stepper motor. It is centrally located on the carriage with its shaft sticking out at the bottom to allow the mounting of the measurement head as depicted in Fig. 7.3

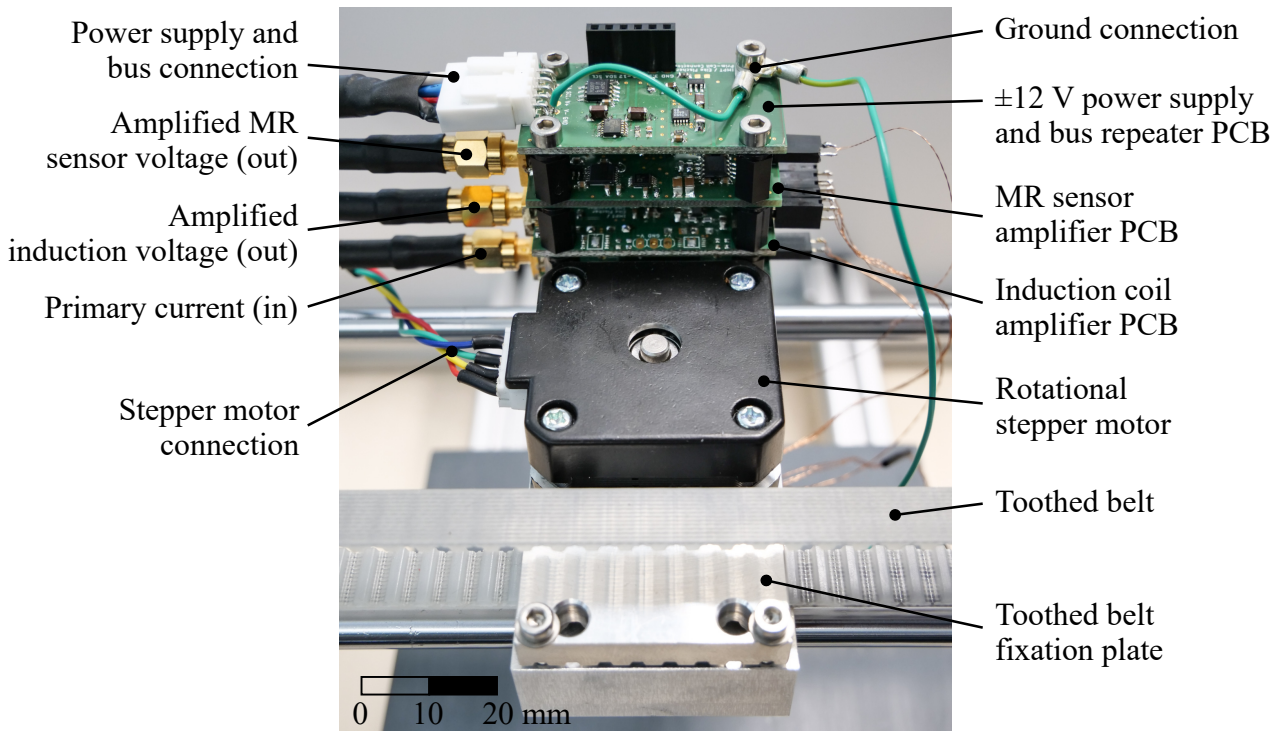


**Figure 7.2** Top view of the moveable carriage with the amplifier boards, stepper motor and toothed belt

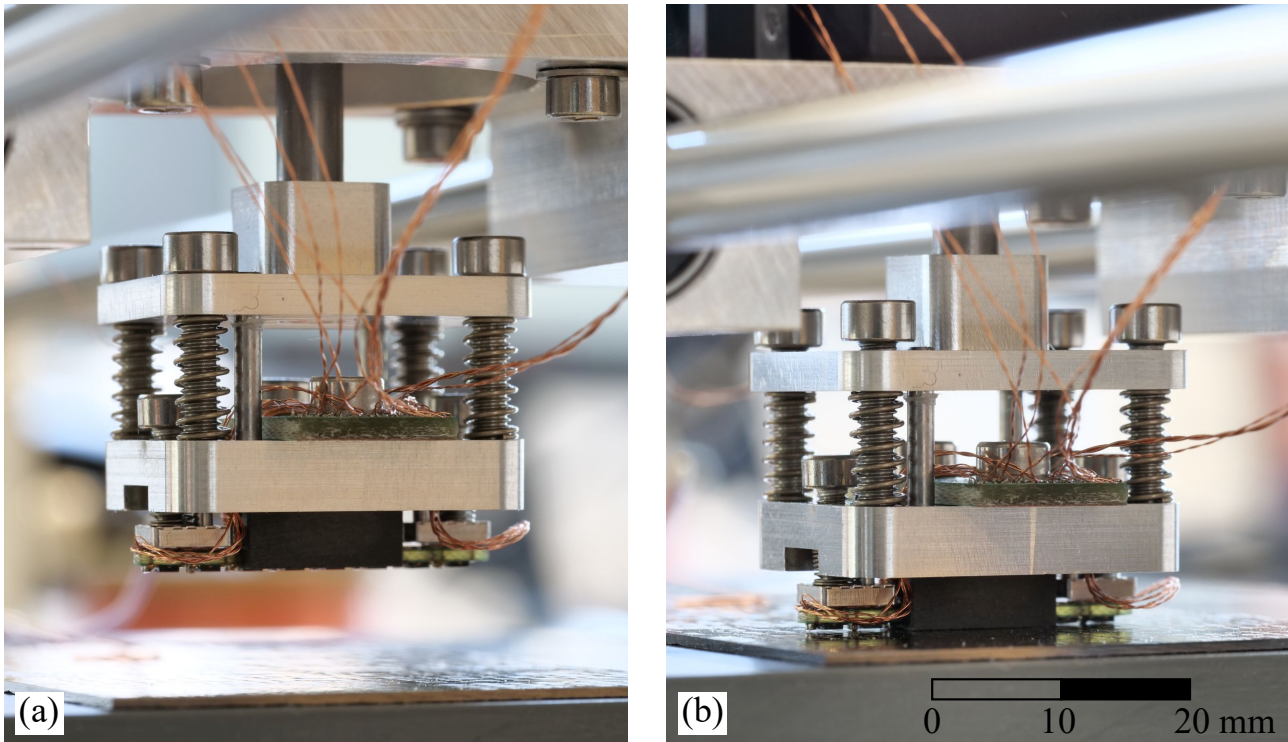


**Figure 7.3** Bottom view of the moveable carriage with the mounted measurement head 10 mm above an exemplary sample (a) and in contact with it (b)

### 7.1.1 Stepper Motor Controller

While there is good reason to locate the amplifier boards on the carriage close to the sensors, the other electronic subcircuits can be housed in a separate case next to the measurement stand. However, due to the setup of the measurement stand with the four comprised stepper motors configured in three axes, a stepper motor controller is added to the electronics. By using an in-house solution instead of a commercial one, it is possible to fully integrate the motor control in the same LabVIEW instrument used for the driving of the measurement head.

Consequently, another PCB was designed, which allows the integration into the existing I<sup>2</sup>C bus and the link to the microcontroller on the programmable waveform generator, which serves as communication hub with the host computer. In contrast to the other boards, which have been described extensively in chapter 5, this additional one can be held very simple. As can be seen in Fig. 7.4, there are barely any further ICs employed in the circuit apart from the microcontroller ‘ATmega168’.

This simplicity is due to the easy control of stepper motors in general and the popularity of 3D printers, which also employ stepper motors and ensured a flooding of the market with cheap components in the recent years. Therefore, there are many motor driver ICs available, which already come fully assembled on small PCBs together with all necessary passive components. These driver boards allow the direct interfacing of a microcontroller on the one side with the motor on the other and only require two 8-pin sockets. In Fig. 7.4, the drivers for axis #2 and #3 are inserted already, while the slot for driver #1 is empty.

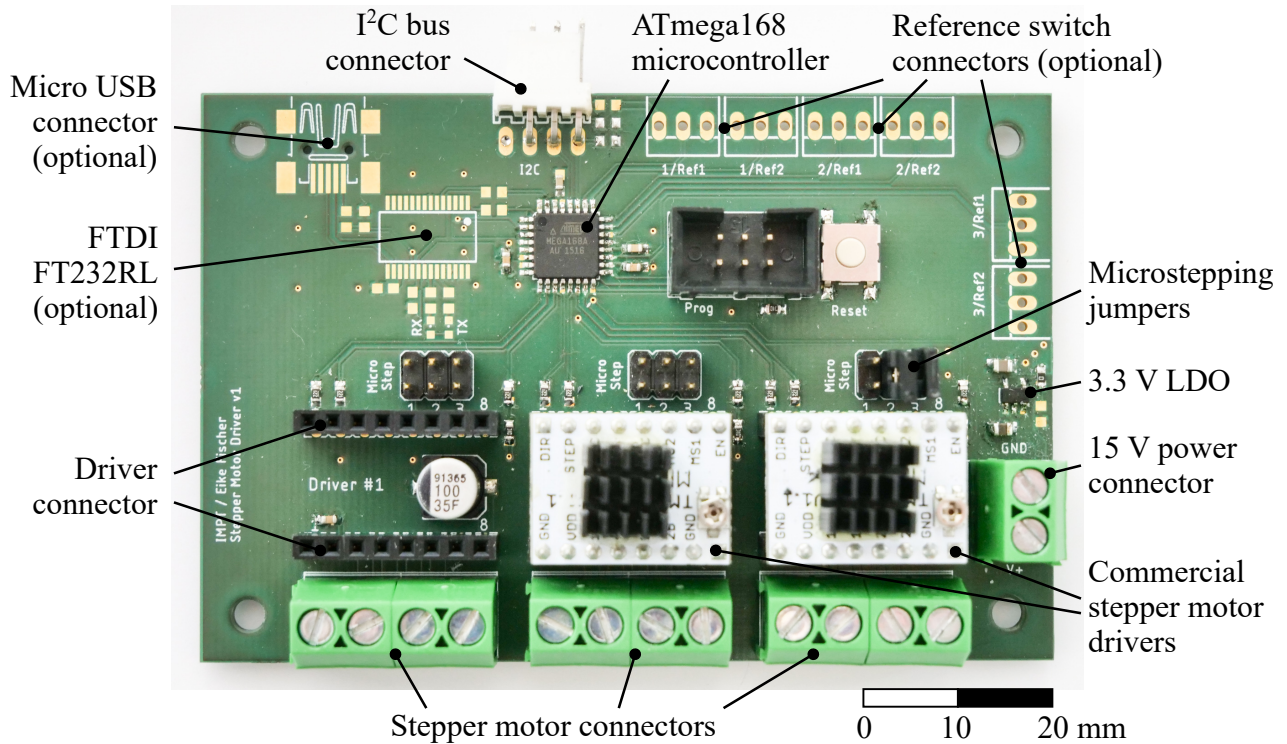


**Figure 7.4** Picture of the PCB comprising the stepper motor controller

Eventually, two digital signals for each driver control the stepper motors. One of these signals sets the rotation direction while the other has to be a square wave of variable frequency. Each cycle of that wave forces the driver to move the motor one step further in the corresponding direction. A common ability of most drivers is the possibility of not moving the motor a whole step per cycle but only a ‘microstep’. This is achieved by modulating the output currents on the two windings of the motor with the effect that different intermediate positions between two full steps can be set. In this case, the chosen drivers allow the setting of 2, 4, 8 or 16 microsteps per cycle. In combination with the motors’ step angle of  $1.8^\circ$ , there are 400, 800, 1600 or 3200 cycles required for one revolution. The choice of the microstepping setting therefore affects the step resolution of the axis but also the smoothness of the motion, which usually is better at high values. The applied microstepping settings and the resulting resolutions of the three axes are listed in Table 7.1.

**Table 7.1** Transmission ratios and resolutions of the axes in the measurement stand

Axis	Transmission ratio	Microstepping setting	Resulting resolution
Linear z-axis	5 mm/rev	8	$3.1 \mu\text{m}/\text{clock cycle}$
Linear x-axis	55 mm/rev	8	$34.4 \mu\text{m}/\text{clock cycle}$
Rotational z-axis	$360^\circ/\text{rev}$	16	$0.11^\circ/\text{clock cycle}$

The supply of the stepper motor driver with the appropriate square wave signal is a straightforward task since almost all microcontrollers feature dedicated hardware units designated for this kind of application. These ‘timer/counter’ units can be configured very flexibly to output a square wave of

different frequency, duty cycle, and timing resolution without the need of the main processor to actively take care of it. Therefore, the control of these hardware units is handled with interrupts that only require processor time on distinct events. In case of the ‘ATmega168’, there are three ‘timer/counter’ units that are configured to generate an interrupt after every clock cycle.

The source code of the microprocessor was developed in order to activate the square wave output once a position different from the momentary one is transmitted. Afterwards, the interrupt occurring after every cycle triggers the compare of the momentary position with the desired value. Depending on the remaining steps, the subroutines apply an acceleration and deceleration of the motors by using successive stepping frequencies. This way, a slow startup and high final speed are combined, which protects the motor and the mechanics from high mechanical loads. For each motor different maximum speeds and (de-)accelerations can be set with the absolute maximum accounting to 2.6 rev/s and  $\pm 10.4 \text{ rev/s}^2$  respectively. The chosen values are listed in Table 7.2.

**Table 7.2** Set speed and accelerations of the axes in the measurement stand

Axis	Max. frequency	Resulting maximum speed	Acceleration
Linear z-axis	2716 Hz	8.5 mm/s	6.2 mm/s <sup>2</sup>
Linear x-axis	1488 Hz	51.1 mm/s	68.8 mm/s <sup>2</sup>
Rotational z-axis	601 Hz	67.6°/s	96.5°/s <sup>2</sup>

### 7.1.2 Electronics Enclosure

The communication with the stepper motor controller board is realized using the I<sup>2</sup>C bus as mentioned above. Therefore, the commands supported by the programmable waveform generator, which are listed in Table 6.1, are extended by another entry. By sending a first character ‘M’ to the microcontroller, all the motor control register can be addressed using the next two characters. This way, not only motion commands can be sent but also the preset speed and acceleration values can be changed. Since 32 bit values are necessary for the storage of the momentary and desired position, eight hex characters are required as final payload of the message. The microcontroller of the programmable waveform generator only works as forwarder and puts the information from the host computer on the bus without checking the content of the message.

Together with the Howload current source PCB, a total of three boards are housed in a separate enclosure next to the measurement stand. As depicted in Fig. 7.5, they are stacked on top of each other with enough space in between to allow the dissipation of the generated heat. The power and auxiliary connections of the boards are located in the back of the case facing the fan while the signal outputs are in the front. Two switching power supplies are placed at the right of the case and provide  $\pm 15 \text{ V}$  for the amplifiers and a single 15 V for the stepper motor controller. Behind them, there is the AC power inlet and the USB connector. The current output to the primary coil is placed at the front of the case next to the I<sup>2</sup>C bus and power connector that leads to the amplifier boards shown in Fig. 7.2.

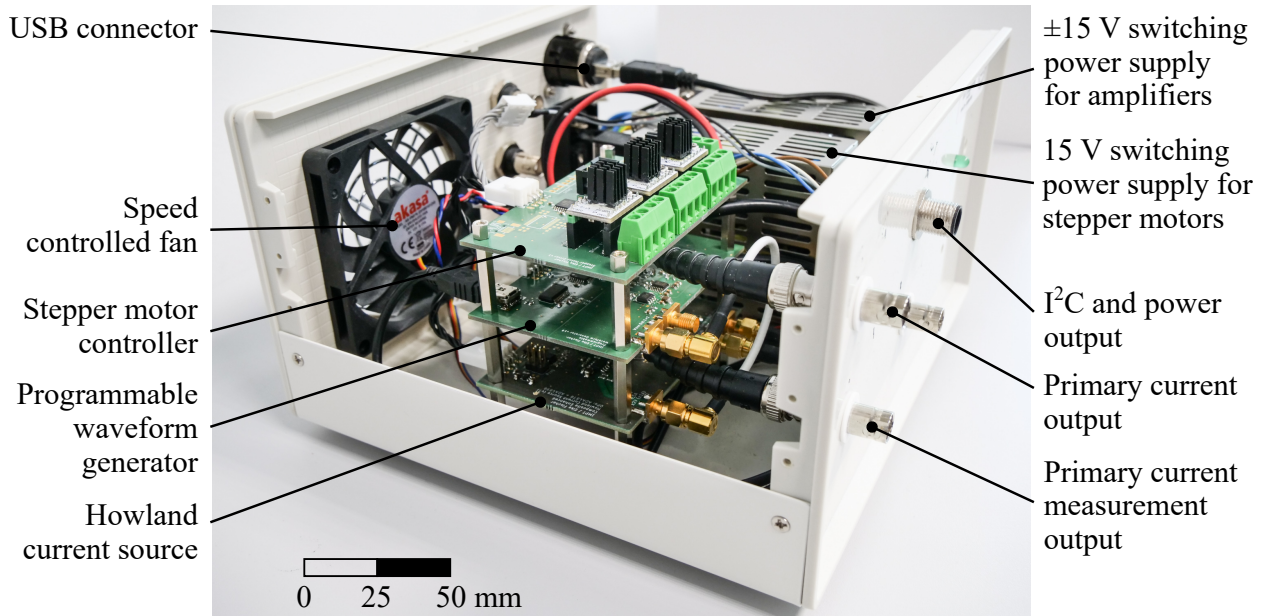


**Figure 7.5** Picture of the PCB featuring the stepper motor controller

## 7.2 Noise Characterization

Now that all the components of the measuring system listed in Table 3.1 are realized and combined in a working measurement system, its properties can eventually be characterized. Due to the versatility of the device, many aspects have to be assessed. Primarily, this section deals with the characterization of the sensors in terms of noise, which defines the achievable resolution. The final frequency range, however, depends very much on the analyzed material and is examined in the next chapter.

### 7.2.1 DAQ Noise Measurements

To be able to estimate the resolution and accuracy of the measurement system, various noise measurements were carried out. Therefore, the DAQ ‘NI 9775’ was characterized in combination with the employed sensors. However, in order to distinguish between the noise of the sensors and the one originating from the ADC itself, the inputs are characterized first without the amplifier boards attached. The fast fourier transformation (FFT) of the input noise is depicted in Fig. 7.6 for both modes which the DAQ supports. The measurement reveals the benefit of the high resolution mode as the noise floor is about 6 dB lower. In this mode every four subsequent measurements values are internally averaged, which results in a higher SNR but also in a lower maximum speed, which is reduced from 20 to 5 MS/s. The option to substitute speed with lower noise provides some extra flexibility, which is especially useful for low excitation frequencies. According to the noise levels of  $2.3$  and  $1.04 \mu\text{V}/\sqrt{\text{Hz}}$  for the high speed and high resolution mode respectively, the root mean square (RMS) voltage noise can be calculated. Therefore, the noise floor is multiplied with the frequency spectrum of each mode. In high resolution mode, the spectrum is limited by an internal 6<sup>th</sup> order Bessel filter with a corner

frequency of 2.36 MHz, while in high speed mode, there is only a 1<sup>st</sup> order filter at 13.9 MHz. Due to this low order, signals above that frequency contribute to the noise also, which is accounted for by a shape factor of 1.57. Since there are no other filters, which reduce the frequency range, the final RMS noise amounts to

$$U_{\text{RMS,HiRes}} = 1.04 \mu\text{V}/\sqrt{\text{Hz}} \cdot \sqrt{2.36 \text{ MHz}} = 1.6 \text{ mV}_{\text{RMS}} \quad (7.1)$$

$$U_{\text{RMS,HiSpeed}} = 2.3 \mu\text{V}/\sqrt{\text{Hz}} \cdot \sqrt{13.9 \text{ MHz}} \cdot 1.57 = 13.5 \text{ mV}_{\text{RMS}} \quad (7.2)$$

The RMS noise values reveal that the high resolution mode features three more noise-free bits, mostly due to the lower frequency range and the high order filter. It is therefore considered as the better mode on the condition that the filter does not significantly alter the phase. The high speed mode on the other hand can be used if sample rates above 5 MS/s are required.

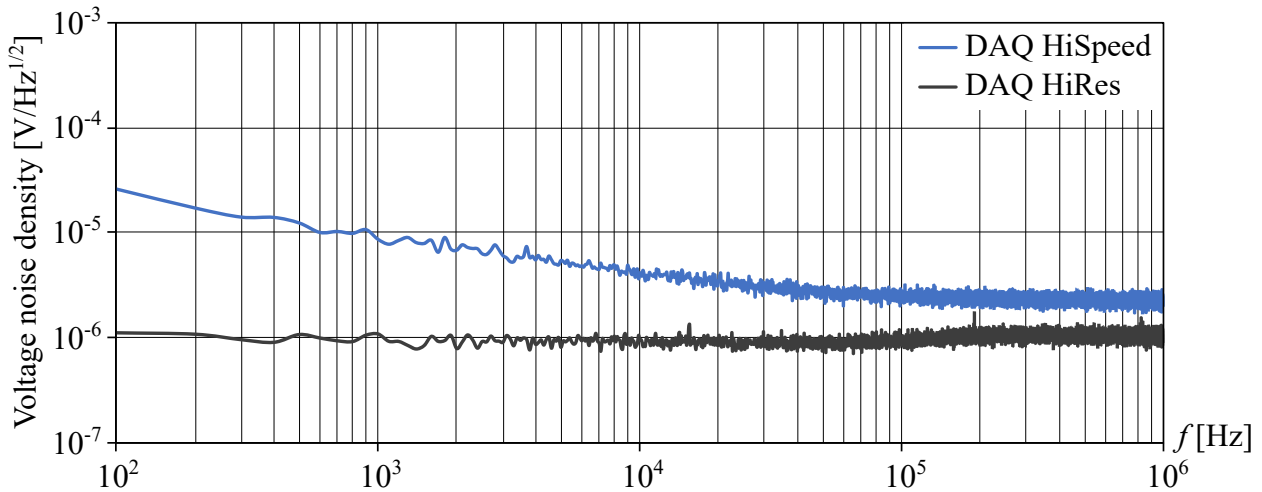


**Figure 7.6** Voltage noise spectral density of the NI 9775 DAQ inputs (10,000 points, 20 FFTs averaged)

Another way of improving the signal-to-noise ratio was formulated in subsection 6.2.1. The described algorithm is the first one comprised in the signal processing chain of the virtual instrument and takes care of the input capturing. By not only measuring a single sine wave but multiple consecutive ones, it is possible to average the results. Principally, any integer multiple of cycles can be averaged but the preset of a handful of values that can be selected by the user seems reasonable. Therefore, the option of averaging 4, 16 and 64 consecutive sine waves is implemented in the front panel of the VI. The impact of this feature is demonstrated in the measurements in the next subsections with the sensors connected to the DAQ.

## 7.2.2 Calibration of the MR Sensors

Prior to the noise measurements of the MTJ based MR sensors ‘CT100’, these are calibrated since the sensitivity in the data sheet is given with a relatively large tolerance range (see Table 4.3). Therefore, the sensors are exposed to a static magnetic field set to different values and the resulting bridge

voltage is measured. This way, the true sensitivity, the offset and the linearity error can be determined. The results are summarized in Table 7.3 and visualized in Fig. 7.7. Due to the symmetry of the measurement head, only four of the eight sensors in the array are used.

The results prove the excellent performance of the chosen MR sensors. The maximum non-linearity error in the evaluated range of  $\pm 2.5$  kA/m accounts to 0.6 % and the offset voltage is well below the  $\pm 5$  mV/V given in the data sheet. However, due to the offset correction algorithm described in subsection 6.2.1, this value does not play a role, anyway. The measured sensitivities are of greater interest. They differ slightly from the stated 5.7 mV/V/kA/m but are within the given tolerance range. The sensitivity values were stored in the LabVIEW instrument individually for each sensor.

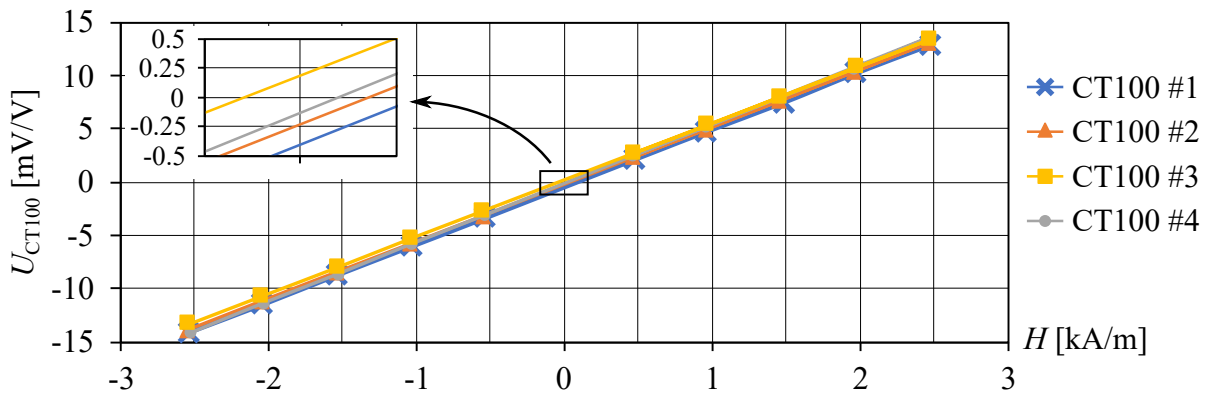


Figure 7.7 Calibration curves of the used ‘CT100’ MR sensors

Table 7.3 Sensitivity, offset and non-linearity error of the ‘CT100’ MR sensors used

Sensor	Position	Sensitivity [ $\mu$ V/V/A/m]	Offset [mV/V]	Non-linearity error [%]
CT100 #1	$x = 1.6$ mm	5.35	-0.40	$\pm 0.6$
CT100 #2	$x = 4.8$ mm	5.35	-0.23	$\pm 0.4$
CT100 #3	$x = 8.0$ mm	5.31	+0.20	$\pm 0.5$
CT100 #4	$x = 11.2$ mm	5.52	-0.13	$\pm 0.6$

### 7.2.3 MR Sensor Noise Measurements

With the MR sensor ‘CT100’ and the corresponding amplifier PCB attached to the input of the DAQ, the resulting FFT depicted in Fig. 7.8 looks different as it is not as flat as before. Without averaging, the noise at 100 Hz is two magnitudes higher in comparison to the noise of the unconnected input, which is also inserted in the graph for comparison. It decreases with frequency showing nearly  $1/f$  behavior and eventually overlaps with the baseline from the DAQ. This slope is probably due to the employed multiplexer, which is necessary to switch between the different MR sensors. Furthermore, there are spurs at 28 kHz and its harmonics at 56 kHz, 84 kHz and so on, whose cause is not known as there is no IC present using such a low frequency as clock source. The averaged measurements show



noise figures, which are similar to the non-averaged one but are decreased by 6 dB from one preset to the next. In summary, the noise level of the sensor signal is just slightly higher for the non-averaged measurement compared to the basic noise of the DAQ. In case of 64 iterations, however, it is much lower since the corresponding curve lies mostly below the one of the DAQ, especially at high frequencies, which contribute most to the noise. Apparently, it is possible to decrease the voltage noise by 18 dB or a factor of eight, when averaging 64 cycles. Hence, the noise reduction can be calculated by taking the square root of the number of averaged sine waves. Furthermore, by averaging 64 cycles most of the spurs are reduced in their amplitude.

Instead of calculating the RMS noise values from the FFT, the corresponding signals are evaluated in the time domain. Therefore, a 10 ms time frame is captured, which is displayed in Fig. 7.9. The noise levels of all the signals also shown in the FFT are arranged side by side. The measurements are referred to the input of the amplifier placed behind the ‘CT100’ sensors, which is why the amplitude is decreased by the amplifier’s gain of 40 dB. This allows the direct conversion of the measured noise to the field strength by dividing it by the supply voltage and the sensitivity of the MR sensor.

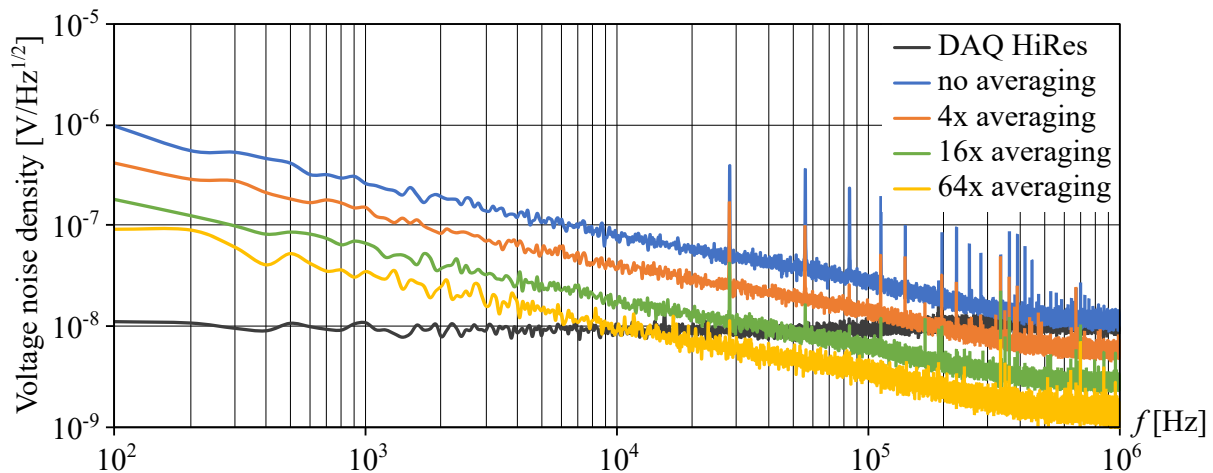


**Figure 7.8** Voltage noise spectral density referred to the amplifier input of the ‘CT100’ sensors at different averaging presets (10, 000 points, 20 FFTs averaged)

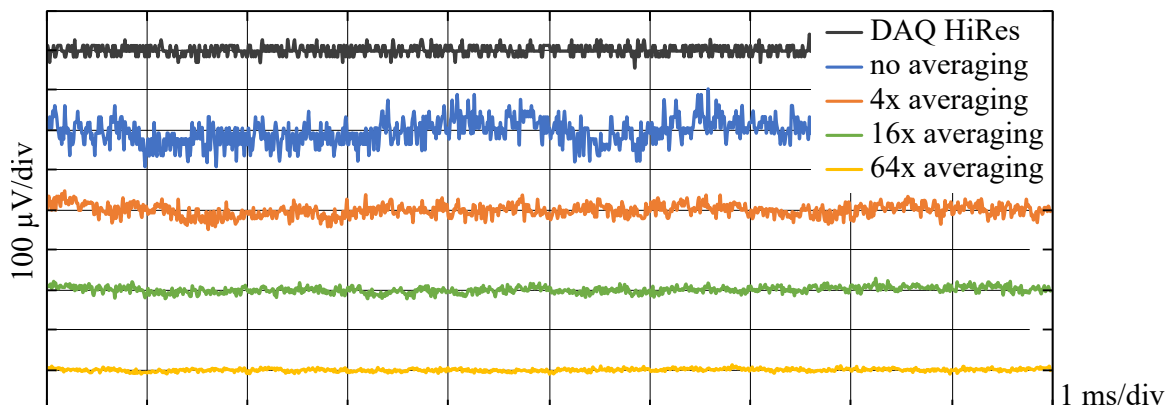


**Figure 7.9** Voltage noise referred to the amplifier input of the ‘CT100’ sensors in the time domain

Fig. 7.9 also contains the noise level of the DAQ, which can be calculated to a noise of  $11.2 \mu\text{V}_{\text{RMS}}$  referred to the amplifier input and corresponds to  $1.12 \text{ mV}_{\text{RMS}}$ . This is slightly lower than the previously calculated  $1.6 \text{ mV}_{\text{RMS}}$  (Eq. 7.1). Once the amplifier board and the sensor are connected to the DAQ, the noise increases to  $30.8 \mu\text{V}_{\text{RMS}}$ . In subsection 5.4.1, it was calculated to  $3.3 \text{ mV}_{\text{RMS}}$  (which corresponds to  $33 \mu\text{V}_{\text{RMS}}$  referred to the input) and therefore matches the measured value well. The higher noise floor at low frequencies observed in the FFT does not play a significant role. This level of noise is already very low and would not necessarily need further reduction as it is the equivalent of  $1.51 \text{ A/m}$  in terms of field strength. By averaging however, the noise can be reduced to below  $1 \text{ A/m}$  as shown in Table 7.4 where all values are summarized. For illustration purposes, a  $100 \text{ Hz}$  sine wave with an amplitude of  $100 \text{ A/m}$  is captured and depicted in Fig. 7.10.

**Table 7.4** Achieved RMS noise levels for the ‘CT100’ MR sensors in terms of voltage and field strength

Averaging	RMS voltage noise [ $\mu\text{V}_{\text{RMS}}$ ]	RMS field strength noise [ $\text{A/m}$ ]
n/a	30.8	1.51
4x	15.2	0.57
16x	8.3	0.31
64x	3.7	0.14

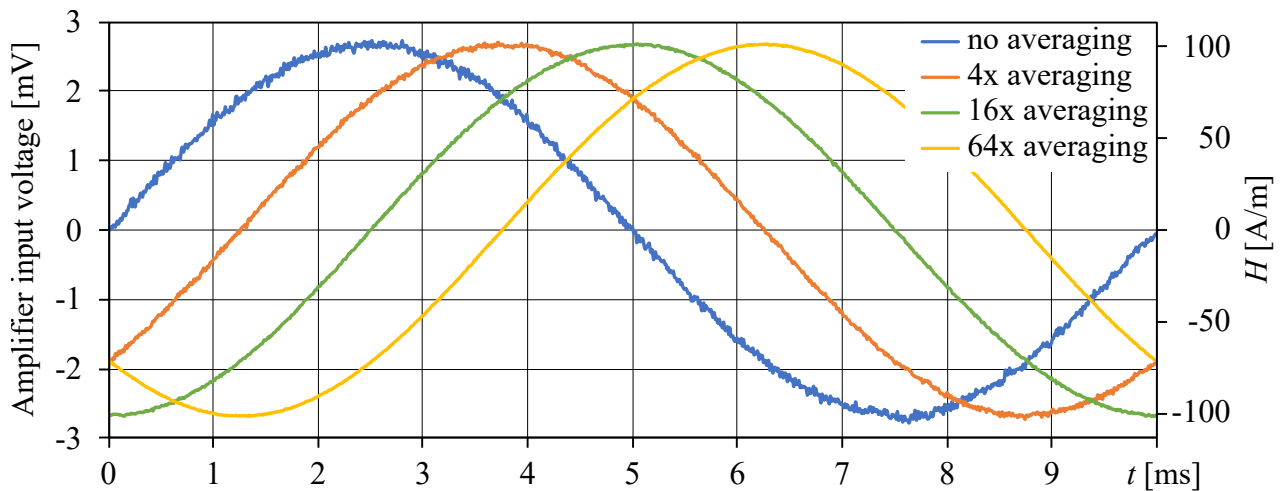


**Figure 7.10** ‘CT100’ output signal at a  $100 \text{ Hz}$  sine wave excitation with an amplitude of  $100 \text{ A/m}$

#### 7.2.4 Induction Coil Noise Measurements

Regarding the induction coil signal path, the same noise analysis is performed as for the MR sensor. However, as described in subsection 5.5.2, there are four different gain stages that can be chosen depending on the amplitude of the induction voltage. Therefore, noise measurements are carried out for all of them. Figure 7.11 shows the resulting FFT of the sole amplifier while the FFT depicted in Fig. 7.11 is recorded with the coil connected and the one in Fig. 7.13 with 64 cycles averaged.

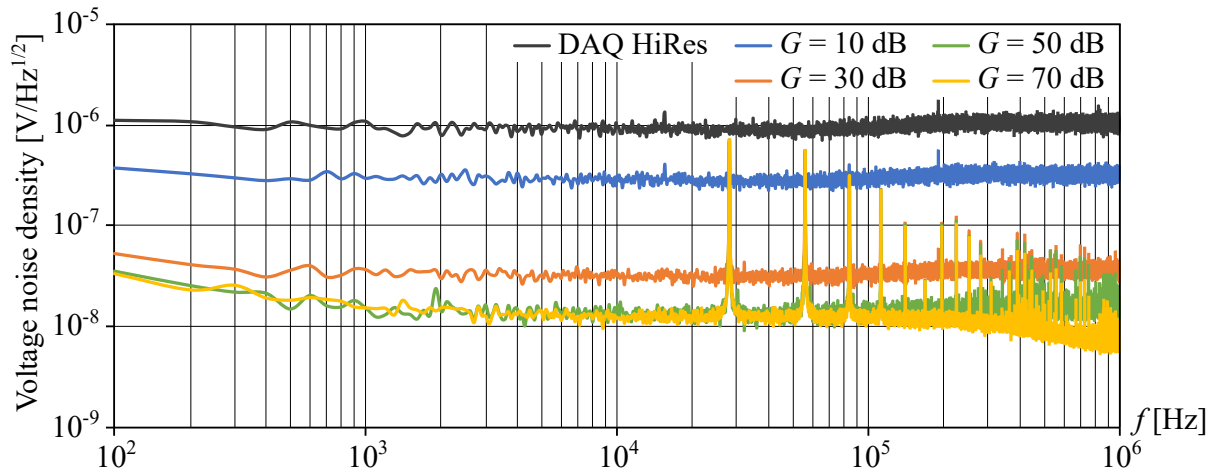


**Figure 7.11** Voltage noise spectral density referred to the amplifier input of the induction coil at all gains without coil connected (10,000 points, 20 FFTs averaged)

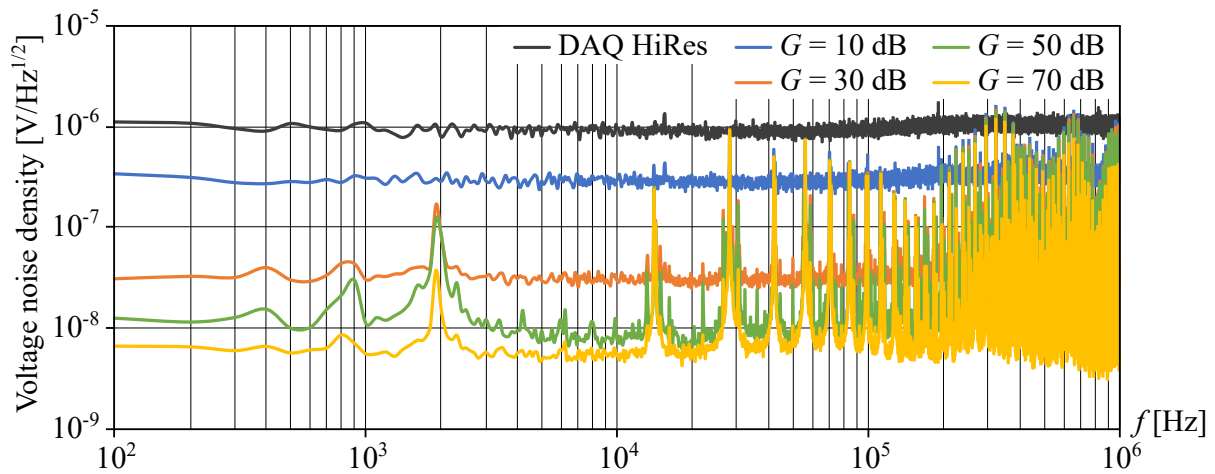


**Figure 7.12** Voltage noise spectral density referred to the amplifier input of the induction coil at all gains with coil connected (10,000 points, 20 FFTs averaged)

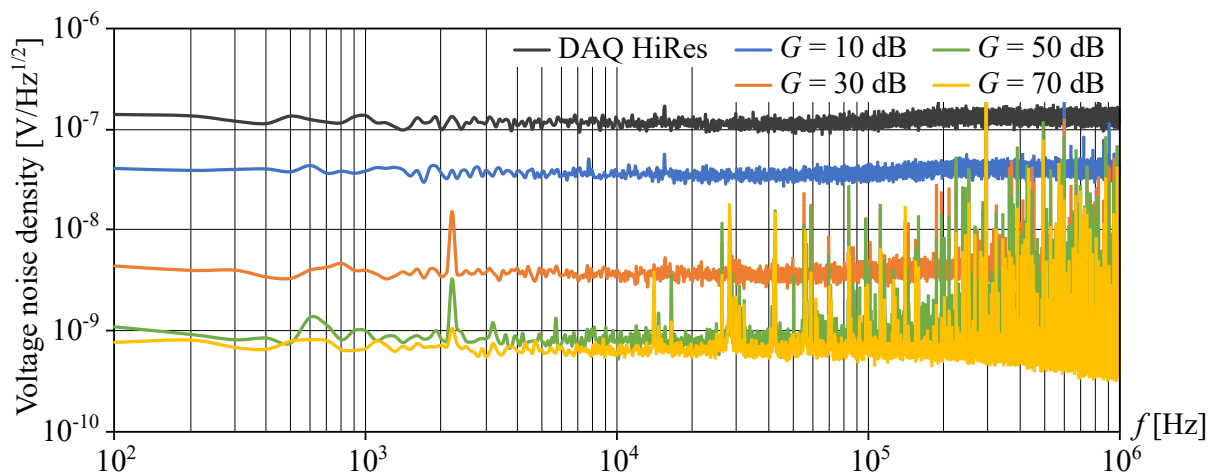


**Figure 7.13** Voltage noise spectral density referred to the amplifier input of the induction coil at all gains with coil connected and 64 cycles averaged (10,000 points, 20 FFTs averaged)

According to the measurements, the noise emitted by the amplifier stage is very low and reaches about the same noise floor of  $10 \text{ nV}/\sqrt{\text{Hz}}$  as the combination of the MR sensor and its amplifier shown in Fig. 7.8. For the gains of 10 dB and 30 dB, the noise floor is higher since it is limited by the resolution of the DAQ. In all measurements of the induction coil, the spurs at 28 kHz and its harmonics observed before are present again, which indicates an external cause for it. However, a much more significant disturbance arises once the induction coil is connected as it couples excessive noise into the amplifier inputs. The FFT in Fig. 7.12 reveals a small peak at 1.9 kHz, but apart from that, the noise is primarily located at the end of the measured spectrum and shows a significantly increased noise floor in the frequency range above 100 kHz. Since this range covers 90 % of the noise in the shown spectrum of up to 1 MHz, it has a great impact on the RMS noise.

Again, the method of averaging yields an improvement as Fig. 7.13 illustrates. The changed  $y$ -scale reveals a decrease of all noise by a factor of almost ten as could be expected already from the observations in the previous subsection. Even though the noise floor at a gain of 70 dB is decreased to  $0.8 \text{ nV}/\sqrt{\text{Hz}}$ , the high frequency components will probably increase the noise above that level. Using Eq. 7.1, a calculated RMS noise of  $1.23 \mu\text{V}_{\text{RMS}}$  results. However, the observation of the idle signal in the time domain recorded at all gains and shown in Fig. 7.14 proves that the noise is higher and actually corresponds to  $3.7 \mu\text{V}_{\text{RMS}}$  at a gain of 70 dB. Therefore, it confirms the assumption that the high frequency noise increases the RMS noise. All noise levels are calculated from the time domain and summarized in Table 7.5.

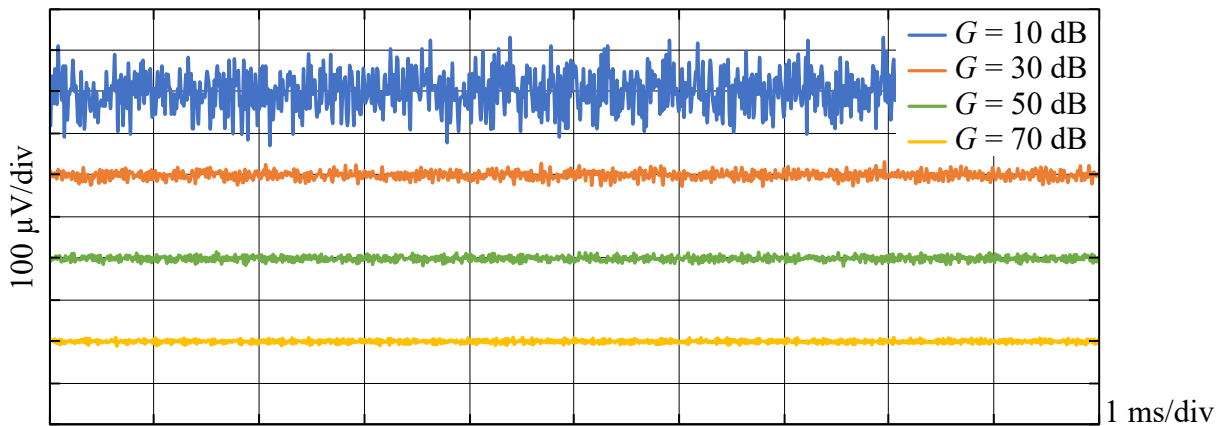


**Figure 7.14** Voltage noise referred to the amplifier input of the induction coil for all gains in the time domain with 64 cycles averaged

**Table 7.5** Achieved RMS noise levels for the induction coil at different gains and averaged for 64 cycles

Gain [dB]	RMS voltage noise [ $\mu\text{V}_{\text{RMS}}$ ]
10	46.4
30	9.5
50	6.5
70	3.7

Eventually, a 100 Hz test signal is captured, which is shown in Fig. 7.15. The observed noise in the resulting signals, however, is much higher than expected accounting to about  $70 \mu\text{V}_{\text{RMS}}$ . Apparently, additional high frequency noise from the primary winding, which was not connected to the amplifier before, is coupled into the induction coil and raises the noise level by a factor of almost 20. At 100 Hz and an amplitude of 100 A/m, this causes a signal-to-noise ratio as bad as 1.15, since the measured signal strength of  $81 \mu\text{V}_{\text{RMS}}$  is only slightly higher than the noise level. However, it should be kept in mind that the induction voltage is integrated over time in order to obtain the momentary value of the flux. Since the process of integration actually means the operation of a low pass filter in the stopband, it filters out noise better the higher its frequency is. Accordingly, when the signals from Fig. 7.15 are integrated and divided by the number of turns of the induction coil  $n = 10$ , the flux depicted in Fig. 7.16 results.

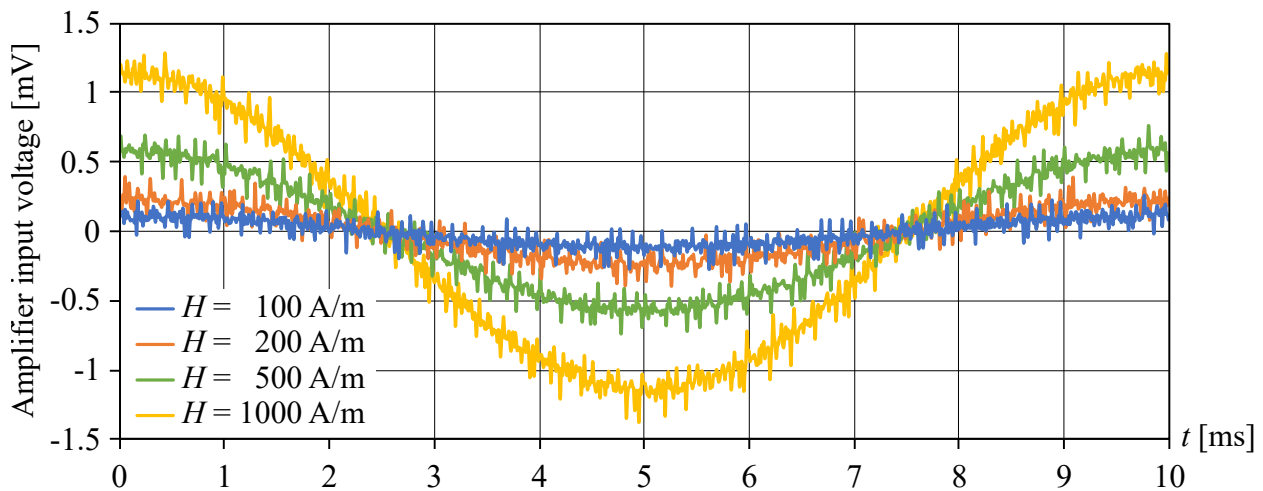


**Figure 7.15** Induction coil output signal at a 100 Hz sine wave excitation of different amplitudes captured at a gain of 70 dB and 64 cycles averaged

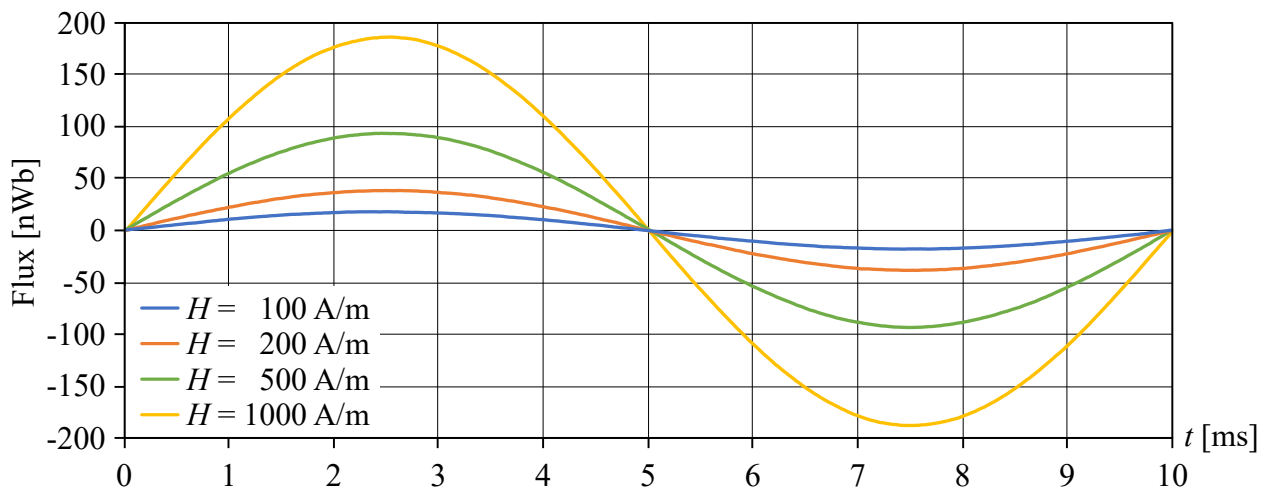


**Figure 7.16** Resulting flux in the induction coil at a 100 Hz sine wave excitation and different amplitudes captured at a gain of 70 dB and 64 cycles averaged

Not only the cosinusoidal progression of the induction voltage has changed to a sinusoidal shape but moreover all the noise has disappeared. Actually, there still is noise but it can barely be seen in the plot. It can be made visible with the help of mathematics by subtracting a sine wave with the corresponding amplitude from the curves. Another way is again the calculation of the FFT of the signal as shown in Fig. 7.17. While the noise floor is wrong in the chart due to the FFT processing gain, it well illustrates the resulting  $-20$  dB/dec slope in the flux signal, effectively decreasing high frequency noise. At 10 kHz for example, the noise is attenuated 100 times stronger in comparison the signal at 100 Hz. Eventually, the noise level in terms of flux amounts to approximately  $0.2 \text{ nWb}_{\text{RMS}}$  calculated with the method of subtracting a sine wave.

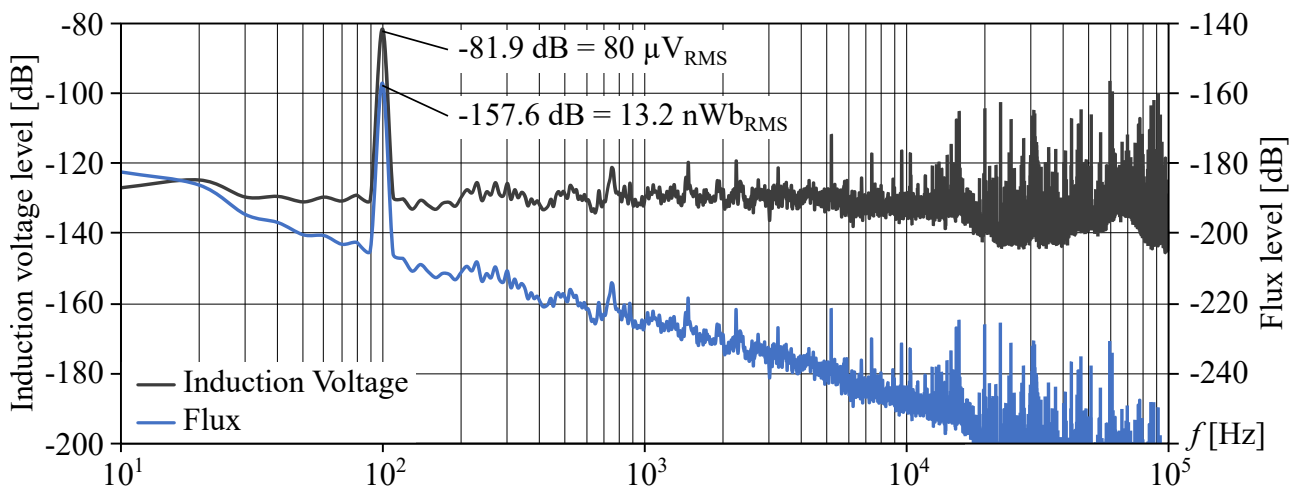


**Figure 7.17** FFT of the signal levels of the induction voltage and the resulting flux captured at a gain of 70 dB and 64 cycles averaged (10,000 points, 20 FFTs averaged)

While a noise of  $0.2 \text{ nWb}_{\text{RMS}}$  does not appear significant in the first place, some considerations make clear the meaning of this value. Since the assumption of the whole measurement concept formulated in chapter 3 is that the flux in the magnetic thin film also passes the induction coil and is measured there, the flux density corresponding to this noise has to be calculated. In a layer of  $1 \mu\text{m}$  height and the same width as the coil (12 mm) for example,  $0.2 \text{ nWb}$  of flux correspond to a flux density of  $16.7 \text{ mT}$ , which is already a significant part of the maximum value to be expected. Consequently, in a layer of only 100 nm, the flux density is a magnitude higher even and a noise of  $0.2 \text{ nWb}_{\text{RMS}}$  renders the device unusable for layers of this height.

To summarize, the noise and hence the achievable resolution of the two sensors has been well characterized. However, the tests were carried out in air only and the verification if the device allows the capturing of hysteresis loops of magnetic materials attached to the measurement head is up next. Also, frequencies other than the used 100 Hz have to be examined. Since the induction voltage increases with frequency, noise will become less of an issue and it is expected that the signal quality will improve. This is especially important regarding the measurement of thin films of below  $1 \mu\text{m}$ .

## 8 Measurement of Magnetic Samples

The measurement of magnetic samples will show how much the detected noise levels will alter the resolution of the device. As already indicated in section 7.2, its versatility will be examined by analyzing different samples and multiple excitation frequencies. For relatively thick samples of up to  $100\ \mu\text{m}$  in height, it is expected that the demagnetization effect will be the limit regarding the true field strength in the sample. Also, eddy currents will most likely play a role and limit the maximum frequency. For thin sample down to  $0.1\ \mu\text{m}$  on the other hand, both these effects are expected to be small while the noise will most likely be the limiting factor. To be able to rate the absolute precision of the device, the results will be compared to reference measurements, which are subject of section 8.1. They are carried out with a VSM and a hysteresis loop tracer.

### 8.1 Reference Measurements

Since vibrating sample magnetometers and hysteresis loop tracers have individual strengths and properties, it is reasonable to use both devices for reference measurements. The VSM applies a DC field to an oscillating sample, which therefore induces a voltage in the surrounding induction coils (for details on the assembly and the working principle refer to subsection 2.3.1). Due to the small sample size, it suffers from a significant demagnetization effect for layer heights of above one micron. On the other hand, it features a high accuracy and the saturation magnetization and the coercivity (in a static field) can be determined with great precision because a single data point can be averaged over multiple seconds. A hysteresis loop tracer on the other hand requires a time varying field and records a whole loop in the fraction of a second. The field is typically created by a solenoid or a Helmholtz pair with the benefit of a greater area of uniform field (subsection 2.3.3), which allows the specimen to be larger in size. Consequently, when using an appropriate setup and sample size, the demagnetization effect can be significantly reduced. A suitable hysteresis loop tracer consisting of a small measurement coil with a high winding count is constructed accordingly and presented in the first subsection 8.1.1. Operated in a magnetic field of 50 Hz, its results are well comparable to the measurement system when it is set to the same excitation frequency. Subsequently, they should show the same dynamic effects, that do not appear in the DC field of the VSM. Despite its lower precision, the hysteresis loop tracer is therefore believed to allow for more suitable reference measurements. Since the saturation magnetization is not affected by the frequency, its value is retrieved from the VSM due to its higher accuracy. A 'series 7400' model from *Lake Shore Cryotronics, Inc.* is used for this purpose.

### 8.1.1 Reference Hysteresis Loop Tracer

The constructed reference hysteresis loop tracer consists of a single printed circuit board as depicted in Fig. 8.1a. It features a ‘CT100’ MTJ based magnetoresistive sensor that has already proven in the sensor array in section 4.3. It is located close to an instrumentation amplifier type ‘AD8221’ from *Analog Devices*, which is the sister device of the ‘AD8421’ with the same excellent properties in terms of noise, precision and CMRR but with less speed. Since the reference measurements will be obtained in a Helmholtz pair operated at the main frequency of 50 Hz, this is not an issue. At the chosen gain of  $G = 23.45$  ( $R_G = 2.2 \text{ k}\Omega$ ), the cutoff frequency accounts to approximately 200 kHz, which is more than sufficient.

Regarding the measurement of the flux density, multiple identical coils have been ordered at the specialized coil winder company *hr electronic*. The coils feature a total of 480 windings of  $32 \mu\text{m}$  diameter wire in four layers at a length of 4 mm. One of these coils is fixed close to the right edge of the board to take up the magnetic sample. According to the coil’s inner dimensions, the sample can have a maximum width of 5 mm and a height of 0.8 mm. The length is not limited but should be at least four times as long as the coil. This ensures that all turns are properly influenced by the magnetization of the sample and additionally decreases the demagnetization effect. Not only ferromagnetic sheets but also diced wafers with a magnetic coating fit into this ‘sample coil’ as shown in Fig. 8.1b.

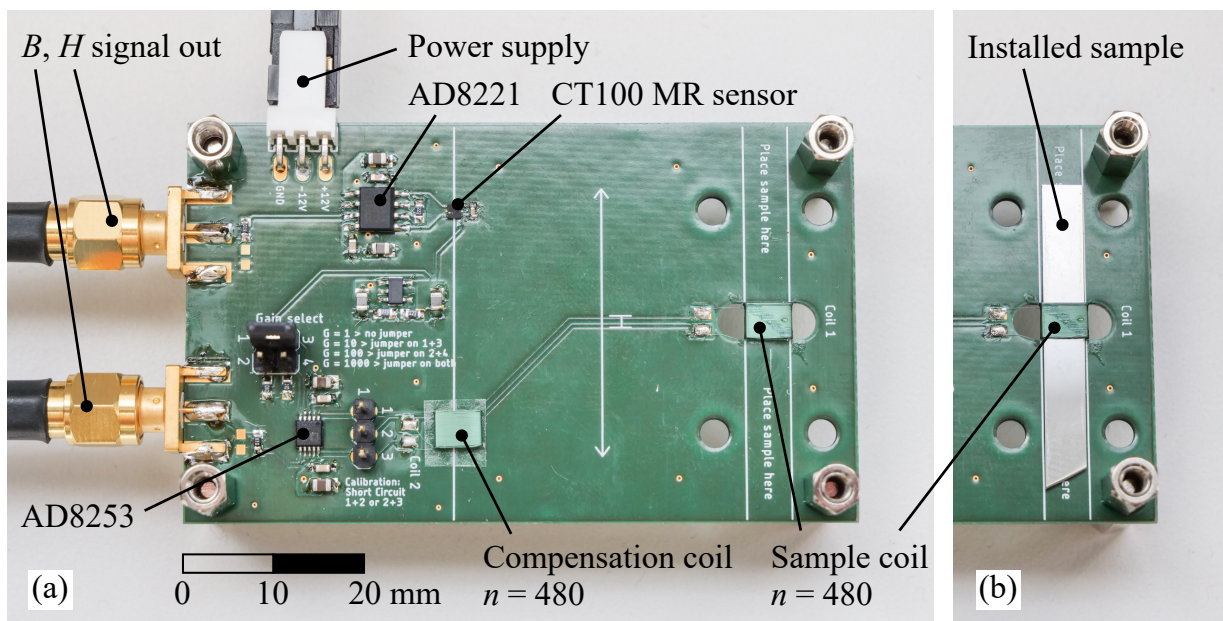


**Figure 8.1** Reference measurement PCB placed in a homogenous magnetic field

A second compensation coil is located on an adhesive tape in the same axis as the magnetoresistive sensor. Both the sensor and the second coil have a distance of several centimeters from the sample to ensure that they are not affected by the additional magnetic field created by it. By connecting the two coils in series but with reverse polarization, the common signals cancel out. Thereby the deviation between the two coils’ sensitivities can be balanced by slightly rotating the compensation coil, which



is only loosely fixed by a tape. The right rotation angle can be determined by observing the output voltage while slowly rotating the compensation coil. Eventually, the sum of the induction voltages in the two coils caused by the excitation field  $H$  is exactly zero. This way only the part of the voltage caused by the additional magnetization  $M$  within the sample is visible at the coil terminals as given in Eq. 8.1. This allows for large gains of the subsequent amplifier as there is no voltage offset resulting from the field strength that would be amplified with it.

$$U_{\text{ind}}(t) = nA \frac{\mu_0 M(t)}{dt} \quad (8.1)$$

It is important to point out that the cross section  $A$  in Eq. 8.1 is not the cross section of the coil but the one of the sample. Therefore, high gains are necessary when using the device for the evaluation of thin films with a height in the nanometer range while sheets with a thickness of several tens of microns probably produce a output signal strong enough without the need for further amplification. Consequently, the ‘AD8253’ with its versatile gain range from 1 to 1000 is employed once more and the desired gain can be set by two jumpers.

The signal processing of this device is done in the same way as described in subsection 6.2.1 with slightly different equations. The output voltages from both amplifiers are averaged and converted to  $H$  and  $M$  including digital integration in the case of the magnetization. Afterwards, the loop is centered along the horizontal axis and the flux density is retrieved by the equation  $B = \mu_0(H + M)$  (Eq. 2.10).

### 8.1.2 Reference Samples

In order to evaluate the performance and versatility of the developed measurement device, a variety of samples are used for characterization. According to Table 8.1 these range from sheet material with a thickness of up to  $80 \mu\text{m}$  to thin film layers with a height of  $100 \text{ nm}$  covering a range in height of three magnitudes. The selection of materials includes both anisotropic and isotropic samples manufactured in different ways like sputtering, electroplating, rolling and sintering. The expected frequency dependence of the magnetic properties varies as well as the coercivity and saturation flux density.

**Table 8.1** Magnetic samples used for the characterization of the measurement device

Material	Type	Total layer height
<i>DMEGC</i> ‘FS 1000’	Ferrite sheet	$80 \mu\text{m}$
<i>Vacuumschmelze</i> ‘MuMetall’	Metallic foil	$50 \mu\text{m}$
‘Metglas 2605SA1’	Amorphous iron-based foil	$23 \mu\text{m}$
CoZrTa	Sputtered multilayer stack on wafer	$6 \mu\text{m}$
$\text{Ni}_{81}\text{Fe}_{19}$	Electroplated layer on wafer	$500 \text{ nm}$
$\text{Ni}_{81}\text{Fe}_{19}$	Sputtered layer on wafer	$100 \text{ nm}$

The ferrite sheet ‘FS1000’ from *DMEGC* is expected to have isotropic magnetic properties and have the best high frequency behaviour due to the bad conductivity of ferrite. Its saturation flux density

should be the lowest among the samples. Both ferromagnetic foil materials ‘MuMetall’ and the ‘Met-glas’ type are not annealed and therefore should be isotropic as well but highly frequency dependent due to the arising eddy currents. Among the thin film samples the quite novel CZT multilayer should have the highest saturation flux density and a low coercivity (see section 2.2). Due to a prior annealing it is highly anisotropic and its easy and hard axis are therefore measured individually. Both  $\text{Ni}_{81}\text{Fe}_{19}$  samples are not annealed and should have a quite high coercivity and no preferred axis.

For the analyzation in the VSM each of these materials is diced to obtain a rectangular shape in the case of a silicon wafer used as substrate or punched to a flat cylinder in case of a substrate-free foil or sheet. For the reference measurements performed with the previously described hysteresis loop tracer, the materials are diced/cut into strips with a width of approximately 4.5 mm. The exact dimensions vary slightly from sample to sample as can be seen in Fig. 8.2. Since the VSM measures the magnetic moment of the samples, the knowledge of its volume is crucial to calculate the magnetization. For the hysteresis loop tracer, only the cross section has to be measured while the length is not of interest.

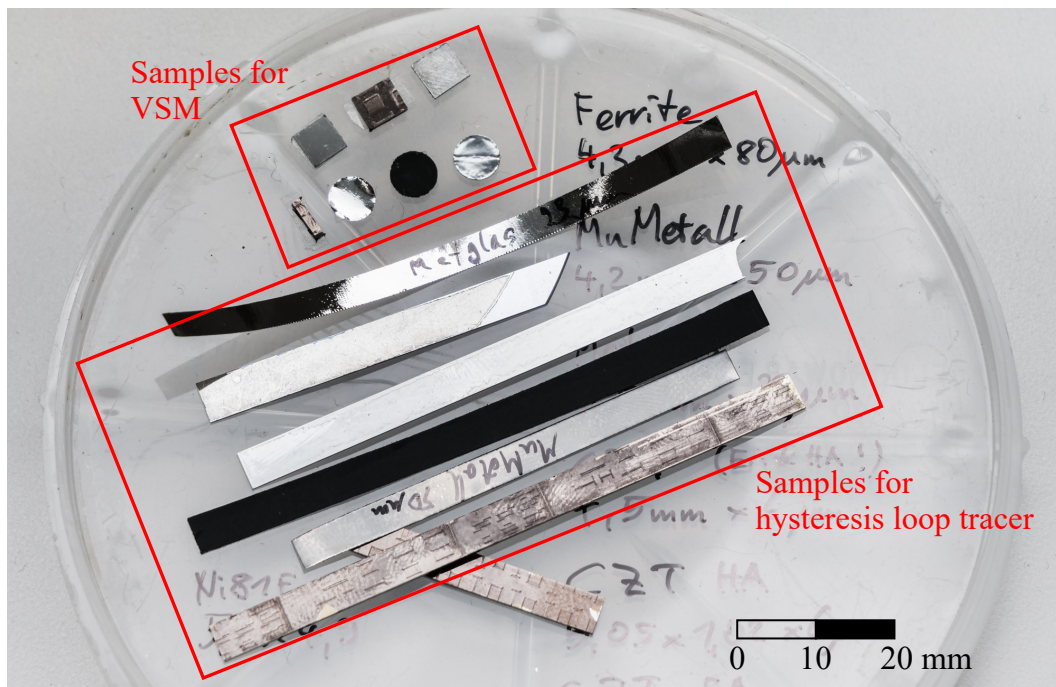


**Figure 8.2** Reference samples used for characterization

### 8.1.3 Results

The results of all the measurements are shown in the seven figures from Fig. 8.3 to Fig. 8.9 in the same order as in the Table 8.1. The left graph in each figure contains the raw data as provided by the VSM and hysteresis loop tracer in a magnetic field of  $\pm 8$  kA/m. The right graph shows the same data with demagnetization correction applied (according to Eq. 6.10) and in a factor ten smaller range of  $\pm 800$  A/m. The individual values for  $N_d$  are noted in the graphs next to the curves. They are estimated from comparisons with hysteresis loops published in literature or data sheets.

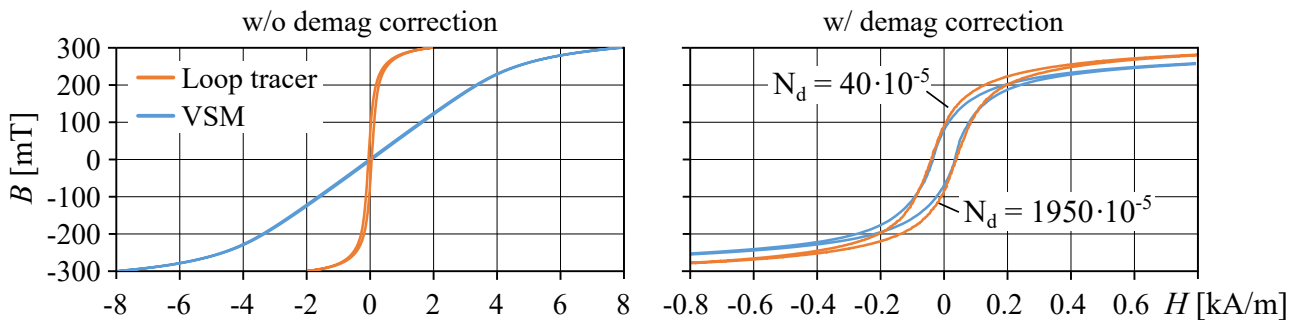


**Figure 8.3** Reference measurements of the 80  $\mu\text{m}$  'FS1000' ferrite sheet

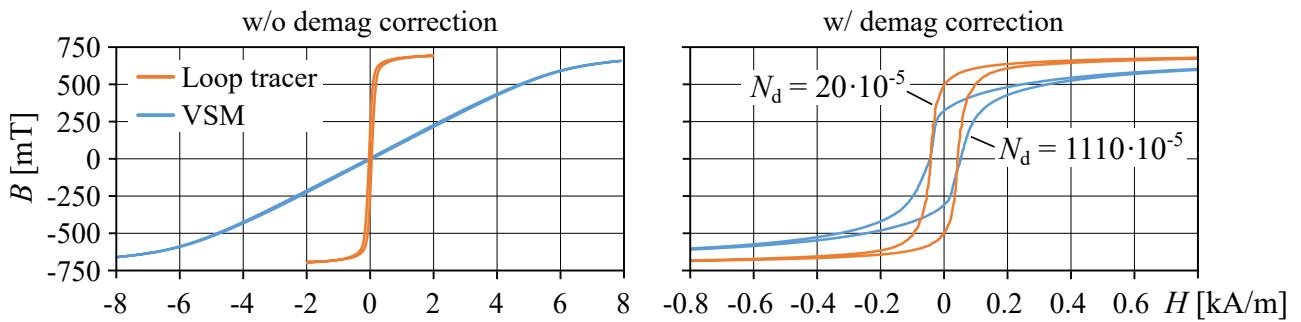


**Figure 8.4** Reference measurements of the 50  $\mu\text{m}$  'MuMetall' foil

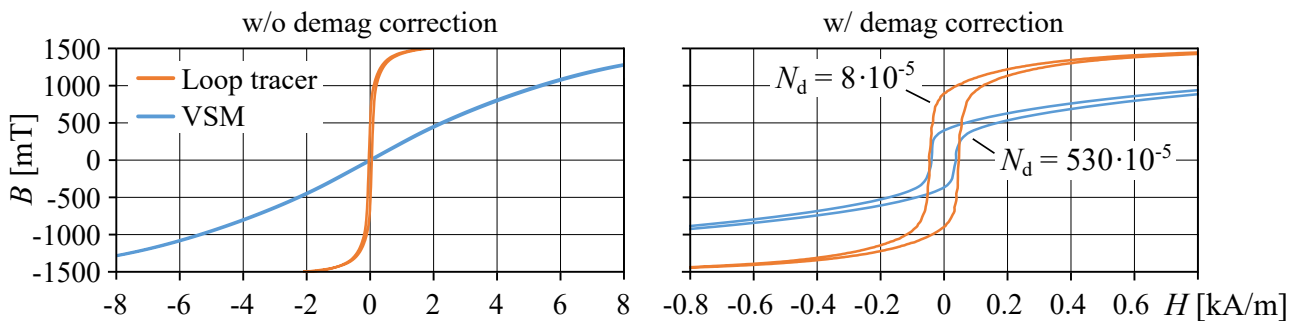


**Figure 8.5** Reference measurements of the 23  $\mu\text{m}$  'Metglas' foil

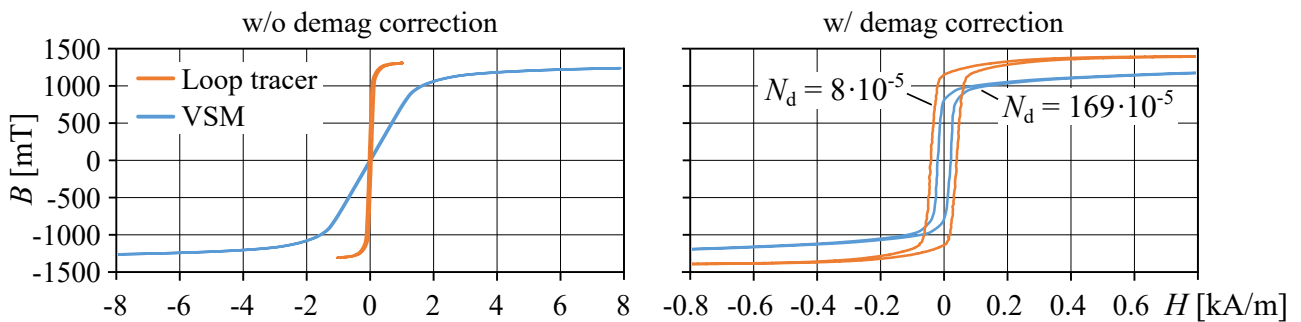


**Figure 8.6** Reference measurements of the 6  $\mu\text{m}$  CZT multilayer (easy axis)

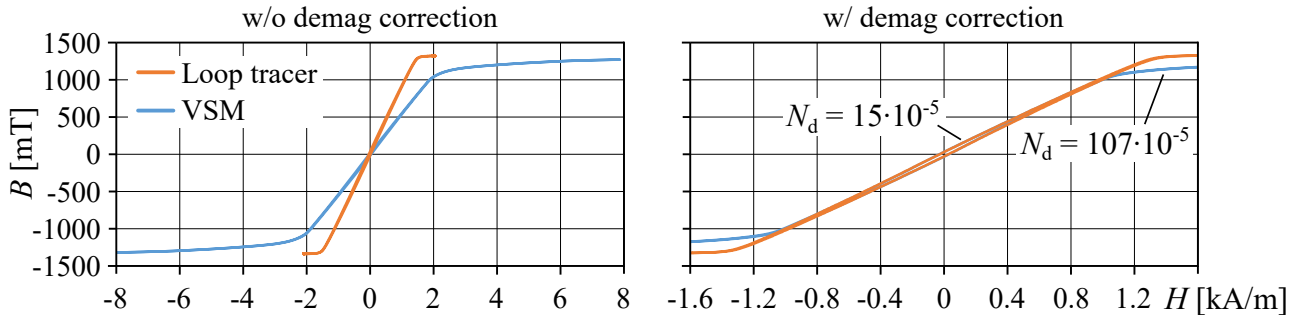


**Figure 8.7** Reference measurements of the 6  $\mu\text{m}$  CZT multilayer (hard axis)

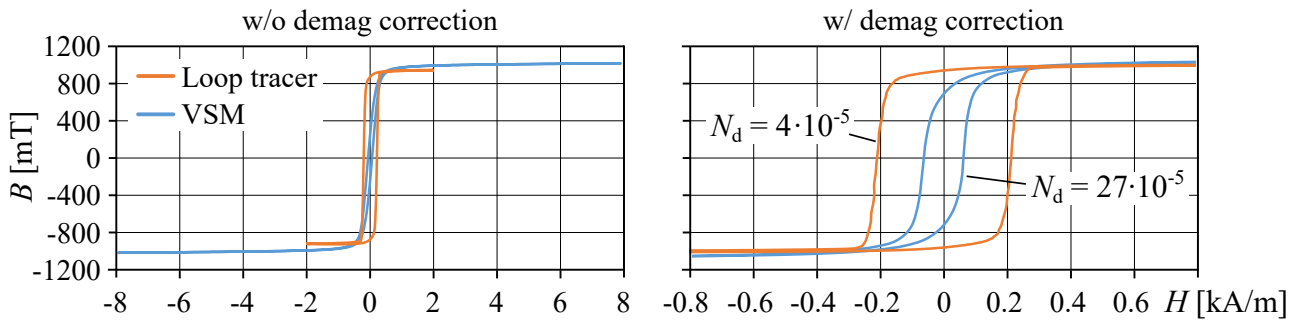


**Figure 8.8** Reference measurements of the 500 nm electroplated  $\text{Ni}_{81}\text{Fe}_{19}$  layer

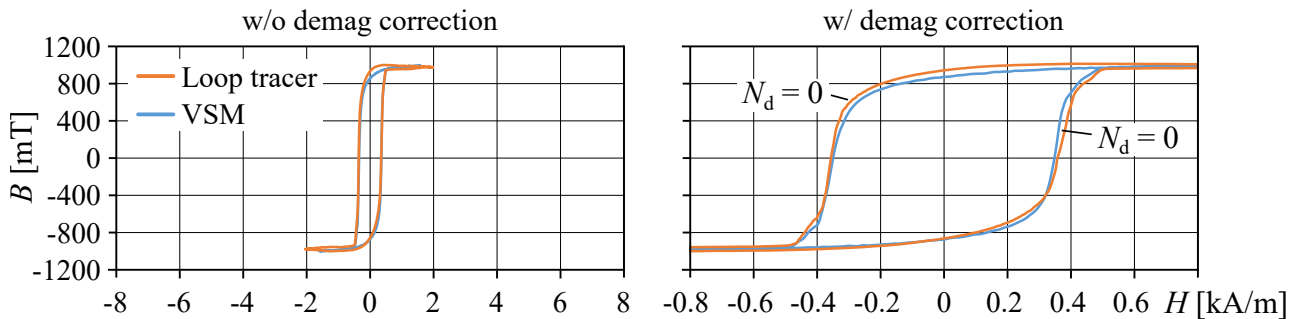


**Figure 8.9** Reference measurements of the 100 nm sputtered  $\text{Ni}_{81}\text{Fe}_{19}$  layer

The first thing to note from the graphs is the discrepancy between the measurements of the hysteresis loop tracer and the VSM for samples with a height in the micrometer range. When considering the raw data, all the measurements taken with the VSM show a significant demagnetization effect, which results in the faulty slope of the corresponding hysteresis loop. For the 80  $\mu\text{m}$  ferrite sheet for example, the value for  $N_d$  accounts to almost 0.02, while it is 50 times lower for the sample measured with the hysteresis loop tracer. Hereby, the demagnetization factors were chosen empirically in order to achieve an almost vertical increase at the coercivity field strength. With the corresponding corrections applied, the graphs (on the right) look much more alike. However, especially for the very soft magnetic samples, the correction does not work perfectly in case of the VSM as the measurement of the ‘Metglas’ sample shows most impressively. Since rectangular and cylindrical samples do not

have one single demagnetization factor but instead it varies throughout its body, it is impossible to correct it with a single value for  $N_d$  (subsection 2.1.5). The result of such an unsuccessful correction attempt can be observed in the distorted graphs on the right: While the measured saturation flux density shown in the left graphs generally matches well between the VSM and the hysteresis loop tracer, it is reached apparently at different field strengths: as can be seen in the graphs the gradient of the hysteresis loop decreases to almost zero at a flux density still far away from saturation. In conclusion, the VSM gives accurate results for the coercivity and the saturation flux density but not for the true shape of the hysteresis loop in between these points in the curve. Exceptions apply if the material has a comparatively low permeability of less than about 100 or is below one micron in height.

The hysteresis loop tracer on the other hand displays the almost correct curve progression and there is a noticeable difference between the materials showing either a hard or soft transition from the steep slope at the coercivity field strength to the saturation area. The accuracy is due to the almost two magnitudes lower demagnetization factor in comparison to the samples used in the VSM. On the other hand, the hysteresis loop tracer will probably lack in precision when it comes to layer heights of 100 nm or below. This is because of the decreased induction voltage and the subsequently necessary higher gain of the attached amplifier, which in turn lowers its speed.

From the plot of the calculated phase shift of the ‘AD8253’ in Fig. 5.18 it was already concluded that there is a significant phase shift to be expected for a gain of 1000. Though the phase shift at the excitation frequency of 50 Hz accounts to a little less than  $0.1^\circ$ , it has to be kept in mind that this is related to a sine wave signal. For the abruptly increasing induction voltage created by the sharply increasing flux at the point of coercivity, this graph is of limited significance. For a better understanding of this context, Fig. 8.10 shows the amplified time based input voltages of the MR sensor and the induction coil occurring during the measurement of the 100 nm  $\text{Ni}_{81}\text{Fe}_{19}$  sample. While the MR sensor signal accurately reflects the sinusoidal course of the field strength, the induction voltage in the coil is zero most of the time with a single negative peak just after the zero crossing of the magnetic field and a second positive peak a half-period later when the field has reversed. Some voltage slopes are calculated and inserted in the enlarged view on the right side. The values of 8 V/ms and  $-16$  V/ms correspond to the maximum gradient of a sine wave of approximately 1 and 2 kHz respectively and make clear that the signal contains components of much higher frequencies than the exciting field.

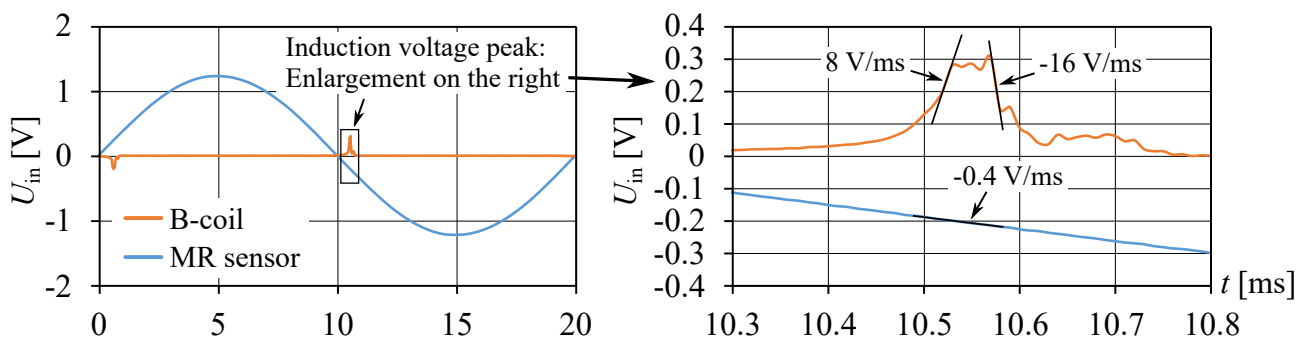


**Figure 8.10** Time based input voltages from the magnetic field sensor ‘CT100’ and the induction coil acquired for the determination of the hysteresis loop of the 100 nm  $\text{Ni}_{81}\text{Fe}_{19}$  sample

Eventually, it is rather the step response of the amplifier and its slew rate that are of importance. From the enlargement of the peak it is noticeable that its plateau is only about  $50 \mu\text{s}$  wide before the voltage falls off again. According to the step response charts depicted in the data sheet of the ‘AD8253’ the device has a settling time of more than  $10 \mu\text{s}$  at a gain of 1000. Because this is a significant time in relation to the size of the peak, a gain of 100 was selected for the measurement since the settling time is less than one microsecond in that case [Ana, 2012, p. 14]. The drawback, however, is a ten times smaller input voltage available at the input of the ADC and a subsequently reduced resolution. In any way, the measurements of the  $100 \text{ nm Ni}_{81}\text{Fe}_{19}$  sample performed with the VSM and the hysteresis loop tracer match with remarkable accuracy and noise does not seem to be an issue.

In general, the measured saturation flux density values match well as the resulting deviations amount only to a few percent, which is within the measurement uncertainties. In terms of coercivity, the situation is a little more diverse. There is a good consistency for most of the samples except for the weak axis of the CZT stack and the electroplated  $\text{Ni}_{81}\text{Fe}_{19}$  layer. In case of the CZT stack, an external measurement is available which strongly supports the one made with the hysteresis loop tracer. Local irregularities of the coating may have caused the wrong coercivity measured with the VSM. Regarding the electroplated sample, it was found out that the coating is very inhomogeneous and that the coercivity is strongly angle dependent. Apparently, there is an imprinted preferred axis that varies between the sample of the hysteresis loop tracer and the one used in the VSM. Therefore, the results of this sample should be treated with caution. On the other hand, it is an interesting challenge for the developed device, which is able to apply different measurement angles easily.

### 8.2 First Measurement Series with the Developed System

The reference measurements presented and evaluated in subsection 8.1.3 show that the hysteresis loop tracer gave the better results, especially for the samples with a thickness in the micrometer range due to the much lower demagnetization field. Therefore, these measurements will be used as reference for the comparison with the ones obtained using the developed device.

The general aim now is to reproduce the measured hysteresis loops of all sample materials. This serves the verification of the principle to use an indirect flux measurement to determine the properties of a magnetic sample. The mathematical model behind it is included in the signal processing algorithms, that were explained in section 6.2. To summarize it once more, there are basically three subsequent calculations, which are performed to convert the flux measured by the induction coil and the apparent field strength captured by the MR sensors into the hysteresis loop of the sample. At first, the offset flux per field strength  $\Phi_0/H$  is subtracted from the measured flux, which was calculated to  $186 \text{ nWb/A/m}$  in subsection 6.2.3. Anyway, this value can vary slightly due to variations of the magnetic circuit and its different behavior at different frequencies. It therefore represents a first variable, which, however can easily be determined by the condition that the remaining flux has to be zero if the magnetic circuit is open. Therefore, the value is determined prior to each measurement and afterwards treated as being

constant. Once the circuit is closed by attaching the core to a magnetic material, it is assumed that the extra flux must have passed the analyzed material. Therefore, the flux density is obtained by dividing this remaining flux by the sample's effective cross section. While its height is usually known, the determination of the width remains the main challenge of this measurement technique as stated in the introduction. The use of the MR sensor array can help but ultimately, it is found by comparing the measurement to the reference hysteresis loop. If the apparent flux density is too high, the width has to be increased and vice versa. Therefore, the effective width represents a second variable, which at first is selected in order that the measurement matches the reference data. However, it is the aim to predict this value depending on the material type and thickness of the sample and therefore be able to analyze unknown materials as well. Eventually, the last calculation concerns the true field strength within the sample, which is lower than the apparent one due to the demagnetization effect. The correct value for  $N_d$  can only be estimated in the first place and is also found by comparison with the reference data. Its uncertainty is a general problem of magnetic measurements (subsection 2.1.5).

These three consecutive calculations are visualized for an exemplary measurement of the 'FS1000' ferrite sheet in Fig. 8.11. Here, the red curve shows the initial flux measurement while the yellow one corresponds to the remaining flux with the offset subtracted. Both curves are referred to the axis on the left. By dividing the remaining flux by the sample's cross section, the light green curve is obtained, now corresponding to a flux density and referred to the axis on the right. The dark green curve eventually represents the final hysteresis loop with the demagnetization correction applied. Because the looks of the hysteresis loop strongly depends on the three described variables, their individually values used for the calculations are shown in the graphs of the following measurements.

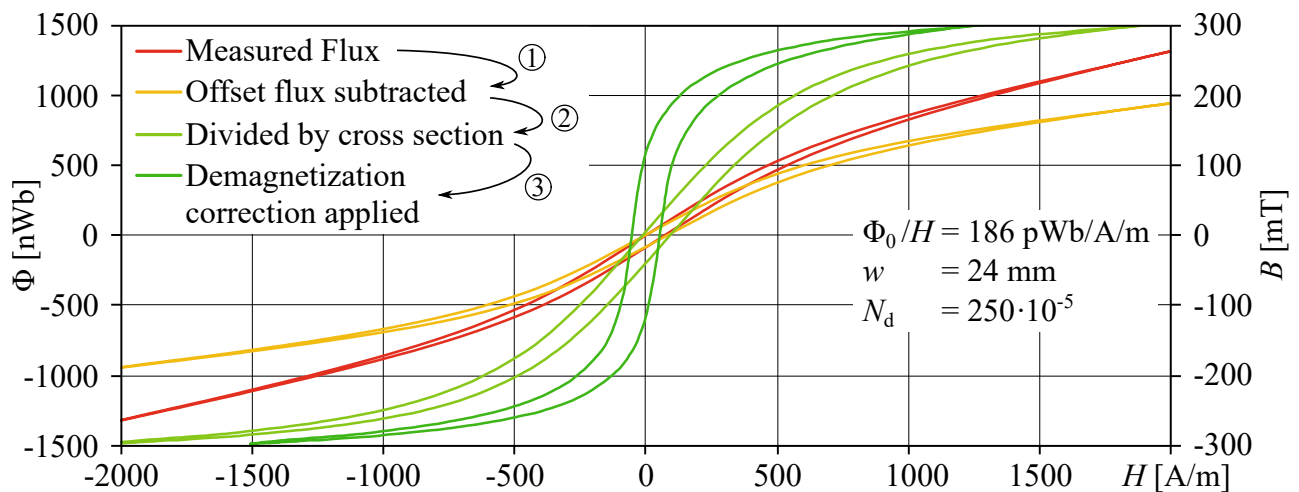


**Figure 8.11** Exemplary visualization of the steps for calculating the hysteresis loop in case of the 80  $\mu\text{m}$  'FS1000' ferrite sheet from the measured flux in the yoke

The next six figures from Fig. 8.12 to Fig. 8.17 contain the hysteresis loops of the first five sample materials ordered as in Table 8.1. For the CZT multilayer, both the easy and the hard axis are shown in separate figures, while the measurement of the 100 nm nickel iron layer is not shown at all due to excess noise. All loops were recorded at an excitation frequency of 100 Hz and 50 dB gain.

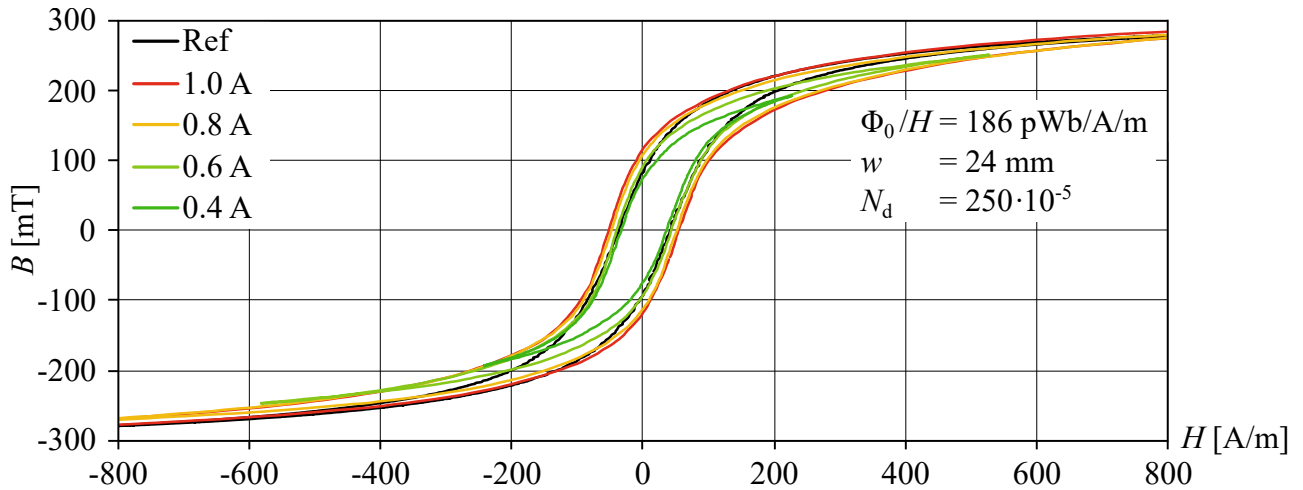


**Figure 8.12** Measured hysteresis loop of the 80  $\mu\text{m}$  'FS1000' ferrite sheet at 100 Hz and different currents

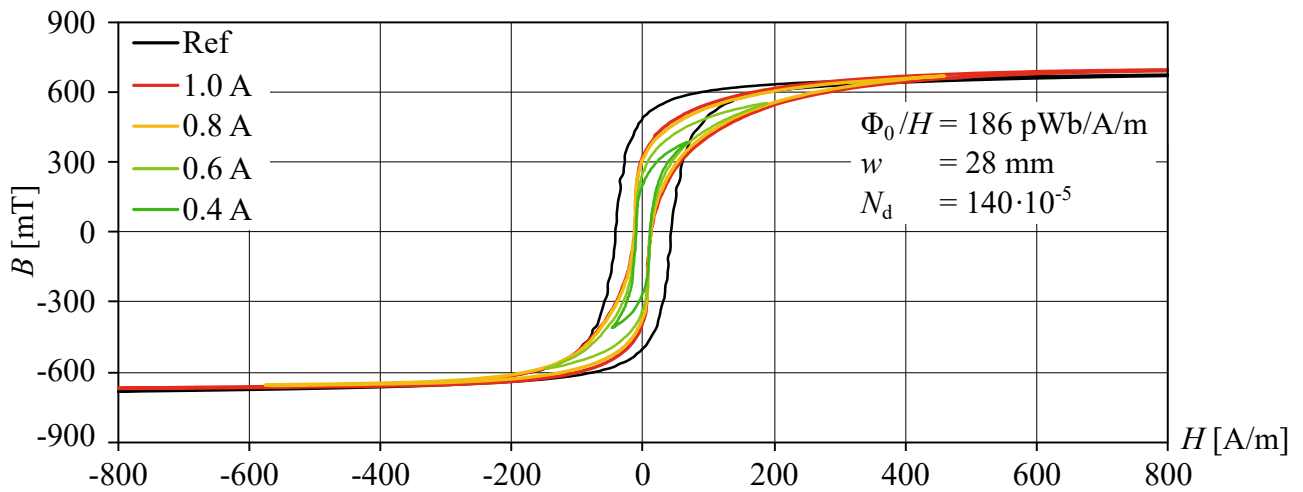


**Figure 8.13** Measured hysteresis loop of the 50  $\mu\text{m}$  'MuMetall' foil at 100 Hz and different currents

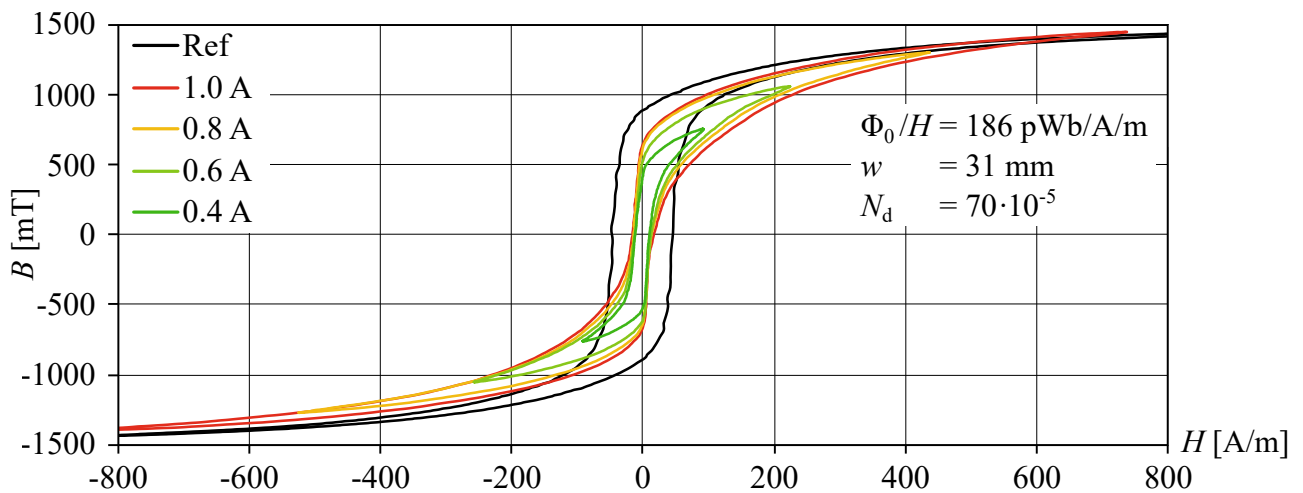


**Figure 8.14** Measured hysteresis loops of the 23  $\mu\text{m}$  'Metglas' foil at 100 Hz and different currents



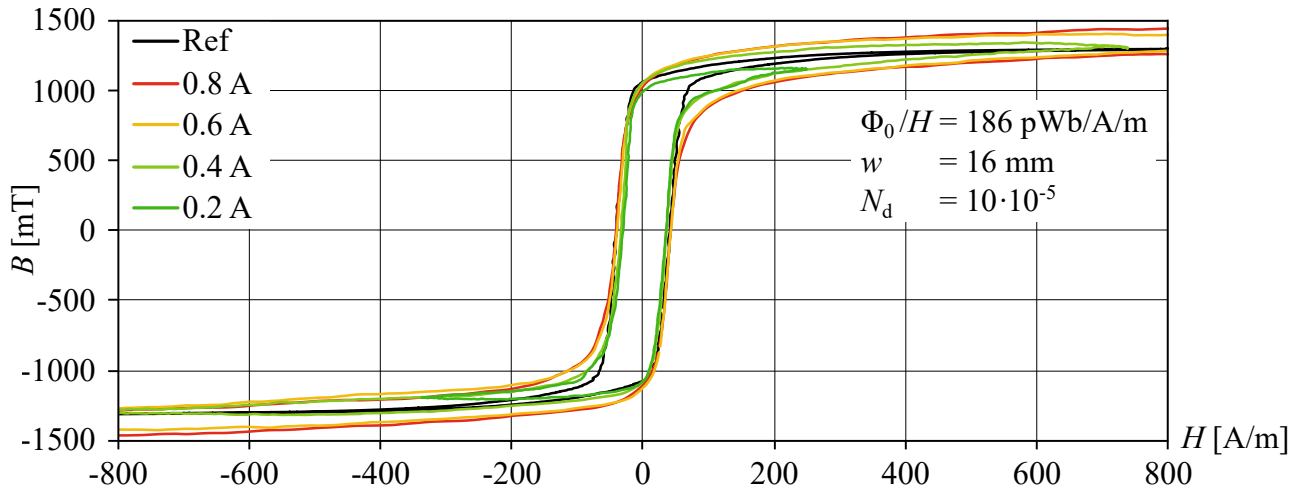


**Figure 8.15** Measured hysteresis loops of the 6  $\mu\text{m}$  CZT multilayer (EA) at 100 Hz and different currents

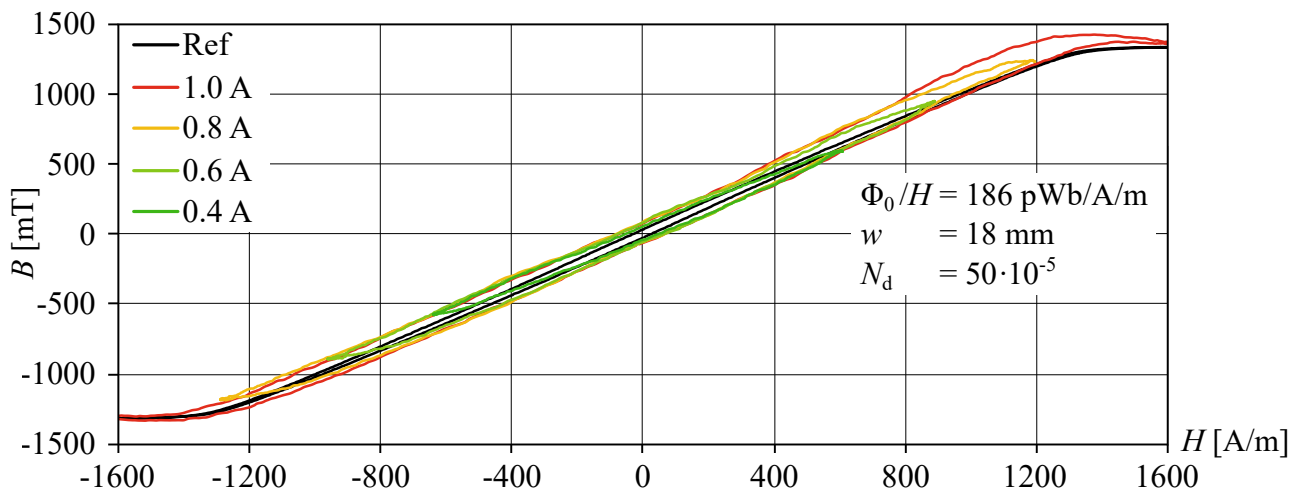


**Figure 8.16** Measured hysteresis loops of the 6  $\mu\text{m}$  CZT multilayer (HA) at 100 Hz and different currents

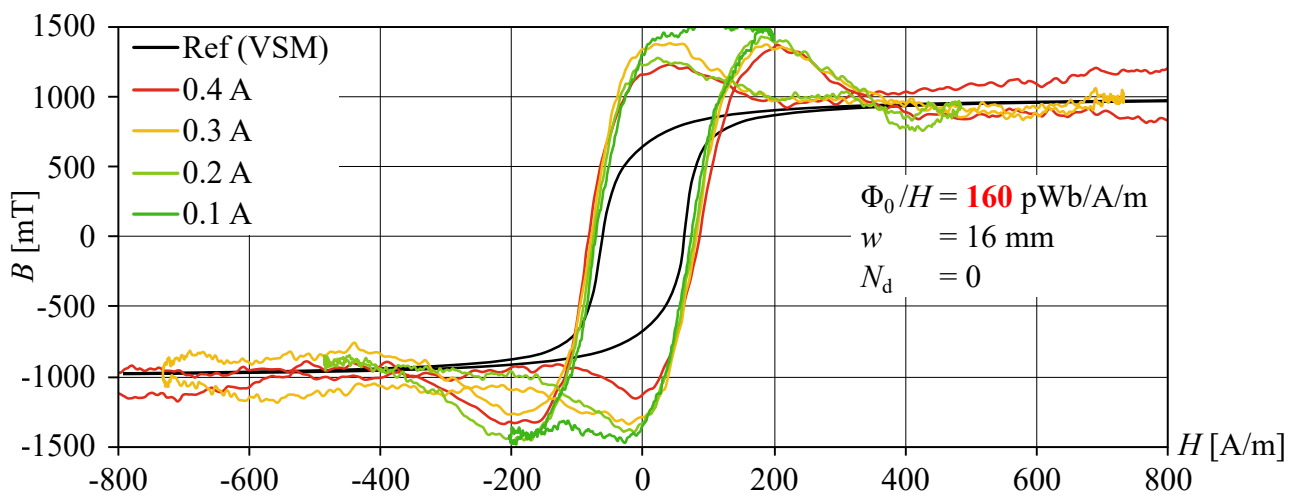


**Figure 8.17** Measured hysteresis loops of the 500 nm  $\text{Ni}_{81}\text{Fe}_{19}$  layer at 100 Hz and different currents

Generally, it is to say that the system is capable of measuring hysteresis loops with satisfying accuracy when using the right parameters for the offset flux, the cross section and the demagnetization factor. As stated before, the offset flux was kept at the same value of 186 pWb/A/m and only the cross section and the demagnetization factor  $N_d$  have been varied for each sample. However, regarding the three sheet samples, the effective width had to be chosen very high in order to match the reference measurement. The values range from 24 mm for the 80  $\mu\text{m}$  ‘FS1000’ ferrite sheet to 31 mm for the 23  $\mu\text{m}$  nanocrystalline ‘Metglas’ foil and are all far away from the true width of the core of 12 mm. Apparently, the effective width does not correlate with the sample height alone. It is rather assumed that the combination of its height and permeability increase the effective width allowing the flux to rather pass in a region further away from the core. For unknown magnetic properties, however, this varying value of the effective width is problematic as the true maximum flux density can not be determined with certainty. Apart from the difficulties with the flux density, the measured coercivity deviates significantly from the reference hysteresis loop for the ‘MuMetall’ and the ‘Metglas’ sample. Furthermore, there is a deviation at the point when the material reaches the saturation region since the transition is not as sharp as in the reference measurement. Both these samples are relatively thick and magnetically weak, which apparently are the most difficult ones to measure.

Regarding the analyzed thin film samples, the results match the reference more closely. The determined effective width accounts to 16 mm both for the CZT and the NiFe sample, which seems as a comprehensible value for the core. That corresponds to its physical width of 12 mm plus a 2 mm section on each side of it. In case of the CZT sample, the transition to the saturation region is sharp and the coercivity matches the reference with an error of only a few A/m. The hard axis, however, shows a higher width and demagnetizing field, which is also comprehensible as the flux travels easier along the sample’s preferred axis, which is aligned perpendicular to the excitation field in this case. The measurement of the 500 nm NiFe sample matches the reference in terms of saturation flux density and also in terms of coercivity when comparing it to the VSM data. (The reference measurements were quite non-compliant for this sample.) However, it shows other issues like a flux density overshoot at the transition point to the saturation region. Also, the flux offset value had to be changed in order to have the flux density becoming level in the saturation range instead of pointing downwards due to the subtraction of a too high offset value. The used value of 160 pWb/A/m was found from the knowledge that the flux density is level in the saturation range. Another issue is the high noise in the measurement, which fits to the estimated noise level in the end of subsection 7.2.4 corresponding to 33 mT<sub>RMS</sub> in a 500 nm thick sample. However, apart from the high frequency noise causing the ripple, there is also a more disturbing low frequent noise, that can be observed especially in the saturation region. It causes irregular and quite high deviations from the expected straight line altering the measurement much more significantly than the ripple.

While the noise (or at least the high frequency part of it) was expected, the occurring overshoot in the measurement was not. It is probably caused by the fact that prior to the saturation of the sample, the magnetic circuit is almost closed. This lowers the demagnetization effect and therefore increases the measured offset flux, which is also affected by demagnetization in the core (subsection 6.2.3). Therefore, the flux offset value should technically be higher as long as the sample is not saturated. It

is expected that this issue also occurs for the other samples but is not visible in the measurements due to their higher film thickness. The measured overshoot of 400 mT above the saturation flux density corresponds to a flux of 3.2 nWb, which only causes an error of 33 mT in the 6  $\mu\text{m}$  CZT sample. However, this consideration does not explain why the offset flux is lower and accounts only to 160 pWb/A/m. This would mean that there is less flux flowing within the core with the magnetic sample placed close to the measurement head than without it, which does not make sense. However, the increase of the distance between the measurement head and the sample resolves the issue. This way, the circuit remains open regardless if the material is saturated or not. Due to the stepper motors and the precise mechanics, distances with a resolution of ten microns can reproducibly be set. The measurement from a distance of 500  $\mu\text{m}$  depicted in Fig. 8.18 shows the benefit of this method. While the overshoot is almost gone, a drawback of the increased distance is the lower maximum field strength reduced by a factor of 1.81 and therefore, also the offset flux is reduced by this factor.

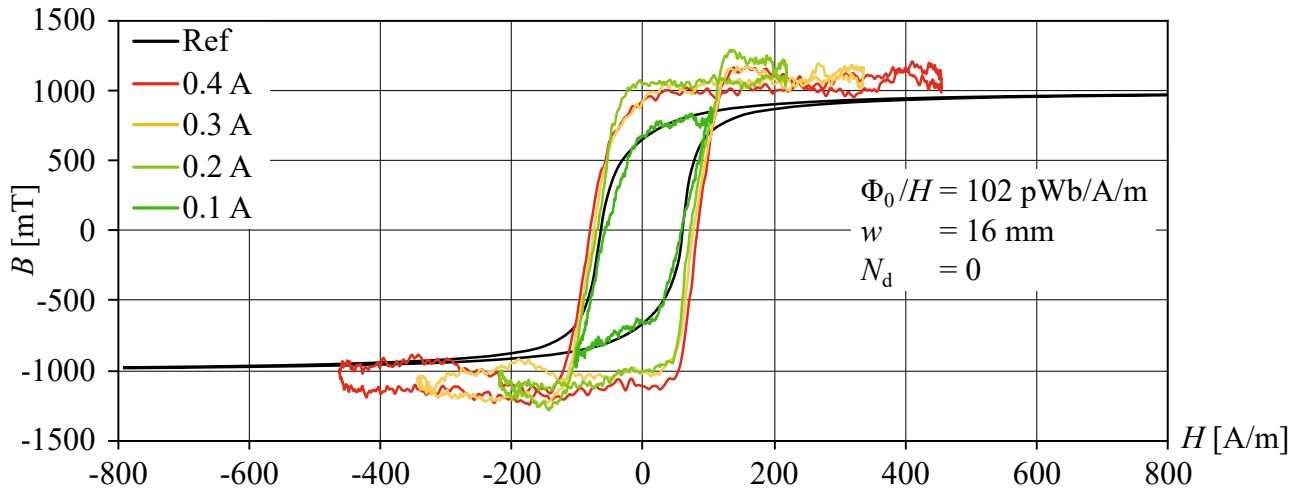


**Figure 8.18** Hysteresis loops of the 500 nm  $\text{Ni}_{81}\text{Fe}_{19}$  layer at 100 Hz and different excitation currents measured from a distance of 500  $\mu\text{m}$  between the ferrite core and the wafer

It has to be noted that the minimum distance during all measurements is 40  $\mu\text{m}$  defined by thickness of a polymer film attached to the ferrite core, which prevents harm to the wafer's surface when the measurement head is pressed against it. The minimum gap between the ferrite core and the sample helps to keep the demagnetization effect in the core at a more uniform level. Therefore, it prevents a current overshoot in the primary winding, that can occur at the beginning of a measurement (in the non-steady magnetization state of the sample). It is caused by random mismatches between the remanence magnetization in the sample and the direction of the excitation field and is an issue also known from the switching of large transformers, which can randomly trigger the fuse.

In this case, the short circuit protection of the main amplifier was often tripped when currents above 0.8 A were applied even though the threshold is at 1.2 A. During the evaluation of the measuring system, it was found that a 40  $\mu\text{m}$  film represents a good compromise between a maximum applicable field strength and sufficient amplifier stability. This way, currents as high as 1.2 A can be set at various frequencies without any problems.

These first results prove that the developed system works in general but also make clear that the determination of the width of magnetically excited region within the sample is crucial. However, this issue was already taken into account during the design of the measurement head, which therefore features an array of MR sensors (see section 4.3). For all measurements shown in the previous charts, the field strength was recorded by the four attached sensors. The results are depicted in the graphs in Fig. 8.19. To be able to compare them more easily, the field strength is normalized by dividing the values by the individual maximum. Consequently, the values along the y-axis range from  $-1$  to  $1$  while the x-axis corresponds to the time scale and shows a single period of  $T = 10$  ms.

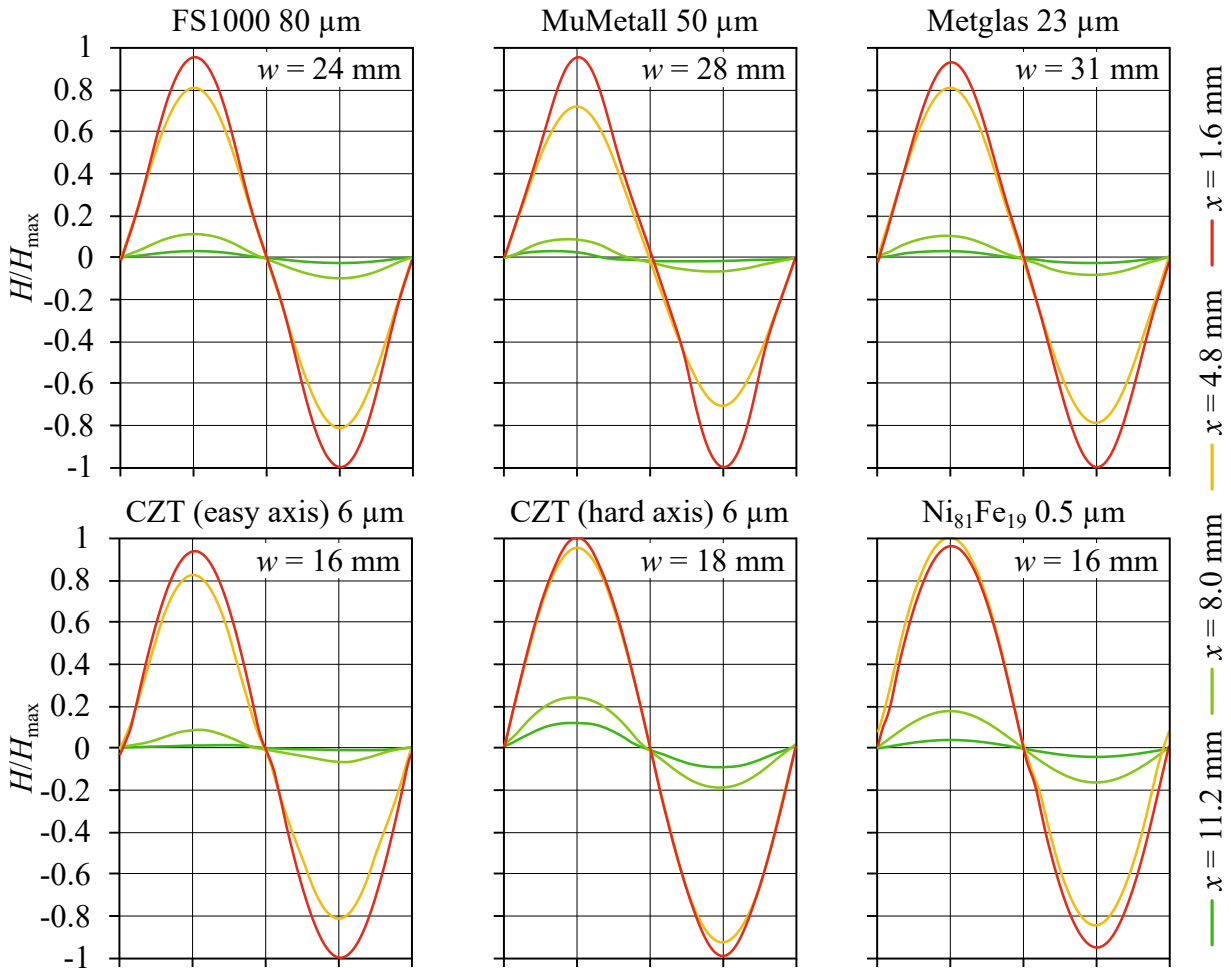


**Figure 8.19** Normalized course of the field strength recorded by the four MR sensors in the array during the hysteresis loop measurement of all samples

Generally, it is to say that the field strength at a distance of 8 mm from the center of the ferrite core accounts to only about 10 % of the maximum field strength while it is about 80 % at 4.8 mm distance. This is similar for all samples and it is not obvious why the effective width of the three sheet materials is about 1.5 to two times higher in comparison to the thin films. Striking, however, is the form of the sine wave of the two central sensors, which it is altered in a way that it resembles a straight line around the zero crossing point. For the ‘FS1000’ sheet, this is the case in the range of  $\pm 0.3 H_{\max}$  while for the ‘MuMetall’ and the ‘Metglas’ sample, it is altered between  $\pm 0.4 H_{\max}$ . Even for the

CZT sample, this alteration is visible in a small range of  $\pm 0.07 H_{\max}$ . This effect is an indicator for the weak magnetic samples to decrease the field strength close to them when they are not saturated. It allows the distinction of the soft from the hard axis of a material as in this case the waveform remains almost unchanged as can be seen for the CZT sample. The measurement along the hard axis of this sample also shows an increased field strength further away from the center as the sensor  $x = 11.2$  mm indicates an amplitude of 13 % in relation to the centric field strength. For the other samples, the field strength at this point accounts to about 3 to 4 %. Only the NiFe sample shows also a comparably high field strength at the outer sensors, which explains the slightly too high flux density since the width was chosen too small (Fig. 8.18).

In summary, the use of the MTJ based MR sensor array presents a useful way to tell the easy and hard axis apart and to estimate small adaptations of the effective width of the magnetic flux within the sample. Therefore, the comparison of the amplitude at the outer sensors with the one measured in the center of the core can be used. The success of this method could be demonstrated for the CZT sample with its soft and hard axis. According to this sample's results in Fig. 8.19, it seems reasonable that the effective width for the hard axis is increased. Apparently, the results of the MR array are in compliance with the different widths used during the hysteresis loop calculations regarding the thin film samples. For the sheet samples, however, there is no indication for the assumption that the effective width deviates much from 16 mm, especially not as much as +50 % and more. Consequently, for the measurements to still match the reference data, it has to be the offset flux that is much higher than assumed, at least in the beginning of the measurement when the sample is not saturated. Even though, the induction coil is located far away from the ends of the core and there is a minimum 40  $\mu\text{m}$  air gap between the sample and the core (ensured by the protective film), the demagnetizing factor in the core varies at the position of the coil. Evidently, the magnetic circuit is so strongly influenced by the sheet samples that they (partially) close the magnetic circuit and lower the demagnetization effect significantly. Therefore, the offset flux appears to be higher and eventually a higher amount has to be subtracted. Once the sample under evaluation saturates and therefore behaves like a non-magnetic material, the offset flux approaches the open circuit value of 186 pWb/A/m. Accordingly, the demagnetization factor must not be treated as being constant but moreover, it varies in dependence on the saturation state and therefore on the momentary flux density  $B(t)$  in the sample. This, however, is the unknown unit that is intended to be measured by the developed device, which results in a mutual dependence and illustrates the severity of the issue of an uncertain demagnetization factor in the core. A possible solution is the increase of the distance between the sample and the ferrite core as already suggested for the NiFe sample since this lowers the influence of the sample on the core. On the downside, this will significantly reduce the achievable field strength. Another idea is to use the measurement of the field strength and conclude on the saturation state of the sample from the amount the sine wave is altered (Fig. 8.19). However, since it is not the intention to develop a measurement system for sheet samples but for thin films, which indeed were successfully measured, none of these enhancements will be implemented for now. Instead, the focus is laid on improving the signal quality to allow the measurement of thin films with a height of below one micron with less noise.

## 8.3 Improvements

### 8.3.1 Consecutive Averaging

According to the measurement results of the 500 nm NiFe thin film depicted in Fig. 8.17, there is too much noise for the analyzation of even thinner layers. The displayed noise level corresponds to the expected value for the induction coil calculated on the basis of the noise measurements in subsection 7.2.4 performed at 100 Hz. Using the effective width of 16 mm, it accounts to

$$B_{\text{RMS}} = \frac{2 \cdot 10^{-10} \text{ Wb}_{\text{RMS}}}{16 \cdot 10^{-3} \text{ m} \cdot d} = \frac{1.25 \cdot 10^{-8} \text{ Tm}}{d}. \quad (8.2)$$

where  $d$  is the thickness of the layer. Inserting a value of  $d = 100 \text{ nm}$  results in a noise of  $125 \text{ mT}_{\text{RMS}}$ . This value already benefits from the method of cycle averaging explained in subsection 6.2.1 and would be higher even without it. The noise reduction was evaluated in subsection 7.2.3 and 7.2.4, which showed that it decreases by 6 dB when the number of averaged cycles  $n$  is increased by a factor of four. Consequently, the noise reduction can be calculated by

$$\Delta B_{\text{RMS}}[\text{dB}] = 10 \cdot \log(n). \quad (8.3)$$

It seems natural to further decrease the noise by averaging even more cycles. However, there is a limitation of this method since the inaccuracy of the direct digital synthesis has to be taken into account at low excitation frequencies. At these conditions, its resolution of 0.186 Hz (subsection 5.2.1) represents a significant error with the consequence that there is a mismatch between the generated frequency and the sampling rate of the DAQ, which eventually leads to a degradation of the measurement data. However, at low frequencies, the high speed of the DAQ allows another way of acquiring more samples to average. By default, 1,000 data points are recorded for one cycle, which results in a sampling rate of 100 kS/s for a 100 Hz signal. Therefore, there is enough headroom to increase the speed by factor of up to 200 in this case (20 MS/s is the maximum sample rate) and average the 200 consecutive samples for a single data point. Eventually, the combination of both averaging types offers the possibility to record a multitude of the 1,000 data points. At low frequencies, a high amount of consecutive samples can be averaged while at higher frequencies, the already described cycle averaging comes in place. The only limit of this method is the size of the internal memory of the DAQ, which stores up to 2.1 million samples when two channels are used.

Another benefit of increasing the sample rate is the avoiding of aliasing effects that are believed to be the cause for the apparent low frequency noise observed in the measurement of the 500 nm NiFe sample shown in Fig. 8.17. Since these first measurements were captured at a rate of 100 kS/s, the highest detectable frequency is 50 kHz. The spectral density graph depicted in Fig. 7.12, however, proves the presence of excessive noise above that threshold. Therefore, it is likely that this noise causes the occurrence of random signals with apparent lower frequencies known as aliasing. Also the other measurements are subject to this erroneous effect but due to the signal strength resulting from the higher layers, it is not visible in the corresponding graphs.

### 8.3.2 Additional Induction Coil

Apart from the metrological improvement, there was also a hardware modification carried out, which is believed to allow for more accurate results. Based on the finding that the offset flux varies and must not be assumed as having the same value for all samples, the initial reason to locate the induction coil at the midpoint of the ferrite core no longer exists. Instead, the choice of the offset value based on the knowledge that the course of the hysteresis loop eventually runs in parallel to the x-axis has proven successful. Consequently, the induction coil can be wound at any position on the ferrite core, which also offers the possibility to put it in small slots at the very bottom of the core as shown in Fig. 8.20. The slots are fabricated by laser-cutting and are 8 mm apart from each other, about 1.5 mm deep, 200  $\mu\text{m}$  wide at the entry point, and tapered. The inserted coil has ten turns and is wound by hand with a 70  $\mu\text{m}$  enamelled copper wire and fixed in the slots with cyanoacrylate.

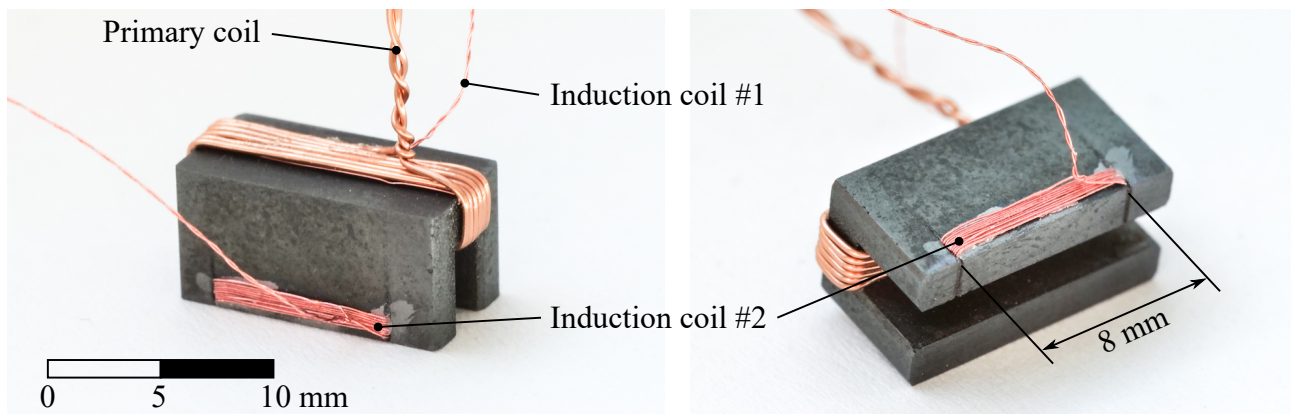


**Figure 8.20** Ferrite core with an additional induction coil, inserted in two laser-cut slots at the bottom

The magnetic circuit now features two induction coils for comparison. The main difference for the new one is that it only captures the flux in the central  $\pm 4$  mm. As shown by the field simulations (Fig. 4.7), the magnetic field between the core's poles is uniform and of similar strength in this range. This assumption was also proven empirically using the MR sensor array, whose output data (visualized in Fig. 8.19) reveals that for all thin film samples, the field at 4.8 mm distance from the center amounts to at least 80 % of the maximum value. Apart from this benefit, it can be assumed with great certainty that the measured width of the sample accounts to 8 mm since the flux occurring at the sides of the core is not flowing through the cross section of the coil. That leaves the offset flux as the only variable despite the general issue with the demagnetization effect in the sample.

## 8.4 Second Measurement Series with the Developed System

With both improvements applied, the measurements of the magnetic materials are repeated. However, the difficulty of measuring sheet samples with a comparably high thickness persists. The results of the high permeable 'MuMetall' and 'Metglas' are altered in a similar way as already visible in Fig. 8.13

and Fig. 8.14 while the one of 'FS1000' matches the reference slightly better. More interesting are the measurements of the 500  $\mu\text{m}$  NiFe thin film, which are depicted in Fig. 8.21. Apart from the previous and the reference measurement, there are three hysteresis loops shown, that were recorded just after another but calculated with different flux offset values of 29, 29.5, and 30 pWb/A/m to visualize the effect of such a small change. The width used in the calculation is 8 mm and there is no demagnetization correction applied.

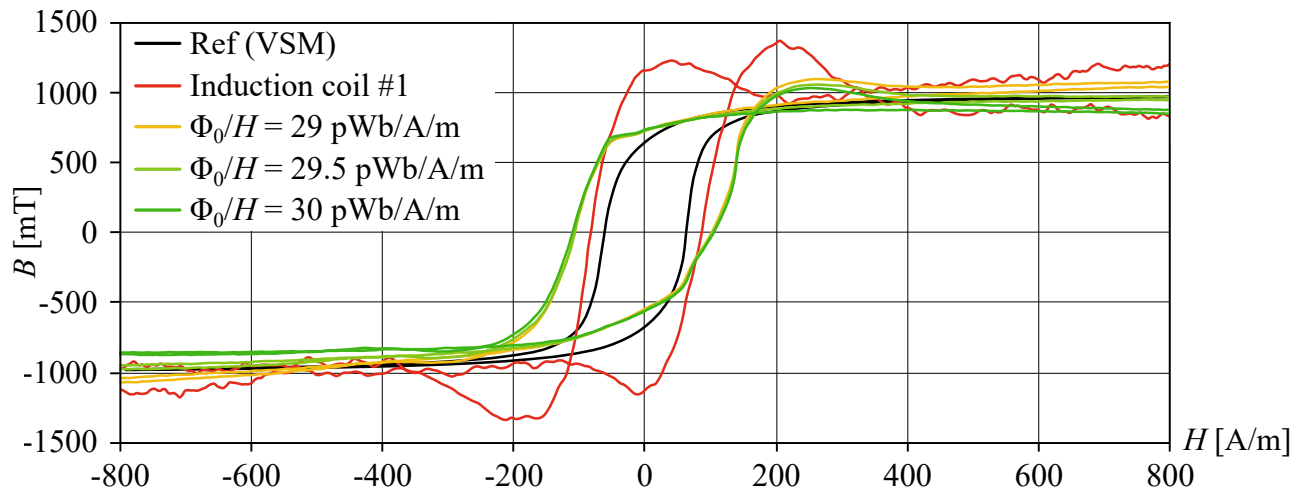


**Figure 8.21** Hysteresis loops of the 500 nm  $\text{Ni}_{81}\text{Fe}_{19}$  layer measured at 100 Hz with different offset flux values used for the calculation

The results look quite different in comparison to the one made with the first induction coil. On the positive side, the overshoot is less noticeable and the noise is much lower and barely visible. This proves the success of the method of consecutive averaging. Every single of the 1,000 data points is calculated by averaging 25 consecutive samples over 16 sine wave cycles, which makes a total of 400 samples. Technically, this should decrease the noise only by a factor of 2.5 in comparison to the previous measurement. However, the higher sampling rate effectively avoids aliasing effects and therefore decreases the noise even more significantly than expected. Generally, the noise level of the second coil is found to be slightly lower than the one of the first coil, possibly because it is further away from the primary winding and there is a lower coupling between them.

On the negative side, there is a noticeable error regarding the coercivity, which is 60 % larger than the reference value and still 23 % larger than the one obtained with the first coil. The latter difference results from the fact that the whole width of 8 mm is subject to the same field strength now. Previously, the side areas of the core were subject to lower values and subsequently, the point of zero flux density is altered. The general error in comparison to the reference probably results from the distance of the MR sensor to the layer, even though it accounts to only 200  $\mu\text{m}$  (Fig. 4.5). The corresponding simulation of the course of the field strength (Fig. 4.11) shows that the sensor is located at a point of higher field strength. However, this simulation was performed for a 2  $\mu\text{m}$  permalloy layer and depending on the sample's properties the difference between the apparent and the true field strength varies. This becomes evident from the measurements of the other thin film samples.



Due to the improved signal quality, the analyzation of the 100 nm NiFe film is eventually possible. To demonstrate the capabilities of the developed system, the sample's properties are not only determined at 100 Hz but at different frequencies ranging from 50 Hz to 10 kHz (Fig. 8.22). All measurements show about the same coercivity with only a slightly increase at elevated frequencies. Again, it is higher than the reference value while the saturation flux density matches the reference well.

It is worth to examine the acquired signals more closely. Therefore, Fig. 8.23 shows the time-based course of the flux measured by the induction coil and the offset flux calculated from the field strength for a 100 Hz excitation. The difference of both signals in green colour represents the part of the flux, that is conducted by the thin film and accounts to 0.8 nWb (referred to the magnified y-axis on the right). Its noise is as low as 20 pWb<sub>RMS</sub>, which corresponds to an achievable accuracy of 25 mT<sub>RMS</sub> in terms of flux density in a 100 nm layer, which is an impressive value. As the enlargement in the window reveals, it is not the flux density that increases at the point of coercivity as it was expected, but it is the field strength whose progression is altered similar as in Fig. 8.19.

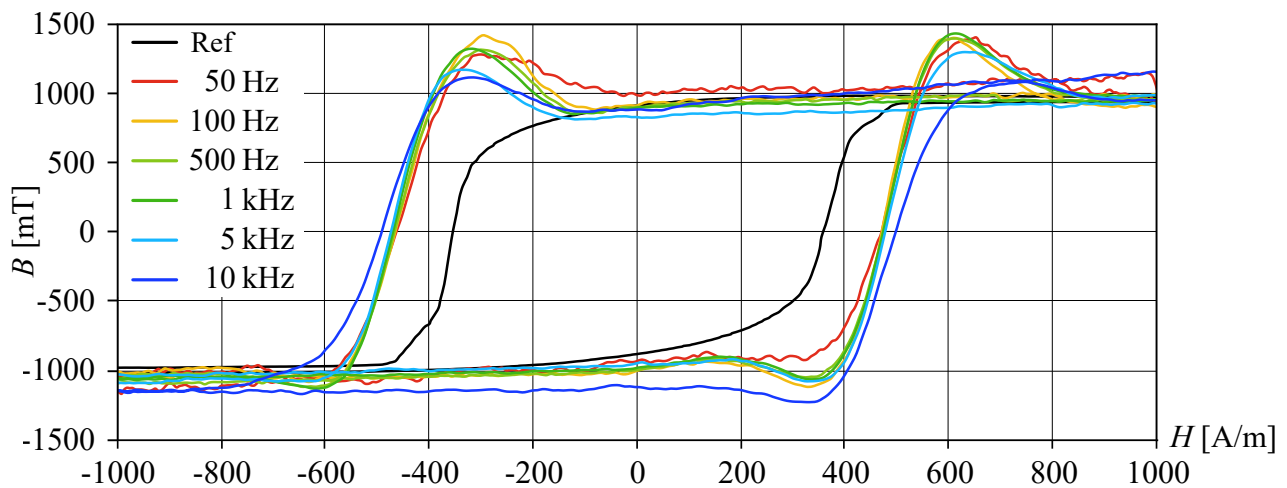


**Figure 8.22** Hysteresis loops of the 100 nm Ni<sub>81</sub>Fe<sub>19</sub> layer measured at different excitation frequencies

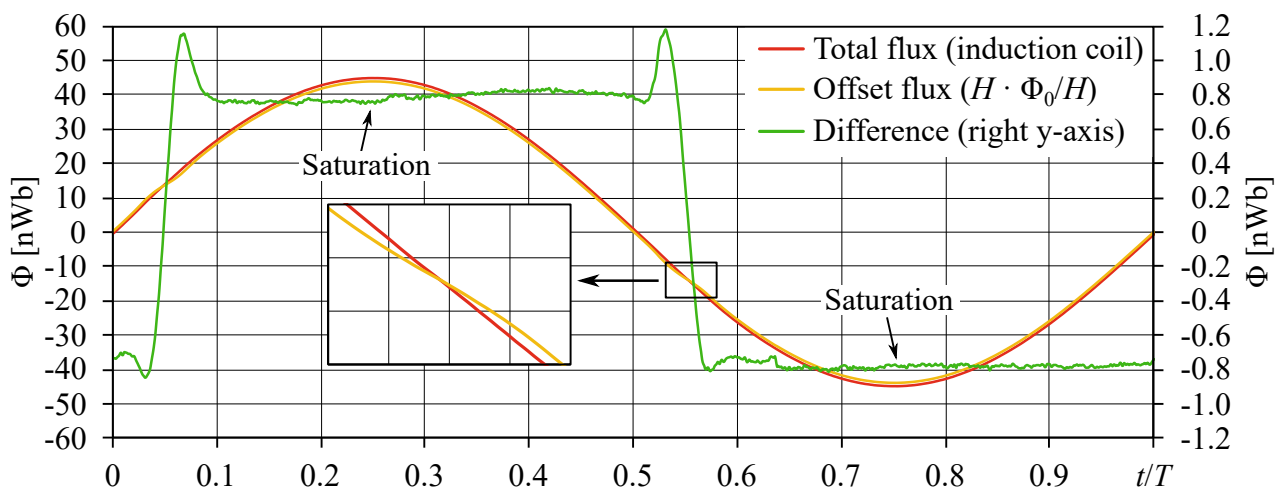


**Figure 8.23** Measured and calculated offset flux for the 100 nm Ni<sub>81</sub>Fe<sub>19</sub> sample

The same frequency dependent measurement is carried out for the easy axis of the  $6 \mu\text{m}$  CZT sample. Due to the stronger signal resulting from the higher layer thickness, the measurement is also possible at 20 Hz and up to 50 kHz. As shown in Fig. 8.24, there is a much larger frequency dependence as the coercivity increases with higher values. The subsequently growing area enclosed by the loop indicates the rising eddy current and anomalous losses (subsection 2.2.3) above 1 kHz. For this sample, the quasi-static measurement at 20 or 50 Hz show a slightly lower coercivity than the reference measurement. While this error requires a closer examination in future, the measurements are consistent and therefore comparable with each other.

The underlying time-based signals for a 100 Hz excitation are depicted in Fig. 8.25. This time, the flux conducted by the layer is much larger than the offset flux, which shows a significant deviation from a sinusoidal form. While this partially results from the demagnetization correction ( $N_d = 10^{-4}$ ), the linear course of the signals around the point of zero field strength is notable. It reveals the effect that the flux, which usually passes the air, is diverted into the ferromagnetic thin film (Fig. 2.4).

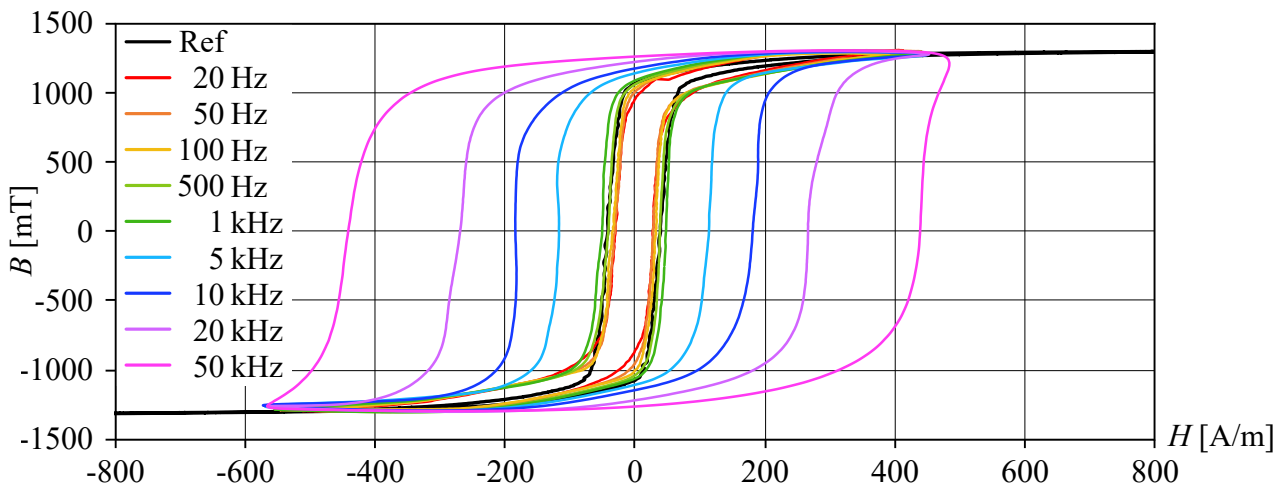


**Figure 8.24** Hysteresis loops of  $6 \mu\text{m}$  CZT layer (EA) measured at different excitation frequencies

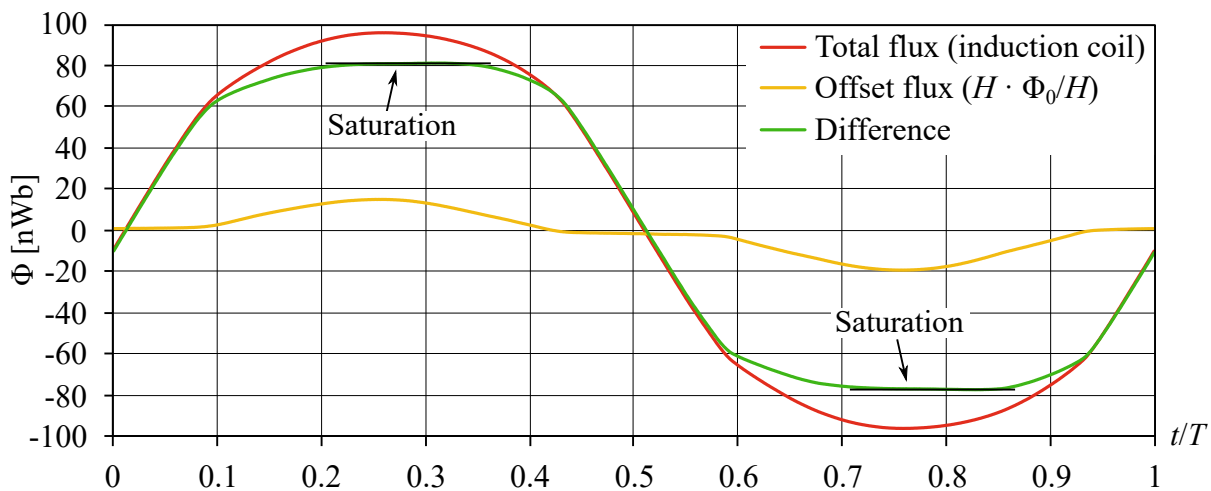


**Figure 8.25** Measured and calculated offset flux for easy axis of the  $6 \mu\text{m}$  CZT multilayer sample

## 9 Summary and Outlook

With the presentation and evaluation of the carried out measurement series and the advantages resulting from the improvements laid out in the previous chapter, the conducted work will be summarized and evaluated regarding the realized achievements. Eventually, an outlook will be given on this basis in order to specify how this novel measurement method can be further optimized and where and for what it can be used in future.

The concept of the measurement system laid out in chapter 3 made clear that it follows a novel approach for the examination of magnetic properties of thin films. With the aim of developing a device suitable for the non-destructive examination of wafers, none of the state-of-the-art metrologies served as a suitable reference. Instead, the adaption of a characterization method used for transformer steel sheets was considered as a promising way also for the examination of thin films, since Tumanski showed the feasibility of a one-yoke single sheet tester. The omission of the lower yoke offers the advantage of an easier measurement setup in comparison to a two-yoke system and also is a prerequisite for examining thin films, whose substrate prevents a proper magnetization from the back. The greater peculiarity, however, is not to measure the flux directly in the sample as usual, but to calculate it indirectly from the measured flux in the yoke and the field strength close to the specimen. With this approach, the concept represents a strong contrast to existing measurement methods.

Consequently, the subsequent chapters dealt with the special characteristics regarding the design of the measurement head, the necessary electronic circuits, and the algorithms used for the calculation of the hysteresis loop. For the head a customized U-core was obtained from a supplier after simulations and measurements have shown that the standard-sized cores are not suitable for the task due to their large area of non-uniform field. The customized core was chosen just big enough to fit the smallest commercially available magnetoresistive field strength sensors between its poles as the small size increases the maximum field strength and reduces the inductance. Eight of these sensors, which are based on the technology of magnetic tunnel junctions, were placed in a dense line array to be able to analyze the uniformity of the field propagation.

The electronic circuit was designed with respect to the head and allows the generation of sine waves up to the megahertz range while the primary coil limits the frequency up to some hundred kilohertz, achieving a field strength of up to 2.5 kA/m. Great effort was put in realizing sufficiently fast and low-noise amplification stages, that allow a phase shift free acquisition of the field strength and the flux. However, only by developing the suitable LabVIEW virtual instruments the high precision of the measurement device was achieved. Especially the decision to perform the signal integration of the induction coil in the digital domain and the implementation of a two-way averaging algorithm, which exploits the high speed of the data acquisition device have to be mentioned here.

Subsequently, all components were integrated in a fully motorized test stand enabling reproducible and automatable measurements of specimens as large as a twelve inch wafer. The characterization of this setup revealed RMS noise levels of 1.5 A/m in terms of field strength and 1.6 nWb in terms of flux. These values, however, were significantly reduced to 0.08 A/m and 0.02 nWb respectively by the applied averaging algorithms and eventually, measurements of six different thin film samples and metallic sheets ranging from 100 nm to 80  $\mu\text{m}$  in height were carried out. They were compared to reference measurements made with a vibrating sample magnetometer and a hysteresis loop tracer. The results show that the developed device is not able to examine magnetize samples with both a high permeability and a layer height of more than approximately 10  $\mu\text{m}$  due to the large demagnetization effect. However, for layer heights below that threshold, which corresponds to typical layer heights in microtechnology, good results were achieved. The feasibility of excitation frequencies from 50 Hz up to 50 kHz was demonstrated accounting to three magnitudes. Even though the output amplitude of the induction coil at 50 Hz is as low as  $\pm 130 \mu\text{V}$  and in case of a 100 nm layer only about 2 % of that induction voltage is related to the layer, a resolution of 25 mT in terms of flux density is achieved. The final specifications of the measurement system are summarized in Table 9.1. The last item in the list corresponds to the area on the thin film whose properties are examined by the device. It is given by the width of the coil (8 mm) and the size of the air gap (2 mm).

**Table 9.1** Specifications of the Measurement System

Dimension	Value
Maximum sample rate	20 MS/s
Frequency range	50 Hz - 50 kHz
Suitable layer height	100 nm to 10 $\mu\text{m}$
Maximum excitation field strength	2500 A/m
RMS noise level (field strength)	$8 \cdot 10^{-2}$ A/m
RMS noise level (flux)	$2 \cdot 10^{-11}$ Wb
Measurement spot size	8 x 2 mm <sup>2</sup>

Despite the good results in terms of sensitivity and noise, the comparison of the measurements with the reference hysteresis loops revealed that there is a discrepancy regarding the coercivity. For the analyzed nickel iron layers, it is determined to about 50 % higher than the reference, while for the CZT sample, it is 30 % lower (30 A/m instead of 40 A/m). This error is due to use of only one sensor distance for the magnetic field strength, which precludes the method of extrapolation reported in literature. The distance of the magnetoresistive element within the package of the sensor to the layer accounts to only 200  $\mu\text{m}$  but is apparently too large to allow the assumption that the error is negligible. In future, either an unpackaged die in an even closer distance or a pair of sensors for extrapolation should be used. However, this second sensor should probably be located below the wafer as the simulations showed that this would lead to a better result.

The correct determination of the field strength is crucial as it has an impact also on the calculated flux density due to the offset flux subtraction, which is based on it. While this method has generally proven successful and allows a quite accurate determination of the saturation flux density, it lacks in

precision in the part of the hysteresis loop where the sample is not saturated. One source of error is the inaccurate field strength measurement as just mentioned and the other is the influence of the layer on the demagnetization factor in the core at the point where the coil is located.

A possible solution is the increase of the distance between the U-core and the specimen as it was tested for the 500 nm nickel iron sample. This way the influence of the sample on the core is decreased and the demagnetization error becomes smaller. Also Stupakov [2012] used a setup with a large distance for his examination of transformer steels with good results. On the downside, this approach requires a higher field strength to be applied as its value in the layer decreases with distance. This could be achieved with more turns on the primary coil resulting in a lower maximum frequency.

In summary, this very first attempt of developing a measurement device for thin films based on a novel approach is rated successful. While there is still plenty of room for improvements regarding the discussed errors, the advantages are a much easier and faster measurement procedure, which allows an integration of the device in the production environment. Furthermore, it enables measurements that have not been possible before like an automatable mapping of spatially resolved magnetic properties over a whole wafer or the quick determination of the properties in between two process steps allowing for a better understanding of the influence of individual treatments. Also angle-dependent measurements are feasible as exemplarily shown for the 100 nm nickel iron sample (Fig. 9.1) e.g. to analyze anisotropic properties. Though the curves for  $0^\circ$  and  $-30^\circ$  show a deviation from the reference hysteresis loop in terms of coercivity, it is noticeable that they represent an easy axis behavior because of their steep rise. The obvious assumption that the easy axis probably points along  $-15^\circ$  is supported by the measurements along  $90^\circ$  and  $60^\circ$  as these show a significantly lower gradient of the curve with the hard axis probably pointing along  $75^\circ$ , which would be perpendicular to the  $-15^\circ$  direction.

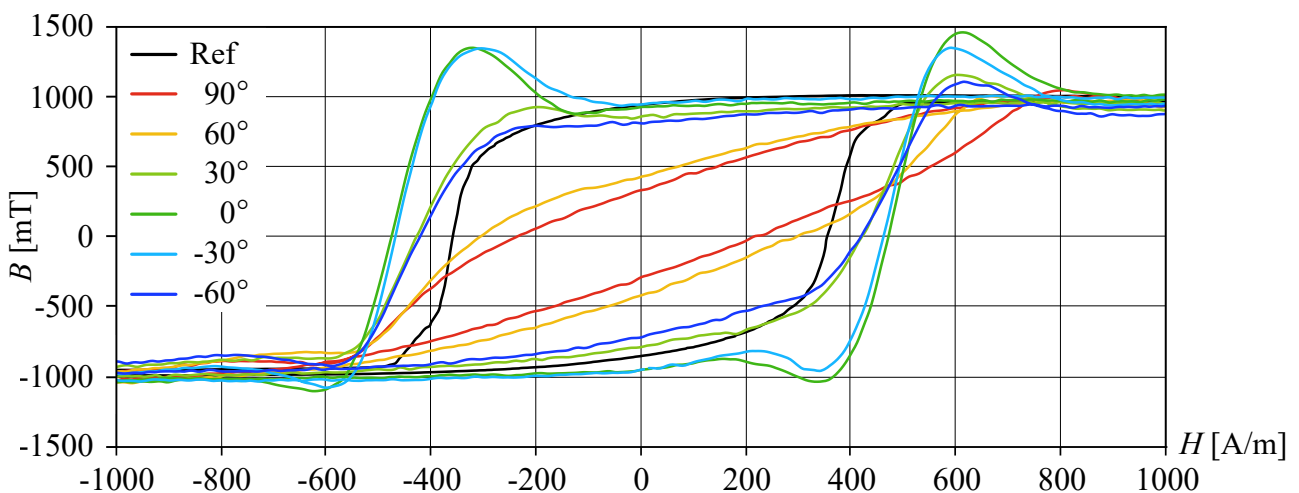


**Figure 9.1** Exemplary hysteresis loops of the 100 nm  $\text{Ni}_{81}\text{Fe}_{19}$  sample measured at 100 Hz with different excitation angles

The limitations of the device in terms of frequency range might be overcome in future by employing a smaller measurement head to allow the usage up to the megahertz range, which would help further in

developing novel high-frequency alloys for thin-film transformers. The range of this device covering already three magnitudes, however, is helpful as the hysteresis loops of the CZT film reveals. On this basis, a better forecast on the behavior and the losses at increasing frequencies is possible.

## Bibliography

- A. A.-E. Abdallah and L. Dupré. A rogowski-chattock coil for local magnetic field measurements: Sources of error. *Meas. Sci. Technol.*, 21(10):107–127, 2010. doi: 10.1088/0957-0233/21/10/107003.
- A. A.-E. Abdallah, P. Sergeant, G. Crevecoeur, L. Vandenbossche, L. Dupré, and M. Sablik. Magnetic material identification in geometries with non-uniform electromagnetic fields using global and local magnetic measurements. *IEEE Transaction on Magnetics*, 45(10):4157–4160, 2009. doi: 10.1109/TMAG.2009.2022021.
- A. Aharoni. Demagnetizing factors for rectangular ferromagnetic prisms. *Journal of Applied Physics*, 83(6):3432–3434, 1998. doi: <https://doi.org/10.1063/1.367113>.
- M. Albach. *Induktivitäten in der Leistungselektronik*. Springer Vieweg, 2017. ISBN 978-3-658-15080-8. doi: 10.1007/978-3-658-15081-5.
- Low Cost 270 MHz Differential Receiver Amplifiers*. Analog Devices, 2005. URL [https://www.analog.com/media/en/technical-documentation/data-sheets/AD8129\\_8130.pdf](https://www.analog.com/media/en/technical-documentation/data-sheets/AD8129_8130.pdf). Rev. C.
- 10 MHz, 20 V/ $\mu$ s, G = 1, 10, 100, 1000 iCMOS Programmable Gain Instrumentation Amplifier*. Analog Devices, 2012. URL <https://www.analog.com/media/en/technical-documentation/data-sheets/AD8253.pdf>. Rev. B.
- 20 mW Power, 2.3 V to 5.5 V, 75 MHz Complete DDS*. Analog Devices, 2014a. URL <https://www.analog.com/media/en/technical-documentation/data-sheets/AD9834.pdf>. Rev. D.
- High Speed, High Voltage, 1 A Output Drive Amplifier*. Analog Devices, 2014b. URL <https://www.analog.com/media/en/technical-documentation/data-sheets/ADA4870.pdf>. Rev. 0.
- Low Cost, DC to 150 MHz, Variable Gain Amplifier*. Analog Devices, 2016. URL <https://www.analog.com/media/en/technical-documentation/data-sheets/AD8330.pdf>. Rev. H.
- Application Note: Voltage to Current Conversion*. Apex Microtechnology, Inc., 2013. URL <https://www.apexanalog.com/resources/appnotes/an13u.pdf>. Rev. F.

- H. Aschenbrenner and G. Goubau. Eine anordnung zur registrierung rascher magnetischer störungen. *Hochfrequenztechnik und Elektroakustik*, 47:177–181, 1936.
- M. N. Baibich, J. M. Broto, A. Fert, F. Nguyen Van Dau, P. F., P. Etienne, G. Creuzet, A. Friederich, and J. Chazelas. Giant magnetoresistance of (001)Fe/(001)Cr magnetic superlattices. *Physical Review Letters*, 61(21):2472–2475, 1988.
- C. Beatrice, S. Dobák, E. Ferrara, F. Fiorillo, C. Ragusa, J. Füzér, and P. Kollár. Broadband magnetic losses of nanocrystalline ribbons and powder cores. *Journal of Magnetism and Magnetic Materials*, 420, 7 2016. doi: 10.1016/j.jmmm.2016.07.045.
- G. Binasch, P. Grünberg, F. Saurenbach, and W. Zinn. Enhanced magnetoresistance in layered magnetic-structures with antiferromagnetic interlayer exchange. *Physical Review B*, 39(7):4828–4830, 1989.
- O. Bottauscio, F. Fiorillo, C. Beatrice, A. Caprile, and A. Magni. Modeling high-frequency magnetic losses in transverse anisotropy amorphous ribbons. *IEEE Transactions on Magnetics*, 51(3):1–4, 2015. doi: 10.1109/TMAG.2014.2361534.
- R. M. Bozorth. *Ferromagnetism*. D. Van Nostrand Company, Inc., 1951.
- W. Brix, K. A. Hempel, and W. Schroeder. Method for the measurement of rotational power loss and related properties in electrical steel sheets. *IEEE Transactions on Magnetics*, 18(6):1469–1471, 1982. doi: 10.1109/TMAG.1982.1062088.
- W. Brix, K. A. Hempel, and F. J. Schulte. Improved method for the investigation of the rotational magnetization process in electrical steel sheets. *IEEE Transactions on Magnetics*, 20(5):1708–1710, 1984. doi: 10.1109/TMAG.1984.1063242.
- R. Busch. *Elektrotechnik und Elektronik*. Springer Vieweg, 2015. doi: 10.1007/978-3-658-09675-5\_2.
- M. Butta and J. Urdahl. Device for precise measurement of magnetic microwire bh loop at low frequency. In *Measurement 2009, Proceedings of the 7th International Conference*, pages 302–305, 2009.
- M. Butta, G. Infante, P. Ripka, G. A. Badini-Confalonieri, and M. Vázquez. M-h loop tracer based on digital signal processing for low frequency characterization of extremely thin magnetic wires. *Review of Scientific Instruments*, 80(8):083906, 2009. doi: 10.1063/1.3206264.
- A. P. Chattock. IX. on a magnetic potentiometer. *The London, Edinburgh, and Dublin Philosophical Magazine and Journal of Science*, 24(146):94–96, 1887. doi: 10.1080/14786448708628063.
- D.-X. Chen, E. Pardo, and A. Sanchez. Demagnetizing factors for rectangular prisms. *IEEE Transactions on Magnetics*, 41(6):2077–2088, 2005. doi: 10.1109/TMAG.2005.847634.



- D.-X. Chen, E. Pardo, and A. Sanchez. Fluxmetric and magnetometric demagnetizing factors for cylinders. *Journal of Magnetism and Magnetic Materials*, 306(1):135–146, 2006. ISSN 0304-8853. doi: 10.1016/j.jmmm.2006.02.235.
- A. P. Colombo, T. R. Carter, A. Borna, Y.-Y. Jau, C. N. Johnson, A. L. Dagele, and P. D. D. Schwindt. Four-channel optically pumped atomic magnetometer for magnetoencephalography. *Optics express*, 24(14):15403–15416, 2016. doi: 10.1364/OE.24.015403.
- T. Coussens, C. Abel, A. Gialopsou, M. G. Bason, T. M. James, F. Orucevic, and P. Kruger. Modular optically-pumped magnetometer system. *arXiv preprint arXiv:2106.05877*, 2021.
- CT100 1D Linear Sensor*. Crocus Technology, 2020. URL <https://crocus-technology.com/wp-content/uploads/2020/04/CT100-Data-Sheet-Rev1.9.pdf>. Rev. 1.9.
- B. D. Cullity and C. D. Graham. *Introduction to Magnetic Materials*. IEEE Press, 2009.
- J. G. Deak, Z. Zhou, and W. Shen. Tunneling magnetoresistance sensor with pt level 1/f magnetic noise. *AIP Advances*, 7(5):056676, 2017. doi: 10.1063/1.4978465.
- I. Fergen, K. Seemann, A. Weth, and A. Schüppen. Soft ferromagnetic thin films for high frequency applications. *Journal of Magnetism and Magnetic Materials*, 242-245:146–151, 2002. ISSN 0304-8853. doi: [https://doi.org/10.1016/S0304-8853\(01\)01185-4](https://doi.org/10.1016/S0304-8853(01)01185-4). URL <https://www.sciencedirect.com/science/article/pii/S0304885301011854>.
- F. Fiorillo. Measurements of magnetic materials. *Metrologia*, 47(2):S114–S142, mar 2010. doi: 10.1088/0026-1394/47/2/s11.
- E. C. Fischer, T. N. Bierwirth, F. Dencker, and M. C. Wurz. Fabrication of a low profile planar transformer using a dual pcb approach. In *MikroSystemTechnik Congress 2021*, pages 1–4, 2021.
- P. J. Flanders. An alternating-gradient magnetometer (invited). *Journal of Applied Physics*, 63(8):3940–3945, 1988. doi: 10.1063/1.340582.
- S. Foner. Versatile and sensitive vibrating-sample magnetometer. *Review of Scientific Instruments*, 30(7):548–557, 1959. doi: 10.1063/1.1716679.
- Y. Gao, Y. Araki, H. Dozono, K. Muramatsu, W. Guan, J. Yuan, C. Tian, and B. Chen. Modeling of anomalous eddy current losses due to movement of domain walls in particles of a soft magnetic composite. *IEEE Transactions on Magnetics*, 56(4):1–4, 2020. doi: 10.1109/TMAG.2019.2956977.
- N. Ghodke, S. N. Kane, S. S. Khinchi, and A. Gupta. Ac/dc constant current driver for inductive load (2ma to 2a). *National Symposium on Instrumentation (NSI-30)*, 38, 2005.
- T. Gilbert. A phenomenological theory of damping in ferromagnetic materials. *IEEE Transactions on Magnetics*, 40(6):3443–3449, 2004. doi: 10.1109/TMAG.2004.836740.

- C. A. Grimes, P. L. Trouilloud, and R. M. Walser. A new swept-frequency permeameter for measuring the complex permeability of thin magnetic films. *IEEE Transactions on Magnetics*, 24(1):603–610, 1988. doi: 10.1109/20.43991.
- G. Herzer. Chapter 3 nanocrystalline soft magnetic alloys. volume 10 of *Handbook of Magnetic Materials*, pages 415–462. Elsevier, 1997.
- G. Herzer. Modern soft magnets: Amorphous and nanocrystalline materials. *Acta Materialia*, 61(3): 718–734, 2013. ISSN 1359-6454. doi: 10.1016/j.actamat.2012.10.040.
- H.-I. Hsiang. Progress in materials and processes of multilayer power inductors. *Journal of Materials Science: Materials in Electronics*, 31:16089–16110, 2020. doi: 10.1007/s10854-020-04188-8.
- E. Huber and M. Urban. Helmholtzspulen zur kalibrierung von magnetfeldsensoren. *EUR(Luxembourg)*, 1995. ISSN 0947-8620.
- A. Hubert and R. Schäfer. *Magnetic Domains: the Analysis of Magnetic Microstructures*. Springer Science & Business Media, 2008.
- D. Hunter. Two new devices help reinvent the signal generator. *Analog Dialogue*, 48(4):19–22, 2014. URL <https://www.analog.com/media/en/analog-dialogue/volume-48/number-4/articles/reinvent-the-signal-generator.pdf>.
- IEC. *IEC 60404-2: Magnetic materials – Part 2: Methods of measurement of the magnetic properties of electrical steel strip and sheet by means of an Epstein frame*. International Electrotechnical Commission, 2008. ISBN 2-8318-9835-8.
- S. Ikeda, J. Hayakawa, Y. M. Lee, F. Matsukura, Y. Ohno, T. Hanyu, and H. Ohno. Magnetic tunnel junctions for spintronic memories and beyond. *IEEE Transactions on Electron Devices*, 54(5): 991–1002, 2007. doi: 10.1109/TED.2007.894617.
- E. Ivers-Tiffée and W. von Münch. *Werkstoffe der Elektrotechnik*. B.G. Teubner Verlag, 2007. ISBN 978-3-8351-0052-7.
- N. Jiang. A large current source with high accuracy and fast settling. *Analog Dialogue*, 52(4):8–11, 2018. URL <https://www.analog.com/media/en/analog-dialogue/volume-52/number-4/a-large-current-source-with-high-accuracy-and-fast-settling.pdf>.
- D. C. Jiles. Frequency dependence of hysteresis curves in conducting magnetic materials. *Journal of Applied Physics*, 76(10):5849–5855, 1994. doi: 10.1063/1.358399.
- M. Julliere. Tunneling between ferromagnetic films. *Physics Letters A*, 54(3):225–226, 1975. ISSN 0375-9601. doi: 10.1016/0375-9601(75)90174-7.

- E. Kallenbach, R. Eick, P. Quendt, T. Ströhla, K. Feindt, M. Kallenbach, and O. Radler. *Elektromagnete*. Vieweg+Teubner Verlag, 2012. ISBN 978-3-8348-0968-1.
- C. Kitchin and L. Counts. *A Designer's Guide to Instrumentation Amplifiers, 3<sup>rd</sup> Edition*. Analog Devices, Inc., 2006.
- T. Kubota, Y. Ina, Z. Wen, and K. Takanashi. Interface tailoring effect for heusler based CPP-GMR with an L1<sub>2</sub>-type Ag<sub>3</sub>Mg spacer. *Materials*, 11(2), 2018. ISSN 1996-1944. doi: 10.3390/ma11020219.
- H. T. Le, R. I. Haque, Z. Ouyang, S. W. Lee, S. I. Fried, D. Zhao, M. Qiu, and A. Han. MemS inductor fabrication and emerging applications in power electronics and neurotechnologies. *Microsystems and Nanoengineering*, 7, 2021. doi: 10.1038/s41378-021-00275-w.
- P. Lenox, L. K. Plummer, P. Paul, J. E. Hutchison, A. Jander, and P. Dhagat. High-frequency and high-field hysteresis loop tracer for magnetic nanoparticle characterization. *IEEE Magnetics Letters*, 9: 1–5, 2017. doi: 10.1109/LMAG.2017.2768521.
- J. Lenz and A. S. Edelstein. Magnetic sensors and their applications. *IEEE Sensors Journal*, 6(3): 631–649, 2006. doi: 10.1109/JSEN.2006.874493.
- B. Li, Q. Li, and F. C. Lee. A novel PCB winding transformer with controllable leakage integration for a 6.6 kW 500 kHz high efficiency high density bi-directional on-board charger. In *2017 IEEE Applied Power Electronics Conference and Exposition (APEC)*, pages 2917–2924, 2017. doi: 10.1109/APEC.2017.7931111.
- L. Li and D. W. Lee. High-frequency responses of granular CoFeHfO and amorphous CoZrTa magnetic materials. *Journal of Applied Physics*, 101(12):631–649, 2007. doi: 10.1063/1.2749419.
- N. Marconato, R. Cavazzana, P. Bettini, and A. Rigoni. Accurate magnetic sensor system integrated design. *Sensors*, 20(10), 2020. ISSN 1424-8220. doi: 10.3390/s20102929.
- M. Marks, Z. Hassan, and K. Cheong. Ultrathin wafer pre-assembly and assembly process technologies: A review. *Critical Reviews in Solid State and Materials Sciences*, 40(5):1–40, 2015. doi: 10.1080/10408436.2014.992585.
- L. Ming, Z. Xin, C. Yin, M. Chen, and P. C. Loh. Integrator design of the rogowski current sensor for detecting fast switch current of sic devices. In *2019 IEEE Energy Conversion Congress and Exposition (ECCE)*, pages 4551–4557, 2019. doi: 10.1109/ECCE.2019.8911874.
- D. Miyagi, D. Otome, M. Nakano, and N. Takahashi. Measurement of magnetic properties of nonoriented electrical steel sheet at liquid nitrogen temperature using single sheet tester. *IEEE Transactions on Magnetics*, 46(2):314–317, 2010. doi: 10.1109/TMAG.2009.2033551.

- T. Miyazaki and N. Tezuka. Giant magnetic tunneling effect in fe/al<sub>2</sub>o<sub>3</sub>/fe junction. *Journal of Magnetism and Magnetic Materials*, 139(3):L231–L234, 1995. ISSN 0304-8853. doi: 10.1016/0304-8853(95)90001-2.
- F. Müller, G. Bavendiek, B. Schauerte, and K. Hameyer. Measurement and simulation of a rotational single sheet tester. *Archives of Electrical Engineering*, 68(1), 2019.
- A. C. Munce and J.-U. Thiele. Hitachi’s overseas research on hard disk drive. *Hitachi Rev.*, 55: 150–154, 2006.
- T. Nakata, Y. Kawase, and M. Nakano. Improvement of measuring accuracy of magnetic field strength in single sheet testers by using two h coils. *IEEE Transactions on Magnetics*, 23(5):2596–2598, 1987. doi: 10.1109/TMAG.1987.1065607.
- A. Neudert, J. McCord, R. Schäfer, and L. Schultz. Dynamic anisotropy in amorphous cozrta films. *Journal of Applied Physics*, 95(11):6595–6597, 2004. doi: 10.1063/1.1667796.
- S. Nguedjang Kouakeuo, Y. Tena Deffo, B. Ducharne, L. Morel, M. Raullet, P. Tsafack, J. Garcia-Bravo, and B. Newell. Embedded printed magnetic needle probes sensor for the real-time control of the local induction state through a laminated magnetic core. *Journal of Magnetism and Magnetic Materials*, 505:166767, 2020. ISSN 0304-8853. doi: 10.1016/j.jmmm.2020.166767.
- C. Ó Mathúna, N. Wang, S. Kulkarni, and S. Roy. Review of integrated magnetics for power supply on chip (PwrSoC). *IEEE Transactions on Power Electronics*, 27(11):4799–4816, 2012. doi: 10.1109/TPEL.2012.2198891.
- J. A. Osborn. Demagnetizing factors of the general ellipsoid. *Phys. Rev.*, 67:351–357, 1945. doi: 10.1103/PhysRev.67.351.
- G. Pan. Chapter 10 - Thin films for high-density magnetic recording. In H. Singh Nalwa, editor, *Handbook of Thin Films*, pages 495–553. Academic Press, Burlington, 2002. ISBN 978-0-12-512908-4. doi: 10.1016/B978-012512908-4/50075-8.
- J. A. J. Pettinga and J. Siersema. A polyphase 500 ka current measuring system with rogowski coils. In *IEE Proceedings Pt. B (Electric Power Applications)*, volume 130, pages 360–363, 1983. doi: 10.1049/ip-b.1983.0054.
- H. Pfützner and G. Krismanić. The needle method for induction tests: Sources of error. *IEEE Transactions on Magnetics*, 40(3):1610–1616, 2004. doi: 10.1109/TMAG.2004.826617.
- H. Pfützner and G. Shilyashki. Concept for industrially relevant magnetic power loss measurements by single sheet tester and epstein frame testers. *CIGRE Science&Engineering*, 9:95–109, 2017.
- H. Pfutzner, E. Mulasalihovic, H. Yamaguchi, D. Sabic, G. Shilyashki, and F. Hofbauer. Rotational magnetization in transformer cores – a review. *IEEE Transactions on Magnetics*, 47(11):4523–4533, 2011. doi: 10.1109/TMAG.2011.2151201.

- P. Plötz and W. Eichhammer. *Zukunftsmarkt effiziente elektromotoren*. Karlsruhe: *Fraunhofer Institut für System- und Innovationsforschung (ISI)*, 2011.
- R. H. Pry and C. P. Bean. Calculation of the energy loss in magnetic sheet materials using a domain model. *Journal of Applied Physics*, 29(3):532–533, 1958. doi: 10.1063/1.1723212.
- C. Reig, S. C. de Freitas, and S. C. Mukhopadhyay. *Giant Magnetoresistance (GMR) Sensors*. Springer Science+Business Media, 2013. ISBN 978-3-642-37171-4. doi: 10.1007/978-3-642-37172-1.
- P. Ripka. *Magnetic sensors and magnetometers*. Artech house, 2021. ISBN 9781630817428.
- P. Ripka and M. Janosek. Advances in magnetic field sensors. *IEEE Sensors journal*, 10(6):1108–1116, 2010. doi: 10.1109/JSEN.2010.2043429.
- R. L. Sanford. Performance of the fahy simplex permeameter. *Bureau of Standards Journal of Research*, 4:703–709, 1930. doi: 10.6028/JRES.004.046.
- R. L. Sanford and J. M. Barry. Determination of the magnetic induction in sheet steel. *Scientific Papers of the Bureau of Standards*, 21:727–742, 1927.
- S. L. Selvaraj, M. Haug, C. S. Cheng, D. Dinulovic, L. Peng, K. E. Shafey, Z. Ali, M. Shousha, Y. C. Ng, N. Aziz Yosokumoro, L. Lehmann, and M. Wieland. On-chip thin film inductor for high frequency DC-DC power conversion applications. In *2020 IEEE Applied Power Electronics Conference and Exposition (APEC)*, pages 176–180, 2020. doi: 10.1109/APEC39645.2020.9124544.
- K. Senda, M. Ishida, K. Sato, M. Komatsubara, and T. Yamaguchi. Localized magnetic properties in grain-oriented electrical steel measured by needle probe method. *Journal of Magnetism and Magnetic Materials*, 126(4):942–949, 1999. doi: 10.1002/(SICI)1520-6416(199903)126:4<1::AID-EEJ1>3.0.CO;2-7.
- K. Senda, M. Kurosawa, M. Ishida, M. Komatsubara, and T. Yamaguchi. Local magnetic properties in grain-oriented electrical steel measured by the modified needle probe method. *Journal of Magnetism and Magnetic Materials*, 215-216:136–139, 2000. doi: 10.1016/S0304-8853(00)00096-2.
- TF952 MagnetoResistive Magnetic Field Sensor*. Sensitec, 2020. URL [https://www.sensitec.com/fileadmin/sensitec/Service\\_and\\_Support/Downloads/Data\\_Sheets/Tx900/SENSITEC\\_TF952\\_DSE\\_02.pdf](https://www.sensitec.com/fileadmin/sensitec/Service_and_Support/Downloads/Data_Sheets/Tx900/SENSITEC_TF952_DSE_02.pdf).
- G. H. Shirkoohi and A. S. Kontopoulos. Computation of magnetic field in rogowski-chattock potentiometer (rcp) compensated magnetic testers. *Journal of Magnetism and Magnetic Materials*, 133(1):587–590, 1994. doi: 10.1016/0304-8853(94)90629-7.
- J. Sievert. Recent advances in the one- and two-dimensional magnetic measurement technique for electrical sheet steel. *IEEE Transactions on Magnetics*, 26(5):2553–2558, 1990. doi: 10.1109/20.104796.

- D. Stephane, I. Cimrak, P. Sergeant, and A. Abdallah. Demagnetizing factors for rectangular prisms. *Mathematical Problems in Engineering*, 2010(3), 2010. doi: 10.1155/2010/574153.
- E. C. Stoner. Xcvii. the demagnetizing factors for ellipsoids. *The London, Edinburgh, and Dublin Philosophical Magazine and Journal of Science*, 36(263):803–821, 1945. doi: 10.1080/14786444508521510.
- O. Stupakov. Controllable magnetic hysteresis measurement of electrical steels in a single-yoke open configuration. *IEEE Transactions on Magnetics*, 48(12):4718–4726, 2012. doi: 10.1109/TMAG.2012.2203139.
- N. A. Stutzke, S. E. Russek, D. P. Pappas, and M. Tondra. Low-frequency noise measurements on commercial magnetoresistive magnetic field sensors. *Journal of Applied Physics*, 97(10):10Q107, 2005. doi: 10.1063/1.1861375.
- KMY KMZ Linear Magnetic Field Sensor*. TE Connectivity, 2017. URL [https://www.mouser.de/datasheet/2/418/5/NG\\_DS\\_KMY\\_KMZ\\_A1-1130282.pdf](https://www.mouser.de/datasheet/2/418/5/NG_DS_KMY_KMZ_A1-1130282.pdf). Rev. 4.
- P. M. Tedrow and R. Meservey. Spin-dependent tunneling into ferromagnetic nickel. *Phys. Rev. Lett.*, 26:192–195, 1971. doi: 10.1103/PhysRevLett.26.192.
- Application Note: AN-1515 A Comprehensive Study of the Howland Current Pump*. Texas Instruments, 2013. URL <https://www.ti.com/lit/an/snoa474a/snoa474a.pdf>.
- OPA548 High-Voltage, High-Current Operational Amplifier*. Texas Instruments, 2019. URL <https://www.ti.com/lit/ds/symlink/opa548.pdf>. Rev. D.
- C. Tran and J. Rombola. A low power, low cost, differential input to a single-ended output amplifier. *Analog Dialogue*, 51(3):53–54, 2017. URL <https://www.analog.com/media/en/analog-dialogue/raqs/raq-issue-145.pdf>.
- S. Tumanski. *Thin Film Magnetoresistive Sensors*. Institute of Physics Publishing, 2001. ISBN 9780429146046. doi: 10.1201/9781420033243.
- S. Tumanski. A multi-coil sensor for tangential magnetic field investigations. *Journal of Magnetism and Magnetic Materials*, 242-245(2):1153–1156, 2002. doi: 10.1016/S0304-8853(01)01302-6.
- S. Tumanski. Induction coil sensors – a review. *Measurement Science and Technology*, 18(3):R31–R46, 2007. doi: 10.1088/0957-0233/18/3/R01.
- S. Tumanski. *Handbook of magnetic measurements*. CRC press, 2011. ISBN 9781439829516.
- S. Tumanski. Modern magnetic field sensors – a review. *Organ*, 10(1):1–12, 2013.
- H. Ueda and T. Watanabe. Several problems about sensitivity and frequency response of an induction magnetometer. *Geophysics*, 22(3-4):107–127, 1975.

- T. Wurft. *Investigation of the Magnetic Vortex State for Spin-Valve Sensors*. Dissertation, Bielefeld University, 2018.
- M. C. Wurz and M. S. Prediger. Physical sensors: Magnetic sensors. In *Reference Module in Biomedical Sciences*. Elsevier, 2021. ISBN 978-0-12-801238-3. doi: 10.1016/B978-0-12-822548-6.00054-6.
- Y.-J. Xia, Z.-D. Zhang, S.-L. Zhu, Z.-X. Xia, and R. Zhang. A precision analog integrator system for heavy current measurement in mfdc resistance spot welding. *Measurement Science and Technology*, 27:025104–11, 12 2015. doi: 10.1088/0957-0233/27/2/025104.
- S. Yang and J. Zhang. Current progress of magnetoresistance sensors. *Chemosensors*, 9(8), 2021. ISSN 2227-9040. doi: 10.3390/chemosensors9080211.
- L. Zhang. Silicon process and manufacturing technology evolution: An overview of advancements in chip making. *IEEE Consumer Electronics Magazine*, 3(3):44–48, 2014. doi: 10.1109/MCE.2014.2317896.
- S. Zurek. *Two-Dimensional Magnetisation Problems in Electrical Steels*. PhD thesis, Cardiff School of Engineering, March 2005.





# Wissenschaftlicher Werdegang

## Persönliche Angaben

Eike Christian Fischer

geboren am 08.08.1988 in Kiel

## Berufstätigkeit

- |                   |   |
|-------------------|---|
| 04/2021 – 10/2022 | Co-Gruppenleiter für Magnetische und Biomedizinische Anwendungen  |
| 09/2016 – 10/2022 | Wissenschaftlicher Mitarbeiter am Institut für Mikroproduktionstechnik, Leibniz Universität Hannover                                  |
| 09/2014 – 02/2015 | Praktikant im Bereich der Testautomatisierung bei der F&E Abteilung der Volkswagen Group China in Peking                              |
| 10/2011 – 05/2014 | Studentische Hilfskraft am Institut für Mikroproduktionstechnik und Institut für Mechatronische Systeme, Leibniz Universität Hannover |

## Studium

- |                   |  |
|-------------------|--|
| 05/2015 – 11/2015 | Diplomarbeit am Institut für Montagetechnik, Leibniz Universität Hannover  |
| 10/2008 – 01/2016 | Diplomstudiengang Maschinenbau mit den Vertiefungsrichtungen Maschinen, Systeme und Automatisierung in der Produktionstechnik und Bewegungstechnik und Robotik |

## Schulbildung

- |                   |  |
|-------------------|--|
| 09/1998 – 07/2007 | Gymnasium der Isarnwohld-Schule, Gettorf |
|-------------------|--|